Faraday Slicing Polarized Radio Sources

by
Wasim Raja

A Thesis submitted to
Jawaharlal Nehru University
New Delhi
for the Degree of
Doctor of Philosophy

2014

Raman Research Institute
Bangalore – 560 080
India

Declaration

I hereby declare that the work reported in this thesis is entirely original. This thesis is composed independently by me at Raman Research Institute under the guidance of Prof. Avinash Deshpande. I further declare that the subject matter presented in this thesis has not previously formed the basis for the award of any degree, diploma, membership, associateship, fellowship or any other similar title of any university or institution.

Wasim Raja
Astronomy and Astrophysics
Raman Research Institute
Bangalore, 560080
INDIA.

Certificate

This is to certify that the thesis entitled **"Faraday slicing polarized radio sources"** submitted by Wasim Raja for the award of the degree of Doctor of Philosophy of Jawaharlal Nehru University is his original work. This has not been published or submitted to any other University for any other Degree or Diploma.

Director
Raman Research Institute
Bangalore, 560080
INDIA.

Avinash Deshpande
(Thesis Advisor)

Acknowledgments

After the many years that I have spent at the institute trying(?) to get to a stage where I would be writing the piece that you are reading this moment (hopefully with intent) I can only tell you that you are sharing a very special moment in the history of my life this far. Is this a happy moment? Well, it could not have been otherwise...

I had fallen in love with the place the very first day I had come to appear for my interview. While the June rains kept fuelling my inner desire to get selected and a fear of failure kept perpetually bothering me, I heard my name being called for the final interview after an eight hour wait. I think it was Dwaraka who asked me if I had ever heard of night vision goggles, and my answer that my recent exposure to Hollywood movies indeed allowed me such a privilege (Wien popped up only later in the discussion), set the whole panel into laughter. I do not remember what Kumar et al did to me in the next half an hour, but I sure enjoyed the experience, so much so that on coming out from the interview, instead of worrying about whether or not I would be inside the campus or out, all I could think of was a way to dissipate my ecstasy! My first girlfriend Radha (sorry Marisa, I met her first) suggested that I visit Vrindavan (gardens).

A month later when I got the call letter, I did not have to think twice about joining. Is there a regret? Well, I have not had the opportunity to think of an answer yet. And for that I would like to thank my friends, my mentors and all my well wishers here at RRI and elsewhere.

The liveliness I witnessed in and around RRI (beginning with the interview panel) extended way beyond the duration of the interview. The open-ness with which the senior students Dipanjan, CSG, Suthirtha, Abhijit, Atish, Harsha, Resmi, Rahul, Brindaban, Sajal, Santanu, Arif, Antara, Hari, Bibhu, RK interacted, and facilitated me to interact, is something I will always cherish. Many sessions (inside as well as

beyond the classroom) with my batchmates JK, Ruta, Peeyush, Yogesh, Arijit, Nandan, Nagaraju, Rakesh, Satyam, Ravi remains memorable till this day.

I would like to take this opportunity to mention and thank some of the people I consider myself lucky to have met and interacted closely with:

Hanumantha, Lakshmamma, Ramanna, Jayamma, Muniyappa, Shiva, Manju and Gangadhara for your efforts in keping the institute clean; Uma Ji, Sharada Ji, Mangala Ji, Padma Ji, Narayanappa and Raju for taking active responsibility in feeding me; Prabu, Som, Aswath, Peeyush and Vinutha for the many things I could learn from you and for being a constant source of inspiration; Shantha, Dr. Baliga and Dr. Sanjay Rao for ensuring our healthy stay; Jacob, Sridhar and Krishnamurthy for keeping all our computation facilities healthy and for all those innumerable chats we have had on so many diverse topics (I will always cherish those ;-) ; Balaram, Pasha, Mohan, Prakash, Venkatesh for making the many drives we had to Ooty, GBD, Tirupati as well as within Bangalore pleasurable and safe; Patil, Meera, Geetha, Vrinda, Manjunath, Nagaraj, Kiran, Girija for your inspiring efforts in making the RRI library facility one of the best I have come across; Ateequllah, Durai, Elumalai, Gokul and Damodaran for providing all the help required during various stages of several projects I participated in, even at the shortest of notice; Murthy for ensuring any item I had ever indented, was delivered at the shortest possible time; Radha, Marisa and Krishna for not just ensuring smooth administration, but for being there whenever I had needed you; Mamatha, Radhakrishna, Manju, Latha, Harini and Vidya for your tireless efforts in managing most of us weirdos and taking all the care needed to ensure smooth functioning of almost everything associated with our daily lives at the institute; Sarabagopalan, Sujatha, Girish, Vani, KBR, Nagaraj, GK, Madhavi, Kamini, Kasturi, Mamatha, Arasi, Vinod, Raghu, Sandhya, Rishin, Durai for your constant encouragement and the lively discussions during tea; Ram (hope you will keep enlivening the musical events to be organised in future as well), Jayaram, Pushparaj, Meena, Vasudha, Chandra Sekara, Sashi (cherish robbing you of your *appams*

at lunch), my badminton buddy GB and my photographer friend Raju, for your valuable friendships; Biman, Biswajit, Desh, Dwaraka, Udaya, Ramesh, Shiv, Sridhar, Dipankar, Sunita, Lakshmi, Shukre, Bhandari, CRS and Ravi for the many technical discussions at the Astro lounge.

The data presented in the thesis were collected from several facilities. I would like to thank the staff members and the observers of the GMRT, the MST Radar (Tirupati), the Gauribidanaur Telescope, and the Arecibo Observatory, for the enormous effort they put in in maintaining these systems and enabling reliable monitoring of the Universe. I cherish the several observing sessions conducted together with Prasad, Yogesh and Desh at the MST; Juan, Chris and Tapasi at the Arecibo Observatory; Yogesh, Vinutha, Desh, Aswath and Prabu at GBD & Ooty; Arvind, Udaya, Desh, Richard, Sanjay, Shilpa, Deepak, Jaiprakash, Santaji, Jitendra and Nilesh at the GMRT. There is so much I could learn from you all.

The many visits to NCRA and GMRT would not have been as pleasant without friends like Nirupam, Susmita, Vishal, Sambhit, Dipanjan, Ishwar, Reena, Yashwant, Nimisha, Bhaswati and Jayanto. It has always been a pleasure to talk to the insightful Rajaram.

PhD life would have been dull and much less interesting and colourful without some wonderful people. Thank you Renu, Mamta, Ruta, Rabbi, CSG, Atish, Kanhaiya, Rahul, Shraddha, Sanghamitra, Brindaban, Dipanjan, Abhijit, Tanmoy, Jayant, Nikhil, Harshad, Ajinkya, Chandrika, Sonal, Abha, Prakriti, Nayana, Nivedita, Gayathri (J), Anupam, Deepak, Mriganko, Kshitij, Suman, Arnab, Debasish, Rajib, Jyothi, Samim, Anjan, Giri, Chandrakant, Tridib, Mahavir, Jagdish, Lijo, Sourav, Arpita, Nazma, Karamveer, Gayathri (R), Priyanka, Rekhesh, Sushila, and my younger friends Mitali, Nandika, Roshni, Nachi, Ani, Kush, Tush, Steve, Alan, Mithi, Manasa, Ambu, Akshu, Tukun, Ananya, Isa, Sahana and Vaishnavi for adding to the liveliness of this place.

I feel privileged to have in my life my friends Sankhadeep, Vineet, Kumarjit, Prasun, Trideep, Santanu, Chaitra, Arif, Nishant, Subhash, Sandeep and Yogesh whose unfailing trust in my abilities and unforgiving criticisms on my actions inspire me to propel myself in the desired direction; Antara, Vedaprana, Vidya, Venkatesh, Harsha, Chandreyee (Gunja), Kshitija (Chuttki), Apu and Hanif Ka for your love and for accepting me the way I am; Nandan, Arijit, Amrita and Mamta for ensuring that I do not miss the fun outside of "research" life; JK for being a wonderful sportsman both in spirit and in practice.

Of the things I would miss are the badminton games at RRI, fights with Arif and Nandan, the swimming challenges at IISc together with Abhijit, the football games and the associated commotion, Chitra's breads, Udaya's laughter, Kumar's questions, Chandreyee and Nipanjana's "barkings", Vidya's scoldings and Ranjana's modakas during Ganesha. I will miss the many walks with Desh, which would often extend to hours, and during which I was introduced to many key concepts in imaging, signal processing as well as other philosophies.

I am grateful to Shiv and Bhargavi for all their help and for being there at a crucial stage of this thesis. Gita aunty and Subhas, I am grateful that you allowed me place in your hearts. I cannot imagine those last days without all of you around.

This thesis would never have been possible without the constant encouragement from and the unimaginable patience of Desh whose role as my thesis guide kept propelling me forward towards reaching this end.

I thank Chris Salter, Harsha, Yogesh and Nishant who painstakingly read the manuscript at various stages, and whose suggestions have led to significant improvement in the presentation of its contents. Thank you Hema and Sridhar for your role as members of my advisory committee, as well as all your encouragement and support that has

come a long way in ensuring the completion of this thesis.

My gratitude to Maa, Baba, Aaya and Apu for the faith they have posed, the patience they have demonstrated and the support they have been unquestioningly extending throughout the course of my life.

Wasim Raja
(Raman Research Institute)

Contents

List of Figures

List of Tables

Chapter 1

Introduction

"...But in every case that I have discussed, and many which I have not, it is the polarization that is laying bare the magnetic field which Eugene Parker, its highest priest, has called 'the radical element responsible for the continuing thread of cosmic unrest.' " – Rad, XIIth Milne Lectures, 1988 (Radhakrishnan, 1989).

1.1 A brief history of radio polarization measurements

The term "polarization" was coined by the French engineer, mathematician and physicist Etienne-Louis Malus who discovered in 1808 the phenomenon while looking at the reflection of the setting sun from the window panes of the Luxembourg Palace in Paris, through a piece of Iceland spar that showed variation in the intensity of the images as he rotated the crystal.

Polarization observations provide information that are complementary to those provided by total intensity observations. They reveal useful information about various physical properties of the source of radiation as well as the intervening medium through which the radiation propagates. Over the years, progress in technology has

enabled studying polarization in not just the optical band of the electro-magnetic spectrum, but also in the radio and the X-ray wavelengths. Radio polarization measurements are used to map astrophysical magnetic fields. From emission mechanisms of pulsars to the magnetic morphology of the Galaxy, polarization studies have been crucial in providing vital clues.

Although we now know that radiation at the low radio frequencies are associated with the synchrotron emission mechanism, their origin was not clear until a long time after Jansky's discovery of cosmic radio emission in 1933, and Reber's mapping of it in 1944. This was so because at shorter wavelengths, where most of the astronomical observations were carried out in the earlier years, the sources are of thermal origin. However, the spectra of sources observed at radio wavelengths clearly showed non-thermal component. The observation of cosmic radio emission thus eluded interpretation for some time.

The solar astrophysicists were the first ones to look for alternate explanation. Their observation of the sun also showed non-thermal emission components. Alfvén & Herlofson (1950) suggested that the radio radiation could result from synchrotron mechanism wherein highly energetic electrons gyrate in a magnetic field. In the same year, Kiepenheuer (1950) extended this to explain the non-thermal halo component of the galactic radio emission. He suggested that cosmic-ray electrons trapped in the galactic magnetic field produced the observed radio emission. The acceleration of the particles being perpendicular to the direction of the magnetic field, synchrotron radiation would be linearly polarized in a plane perpendicular to both the direction of propagation and the magnetic field. Thus, detection of linear polarization in the emission would provide unfailing evidence for the emission mechanism to be synchrotron in nature. A positive indication indeed resulted from the observations by Razin in the Soviet Union. Unfortunately however, these results could not be verified by others owing to enormous complexity associated with polarization observations.

It was the Crab nebula that finally provided compelling evidence for the synchrotron emission mechanism. The Russian astrophysicist Shklovsky, in 1953, proposed "*... that emission of the Crab nebula at radio and optical bands is synchrotron radiation of relativistic electrons in the magnetic field.*" Gordon and Ginzburg independently pointed out in 1954 that if Shlovsky's hypothesis were to be true, the optical radiation should also be polarized. The same year, Dombrovskii confirmed this through his optical observations of the Crab nebula. These early findings were confirmed in the studies by Oort and Walraven who provided the first maps of magnetic fields in a source of astrophysical origin.

In the radio regime, polarization studies were pioneered by the group led by Cornell Mayer at the Naval Research Laboratory (NRL) in Washington, D.C. Interestingly enough the first polarized source they detected was none other than the Crab nebula. This was in 1957. At very short radio wavelengths ($\lambda \sim 3$ *cm*), they found that the radio emission from the nebula was substantially polarized ($\sim 8\%$). The polarization position angle was also close to those derived at optical frequencies. Surprisingly however, for half a decade thereafter, although hundreds of non-thermal radio sources, both galactic and extra-galactic, had been discovered, not a single one could be detected in polarization with confidence, barring of course the Crab nebula, which in the words of Richard Wielebinski, "*... is like the 'Rosetta Stone' of radio astronomy as it allowed progress in our understanding of cosmic radio emission.*" (Wielebinski, 2012).

With little doubt remaining about the nature of the emission mechanism being synchrotron, and with theories suggesting high degree of intrinsic linear polarization (up to 75%) from such non-thermal sources (Westfold, 1959; Ginzburg & Syrovatskii, 1969), non-detection of polarized emission from so many non-thermal radio sources led some of the radio astronomers to put in considerable effort in devising better measurements of polarization by designing suitable instruments as well as developing appropriate calibration techniques. However, even for the Crab nebula, the polarization detected at relatively longer wavelengths (~ 20 cm) by the group at Caltech

observatory, was lower than 2%. For the other three brightest radio sources (Virgo-A, Cas-A and Cygnus-A), the degree of linear polarization observed at 20 cm was even more feeble. The reason for such severe depolarization was not immediately clear, and it took a while before the community of radio astronomers understood these aspects in detail, and started restoring faith in the practical usefulness of any polarimetric measurements.

The emphasis on polarimetric observation was revived in the 1960's, largely due to the efforts of several pioneers in the field of radio polarimetry – Radhakrishnan & Roberts (1960) detected polarized emission from Jupiter. Galactic diffuse polarized emission was detected by Westerhout et al. (1962) and Wielebinski & Shakeshaft (1962). About the same time, polarization was detected in two important extragalactic sources – Cygnus-A (Mayer et al., 1962a,b) and Centaurus-A (Mayer et al., 1962b; Bracewell et al., 1962). The polarization measured in these carefully designed experiments could not be attributed to the instrument, confirming on one hand, the synchrotron emission interpretation, and at the same time, laying the foundation for the study of cosmic magnetic fields in radio sources.

The resulting surge in radio polarization studies led to the discovery of many polarized sources. The understanding of many of the reasons for which earlier observations failed to detect polarized radiation also started becoming clearer – non-idealities in the instruments as well as depolarization within the telescope beam being the obvious reasons. Indeed, while the polarization in the Crab nebula was only about a few percent on the average, interferometric observations having high angular resolution revealed, in parts of the nebula, degree of polarization as high as 60% which is close to the theoretical limit. Detailed studies of the causes of depolarization continued (Sokoloff et al., 1998).

Multi-wavelength studies of polarized sources revealed that the Faraday effect – wherein the plane of polarization of linearly polarized radiation rotates in proportion

to λ^2, as the radiation traverses through a medium containing free electrons, and magnetic fields aligned in the propagation direction – could be another cause of depolarization of an otherwise intrinsically polarized radiation. The proportionality constant is called Rotation Measure (RM). The RM bears information about the magneto-ionic properties of the propagation medium. Denoting χ as the polarization position angle at a given λ^2,

$$\chi(\lambda^2) = RM\lambda^2 + \chi_0$$

where, χ_0 is the intrinsic position angle of the source polarization vector, and

$$RM = \int_s n_e(s) B_{\parallel}(s) ds$$

The integration is over the distance traversed by the radiation along the line-of-sight. $n_e(s)$ is the thermal electron density of the propagation medium within the region s and $s+ds$, and $B_{\parallel}(s)$ is the line-of-sight component of magnetic field at that location.

For a medium external to the source (external *Faraday screen*), the measured polarization angles at different wavelengths are expected to show a linear trend as a function of λ^2. If the spectral span within a given band is large, differential rotation of the polarization vector within the band will lead to significant depolarization (bandwidth depolarization). However such depolarization can be minimized by having high spectral resolution. For sources that are extended in Faraday-depth (*i.e.* when non-thermal emission components are mixed within Faraday-rotating thermal plasma), the observed rotation will in general be a complicated function of λ^2, and will lead to additional depolarization. This internal depolarization is wavelength dependent, and would be minimal at shorter wavelengths, where Faraday rotation become negligible.

These revelations about the causes of depolarization led to the notion (at least initially) that radio polarimetric studies are best suited at higher radio frequencies. Of course, if the magnetic fields corresponding to the synchrotron emission components

distributed along the line-of-sight are differently oriented, the resulting depolarization in the line-of-sight integrated emission without any Faraday rotation within the emission regions, would be independent of the wavelength of observation.

Observations that followed, mostly at the higher radio frequencies, discovered polarization in many galactic as well as extra-galactic sources (see Saikia & Salter (1988)). The polarized extra-galactic sources were used for probing the magneto-ionic medium of the Galaxy that acts like a foreground Faraday screen. The rotation measures of pulsars together with their dispersion measures (derived independently), allowed reliable estimates of the average line-of-sight component of the medium's magnetic fields. However, probe of the Galactic magneto-ionic structure using background sources is limited to only those discrete lines-of-sight having bright polarized sources.

Several radio continuum surveys have also mapped the polarized intensity of the extended Galactic emission over a range of frequencies using both single dish and synthesis imaging (Spoelstra, 1984; Wieringa et al., 1993; Duncan et al., 1999; Gaensler et al., 2001; Tucci et al., 2002) [1]. Derived images of the net polarization percentage, the position angle and the apparent rotation measure have revealed rich structure over a range of angular scales. In almost all such studies made to date, the spectral signatures of the polarized intensity have been studied explicitly, but to seek only a single RM value per image pixel. This would correspond to an RM in the foreground of the dominant polarized emission component along the relevant line of sight. However, it is expected that the extended polarized emission is extensively spread in depth along each sight-line, in principle over the entire extent of the Galaxy, and not merely across the sky-plane (*i.e.* the two angular coordinates).

[1] for a complete list of references, see Wielebinski (2012)

1.2 Probing the 3rd dimension: Faraday tomography

As early as 1966, Burn had proposed that the Faraday modulation signatures in the spectral domain for polarized emission can be used to distinguish polarized components originating from different Faraday depths (Burn, 1966). Decomposing the spectra of the linear Stokes into their Fourier components *viz.* RMs is the basis for "Faraday tomography" or "RM-synthesis". Burn had also demonstrated the potential of the technique using spectro-polarimetric data on the widely observed Crab nebula. However, application of the technique to other astrophysical sources had to wait for another 3 decades until the emergence of appropriate technology for wide-band polarimetry with high spectral resolution, that is required for Faraday tomography. Ramkumar & Deshpande (1999) demonstrated the essence of the technique and the Fourier relation in the context of pulsar polarization & rotation measure studies using a single polarization channel. Independently, Kileen, Ekers *et al.* (2000) had communicated their proposal & application of the Fourier technique to studies of polarized extra-galactic sources, but unfortunately their work remain un-published. In 2003, Deshpande, Salter & Ghosh proposed this technique for studying extended diffuse component using observation from Arecibo (Arecibo proposal Id: A1765 (2003)[2] & NAIC newsletter #37, 2004[3]) and a preliminary tomograph was even produced (Figure 1-1).

[2] `http://www.naic.edu/science/proposals_set.htm`
[3] `http://www.naic.edu/~newslet/no37/NAICNo37.pdf`

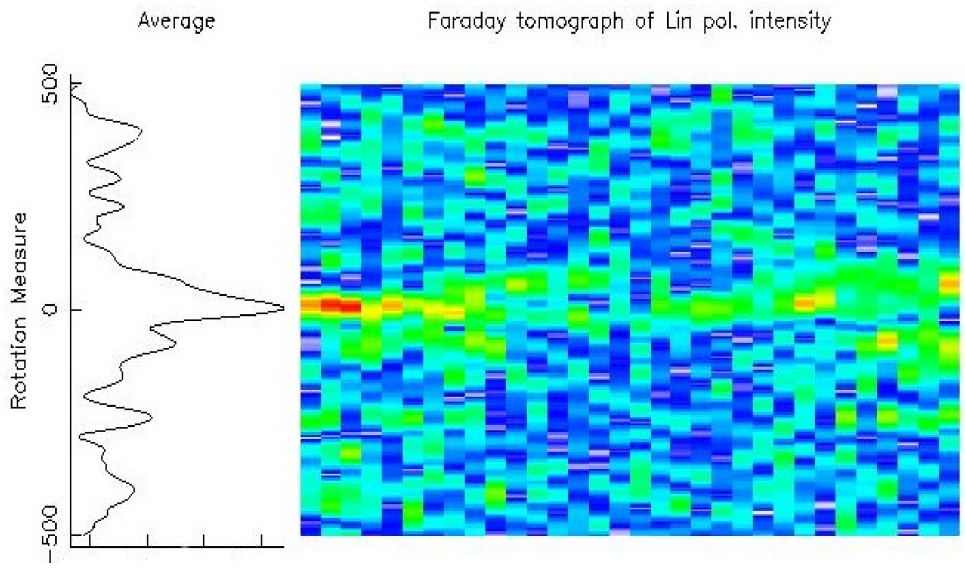

Figure 1-1: *Faraday tomograph of diffuse Galactic polarized emission, possibly the first tomograph ever produced (Deshpande, Salter & Ghosh, 2003). The tomograph corresponds to a drift scan across a piece of sky free of strong discrete sources. The observations were conducted at the 327 MHz band of the Arecibo Telescope.*

It was only after Brentjens & de Bruyn (2005) revisited the mathematical formalism, drawing analogy from aperture synthesis imaging, that RM-synthesis or Faraday tomography got an impetus, and has begun to be recognized as a powerful tool in all spectro-polarimetric studies.

1.3 Some pertinent issues

For meaningful tomography, the strategy of spectral sampling plays a crucial role. While wide-band observations (*i.e.* wide span in λ^2) would enhance the resolution in RM, fine sampling of the spectra dictates the maximum "range" of RMs that can be probed without aliasing. This follows directly from the uncertainty relation between RM and λ^2. However, there is one more aspect where the choice of the observing band plays an important role. Sensitivity of the measurements to polarization features extended in RM is highest at the shortest wavelength sampled. Hence for a fixed

band-width, although designing a wide-band system at the low radio frequencies would be advantageous from the point of view of enhancing RM-resolution, such measurements will not be sensitive to Faraday-thick structures along the lines-of-sight as severe depolarization would attenuate the polarized components below the measurement noise. On the other hand, at high frequencies the band-width required to match the RM-resolution provided by observations at low frequencies, would be rather high. For example, a band-width of 30 MHz at 300 MHz provides an RM-resolution of ~ 15 rad m^{-2}. Similar fractional band-width at 1420 MHz will have an RM-resolution 25 times worse! In other words, to enhance the RM-resolution at high frequencies, one would require much larger fractional band-widths. There are practical limitations in designing such wide-band systems.

1.4 Multiband-tomography: the way out

Seeking an optimum resolution to the issues discussed above, we have proposed and demonstrated a novel method of performing Faraday tomography by combining spectro-polarimetric data observed at widely separated frequencies. With the present achievable fractional band-widths (typically about one-tenth), the contiguous bands at the lower frequencies would dictate the RM-resolution, whereas the shortest wavelength provided by the highest frequency band would make these measurements sensitive to large-scale polarization features as well. The immediate question then would be "How does one de-convolve or 'clean' the tomograph to remove the effect of the side-lobe pattern in RM that would result from such sparse sampling of λ^2s ?" This has been addressed in the thesis through discussion as well as demonstration of a complex de-convolution scheme (RM-clean) suitable for sparsely sampled λ^2s.

The picture that is expected to emerge, when the full potential of this method is realized, consists of a polarized intensity data cube (quite like the spectral-line data cube) with two dimensions being the sky coordinates and the third being the RM. These pictures are expected to reveal unprecedented details in the distribution of the

magneto-ionic matter along Faraday depth, in addition to that in the sky-plane.

1.5 Contents of this thesis

In this thesis we explore the potential of the relatively new spectro-polarimetric tools in studying magneto-ionic media of astrophysical systems, and address general issues one would encounter in such studies.

In Chapter 2 we briefly discuss the recently developed technique of Faraday tomography or RM synthesis. A modified version of the technique capable of handling data that are unevenly sampled in λ^2 space is presented along with a relevant deconvolution (RM-clean) scheme that does not require re-gridding of the data into uniformly spaced λ^2 domain. The potential of the method to study extended polarized features in RM with high RM-resolution using data that are widely separated in frequency, is discussed. The advantages of the method in cases where a significant chunk of even a contiguous band is infested with radio frequency interference (RFI), are pointed out. We draw attention to the complex depolarization occurring within even the finite spectral channel-widths, an effect that had not been considered so far, and derive analytical expressions to help characterize this effect. The additional modulation implied by this effect in the spectrum and its relevance in RM-clean are discussed.

Chapter 3 discusses general issues related to corruption of data due to instrumental imperfections, highlights usefulness and limitations of known methods of calibration, and also explores alternate methods of calibration. Chapter 4 discusses the practical considerations relevant for low frequency GMRT polarimetry. Using several calibrator sources, feasibility of spectro-polametric studies at the low frequencies of the GMRT is demonstrated. It is shown that instrumental polarization leakage could be brought down to $< 0.5\%$ after calibration.

In Chapter 5, we present the results of our Faraday tomographic investigations of the young supernova remnnant Cassiopeia A at 327 MHz using the GMRT. Our analysis reveals significant (although weak) polarized emission from the remnant even at these low radio frequencies where earlier studies had indicated the remnant to be completely depolarized. That the observed polarization is indeed from the source, and not a mere artifact of the instrument, is established rigorously using two independent methods: (a) by establishing the lack of any correlation between the linearly polarized intensity and Stokes-I intensity, and (b) revealing the expected anti-correlation between the degree of linear polarization and soft X-radiation, using a novel method of binning the data in Stokes-I. The calibrated images at 327 MHz show the polarization position angles (PA) to be nearly constant across the entire face of the remnant. This is in marked contrast with observations at higher frequencies where the polarization PAs corresponding to the electric field were found to be tangential (implying a radial orientation for the magnetic field within the remnant). Furthermore, the RMs of the brightest components along all sight-lines passing through the remnant is found to be constant at 327 MHz. This too contradicts observations at high frequencies where considerable spread in the apparent RMs had been observed. The implication of these observations on the magneto-ionic morphology of the supernova remnant is discussed. Two plausible physical scenarios that can consistently explain the observed polarization morphology have also been presented. One of these conjectures the interesting possibility of the observed polarization at 327 MHz to be the result of a pulsar driven wind nebula (PWN) in its formation stage.

Chapter 6 demonstrates application of our proposed multi-band approach for enhancement of the RM-resolution by combining data from widely separated frequency bands using both simulated data, as well as astronomical observations at P and L bands from Arecibo telescope. The conclusions are presented in Chapter 7.

Chapter 2

Introduction to Faraday Tomography

As early as 1966, B. J. Burn had pointed out the prospects of studying the distribution of magneto-ionic matter in astrophysical sources as a function of the two angular sky-coordinates and the Faraday-depth (Burn, 1966), using Faraday rotation of the plane of polarization of linearly polarized radiation travelling through magneto-ionic media. The amount of rotation of the plane of polarization is proportional to the square of the wavelength. The constant of proportionality is called the Rotation Measure, RM.

$$\chi(\lambda^2) = RM\lambda^2 \tag{2.1}$$

$$RM = \int_s n_e(s) B_{\parallel}(s) ds \tag{2.2}$$

The integration is over the distance traversed by the radiation along the line-of-sight from its source to the observer. $n_e(s)$ is the number density of thermal (non-relativistic) electrons in the propagation medium within the region s and $s + ds$, and $B_{\parallel}(s)$ is the strength of the line-of-sight component of magnetic field at that location.

The apparent spectral modulation of the linearly polarized components is the essential feature used here for tomography. The received intensity of the polarized

components depends on the RM associated with the foreground, and would differ for polarized sources at different distances from us.

However non-availability of instruments suitable for such observations (wide-band spectro-polarimeters with sufficient angular resolution) till recent times limited the application of this technique in practice for studying a variety of astrophysical systems. In fact, the Crab nebula was the only source that Burn could use to demonstrate the applicability of this technique on an astrophysical object.

With the advent of modern spectrometers that simultaneously measure wide bandwidths with fine spectral resolutions, the dispersive (λ^2-dependent) Faraday rotation of the plane of polarization, *i.e.* the resultant spectral modulation corresponding to different RMs or Faraday depths, is being used by astronomers today to study the 3D distribution of the magneto-ionic matter. Ramkumar & Deshpande (1999) demonstrated this technique in the context of pulsar rotation measures. Brentjens & de Bruyn (2005) extended the mathematical foundations of this technique of Burn by drawing analogy from *aperture-synthesis* in radio interferometry, and called the technique "RM Synthesis". Since then, the technique is in use to probe the 3D distribution of magneto-ionic matter in astrophysical systems that include both discrete as well as extended sources of polarized emission.

At the heart of the technique, lies the Fourier relationship between the linearly polarized intensity as a function of λ^2 and that as a function of RM. The uncertainty relation in this Fourier pair of parameters λ^2 & RM would imply that higher the bandwidth of observation, finer will be the resolution in RM one can attain. Similarly, finer spectral sampling would allow probing polarized components at higher Faraday-depths without aliasing:

$$\begin{aligned} \Delta\lambda^2 \ \times \ \delta RM \ &\sim \ \pi \\ \delta\lambda^2 \ \times \ \Delta RM \ &\sim \ \pi \end{aligned} \tag{2.3}$$

The resolution and span in RM, in terms of the center frequency f_c, the observation

band-width $\Delta\nu$, number of spectral channels n_{ch}, and the wavelength $\lambda_c(=\frac{c}{\nu_c})$ can be expressed as:

$$\begin{aligned} \delta RM &\sim \frac{\pi}{2\lambda_c^2}\left(\frac{\nu_c}{\Delta\nu}\right) \\ \Delta RM &\sim n_{ch} \times \frac{\pi}{2\lambda_c^2}\left(\frac{\nu_c}{\Delta\nu}\right) \end{aligned} \tag{2.4}$$

δ signifies the *resolution* & Δ the *un-aliased span* in the respective quantities. Sensitivity to large scale polarization structure in RM however depends on the shortest wavelengths of the observation.

2.1 The Fourier relation between $\mathbf{P}(\lambda^2)$ and $\mathbf{F}(RM)$

In this section, we try to demonstrate intuitively how linearly polarized emission connects Rotation measure (denoted by RM, here) and λ^2 through a Fourier relation.

Let us consider a Faraday rotating medium in the foreground of a linearly polarized source. After having traversed through this medium, let the orientation of the linearly polarized component be such that it makes angle $\chi(\lambda^2)$ *w.r.t.* a given linear feed orientation of the antenna, where:

$$\chi(\lambda^2) = \chi_0 + RM\lambda^2 \tag{2.5}$$

where χ_0 is the intrinsic position angle of a source and RM is the rotation measure of the foreground medium. Let E_l, E_c, & E_u be the mean amplitudes of fields corresponding to the linear, circular and the unpolarized components respectively of the radiation. The power received by the antenna at wavelength λ would be:

$$
\begin{aligned}
P(\lambda^2) &= E_l^2 cos^2(\chi) + \frac{1}{2}(E_c^2 + E_u^2) \\
&= \frac{1}{2}E_l^2[1 + cos(2\chi)] + \frac{1}{2}(E_c^2 + E_u^2) \\
&= \frac{1}{2}(E_c^2 + E_u^2) + \frac{1}{2}E_l^2 + \frac{1}{2}E_l^2 cos(2\chi) \\
&= \frac{1}{2}(E_c^2 + E_u^2) + \frac{1}{2}E_l^2 + \frac{1}{2}E_l^2 Re[e^{2i\chi}] \\
&= \frac{1}{2}(E_c^2 + E_u^2 + E_l^2) + \frac{1}{2}E_l^2 Re[e^{2\,i\,\chi_0} e^{2\,i\,RM\lambda^2}] \qquad (2.6)
\end{aligned}
$$

The total power received by a linear feed due to polarized emission components situated at different Faraday-depths (or RMs) will therefore be:

$$
P(\lambda^2) = \sum_{RM} \frac{1}{2}(E_c^2 + E_u^2 + E_l^2(RM)) + \sum_{RM} \frac{1}{2}E_l^2(RM) Re[e^{2i\chi_0(RM)} e^{2iRM\lambda^2}]
$$

The summation is over all Faraday-depths (RM) along the line of sight direction. The first summation is a constant term. Without the loss of generality, we shift the P-axis such that the first summation is zero. Replacing the summation by an integral, we can then write for the case of a single linear dipole:

$$
\begin{aligned}
P(\lambda^2) &= Re \int_{-\infty}^{+\infty} \frac{1}{2}E_l^2(RM) e^{2\,i\,\chi_0(RM)} e^{2\,i\,RM\lambda^2} dRM \\
&= Re \int_{-\infty}^{+\infty} F(RM) e^{2\,i\,RM\lambda^2} dRM \qquad (2.7)
\end{aligned}
$$

where,

$$F(RM) = \frac{1}{2} E_l^2(RM) e^{2\,i\,\chi_0(RM)}$$

We would like to point here that if the medium exhibits linear birefringence (Appendix B), the polarization position angle would be altered due to coupling between the linear and circular components of the radiation. For the purpose of this derivation we ignore the case of such a medium.

Here, the P(λ^2) being real, it samples only the Hermitian symmetric part of F(RM). Additionally, if measurements from the orthogonal dipole too were available, we could include the Imaginary part of P(λ^2) as well. Equation 2.7 can then be written as:

$$P(\lambda^2) = \int_{-\infty}^{+\infty} F(RM) e^{2\,i\,RM\lambda^2} dRM \tag{2.8}$$

Equation 2.8 is similar to a Fourier transform with conjugate variables λ^2 and RM.

In practice, one can only have a finite coverage in λ^2-space. We therefore define a weighting function W(λ^2) such that $W(\lambda^2) = 0$ for λs where we do not have measurements, and $W(\lambda^2) = 1$ for λs that have been sampled. Appropriate, non-unity weightages could be used depending on the sampling schemes, but at this point, we keep the discussion simple by assuming a uniform weightage for all sampled λs.

Thus instead of $F(RM)$ what we shall actually measure is $F^{\dagger}(RM)$ where

$$F^{\dagger}(RM) = \int_{-\infty}^{+\infty} W(\lambda^2) P(\lambda^2) e^{-2\,i\,RM\lambda^2} d\lambda^2 \tag{2.9}$$

The RHS of Equation 2.9 is the Fourier transform of the product of $P(\lambda^2)$ and $W(\lambda^2)$. Hence by the Convolution theorem, $F^{\dagger}(RM)$ would be a convolution of the FT of $P(\lambda^2)$ and the FT of $W(\lambda^2)$. $F(RM)$, we know, is the FT of $P(\lambda^2)$ and let $R(RM)$

be the FT of $W(\lambda^2)$, *i.e.*

$$R(RM) = \int_{-\infty}^{+\infty} W(\lambda^2) e^{-2\,i\,RM\lambda^2} d\lambda^2 \tag{2.10}$$

Therefore,

$$F^{\dagger}(RM) = F(RM) * R(RM) = \int_{-\infty}^{+\infty} W(\lambda^2) P(\lambda^2) e^{-2\,i\,RM\lambda^2} d\lambda^2 \tag{2.11}$$

There exists a close analogy of RM synthesis with synthesis imaging. In synthesis imaging what we measure is the *dirty image*, which is a convolution of the sky brightness distribution with the *dirty beam* or the point-spread function describing the angular response of the instrument. Here, $F^{\dagger}(RM)$ is analogous to the *dirty image* (we call it *dirty tomograph*), $F(RM)$ is analogous to the "clean-ed" image (the tomograph without the artifacts of finite sampling), and $R(RM)$ is analogous to the *dirty beam* (we call it *dirty RM response*). $W(\lambda^2)$ is the sampling-function of the λ^2-space and hence is like the uv-coverage.

2.2 Potential of the tool for studying 3D distribution of magneto-ionic matter

We have seen in the above section, how the spectra of linearly polarized intensity along any sight-line can be expressed as linear sums of polarized emissions coming from various Faraday-depths along the line-of-sight, using Fourier relations. The complex coefficients of the Fourier transform of the linear polarization profile, $\mathrm{P}(\lambda^2)$, at different Faraday-depths, measures the amplitudes and phase-angles of polarized intensity components located at their respective Faraday-depths (or RMs). This provides the basis for the tomographic decomposition. Although a mapping between physical depth and Faraday-depth would be possible in some situation, in general, such mapping would be non-trivial, if not impossible, when the distribution of the magneto-ionic matter within a source as well as in the propagation medium hap-

pens to be complicated. Reversals in the field-directions along the propagation path may even lead to a non-monotonic relationship between physical and Faraday-depths, making the correspondence ambiguous and complicated. Hence the usage of the term "*tomography*" may seem misleading. Nonetheless *Faraday tomography* implicitly assumes the 3rd dimension as the Faraday-depth along the line-of-sight, and associating physical distances to apparent Faraday-depths will involve modeling of magneto-ionic medium, as well as independent estimates of distances to as many discrete sources as possible. In any case Faraday tomographic data is expected to provide unprecedented details, enabling correspondingly detailed modeling. Associating physical and Faraday-depths is a topic, discussions on which within the polarization community, has begun only in the recent months.

2.3 Observation Strategies: Considerations in spectral sampling

Meaningful application of the technique of Faraday tomography requires optimization of several observing parameters:

(1) Band-width: Wide band observations, spanning a wide range in λ^2, are necessary to be able to probe polarized emission components with high resolution along Faraday depth (RM resolution). However how wide a band-width one can use at different radio bands depends on practical issues associated with design and development of wide-band feed & receiver systems.

(2) Spectral resolution: High spectral resolution minimizes the inherent depolarization across the band, as well as enables probing a large range of *un-aliased* RMs. It might appear that having narrow spectral channels would worsen the signal to noise ratio (S/N). Indeed that would be true for the individual spectral channels. However, the S/N in the RM-domain would enhance since the tomography, which is a Fourier transformation of the complex polarized intensity spectra, coherently adds the single

channel polarization vectors.
(3) Optimal choice of the frequency band: for a given bandwidth, lower the frequency, higher is the RM-resolution attainable. However, the beam of the telescope being wider at lower frequencies, beam-depolarization will be correspondingly higher. For systems with fixed bandwidth and array configuration, potential depolarization goes as $\frac{1}{\lambda}$ (product of the resolution elements in RM and the angles). Hence lower frequencies would be preferred from the q-polarization consideration, but the angular resolution could be severely worsened. However although the resolution in RM would enhance at lower frequencies, it is also necessary for the RM-resolution to be useful, that the spectral resolution is also high (*i.e.* large number of spectral channels across the band-width), providing a correspondingly wider range of unaliased RMs that one can probe.

(4) Also at longer wavelengths, for a Faraday-thick source, internal depolarization would be severe, and the polarized radiation seen at the foreground would mostly be dominated by regions within the source closer to the the observer (Burn, 1966; Downs & Thompson, 1972; Sokoloff et al., 1998). Hence the resultant polarized emission at longer wavelengths would not probe the polarized components deep within the source if the source is Faraday thick. Such attenuation is to be understood as due to inadequate resolutions in the spectral as well as the RM domains.

Therefore suitably differing combinations of center frequency, bandwidth and spectral resolution are needed to meaningfully probe the variety of magneto-ionic media in different astrophysical systems. We emphasize that a multi-band approach combined with high spectral resolutions would be an effective optimal solution. Of course, combination of data from disparate frequency bands would require development of appropriate tomograph-deconvolution algorithms. These are discussed in the section on tomograph deconvolution (section 2.5).

2.4 Faraday tomography using data with single linear feeds: prospects and limitations

All single linear polarization feeds measure one of the two orthogonal components of the incoming polarized signal (Equation 2.7). The intensity spectra modulated by the linearly polarized signal in this case, would be *real*, and so the tomograph (which is its Fourier transform) would be Hermitian symmetric. In other words, although it would be possible to locate polarized emission components as a function of RM, one will not be able to distinguish between +ve and -ve RMs with a single linear feed alone.

Many telescopes operational at low and very low radio frequencies, such as those at Ooty, Puschino, Kharkov, Gauribidannaur and Tirupati consist of only single linear polarization feeds. Although the poor angular resolution of these telescopes would wash away the small angular scale polarization structures, due to beam depolarization, the high RM-resolution attainable at these low frequencies, could be useful in probing the distribution of large angular scale polarized emission from "nearby" diffused magneto-ionic media of our Galaxy, along Faraday-depth (see sub-section 2.5.3).

High angular resolution data from dual linear feeds, that do not have the cross-correlation measurements, could also be used to compute Stokes-Q spectra ($Q = E_x E_x^* - E_y E_y^*$). Large volumes of such data are already available in various archives. Although, calibration would be relatively simpler in the case of single linear polarization feed systems as compared to systems with dual linear feeds where cross-coupling between the polarization channels further complicate the calibration process (Chapter 3), data from both kinds of systems can in principle be used for tomographic studies. However, the tomographs would be Hermitian symmetric, and the sign of RM, or equivalently the direction of $B_{||}$, would remain ambiguous.

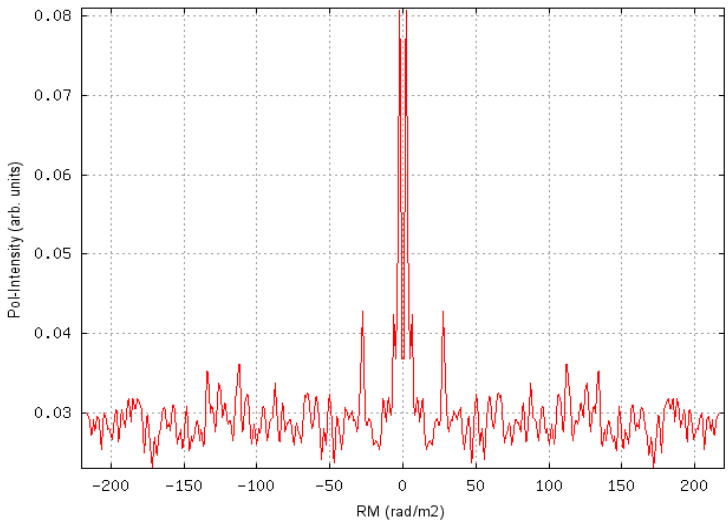

Figure 2-1: *Faraday tomograph of PSR B0834+06 observed using the singly polarized MST dipole phased array at Gadanki, Tirupati. The components seen at* ± 26 rad m^{-2} *are manifestations of the Faraday rotation induced spectral modulation corresponding to the RM to the pulsar. The features close to RM = 0 are a result of the instrumental "band-shape" that has not been band-pass calibrated.*

Figure 2-1 shows the tomographs of the pulsar B0834+06 observed using singly polarized dipole phased arrays (the MST radar system[1]). The RM corresponding to the pulsar's foreground is about $+26$ rad m^{-2}. The tomographs indeed reveal this component (with the sign ambiguity associated with the use of only one singly polarized feed). The means of both the Q and the U spectra had been removed before the tomography so as to keep the dirty tomograph free from the artifacts of the RM = 0 component. The components close to RM = 0 owes its origin to the instrumental "band-shape" that has not been band-pass calibrated.

[1]The Mesospheric Stratospheric Tropospheric Radar system is a facility at the National Atmospheric Research Laboratory of the Department of Space, Govt. of India.

2.5 Faraday tomography & advantages of non-uniform sampling in λ^2

The spectral feature resulting from Fourier-transforming a suitably sampled time sequence over a finite extent in time domain, for an otherwise monochromatic signal, would not be a Dirac-delta. It will have side-lobe responses that will depend, in addition to the width of the window in time, also on the exact sampling scheme of the points within the window. For *e.g.* if the samples within the window are uniformly spaced in time, the response to a monochromatic signal would be a *sinc* function whose peak would lie at the frequency of the monochromatic signal, and the width of the primary lobe would be inversely proportional to the window length. In this scenario of uniformly spaced samples, the spectral response to any monochromatic signal would be independent of its frequency. In case of non-uniform sampling however, the spectral response of monochromatic signals becomes frequency-dependent. In either case, faithful reconstruction from the measured spectra would require deconvolving these artifacts of finite sampling.

In the context of aperture-synthesis using radio interferometry, deconvolution of the dirty-response of a partially-filled and finite aperture is called *Clean*. Following this, and noting the analogous situation in RM-synthesis or Faraday tomography, where λ^2 & RM are the Fourier conjugates, the deconvolution is termed *RMCLEAN* – the difference being the *complex* nature of the dirty response in the case of tomography as against the dirty-beam of an interferometer, which is *real*. We discuss *RMCLEAN* in more detail in section 2.5.4

The tomograph $F(RM)$, is the Fourier transform of the complex linearly polarized intensity $P(\lambda^2)$. However radio spectrometers sample the frequency-space (within a chosen band) uniformly. Therefore the equivalent samples in $\lambda^2(=\frac{c^2}{\nu^2})$ domain become unevenly spaced, although the non-uniformity is systematic. As a result, a Faraday tomograph cannot be directly obtained using Fast Fourier Transform (FFT), since it

would require the sampling in λ^2 to be uniform. In RM-synthesis used so far, the data are re-gridded into uniformly spaced λ^2 grid points using interpolation (Brentjens & de Bruyn, 2005; Heald et al., 2009). The re-gridded data is then FFT-ed to obtain the tomograph. This tomograph is still "*dirty*" in the sense that it would contain the artifacts due to the finite extent in λ^2 used in the FFT. However, the *dirty RM response profile* for a uniformly re-gridded data set would be independent of RM. Such re-gridding is thus advantageous for two main reasons – first it allows for speedy computation of tomographs through the usage of FFT, and secondly, renders the deconvolution or the *RMCLEAN* step simple, since a single *dirty RM response* (independent of RM) need be used for the deconvolution.

However, the data from typical spectrometers providing information over a chosen number of spectral channels correspond to averages within respective narrow spectral channels. In principle, the equivalent averaging across the width in λ^2 is non-uniform. More importantly, the averaging leads to finite depolarization in each channel that depends on RM as well as the wavelength λ. This effect has so far been ignored in literature.

It should however be noted here that a re-gridding of the λ^2 space is possible only for cases where a contiguous band has been covered. Interpolation would be on widely different scales if one were to re-grid from the λ^2s observed, widely separated bands, as is desired for improving RM-resolution and discussed in Chapter 6. Furthermore RFIs that contaminate considerable chunks of contiguous spectral channels within the observed band (such a case is indeed seen for GMRT data and is discussed in Chapter 4 & 5), would make re-gridding unreliable.

It is easy to see that re-gridding the data is not required if one uses DFT (instead of FFT) that does not put any constraint on the way the λ^2s are to be sampled. The deconvolution however, would need to address the RM-dependence of the *RM response profile*, which in any case would be necessary to take into account the effect

of averaging within the narrow spectral channels. Obviously, these would be computationally slower, but such overheads in computation time are hardly an issue today, given the availability of fast computation speeds.

In the following section we address the effect of finite spectral resolution, and derive analytic expressions for the depolarization occurring within the finite spectral channel widths.

2.5.1 Bandwidth depolarization: resultant modification of the complex polarized spectra

In this section, we discuss the effects of the inherent depolarization occurring across the finite channel widths of a typical spectrometer, on the magnitude of linearly polarized intensity and the intrinsic position angle at a given λ^2-bin, given an RM. We formulate analytic expressions for this complex depolarization in terms of the channel-width, the center frequency corresponding to the channel, and the RM component, and point out its use as an additional spectral modulation/envelop to be incorporated while generating the *dirty RM responses* to be used for deconvolving the dirty-tomographs.

For a given RM, the linearly polarized Stokes can be expressed as a function of λ^2:

$$Q(\lambda^2) = cos(2RM\lambda^2 + 2\chi_{0,RM}) \tag{2.12}$$

$$U(\lambda^2) = sin(2RM\lambda^2 + 2\chi_{0,RM}) \tag{2.13}$$

where $\chi_{0,RM}$ is the intrinsic polarization position angle of the emission component at a Faraday depth, RM. The amplitudes of Q and U at any RM are expressed here in

terms of the corresponding linearly polarized intensity at that RM.

The equations above are strictly true for monochromatic radiation only. For any measured signal, the above quantities will be necessarily *smeared* due to the *incoherent* addition of these vector quantities taking place within the "finite" resolution bin-width in the spectral domain of the measuring instrument – the incoherence introduced by the dispersive Faraday Rotation effect (Equation 2.1). This leads to *bandwidth depolarization* (*figure 2-2*).

$$Q(\lambda_i^2) = \int_{\lambda_i^2-\Delta\lambda_i^2/2}^{\lambda_i^2+\Delta\lambda_i^2/2} cos(2RM\lambda^2 + 2\chi_{0,RM})d\lambda^2 \tag{2.14}$$

$$U(\lambda_i^2) = \int_{\lambda_i^2-\Delta\lambda_i^2/2}^{\lambda_i^2+\Delta\lambda_i^2/2} sin(2RM\lambda^2 + 2\chi_{0,RM})d\lambda^2 \tag{2.15}$$

$$P(\lambda_i^2) = e^{i2\chi_{0,RM}} \int_{\lambda_i^2-\Delta\lambda_i^2/2}^{\lambda_i^2+\Delta\lambda_i^2/2} e^{i2RM\lambda^2} d\lambda^2 \tag{2.16}$$

The effect may be easily explained by noting that Equation 2.16 is a *Fourier Transform* of a unit step function of width $\Delta\lambda_i^2$ and centered at $\lambda_i^2/2$. Thus the magnitude of linearly polarized intensity at a given λ_i^2 is a sinc function in (RM$\times\Delta\lambda_i^2$).

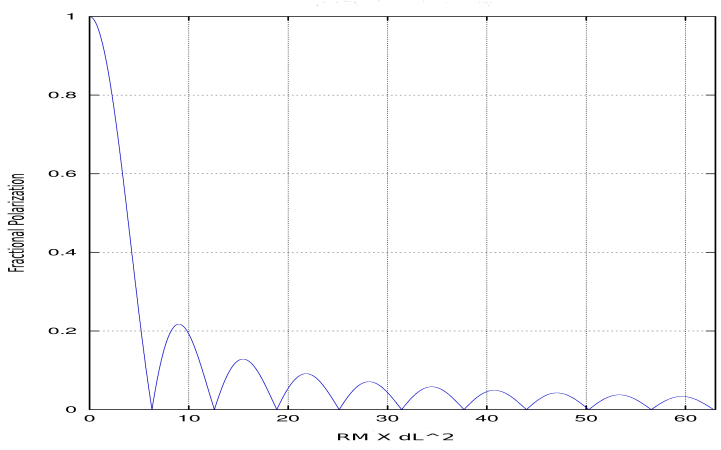

Figure 2-2: *Bandwidth depolarization: The figure shows the degree of polarization (y-axis) as a function of RM* $\times$ $d\lambda^2$ *(x-axis).*

The exercise above has been done in the λ^2 domain to make use of the well known properties of Fourier Transforms to illustrate that wider the bandwidth used, higher will be the depolarization for a given RM as is obvious from the fact that the width of the main lobe of the sinc is inversely proportional to the extent of the λ^2 bin. However, spectrometers used in radio telescopes sample (and average, where relevant), the Stokes intensities uniformly along the *frequency* axis and not along the λ^2 axis, thereby preventing us from using the properties of Fourier Transforms directly, as has already been noted earlier. More importantly, the picture in Figure 2-2 may only be regarded as an approximate (first order) description of the depolarization in situations where the bin-width $d\lambda^2$ varies with λ^2. Nevertheless the uneven sampling in the lambda-squared domain provides additional independent information, which as we will show, can be fruitfully used in RM-clean.

Let k denote the index of the *frequency channel* whose center frequency is ν_k. Let $\Delta\nu$ be the uniform width of the channels. Therefore the linearly polarized intensity as measured by a telescope would be:

$$P(\nu_k) = e^{i2\chi_{0,RM}} \int_{\nu_k - \frac{\Delta\nu}{2}}^{\nu_k + \frac{\Delta\nu}{2}} e^{i2RM\lambda^2(\nu)} d\nu \tag{2.17}$$

Changing variables from ν to $z(= \lambda^2 = c^2/\nu^2)$, eq. 2.17 can be rewritten as

$$P(z_k = \lambda_k^2) = \frac{c}{2} e^{i2\chi_{0,RM}} \int_{z_{k,1}}^{z_{k,2}} z^\beta e^{i2RMz} dz \tag{2.18}$$

where,

$$z_{k,1} = \frac{c^2}{(\nu_k + \frac{\Delta\nu}{2})^2}\ ; \quad z_{k,2} = \frac{c^2}{(\nu_k - \frac{\Delta\nu}{2})^2}\ ; \quad z_k = \frac{c^2}{\nu_k^2}\ ; \quad \text{and} \quad \beta = -\frac{3}{2} \tag{2.19}$$

We evaluate the integral appearing in eq 2.18 for a general real power law index β of z that can, in addition to taking into account the effect of depolarization across the channels, incorporate the effect of band-shape (modeled as a polynomial $g(z)$), as well as any spectral dependence of the flux-density (modeled as $S(z) \sim z^\alpha$), if required. This provides a neat way of calibrating in one shot, the two main instrument induced

spectral features – bandwidth depolarization and band-shape, as well as the effect of power variation across the band due to spectral index whenever such variations are significant. For this general case, the integral in eq 2.18 becomes

$$I(z_k) = \int_{z_{k,1}}^{z_{k,2}} g(z)S(z)z^{-\frac{3}{2}}e^{i2RMz}dz$$

$$= \sum_j \int_{z_{k,1}}^{z_{k,2}} z^{\beta_j}e^{i2RMz}dz \tag{2.20}$$

where,

$$\beta_j = j + \alpha - \frac{3}{2} \tag{2.21}$$

The subscript j of β signifies the orders in the polynomial representation used to model the band-shape $g(z)$ while α is linearly related to the spectral index ${\alpha_\nu}^2$:

$$g(z) = \sum_j c_j z^j \qquad \text{and} \qquad S(z) = \kappa z^\alpha \tag{2.22}$$

For integer values of β_j the integral can be evaluated using a recurrence relation. However β_j in general, is not an integer. We therefore expand z^{β_j} in Taylor Series about z_k and make use of the recurrence relation in solving each integral in the Taylor expansion.

$$f(z) = z^{\beta_j} = \sum_{n=0}^{\infty} \frac{f^n(z_k)}{n!}(z - z_k)^n \tag{2.23}$$

where, $f^n(z_k)$ is the *n-th* derivative of $f(z)$ evaluated at z_k, with

$$f^0(z_k) = z_k^{\beta_j} \tag{2.24}$$

The j^{th} term in 2.20 can therefore be written as

[2] $\alpha_\nu = -2\alpha$, where $S(z) \sim z^\alpha$ & $S(\nu) \sim \nu^{-\alpha_\nu}$

$$
\begin{aligned}
I_j(z_k) &= \int_{z_{k,1}}^{z_{k,2}} \sum_{n=0}^{\infty} \frac{f^n(z_k)}{n!}(z-z_k)^n e^{i2RMz} dz \\
&= \sum_{n=0}^{\infty} \frac{f^n(z_k)}{n!} \int_{z_{k,1}}^{z_{k,2}} (z-z_k)^n e^{i2RMz} dz \\
&= \sum_{n=0}^{\infty} \frac{f^n(z_k)}{n!} \int_{z_{k,1}-z_k}^{z_{k,2}-z_k} z^n e^{i2RM(z+z_k)} dz \\
&= e^{i2RMz_k} \sum_{n=0}^{\infty} \frac{f^n(z_k)}{n!} \int_{z_{k,1}-z_k}^{z_{k,2}-z_k} z^n e^{i2RMz} dz
\end{aligned}
\tag{2.25}
$$

Let us define the indefinite integral

$$
\hat{I}_n(z) \;=\; \int z^n e^{i2RMz} dz \;=\; \hat{C}_n(z) + i\hat{S}_n(z) \tag{2.26}
$$

where

$$
\hat{C}_n(z) = \int z^n cos(2RMz) \tag{2.27}
$$

$$
\hat{S}_n(z) = \int z^n sin(2RMz) \tag{2.28}
$$

It can be shown for non-zero RMs that

$$
\hat{C}_{n+1}(z) = z^{n+1}\hat{C}_0(z) - \left(\frac{n+1}{2RM}\right)\hat{S}_n(z) \tag{2.29}
$$

$$
\hat{S}_{n+1}(z) = z^{n+1}\hat{S}_0(z) + \left(\frac{n+1}{2RM}\right)\hat{C}_n(z) \tag{2.30}
$$

where

$$
\hat{C}_0(z) = \frac{sin(2RMz)}{2RM} \tag{2.31}
$$

$$\hat{S}_0(z) = -\frac{cos(2RMz)}{2RM} \tag{2.32}$$

For $RM = 0$,

$$\hat{C}_n(z, RM = 0) = \frac{z^{n+1}}{n+1} \tag{2.33}$$

and

$$\hat{S}_n(z, RM = 0) = 0 \tag{2.34}$$

Fortunately a recurrence relation also exists for the n^{th} derivative of z^β which makes implementation of the scheme into an efficient code possible.

$$f^{n+1}(z) = \left(\frac{\beta_j - n}{z}\right) f^n(z) \tag{2.35}$$

with f^0 defined by eq 2.24. Equation 2.18, for the j^{th} order of the band-shape, can thus be written as

$$P_j(z_k = \lambda_k^2) = e^{i2RM(z_k + 2\chi_{0,RM})} \left[W_{re}(RM) + iW_{im}(RM)\right] \tag{2.36}$$

$$W_{re}(RM) = \frac{c}{2} \sum_{n=0}^{\infty} \left[\frac{f^n(z_k)}{n!} \left[\hat{C}_n(z_{2,k} - z_k) - \hat{C}_n(z_{1,k} - z_k)\right]\right] \tag{2.37}$$

$$W_{im}(RM) = \frac{c}{2} \sum_{n=0}^{\infty} \left[\frac{f^n(z_k)}{n!} \left[\hat{S}_n(z_{2,k} - z_k) - \hat{S}_n(z_{1,k} - z_k)\right]\right] \tag{2.38}$$

We have derived analytical expressions for the complex weight $\tilde{W}$ ($= W_{re} + i\, W_{im}$), that describes the effect of bandwidth-depolarization within a spectral channel, given its center frequency, the channel-width, and the RM corresponding to the sight-line. Additionally, we have also incorporated within the same analytical framework, modifications to the polarized spectra due to instrumental band-shape and source spectral index.

The number of terms, n_{max} that needs to be retained in the Taylor Series expansion in deriving $\tilde{W}$, would depend on the separation of $z_{k,1}$ and $z_{k,2}$ from z_k. Nevertheless

the formulation has been kept general enough to determine $P(z_k)$ with arbitrary accuracy. For most telescopes, $n_{max} = 2$ would suffice for deriving $\tilde{W}$. It should also be noted that expanding the Taylor Series about the *sampled* values of λ_k^2 facilitates expressing the polarized intensity spectra in terms of the product of the *measured* spectral points (where the signal-to-noise ratio is maximum), and the weight factors that depend on the value of the center frequency, the channel-width and the RM. In the following subsections, we discuss the implications of this result in tomograph deconvolution and *RMCLEAN*.

2.5.2 Sampling scheme for λ^2s & aliasing

The effect of depolarization within a spectral channel can be thought of as a boxcar averaging of time-domain data (except that a moving average is not done here) before a Fourier transform is taken to produce its spectra. Depending on the window-length, the boxcar averaging suppresses corresponding high-frequency components in the data and the resultant spectra would be less severely affected by aliasing. However, the moderately high frequency components with adequate power levels would continue to *fold back* into the spectrum even after the smoothing. Similarly, in the case of Faraday tomography (imagine λ^2 and RM to be analogous to time and angular frequency respectively), spectral modulations in Stokes-Q and U due to very high RMs is more likely to undergo complete cancellation within a spectral channel (band-width depolarization), whereas polarized emission (if substantial) from moderately high RMs would continue to contribute to the spectral modulation in Q and U.

Figure 2-4 shows the depolarization as a function of the unevenly sampled λ^2 bins for a very high RM component. In the case of uniform sampling, the attenuation within each bin would be exactly equal, and the resultant depolarized spectra (green curves) would just be a scaled version of the corresponding monochromatic signal (red curves), unlike the chirped spectra in the uneven sampling case.

Thus, in the case of uniform sampling, any surviving modulation in the Q and the

U spectra due to an RM-component outside of the un-aliased range (equation 2.3) would be an exact, scaled replica of the modulations due to its un-aliased counterpart. In other words, a high RM component would be confused with a low RM one, and there would be no way one could distinguish the two. However, differential depolarization across λ^2 bins would allow resolving the RM-related ambiguity in the case of uneven sampling. The response of a high RM-component at the sampled RMs in the case of uneven λ^2 sampling, would be different from that of its un-aliased counterpart. The two responses, although not *independent*, when used (in turn) to cross-correlate with the dirty-tomograph, would indicate the presence of the high RM-component. The maximum RM that can be probed in this manner, would however be limited by the signal-to-noise ratio of the surviving depolarized signal in the individual λ^2 channels.

2.5.3 Faraday tomography at very low frequencies

The top panel of Figure 2-3 shows the surviving polarized fraction (as a result of band-width depolarization) as a function of RM and center-frequency for a constant channel-width. The channel width is taken as 1 MHz (which is rather large compared to typical channel widths achievable in spectrometers) in the simulations in order to illustrate the qualitative trends of the depolarization clearly. In practice, it is the fractional bandwidth $\Delta f/f$ that is usually more or less constant across frequency, and not the bandwidth Δf.

For a given RM, the depolarization within a spectral channel is higher at lower frequencies than that at higher frequencies. Depolarization increases with increasing RMs. The spectral pattern in phase would, in addition to contributing to depolarization, also lead to shifts in the values of the apparent RMs. However, it is worth mentioning that the effects of channel-bandwidth depolarization are very small and become important in cases where the RMs are very high, and/or at very low frequencies of observation. As pointed in the previous section, the depolarization due

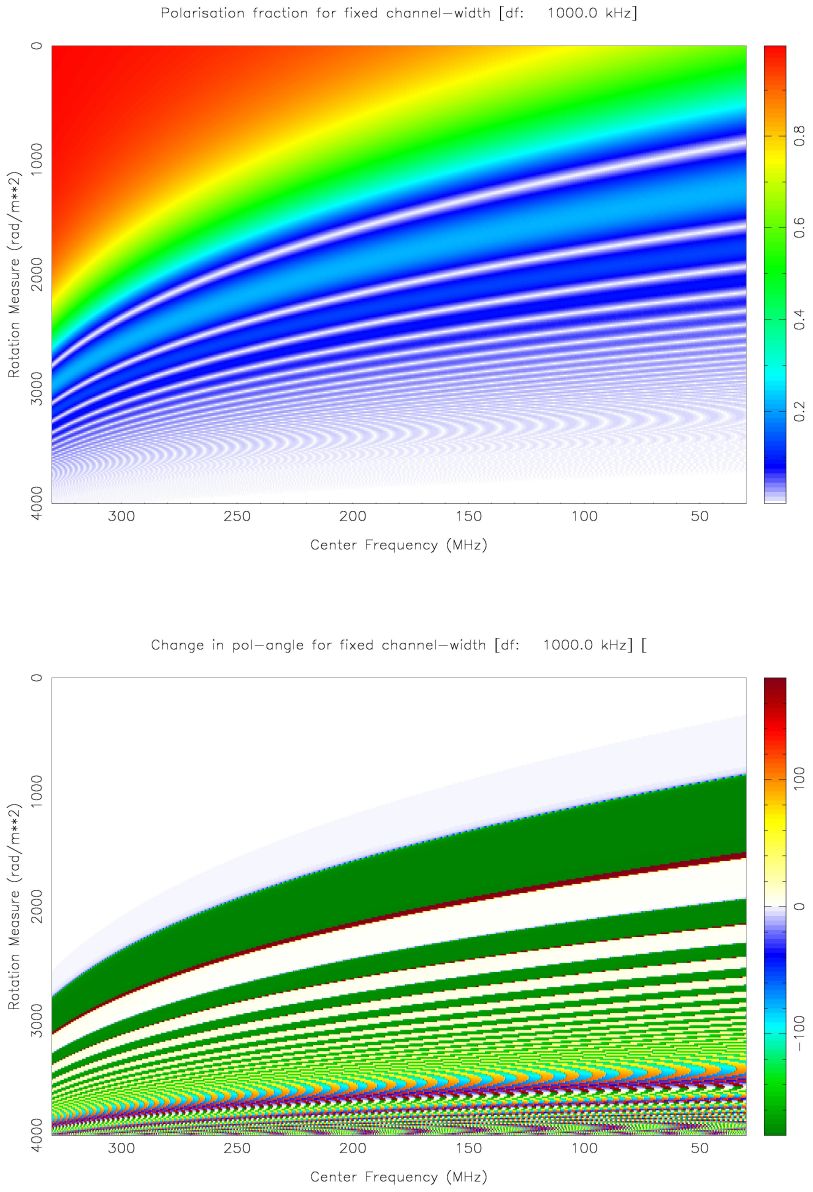

Figure 2-3: *The top panel shows the fractional polarization factor as a function of RM & f_c, while the bottom panel shows the modification to the intrinsic phase, resulting only from the channel-bandwidth depolarization. The width of the spectral channel at each center frequency is kept large ($= 1MHz$) in order to illustrate the qualitative trends clearly. In practice, it is the fractional bandwidth $\Delta f/f$ that is usually more or less constant across frequency, and not the bandwidth Δf.*

to finite spectral resolution acts as a low-pass filter that attenuates polarized components having high RMs. This naturally acts in a way to reduce the confusion arising

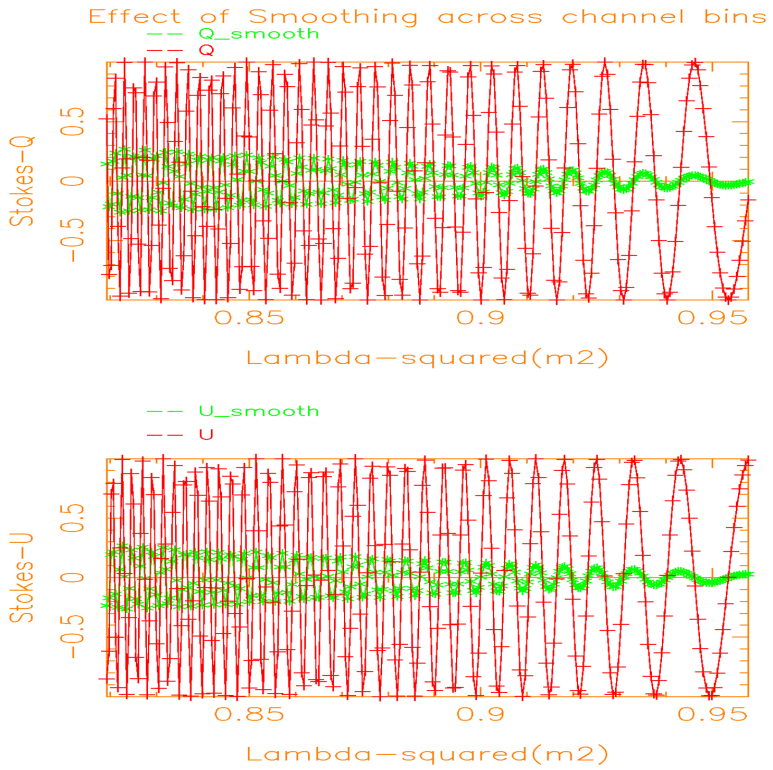

Figure 2-4: *Depolarization in the linearly polarized Stokes parameters occurring across the finite channel widths. The red curves indicate the expected Q and U-spectra measured within infinitesimally narrow (monochromatic) spectral channels and the green curves show the depolarization due to finite channel-width for a representative set of* ν_0, $\Delta\nu$ & RM. *A very high value of RM has been taken here to emphasize the effect of band-width depolarization at high RMs.*

out of *aliasing*.

From equation 2.4 it is clear that for a given fractional band-width $\Delta\nu/\nu_c$, the RM resolution, δRM, enhances quadratically with wavelength. For a given number of spectral channels n_{ch}, the range of un-aliased RMs that can be probed at low frequencies would thus get limited. As an example the Gauribidannaur Telescope with $\nu_c = 34.5$MHz, $\Delta\nu = 1.5$MHz, $\lambda_c = 8.6$m, the attainable RM resolution, δRM is ~ 0.5 rad m^{-2}. Thus with $n_{ch} = 256$, one could probe a maximum absolute RM of only about 60 rad m^{-2}. One may tend to conclude that Faraday tomographic studies from such an observation, even though has very high RM resolution, would be highly *confused* due to aliasing in RM domain, especially if the line-of-sight being observed

comprises of continuum polarized emission in a Faraday thick medium (*i.e.* with large RM range), like the diffused synchrotron emission from our Galaxy. Nevertheless, it is worth noting that band-width depolarization will attenuate contributions from components with high RMs – components that are twice as high as the maximum un-aliased RM would get depolarized by $\sim 50\%$, those that are three times the max RM, would be attenuated to $\sim 30\%$ and so on. Furthermore, polarized emission components with higher RMs are also generally from regions that are farther away along the line of sight. Since the telescope beam covers a larger area in the sky at a greater depth along the sight-line, it is likely that beam-depolarization will further attenuate contributions from high RM-components. Therefore, data from very low frequency radio telescopes with decent bandwidths and good angular resolution would actually allow one to probe the nearby diffused magneto-ionic media of our Galaxy with very fine RM resolution, and without significant contamination from RMs well beyond the unaliased RM range.

2.5.4 Additional spectral modulation relevant to dirty response and RM-clean

CLEAN is a deconvolution technique routinely used in synthesis imaging to remove from the *dirty image*, artifacts produced due to finite and non-regular sampling of the uv-plane. There are several *clean* algorithms (Högbom, 1974; Clark, 1980; Cornwell, 1983; Deshpande et al., 1996), most of which are variants of the one proposed by Högbom (1974). Our RM-clean is a one-dimensional complex version of the Hogbom clean where the dirty response is taken to be RM-dependent (to account for the uneven sampling and averaging in λ^2 domain) and with a provision for including the additional spectral modulation, due to band-width depolarization within narrow spectral channels, while computing the dirty response. We have shown in the previous section that the effect of band-width depolarization on a linearly polarized spectra is a complex scaling of the net polarized intensity within each individual non-uniform

λ^2-bins. The scaling factors depend on the center frequency of the bins, the width of the channel as well as the RM components along the corresponding line of sight. We have also derived analytical expressions for determining these scaling factors. These factors when incorporated in the construction of the *dirty RM responses* for the case of non-uniformly sampled λ^2, would enable a closer realization of a true *matched-filter* for extraction of RM-components using *RMCLEAN*. For a uniformly sampled λ^2 case, this depolarization effect does not modify the shape of the *dirty RM response* with RM, since for any given RM, the resultant polarization within each λ^2-bin would be affected exactly equally by a factor $dp = \frac{sin(RM\Delta\lambda^2)}{RM\Delta\lambda^2}$. However, as we have discussed earlier, there is no way one could distinguish a polarized component from that of its *alias* if uniform averaging & sampling in λ^2 is adopted, whereas in the case of non-uniform sampling in λ^2, signatures of the presence of an aliased component would be distinguishable (thanks to the differential modulation in the amplitude of polarized intensity across the band, and consequently differing RM-domain response), when of course the *signal-to-noise ratio (S/N)* is adequately high.

The salient steps in *RMCLEAN* are outlined below:

1. Locate the maximum, say $|d_{max}|$, in the amplitude profile of the *dirty* tomograph.

2. For the RM and phase corresponding to the detected maxima, generate the complex polarized intensities at each of the sampled λ^2 points (*i.e.* generate the model spectra), taking into account the effect of band-width depolarization within individual channels.

3. Discrete Fourier Transform the above model spectra to obtain the *dirty RM beam*.

4. Complex clean:

- Scale the complex *dirty RM beam* with a *loop-gain* factor, ($\eta < 1$) times the detected maximum amplitude $|d_{max}|$.
- Subtract this scaled complex *dirty RM response* from the complex dirty tomograph to obtain the *residual*.
- Set the *dirty tomograph* to the residual.
- Add to the cleaned components a new contribution, $\eta \times d_{max}$, at the appropriate RM.

5. go to step 1

The application of the RM-clean is illustrated in Chapter 6.

Chapter 3

Instrumental Calibration Issues

3.1 Introduction

The characteristics of the instrument used for detection and recording of astronomical signals modify the very signals they intend to probe. Most of these effects of the instrument in the resultant signal are due to non-idealities in the system and are often regarded as undesirable. However, these non-idealities occur due to a wide variety of reasons, and their manifestations are interesting in themselves. For example, a gain-amplitude mismatch between the two orthogonally polarized signals would lead to apparent dichroism, while a gain-phase mismatch would lead to spurious signatures of birefringence. In general, the net effect on the output signal would be a complex combination of these and other effects as the signal travels through the different stages of the instrument, leading to a significant alteration of the polarization state from the original astronomical signal. Recovery of the original polarization state of the astronomical signal would thus require a very good characterization of the instrumental polarization properties.

We begin by describing the general Jones matrix characterization for the instrument, construct the corresponding Mueller matrix description, as well as the matrix that connects the measured cross correlations with the true ones. We then sketch the signal path through various components of the instrument, and relate the elements of

the corresponding Jones matrix to the mechanical and/or electronic components of the instrument. Several realistic assumptions are pointed out. These assumptions are then made use of in the discussions on the methods for "calibrating out" the instrumental effects. Suggestions for calibration schemes in cases where these assumptions break down are presented.

In all our discussions, we shall use the following notation for the definition of a general state of polarization, modeled using two mutually orthogonal linearly polarized components as the basis:

$$\begin{bmatrix} \tilde{\mathbf{E}}_\mathbf{A} \\ \tilde{\mathbf{E}}_\mathbf{B} \end{bmatrix} = \tilde{g} \begin{bmatrix} \cos(\alpha)\ e^{-i\delta/2} \\ \sin(\alpha)\ e^{+i\delta/2} \end{bmatrix} \tag{3.1}$$

$$\tan^2 \alpha = \frac{\tilde{E}_B \tilde{E}_B^*}{\tilde{E}_A \tilde{E}_A^*} \tag{3.2}$$

Here, δ is the common difference in the phases δ_A & δ_B associated with $\tilde{E}_A$ & $\tilde{E}_B$ respectively, $\tan(\alpha) = |E_B|/|E_A|$ is the ratio of the amplitudes, and $\tilde{g}$ is a common complex scaling factor, that may result from a transformation previously undergone by the input signal. Modeling the phases as $\pm\delta/2$, *i.e.* symmetrically about zero, for the two components does not lead to any loss of generality, since the correlations $\tilde{E}_A\tilde{E}_A^*,\ \tilde{E}_B\tilde{E}_B^*,\ \tilde{E}_A\tilde{E}_B^*$ & $\tilde{E}_A^*\tilde{E}_B$ depend, if at all, on the relative phase $\delta\,(=\delta_B\ -\ \delta_A)$ between the two components, and are independent of the common phase $(\delta_A + \delta_B)/2$. The calibration exercise involves recovering the true correlations from the measured correlation products. The Stokes parameters are describable as linear combinations of these correlation products.

3.2 Description of the instrument using suitable matrices

The effect of any component of the receiver system on an incoming signal can be mathematically represented using matrix transformations. The electric field can be modeled as a 2×1 matrix, the two elements of which represent two mutually orthogonal components of the field. In general, the components are complex numbers. The amplitude and phase relationship between these components determine the state of polarization of the field. Jones matrices are 2×2 matrices that describe the effect of a device on an input electric field modeled as above. Since these are matrices of dimensions (2×2), the algebra involving Jones matrices are easy to handle. However since Jones matrices operate on the electric fields, they may be used only in cases where raw-voltage data (base-band data) is available.

Wherever full Stokes data is recorded, the Mueller matrix can be used to describe the transformation between the true and the measured Stokes parameters. Every Jones matrix will have a corresponding Mueller matrix. We would like to mention here that we have defined the Mueller matrix so as to relate the following more general sums and differences of the correlations, whose structure does not depend on the nature of the feed used. As in equation 3.3, the exact relation of these sums and products with the Stokes parameters and their physical correspondence, would depend on the nature of the feed used, and this must be kept in mind during the calibration.

$$\begin{bmatrix} S1 \\ S2 \\ S3 \\ S4 \end{bmatrix} = \begin{bmatrix} AA^* + BB^* \\ AA^* - BB^* \\ AB^* + A^*B \\ i(A^*B - AB^*) \end{bmatrix} \quad = \begin{bmatrix} I \\ Q \\ U \\ V \end{bmatrix}_{linear} = \begin{bmatrix} I \\ V \\ Q \\ U \end{bmatrix}_{circular} \tag{3.3}$$

Another useful set of quantities are the correlations themselves [AA^*, BB^*, AB^*, A^*B]. In the following sub-sections, we write down the transformations relating the true and

the measured quantities *viz.* the electric fields, the Stokes parameters as well as the correlations. We shall use [**J**], [**M**], & [**C**] to denote the Jones matrix, the Mueller matrix and the matrix connecting the correlations respectively.

3.2.1 The general Jones matrix of any instrument $[\mathbf{J}]_{2\times2}$

In Chapter 1, we have described Jones matrices corresponding to various propagation effects including those induced by the instrument. The net effect on the input fields can be described in terms of the complex Jones matrix as follows:

$$(\mathbf{E_m})_{2\times1} = (\mathbf{J})_{2\times2}\,(\mathbf{E_0})_{2\times1} \tag{3.4}$$

where,

$$(\mathbf{E_m})_{2\times1} = \begin{pmatrix} A_m \\ B_m \end{pmatrix} \;; \qquad (\mathbf{E_0})_{2\times1} = \begin{pmatrix} A_0 \\ B_0 \end{pmatrix} \tag{3.5}$$

$$(\mathbf{J})_{2\times2} = \tilde{j}_{11} \begin{pmatrix} 1 & \tilde{l} \\ \tilde{m} & \tilde{n} \end{pmatrix} \begin{pmatrix} \tilde{A}_0 \\ \tilde{B}_0 \end{pmatrix} \tag{3.6}$$

where, $(\tilde{A}_m, \tilde{B}_m)$ & $(\tilde{A}_0, \tilde{B}_0)$ are the resultant and the input signals respectively, and

$$\tilde{l} = \frac{\tilde{j}_{12}}{\tilde{j}_{11}} = l\,e^{i\theta_l} \;; \qquad \tilde{m} = \frac{\tilde{j}_{21}}{\tilde{j}_{11}} = m\,e^{i\theta_m} \;; \qquad \tilde{n} = \frac{\tilde{j}_{22}}{\tilde{j}_{11}} = n\,e^{i\theta_n} \tag{3.7}$$

Here each element of the original Jones matrix has been defined relative to the first element $\tilde{j}_{11}$ of the original matrix, for the sake of algebraic convenience. The choice of the element $\tilde{j}_{11}$ as the common factor as against any other element of the Jones matrix, has no special advantage. We would like to point out that the measured Stokes parameters are independent of the "*phase*" of this common factor. Since only the relative phases of the electric fields are relevant in the measurements, including the correlations etc., information on the absolute phase of $\tilde{j}_{11}$ is unimportant.

Instrumental calibration thus involves solving for 7 quantities corresponding to the 3 complex numbers $\tilde{l}$, $\tilde{m}$ & $\tilde{n}$ and the amplitude of the common factor, $|\tilde{j}_{11}|$ in our

case. Absolute calibration involves characterization of the term $|j_{11}|^2$ as a function of frequency (the so-called *bandpass calibration*) as well as time. Although the bandpass calibration can be done by observing an astronomical calibrator, the time dependent variations of $|j_{11}|^2$ can be calibrated using an adequately fast-switching noise source injecting additive correlated noise into the two orthogonal polarization channels of the receiver. We shall refer to this source as the *winking cal* or the *correlated cal*. The noise temperatures of the correlated cal must of course be known apriori, and are assumed to be available from separate measurements. Such calibration signals have been used previously, for example, by Max Komesaroff in order to calibrate the orthogonal linear feeds used in the ATCA[1].

3.2.2 The matrix connecting the products or the correlations $[\mathbf{C}]_{4\times4}$

The measured products $(\mathbf{P_m})_{4\times1}$ are connected to the true products $(\mathbf{P_0})_{4\times1}$ through the matrix $(\mathbf{C})_{4\times4}$ (see equations 3.8, 3.9 & 3.10).

$$(\mathbf{P_m})_{4\times1} = (\mathbf{C})_{4\times4}\,(\mathbf{P_0})_{4\times1} \tag{3.8}$$

where,

$$(\mathbf{P_m})_{4\times1} = \begin{pmatrix} A_m A_m^* \\ B_m B_m^* \\ A_m B_m^* \\ A_m^* B_m \end{pmatrix} \quad ; \qquad (\mathbf{P_0})_{4\times1} = \begin{pmatrix} A_0 A_0^* \\ B_0 B_0^* \\ A_0 B_0^* \\ A_0^* B_0 \end{pmatrix} \tag{3.9}$$

$$(\mathbf{C})_{4\times4} = j_{11}^2 \begin{pmatrix} 1 & l^2 & le^{-i\theta_l} & le^{i\theta_l} \\ m^2 & n^2 & mne^{i(\theta_m-\theta_n)} & mne^{-i(\theta_m-\theta_n)} \\ me^{-i\theta_m} & lne^{i(\theta_l-\theta_n)} & ne^{-i\theta_n} & lme^{i(\theta_l-\theta_m)} \\ me^{i\theta_m} & lne^{-i(\theta_l-\theta_n)} & lme^{-i(\theta_l-\theta_m)} & ne^{i\theta_n} \end{pmatrix} \tag{3.10}$$

[1] http://www.atnf.csiro.au/observers/memos/d93780 1.pdf

3.2.3 The antenna Mueller matrix $[\mathbf{M}]_{4\times4}$

The Mueller matrix $(\mathbf{M})_{4\times4}$ transforms the true Stokes parameters $(\mathbf{S_0})_{4\times1}$ into the measured Stokes parameters $(\mathbf{S_m})_{4\times1}$:

$$(\mathbf{S_m})_{4\times1} = (\mathbf{M})_{4\times4}\,(\mathbf{S_0})_{4\times1} \tag{3.11}$$

where,

$$(\mathbf{S_m})_{4\times1} = \begin{pmatrix} S1_m \\ S2_m \\ S3_m \\ S4_m \end{pmatrix} \;; \qquad (\mathbf{S_0})_{4\times1} = \begin{pmatrix} S1_0 \\ S2_0 \\ S3_0 \\ S4_0 \end{pmatrix} \tag{3.12}$$

$$(\mathbf{M})_{4\times4} = j_{11}^2 \begin{pmatrix} \frac{1}{2}(1+l^2+m^2+n^2) & \frac{1}{2}(1-l^2+m^2-n^2) & l\cos(\theta_l)+mn\cos(\theta_m-\theta_n) & -l\sin(\theta_l)+mn\sin(\theta_m-\theta_n) \\ \frac{1}{2}(1+l^2-m^2-n^2) & \frac{1}{2}(1-l^2-m^2+n^2) & l\cos(\theta_l)-mn\cos(\theta_m-\theta_n) & -l\sin(\theta_l)-mn\sin(\theta_m-\theta_n) \\ m\cos(\theta_m)+ln\cos(\theta_l-\theta_n) & m\cos(\theta_m)-ln\cos(\theta_l-\theta_n) & n\cos(\theta_n)+lm\cos(\theta_l-\theta_m) & -n\sin(\theta_n)-lm\sin(\theta_l-\theta_m) \\ m\sin(\theta_m)-ln\sin(\theta_l-\theta_n) & m\sin(\theta_m)+ln\sin(\theta_l-\theta_n) & n\sin(\theta_n)-lm\sin(\theta_l-\theta_m) & n\cos(\theta_n)-lm\cos(\theta_l-\theta_m) \end{pmatrix} \tag{3.13}$$

Both the Mueller matrix and the matrix relating the correlations are written in terms of the general Jones matrix here. Later, we shall express the elements in terms of physical quantities that describe $l,\ m$ & n. The description in terms of $l,\ m$ & n is generally useful in deriving readily, the Mueller matrix corresponding to the Jones matrix of any individual component.

3.3 Brief review of the signal path & its transformation at various stages of propagation

Until now, we had not discussed about the physical origin of the elements of the antenna Jones matrix $l,\ m,\ n$ & j_{11}. In this section, we trace the signal path through the instrument and see what conditions in the various components of the instrument

contribute to the elements of the antenna matrices.

The signal originating from an astronomical source traverses through the intervening medium (that includes the ionosphere), and is finally sensed by the antenna feeds. The shaped reflector surface in cases of dish antennas, which determines the collecting area or aperture size, is regarded ideal in all our discussions unless otherwise mentioned. From the feed, the signal passes through pre-amplifiers, and subsequently through a series of amplifiers, mixers and attenuators *etc* . Additionally, some systems may have a quadrature hybrid for converting signals from a system that has native linear feeds into circular, or vice versa. The hybrid is placed either before the pre-amplifiers, or immediately after it. The consequence of the hybrid's location is discussed in sub-section 3.4.3. We note below the transformation induced by each of the above elements on a pair of input signals.

3.3.1 Orientation of the measurement-frame *w.r.t.* sky (PA_{feed})

The relative orientation of the feed dipoles *w.r.t.* the sky reference frame (where, North is taken as zero, and the angle increases from North through East) would introduce a rotation of the Ex-Ey plane by an angle, say $\mathrm{PA_{feed}}$. The Jones matrix corresponding to the feed orientation is written below:

$$[J_{PA}] = \begin{bmatrix} \cos(PA_{feed}) & \sin(PA_{feed}) \\ -\sin(PA_{feed}) & \cos(PA_{feed}) \end{bmatrix}$$

Calibration of the feed's PA is necessary when comparing polarization angles derived from data observed using different instruments. For data observed with the same instrument however, its determination may not always be crucial. In any case, this calibration may be done at the end, after all the elements of the antenna matrix have been derived, and the data corrected. PA_{feed} can be derived by observing a linearly polarized astronomical source whose polarization position angle is absolutely known. In doing so, the contribution of the changing parallactic angle as a function of hour

angle which is implicit in $\mathrm{PA_{feed}}$, needs to be accounted for before interpreting the $\mathrm{PA_{feed}}$ as a physical offset in feed orientation. In the case of dual circulars, this Position Angle ($\mathrm{PA_{feed}}$) of the feed is a manifestation of any intrinsic phase difference between the R and the L-feeds. In general, this RL-phase is a function of frequency, and must be determined using linearly polarized calibrators whose foreground RM is known.

3.3.2 Ellipticity of an ideal feed $(\psi,\ \chi)$

An ideal dual feed is one that measures, without alteration, a pair of mutually orthogonal polarized components. In general, the response of such a feed would be equivalent of measurement in an elliptical basis (linear and circular bases are special cases which are preferred and commonly used). Following Conway & Kronberg (1969), the response of this feed to an incoming signal described in the $(\hat{e}_x, \hat{e}_y)$ basis may be written as:

$$[J_{feed}] = \begin{bmatrix} \cos(\psi) & e^{i\chi}\sin(\psi) \\ -e^{-i\chi}\sin(\psi) & \cos(\psi) \end{bmatrix} \tag{3.14}$$

where ψ & χ, in certain combination (Conway & Kronberg, 1969), parametrizes the axis-ratios as well as the tilt-angles associated with the polarization ellipses corresponding to the two orthogonally polarized components of the feed. For the sake of reference, we write down, in the linear basis, the two orthonormal components corresponding to the feed above:

$$\begin{bmatrix} \hat{e}_{1,x} \\ \hat{e}_{1,y} \end{bmatrix} = \begin{bmatrix} \cos(\psi)\ e^{i\chi/2} \\ \sin(\psi)\ e^{-i\chi/2} \end{bmatrix}$$
$$\begin{bmatrix} \hat{e}_{2,x} \\ \hat{e}_{2,y} \end{bmatrix} = \begin{bmatrix} -\sin(\psi)\ e^{i\chi/2} \\ \cos(\psi)\ e^{-i\chi/2} \end{bmatrix} \tag{3.15}$$

In general, the polarization ellipses in the $(\hat{e}_x, \hat{e}_y)$ plane, corresponding to the two

orthogonal states of this feed may not have their axes aligned with the $\hat{e}_x$ & $\hat{e}_y$ axes. However, without the loss of generality, such a feed may be defined in a new rotated frame $(\hat{e}_x^m, \hat{e}_y^m)$ such that their components coincide with the axes of the ellipses (Heiles et al., 2001). In this new frame, $\chi = 90^\circ$ always. The ellipticity (or "fatness" of the polarization ellipse) of the feed does not change due to such a rotation. It will only result in a change of the PA of the feed.

The parameter ψ is a measure of the feed ellipticity. The ellipticity of a circular feed is 1, and so $\psi_{circ} = 45^\circ$. A linear feed has zero ellipticity, and hence $\psi_{lin} = 0$.

In the rotated frame discussed above, the feed matrix would take the form:

$$[J_{feed}] = \begin{bmatrix} \cos(\psi) & i\sin(\psi) \\ i\sin(\psi) & \cos(\psi) \end{bmatrix} \tag{3.16}$$

To be able to interpret the true polarization state of the incoming signal correctly, the ellipticity of the feed must be known. We note later, that the ellipticity of the feed can be considered as a part of the general leakage matrix where mutual leakages between the two orthogonal channels are NOT equal. The feasibility of instrumental calibration for this general case is discussed in section 3.6.1. For the sake of completeness however, we look at the result of the response J_{feed} to a few cases with 100% polarized signals that may serve useful for calibration purposes.

General response to 100% polarized state: The following equation shows

the transformation that an ideal feed does to an incoming 100% polarized state.

$$\begin{bmatrix} \bar{E}_{A,f} \\ \bar{E}_{B,f} \end{bmatrix} = \begin{bmatrix} \cos(\psi) & i\sin(\psi) \\ i\sin(\psi) & \cos(\psi) \end{bmatrix} \begin{bmatrix} \cos(\alpha)\ e^{-i\delta/2} \\ \sin(\alpha)\ e^{+i\delta/2} \end{bmatrix}$$

$$= \tilde{g}_f \begin{bmatrix} \cos(\alpha_f)\ e^{-i\delta_f/2} \\ \sin(\alpha_f)\ e^{+i\delta_f/2} \end{bmatrix} \tag{3.17}$$

where,

$$\tilde{g}_f = 1 \tag{3.18}$$

$$\tan(\alpha_f) = \sqrt{\left(\frac{\cos^2\psi \sin^2\alpha \ + \ \sin^2\psi \cos^2\alpha \ + \frac{1}{4}\sin 2\psi \sin 2\alpha \sin\delta}{\cos^2\psi \cos^2\alpha \ + \ \sin^2\psi \sin^2\alpha \ - \frac{1}{4}\sin 2\psi \sin 2\alpha \sin\delta} \right)} \tag{3.19}$$

$$\begin{aligned} \delta_f = & \tan^{-1}\left(\frac{\cos\psi \sin\alpha \sin\frac{\delta}{2} \ + \ \sin\psi \cos\alpha \cos\frac{\delta}{2}}{\cos\psi \sin\alpha \cos\frac{\delta}{2} \ + \ \sin\psi \cos\alpha \sin\frac{\delta}{2}} \right) \\ & + \tan^{-1}\left(\frac{\cos\psi \cos\alpha \sin\frac{\delta}{2} \ - \ \sin\psi \sin\alpha \cos\frac{\delta}{2}}{\cos\psi \cos\alpha \cos\frac{\delta}{2} \ - \ \sin\psi \sin\alpha \sin\frac{\delta}{2}} \right) \end{aligned} \tag{3.20}$$

Special Cases:

1. **Response to linear polarized state ($\delta = 0$):** If the input state is linear, $\delta = 0$. From equations 3.18– 3.20 the response to a linear polarized state can

be written as:

$$\tilde{g}_f = 1 \tag{3.21}$$

$$\tan(\alpha_f) = \sqrt{\left(\frac{\cos^2\psi \sin^2\alpha \ + \ \sin^2\psi \cos^2\alpha}{\cos^2\psi \cos^2\alpha \ + \ \sin^2\psi \sin^2\alpha}\right)} \tag{3.22}$$

$$\delta_f = \tan^{-1}\left(\frac{\tan\psi}{\tan\alpha}\right) \ - \tan^{-1}(\tan\psi \tan\alpha) \tag{3.23}$$

2. **Response to correlated cal:** Additionally if the amplitude ratio of the linear polarized state is 1 (*i.e.* $\alpha = 45°$) then:

$$\tilde{g}_f = 1 \tag{3.24}$$

$$\tan(\alpha_f) = 1 \tag{3.25}$$

$$\delta_f = 0 \tag{3.26}$$

Thus an ideal feed does not modify a 100% linear polarized state with $\alpha = 45°$. The definition of the Stokes parameters would however change depending on the angle ψ that characterizes the feed's ellipticity. For example, for a pure linear feed ($\psi = 0$), a linear polarization state with $\alpha = 45°$ would appear as Stokes U. Whereas, for a circular feed ($\psi = 45°$), the same input state would appear as Stokes Q.

3. **Response to 100% circular polarized calibrator($\alpha = 45°,\ \delta = \pm 90°$):**

$$\tilde{g}_f = 1 \tag{3.27}$$

$$\tan(\alpha_f) = \sqrt{\left(\frac{1 \pm \sin\psi\cos\psi}{1 \mp \sin\psi\cos\psi}\right)} \tag{3.28}$$

$$\delta_f = \pm 90° \tag{3.29}$$

The ideal feed does not alter the phase difference δ of a pure circular polarized

state. It however alters the aspect ratio of the resulting polarization ellipse.

3.3.3 Dipole errors & instrumental leakage ($\epsilon_{BA},\ \phi_{BA},\ \epsilon_{AB},\ \phi_{AB}$)

Cross-coupling leads to non-orthogonality of what may have been otherwise orthogonal polarization states. Although such *leakages* can in principle occur at various stages in the signal path, proper electro-magnetic shielding of the back-end components of the receiver system generally ensures near-perfect isolation. One obvious non-ideality that could introduce cross coupling is a relative misalignment of the dipoles from orthogonality. For example, if the relative orientation of the dipoles in a linear feed were to deviate from 90°, wherein the x-dipole is not oriented exactly along the x axis, then it would respond not only to the x-component of the electric field, but also to a fraction, say $\tilde{\epsilon}_{BA}$ of the y-component. Same would in general be the case for the y-dipole. Although this cross-coupling has traditionally been called the *dipole error*, its source may also be *inductive* in nature, as in cases of two current carrying naked cables lying very close to each other. A "good" system, should have the amplitudes of the coupling (ϵ_{AB} & ϵ_{BA} $<<$ 1). Nevertheless, as will be seen later, our calibration scheme does not require small-ϵ approximations to be made. The relative phases (ϕ_{BA} & ϕ_{AB}) with which the signals couple, are also considered independent.

$$[J_l] = \begin{bmatrix} 1 & \epsilon_{BA}\ e^{i\phi_{BA}} \\ \epsilon_{AB}\ e^{i\phi_{AB}} & 1 \end{bmatrix}$$

When the feed non-ideality is merely in non-orthogonal orientation of linear dipoles, then $\phi_{AB} = \phi_{BA} = 0$ would be a justifiable assumption, and the ϵs would be directly related to the orientation offsets.

General response to 100% polarized state: The following equation shows

the transformation that *leakage* does to an incoming 100% polarized state.

$$\begin{bmatrix} \bar{E}_{A,l} \\ \bar{E}_{B,l} \end{bmatrix} = \begin{bmatrix} 1 & \epsilon_{BA}\ e^{i\phi_{BA}} \\ \epsilon_{AB}\ e^{i\phi_{AB}} & 1 \end{bmatrix} \begin{bmatrix} \cos(\alpha)\ e^{-i\delta/2} \\ \sin(\alpha)\ e^{+i\delta/2} \end{bmatrix}$$

$$= \tilde{g}_l \begin{bmatrix} \cos(\alpha_l)\ e^{-i\delta_l/2} \\ \sin(\alpha_l)\ e^{+i\delta_l/2} \end{bmatrix} \tag{3.30}$$

where,

$$\tilde{g}_l = \sqrt{1 + \epsilon_{BA}^2 \sin^2\alpha + \epsilon_{AB}^2 \cos^2\alpha + 2\cos\alpha\sin\alpha[\epsilon_{BA}\cos(\delta + \phi_{BA}) + \epsilon_{AB}\cos(\delta - \phi_{AB})]} \tag{3.31}$$

$$\tan(\alpha_l) = \sqrt{\left(\frac{\sin^2\alpha + \epsilon_{AB}^2\cos^2\alpha + 2\epsilon_{AB}\sin\alpha\cos\alpha\cos(\delta - \phi_{AB})}{\cos^2\alpha + \epsilon_{BA}^2\sin^2\alpha + 2\epsilon_{BA}\sin\alpha\cos\alpha\cos(\delta + \phi_{BA})}\right)} \tag{3.32}$$

$$\delta_l = \tan^{-1}\left(\frac{\sin\alpha\sin\frac{\delta}{2} + \epsilon_{AB}\cos\alpha\sin(\phi_{AB} - \frac{\delta}{2})}{\sin\alpha\cos\frac{\delta}{2} + \epsilon_{AB}\cos\alpha\cos(\phi_{AB} - \frac{\delta}{2})}\right)$$

$$+ \tan^{-1}\left(\frac{\cos\alpha\sin\frac{\delta}{2} - \epsilon_{BA}\sin\alpha\sin(\phi_{BA} + \frac{\delta}{2})}{\cos\alpha\cos\frac{\delta}{2} + \epsilon_{BA}\sin\alpha\cos(\phi_{BA} + \frac{\delta}{2})}\right) \tag{3.33}$$

It is easy to see that while the polarization state may undergo transformation, the percentage polarization remains 100%.

Special cases

1. **Response to $\alpha = 45°,\ \delta = 0°$ linear polarization:**

$$\tilde{g}_l = \sqrt{1 + \frac{1}{2}(\epsilon_{BA}^2 + \epsilon_{AB}^2) + \epsilon_{BA}\cos(\phi_{BA}) + \epsilon_{AB}\cos(\phi_{AB})} \tag{3.34}$$

$$\tan(\alpha_l) = \sqrt{\left(\frac{1 + \epsilon_{AB}^2 + 2\epsilon_{AB}\cos(\phi_{AB})}{1 + \epsilon_{BA}^2 + 2\epsilon_{BA}\cos(\phi_{BA})}\right)} \tag{3.35}$$

$$\delta_l = \tan^{-1}\left[\frac{\epsilon_{AB}\sin(\phi_{AB})}{1 + \epsilon_{AB}\cos(\phi_{AB})}\right] - \tan^{-1}\left[\frac{\epsilon_{BA}\sin(\phi_{BA})}{1 + \epsilon_{BA}\cos(\phi_{BA})}\right] \tag{3.36}$$

This case would be relevant in the case of correlated calibration signals injected into the polarization channels. Usually these cal signals are added to the system noise (which includes the sky signal), and hence the above equations apply to only the cal component, which is extracted from the difference between cal-ON & cal-OFF measurements.

2. **Response to 100% polarized state with $\alpha = 45°$, $\delta = \pm 90°$:** For a 100% input circular polarized state, the output state attained after leakage are described by:

$$\tilde{g}_l = \sqrt{1 + \frac{1}{2}(\epsilon_{AB}^2 + \epsilon_{BA}^2) \pm ((\epsilon_{AB}\sin(\phi_{AB}) - \epsilon_{BA}\sin(\phi_{BA}))} \tag{3.37}$$

$$\tan(\alpha_l) = \sqrt{\left(\frac{1 + \epsilon_{AB}^2 \pm 2\epsilon_{AB}\sin(\phi_{AB})}{1 + \epsilon_{BA}^2 \mp 2\epsilon_{BA}\sin(\phi_{BA})}\right)} \tag{3.38}$$

$$\delta_l = \tan^{-1}\left[\frac{1 + \epsilon_{AB}(\sin(\phi_{AB}) \mp \cos(\phi_{AB}))}{1 + \epsilon_{AB}(\cos(\phi_{AB}) \pm \sin(\phi_{AB}))}\right]$$

$$+ \tan^{-1}\left[\frac{1 - \epsilon_{BA}(\sin(\phi_{BA}) \pm \cos(\phi_{BA}))}{1 + \epsilon_{BA}(\cos(\phi_{BA}) \mp \sin(\phi_{BA}))}\right] \tag{3.39}$$

3. **A note on the reciprocity ($\tilde{\epsilon}_{BA} = \tilde{\epsilon}_{AB}$) of leakages:** We note here that the

leakages need not in general hold a reciprocal relation between themselves, *i.e.* $\tilde{\epsilon}_{BA} \neq \tilde{\epsilon}_{AB}$. If this non-reciprocity is ignored in modeling the leakage matrix $[J_l]$, not **all** modifications to the polarized state of an incoming signal by the instrument can be correctly accounted for. We would also like to mention that the errors arising from assuming reciprocal leakages, when actually the leakages are non-reciprocal, do not get accounted for by the incorporation of the ideal elliptical feed matrix.

To elaborate the above, let us factorize the leakage matrix into two matrices – one of which replicates the condition of reciprocity, and see if the other can be *clubbed* with the feed matrix of equation (3.16).

$$
\begin{aligned}
[J_l] &= \begin{bmatrix} 1 & \epsilon_{BA}\, e^{i\phi_{BA}} \\ \epsilon_{AB}\, e^{i\phi_{AB}} & 1 \end{bmatrix} \\
&= \begin{bmatrix} 1 & \epsilon\, e^{i\phi} \\ \epsilon\, e^{i\phi} & 1 \end{bmatrix} \begin{bmatrix} \left(\dfrac{1-\epsilon\epsilon_{AB}e^{i(\phi+\phi_{AB})}}{1-\epsilon^2 e^{2i\phi}}\right) & -\left(\dfrac{\epsilon e^{i\phi}-\epsilon_{BA}e^{i\phi_{BA}}}{1-\epsilon^2 e^{2i\phi}}\right) \\ -\left(\dfrac{\epsilon e^{i\phi}-\epsilon_{AB}e^{i\phi_{AB}}}{1-\epsilon^2 e^{2i\phi}}\right) & \left(\dfrac{1-\epsilon\epsilon_{BA}e^{i(\phi+\phi_{BA})}}{1-\epsilon^2 e^{2i\phi}}\right) \end{bmatrix}
\end{aligned}
\tag{3.40}
$$

The denominators in the elements of the 2nd matrix above are equal, and may be taken out as a common factor. Yet the diagonal elements of the 2nd matrix are not equal as must be the case for it to equivalently represent the feed matrix of equation (3.16). As a matter of fact, the product of the above matrix (2nd term) with the feed matrix cannot be transformed in any manner such that the resultant retains the special symmetry of the feed matrix *viz.* equality of diagonal elements, equality of off-diagonal elements, as well as the necessity that its determinant be unity. If ϵ_{BA} & $\epsilon_{AB} \ll 1$, such that 2nd order terms can be neglected, we get

$$[J_l] \simeq \begin{bmatrix} 1 & \epsilon\, e^{i\phi} \\ \epsilon\, e^{i\phi} & 1 \end{bmatrix} \begin{bmatrix} 1 & -(\epsilon e^{i\phi} - \epsilon_{BA} e^{i\phi_{BA}}) \\ -(\epsilon e^{i\phi} - \epsilon_{AB} e^{i\phi_{AB}}) & 1 \end{bmatrix} \tag{3.41}$$

If we further assume that the leakage amplitudes are nearly equal (*i.e.* $\epsilon_{BA} \simeq \epsilon_{AB} \simeq \epsilon$), and force $\phi = \phi_{BA}$ without loss of generality, equation 3.41 would take the form:

$$[J_l] = \begin{bmatrix} 1 & \epsilon\, e^{i\phi} \\ \epsilon\, e^{i\phi} & 1 \end{bmatrix} \begin{bmatrix} 1 & 0 \\ -r\ \epsilon e^{i\phi'} & 1 \end{bmatrix} \tag{3.42}$$

where,

$$\begin{aligned} r &= \sqrt{2 - 2\cos(\phi - \phi_{AB})} \\ \tan(\phi') &= \frac{\sin\phi - \sin\phi_{AB}}{\cos\phi - \cos\phi_{AB}} \\ \epsilon_{BA} &= \epsilon_{AB} = \epsilon \\ \phi_{BA} &= \phi \end{aligned}$$

Even under such an assumption, product of the 2nd matrix in the RHS of equation 3.42 and the feed matrix, cannot be represented by an *effective* resultant feed matrix for any pair of orthogonal feeds. Hence if non-reciprocal leakages are modeled as a combination of reciprocal leakage and a modified feed matrix, there will be certain modifications that such a model will never be able to take into account. However, as long as the ellipticity of the feed remains constant, its parameter ψ, can be re-distributed amongst the $\tilde{\epsilon}$s, $\tilde{\gamma}$ and the constant term $\tilde{j}_{11}$. Hence the case of non-reciprocal leakage is a more general one that takes into account the ellipticity of the feed as well. Therefore, we treat $\tilde{\epsilon}_{BA}$ and $\tilde{\epsilon}_{AB}$ as independent, and do not separately solve for the feed ellipticity.

3.3.4 Amplifier gains & phases ($\tilde{g}_A,\ \gamma,\ \theta$):

Equation B.15 describes the effect of a complex gain block on the input signal. We define the complex *gain ratio*, between the two amplifiers, in terms of amplitude ratio γ, and phase difference θ:

$$\frac{\tilde{g}_B}{\tilde{g}_A} = \gamma\ e^{i\theta} \tag{3.43}$$

Therefore equation B.15 can be written as:

$$[J_g] = \tilde{g}_A \begin{bmatrix} 1 & 0 \\ 0 & \gamma\ e^{i\theta} \end{bmatrix} \tag{3.44}$$

The term $\tilde{g}_A$ would be absorbed in the common factor $\tilde{j}_{11}$ of equation 3.4, and variations in this quantity must be calibrated using appropriate calibrators.

1. **General response to 100% polarized state:** The following equation shows the transformation that the amplifier *gains & phases* induce on the incoming signals in 100% polarized state.

$$\begin{bmatrix} \bar{E}_{A,a} \\ \bar{E}_{B,a} \end{bmatrix} = \begin{bmatrix} 1 & 0 \\ 0 & \gamma\ e^{i\theta} \end{bmatrix} \begin{bmatrix} \cos(\alpha)\ e^{-i\delta/2} \\ \sin(\alpha)\ e^{+i\delta/2} \end{bmatrix}$$

$$= \tilde{g}_a \begin{bmatrix} \cos(\alpha_a)\ e^{-i\delta_a/2} \\ \sin(\alpha_a)\ e^{+i\delta_a/2} \end{bmatrix} \tag{3.45}$$

where,

$$\tilde{g}_a = \tilde{g}_A \cos\alpha \sqrt{1 + \gamma^2\ \tan^2\alpha} \tag{3.46}$$

$$\tan(\alpha_a) = \gamma \tan\alpha \tag{3.47}$$

$$\delta_g = \theta + \delta \tag{3.48}$$

Thus the effect of a complex gain block on the dual polarization signals is to modify the amplitude ratio of orthogonal components by a factor equal to the gain-amplitude ratio γ, and to introduce an additional phase offset equal to the gain-phase difference θ, between two signals.

2. **Response to leakage-affected correlated cal ($\alpha = 45°$):** Here we consider the input to the gain block is the output from the leakage block. The quantities associated with the latter are denoted by subscript "l" in the equations below. The combined effect of the two blocks can be described as

$$\tilde{g}_a = \tilde{g}_A \tilde{g}_l \cos\alpha_l \sqrt{1 + \gamma^2 \ \tan^2\alpha_l} \tag{3.49}$$

$$\begin{aligned} \tan(\alpha_a) &= \gamma \tan\alpha_l \\ &= \gamma \sqrt{\frac{1 + \epsilon_{AB}^2 + 2\epsilon_{AB}\cos\phi_{AB}}{1 + \epsilon_{BA}^2 + 2\epsilon_{BA}\cos\phi_{BA}}} \quad \text{(using eq. 3.35)} \end{aligned} \tag{3.50}$$

$$\begin{aligned} \delta_g &= \theta + \delta_l \\ &= \theta + \tan^{-1}\left[\frac{\epsilon_{AB}\sin\phi_{AB}}{1 + \epsilon_{AB}\cos\phi_{AB}}\right] \\ &\quad - \tan^{-1}\left[\frac{\epsilon_{BA}\sin\phi_{BA}}{1 + \epsilon_{BA}\cos\phi_{BA}}\right] \quad \text{(using eq. 3.36)} \end{aligned} \tag{3.51}$$

The lowercase "a" in the subscript of g signifies the "net" constant term due to the "amplifier". The uppercase "A" stands for the "gain" of channel A. In other words, $\tilde{g}_a$ is the $\tilde{j}_{11}$, and one of the contributing factors of $\tilde{g}_a$ is the "gain" g_A of the amplifier of channel A.

Thus the original signal from its entry into the instrument and until its recording, undergoes the following transformation:

$$[J_{tot}] = [J_g]\,[J_l]\,[J_{feed}]\,[J_{PA}] \tag{3.52}$$

$$[J_{tot}] = \tilde{j}_{11} \begin{bmatrix} 1 & 0 \\ 0 & \gamma\ e^{i\theta} \end{bmatrix} \begin{bmatrix} 1 & \epsilon_{BA}\ e^{i\phi_{BA}} \\ \epsilon_{AB}\ e^{i\phi_{AB}} & 1 \end{bmatrix} \begin{bmatrix} \cos(\alpha) & i\sin(\alpha) \\ i\sin(\alpha) & \cos(\alpha) \end{bmatrix} \begin{bmatrix} \cos(PA_{feed}) & \sin(PA_{feed}) \\ -\sin(PA_{feed}) & \cos(PA_{feed}) \end{bmatrix}$$

$$= \tilde{j}_{11} \begin{bmatrix} 1 & \epsilon_{BA}\ e^{i\phi_{BA}} \\ \gamma\epsilon_{AB}\ e^{i(\phi_{AB}+\theta)} & \gamma\ e^{i\theta} \end{bmatrix} \begin{bmatrix} \cos(PA_{feed}) & \sin(PA_{feed}) \\ -\sin(PA_{feed}) & \cos(PA_{feed}) \end{bmatrix} \tag{3.53}$$

Our case of non-reciprocal leakages makes the feed matrix redundant. Thus instrumental calibration would involve characterization of the gain mismatches and the coupling between the two orthogonal signals. The intrinsic feed position angle PA_{feed} may be determined after the effects of instrumental leakages and gains have been corrected for. Thus the quantities l , m & n of the instrument's Jones matrix are physically related to the instrumental parameters as follows:

$$\begin{aligned} l &= \epsilon_{BA}\ e^{i\phi_{BA}} \\ m &= \epsilon_{AB}\ e^{i\phi_{AB}}\gamma\ e^{i\theta} \\ n &= \gamma\ e^{i\theta} \end{aligned} \tag{3.54}$$

The constant term $\tilde{j}_{11}$ contains the absolute gain term $\tilde{g}_A$ of the channel A, relative to which $l,\ m,\ \&\ n$ are expressed. Relative calibration of instrumental polarization therefore requires estimation of these 6 parameters in general, at each of the spectral channels. Irrespective of the number of gain and leakage blocks, as well as the order in which they physically appear within a receiver chain, the relative instrumental parameters can be modeled in an effective sense, in terms of ONE gain and ONE leakage block as in equation 3.53. We would like to point here a very important assumption implicitly, and commonly made – that is, the temporal variations of only the gain-terms γ & θ are generally considered, and may need appropriately frequent calibration. The leakage terms are assumed constant over time for a given setup. This assumption will be at the heart of the calibration scheme discussed in subsequent sections. The scheme for calibration in cases where even the effective leakage terms are

time-dependent, would depend on the specific location of the time-dependent parameters within the Jones matrix. These are discussed in section 3.4.

3.4 Correlated Noise calibrators: utility and limitations

A correlated noise cal that can be electronically injected at adequately frequent intervals is useful in calibrating the *time-varying* elements of the antenna Jones matrix. Such a cal can be represented, as discussed above, with $\alpha = 45^\circ$ and $\delta = 0$. Usually it is the amplifier gains that vary rather rapidly with time. In section 3.3 we have discussed the net effect due to instrumental leakage and gains on such a calibrator signal. A correlated cal can be used in calibrating the relative gain ratio γ, of the receiver chains for the orthogonal polarization channels, the relative gain phase θ, as well as the absolute gain amplitude g_A, all of which are assumed to have possible temporal variations. This cal cannot however calibrate, on its own, the instrumental leakage parameters.

3.4.1 Relative gain amplitude and phase calibration

Using equations 3.2, 3.3, 3.50 and 3.51 we would get from the measured correlations (linear polarized state with $\alpha = 45^\circ$) corresponding to the correlated cal signal, the following relations:

$$\left(\frac{\tilde{B}_m \tilde{B}_m^*}{\tilde{A}_m \tilde{A}_m^*}\right) = \gamma^2 \left(\frac{1 + \epsilon_{AB}^2 + 2\epsilon_{AB}\cos\phi_{AB}}{1 + \epsilon_{BA}^2 + 2\epsilon_{BA}\cos\phi_{BA}}\right) = \left(\frac{S1_m - S2_m}{S1_m + S2_m}\right) \tag{3.55}$$

$$\tan^{-1}\left(\frac{S4}{S3}\right) = \theta + \delta_l$$
$$= \theta + \tan^{-1}\left[\frac{\epsilon_{AB}\sin(\phi_{AB})}{1+\epsilon_{AB}\cos(\phi_{AB})}\right]$$
$$- \tan^{-1}\left[\frac{\epsilon_{BA}\sin(\phi_{BA})}{1+\epsilon_{BA}\cos(\phi_{BA})}\right] \text{ (using eq. 3.36)} \quad (3.56)$$

For the case of reciprocal leakage, the measurement on a correlated cal exactly solves the gain amplitude ratio γ & the gain phase θ. For the case of the non-reciprocal leakages however, the γ and θ estimated using equations 3.55 & 3.56 would also contain terms that *physically* are a result of the leakages, and so the gain-corrected data would still be corrupted by a remnant gain-amplitude and gain-phase error. Nevertheless, the correction would take out the time-dependent effect of the amplifier gain chains, and the remnant errors should hopefully remain constant, consequent to our assuming the constancy of leakage parameters, during an observing session. The resultant γ & θ of the new gain matrix after the data are corrected for the time-dependent variations using a correlated cal, would be:

$$\gamma' = \sqrt{\frac{1+\epsilon_{BA}^2+2\epsilon_{BA}\cos\phi_{BA}}{1+\epsilon_{AB}^2+2\epsilon_{AB}\cos\phi_{AB}}} \quad (3.57)$$

$$\theta' = \tan^{-1}\left[\frac{\epsilon_{BA}\sin(\phi_{BA})}{1+\epsilon_{BA}\cos(\phi_{BA})}\right]$$
$$- \tan^{-1}\left[\frac{\epsilon_{AB}\sin(\phi_{AB})}{1+\epsilon_{AB}\cos(\phi_{AB})}\right] \quad (3.58)$$

As expected, these depend only on the leakage parameters. Their effects on the data will need to be calibrated further using additional and suitable calibrator sources (discussed in the section 3.6.1).

3.4.2 Absolute calibration of gain amplitude $|g_A|$

From equations 3.45 & 3.49:

$$\begin{bmatrix} \tilde{A}_m \\ \tilde{B}_m \end{bmatrix} = \tilde{g}_a \begin{bmatrix} \cos\alpha_a \; e^{-i\delta_a/2} \\ \sin\alpha_a \; e^{+i\delta_a/2} \end{bmatrix}$$

where,

$$\tilde{g}_a = \tilde{g}_A \tilde{g}_l \cos\alpha_l \sqrt{1+\gamma^2 \; \tan^2\alpha_l}$$

From the above equations and using the relations in section 2 for leakage-affected correlated cal parameters, the absolute gain-amplitude g_A of receiver channel A can be written as:

$$g_A^2 = \left[\frac{1}{1+\epsilon_{BA}^2 + 2\epsilon_{BA}\cos\phi_{BA}}\right]\left(\frac{\tilde{A}_m \tilde{A}_m^*}{2\; T_{cal}}\right) \tag{3.59}$$

In the expression above, we explicitly put in the parameter T_{cal} whose presence had so far been implicitly assumed. Applying corrections to measurements on sky signals by the g_A^2 derived using the correlated cal would take away the overall time-dependent variations from the data as well (the relative variation γ & θ has already been taken out). This will be true only if g_A as well as γ & θ, do not change between the time when the sky and the cal are measured. That is why a winking cal with adequately fast on/off rate is desirable as the correlated cal.

The absolute gain-calibrated flux density ($S^{m,agc}$) would however still be scaled by a leakage-dependent factor:

$$S_i^{m,agc} = (1+\epsilon_{BA}^2 + 2\epsilon_{BA}\cos\phi_{BA})S_i \; ;(\; i \; = \; 1,\; 2,\; 3 \;\&\; 4) \tag{3.60}$$

Observation of an astronomical flux-density calibrator would allow determination of this scaling factor.

It is interesting to note that the leakage term appearing in the expression for g_A is the one corresponding to the leakage from channel B to A (element j_{12} of the Jones

matrix). The other leakage (that from A to B) does not affect the absolute gains since it is the gain term referring to channel A, by our starting definition.

3.4.3 Some important considerations

We summarize below some points to keep in mind when calibrating using a correlated cal:

- **Ensuring calibratibility of the time-varying gains using a correlated cal:** In all conventional calibration strategies, the time-dependent parameters (usually attributed to the gain related components) are calibrated first. The leakages are derived once the gain calibration has been done. However calibratibility of the time-dependent parameters depend on their location in the Jones matrix. For example, in the general case of non-reciprocal leakages, the solutions obtained using conventional gain calibration using a correlated cal (equation 3.55) , when applied to the data, will not be able to get rid of the time-dependence from the elements of the resultant Jones matrix, if the leakages happen to be time-dependent. More specifically, it is crucial that only the element $l = \tilde{j}_{12} = \epsilon_{BA}\ e^{i\phi_{BA}}$ does not vary with time. Any time-dependence of elements m & n can always be modeled in terms of an effective time-dependent complex gain and leakages that are independent of time (see equation 3.54). Such a condition would be violated if for example, an additional amplifier is placed between $[\mathbf{J_l}]$ and $[\mathbf{J_{feed}}]$. It is therefore crucial that in case a *hybrid* is used, it be placed prior to the pre-amplifiers. Otherwise, a winking cal of the kind described, will not suffice in calibrating the time dependent instrumental effects.

  It is not ensured that any path-length differences between the two orthogonal signals occur only after the leakage block. In general, there may be an additional *phase* difference that gets introduced between the two components prior to the

occurrence of leakage. This relative phase angle can however be re-distributed between the gains and the non-reciprocal leakages (terms $j_{12},\ j_{21}$ & j_{22}) without loss of generality. However, if this phase varies with time, the winking cal would not suffice in calibrating the time-dependent effects of the element j_{12} of the Jones matrix since the resultant Jones matrix after the gain calibration would still have time-dependent contributions.

Likewise, as long as the ellipticity of the feed remains constant, its parameter ψ, can be re-distributed amongst the $\tilde{\epsilon}$s, $\tilde{\gamma}$ and the constant term $\tilde{j}_{11}$. The case of non-reciprocal leakage is thus a more general one that inherently takes into account the feed ellipticity. However, unlike with ψ, it may not be straightforward to relate the feed ellipticity with the two $\tilde{\epsilon}$s, $\tilde{\gamma}$ and $\tilde{j}_{11}$. But as long as we can correct for the net induced effects, not being able to resolve the degeneracy between feed-ellipticity, leakages & gains is not of major concern. Nonetheless, their physical meanings remain relevant while interpreting the calibration parameters.

We would like to point out that the assumption about leakage occurring before the signals are amplified is a reasonable assumption for most instruments, since coupling occurs generally at the early stages of the signal path, due to errors in the orientation of the dipoles or improper shielding of the cables close to the feeds. Furthermore, once the signal reaches the Low Noise Amplifiers (LNA – the first stage of amplification) subsequent coupling is practically negligible.

- **Leakages and the derived absolute gain g_A^2:** The absolute gain g_A^2 derived using a correlated cal would be scaled by a term that depends on the amplitude and the phase of only one of the leakages (that occurring from channel B to A in our formulation). This factor, however, is regarded to be a constant for a given instrument, and would get corrected during the flux-density calibration

stage. The apparent g_A relates to its true value in the following way:

$$g_A^2 = \frac{g_{A,true}^2}{1 + \epsilon_{BA}^2 + 2\epsilon_{BA}\cos\phi_{BA}} \tag{3.61}$$

- **Placement of the quadrature hybrid:** For reasons discussed in section 3.4.3 above, it would be worth discussing the appropriate location for the quadrature hybrid in the receiver chain. Quadrature hybrids are devices that are meant to produce sum or difference outputs from the pair of input signals after introducing 90° (relative) phase shift in one of the two input signals. Such hybrids are used to realize the conversion of linear-to-circular polarization channels (or vice versa) as described in equation (B.1) of section B. Strictly speaking, such devices act as quadrature hybrids only for a narrow frequency band. At other frequencies within a wide observation band, the relative phase shift introduced would be in error from the required 90° shift. This would lead to imperfect conversion of polarized states, and equivalently additional leakage. Hence if a hybrid follows the pre-amplifier in the signal-path, the transformation would follow a sequence of the form: L-G-L-G ("L" signifying a leakage block, and "G" a gain block). It is easy to see that the element $l = j_{12} = \tilde{\epsilon}_{BA}$ of the resultant Jones matrix will no longer be independent of the time-dependent gains. As discussed above, this would make the time-varying gain calibration using the correlated cal useless. As long as the quadrature hybrid is placed "before" the pre-amplification stage, a sequence L-L-G-G would be followed. Under the assumption that the leakages at none of the stages have temporal variations, the above can always be transformed to our favourite case of L-G where the element $\tilde{j}_{12}$ of the resulting Jones matrix will be independent of time. A hybrid, if required, should therefore be placed prior to the LNA. Placing the hybrid before the LNA would require that the losses it might introduce to the signal are as minimum as possible.

However, if it is inevitable to place the hybrid "after" the pre-amplification

stage, a potential method for calibrating the antenna Jones matrix could be to use a correlated noise source that successively injects into the orthogonal channels, an appropriate set of synthetically generated polarized signals at adequately frequent intervals. For example, three sets of linearly polarized signals with successive position angles differing by 45° can solve for the 6 parameters (see section 3.6.1 as well as sub-section 3.6.7). The position angle change can be synthesized using appropriate relative attenuation of the correlated signals being fed into the two orthogonal receiver chains. Preliminary demonstration of electronically generating polarized states using a system designed in the DSP lab at RRI, is shown in Figure 3-1. The system comprises of a noise source whose amplified outputs are split and fed into the two receiver input channels after appropriate attenuation of one relative to the other. The relative phase between the two split signals was adjusted to zero so as to generate only linearly polarized signals. Raw voltages corresponding to the input channels were recorded using an FPGA based module. With no relative attenuation, the resultant polarization ellipse (red scatter) appears with a tilt angle of 45° and with an axis-ratio of unity, as expected. Attenuating the signal fed to the X-channel by a factor of 2 relative to the signal going in to the Y-channel, rotates the position angle as well as modifies the axis-ratio by the corresponding amount (blue scatter). By appropriate choice of attenuators, various linearly polarized signals may be synthesized. The feasibility of such a method needs to be explored further.

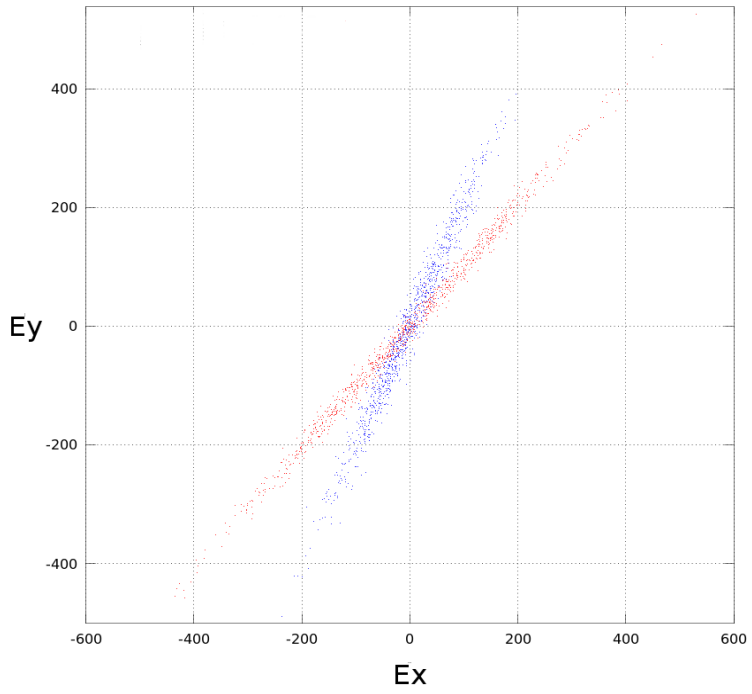

Figure 3-1: *Synthesizing polarized signal using correlated cal: polarization ellipse corresponding to linear polarized states synthetically generated using correlated noise cal with (a) no relative attenuation (red scatter) and (b) after attenuating the X-channel by a factor of 2 relative to the Y-channel (blue scatter).*

3.5 Usefulness of measurements of unpolarized calibrators: diffuse & compact sources

We re-write the Jones matrix corresponding to the instrument:

$$[J_{lg}] = \tilde{g}_A \begin{bmatrix} 1 & \epsilon_{BA}\ e^{i\phi_{BA}} \\ \epsilon_{AB}\ e^{i\phi_{AB}}\gamma\ e^{i\theta} & \gamma\ e^{i\theta} \end{bmatrix} \tag{3.62}$$

The measured [S1, S2, S3, S4] for an unpolarized source of intensity I_{unpol} corresponding to this Jones matrix is:

$$\begin{bmatrix} S1 \\ S2 \\ S3 \\ S4 \end{bmatrix} = g_A^2 \begin{bmatrix} \frac{1}{2}[(1+\epsilon_{BA}^2)+\gamma^2(1+\epsilon_{AB}^2)] \\ \frac{1}{2}[(1+\epsilon_{BA}^2)-\gamma^2(1+\epsilon_{AB}^2)] \\ \gamma[\epsilon_{AB}\cos(\theta+\phi_{AB})+\epsilon_{BA}\cos(\theta-\phi_{BA})] \\ \gamma[\epsilon_{AB}\sin(\theta+\phi_{AB})+\epsilon_{BA}\sin(\theta-\phi_{BA})] \end{bmatrix} I_{unpol} \tag{3.63}$$

Defining,

$$\gamma_{derived}^2 = \left(\frac{BB^*}{AA^*}\right) = \left(\frac{S1-S2}{S1+S2}\right)$$

we get

$$\gamma_{derived}^2 = \gamma^2 \left(\frac{1+\epsilon_{AB}^2}{1+\epsilon_{BA}^2}\right) \tag{3.64}$$

Further,

$$\left(\frac{S4}{S3}\right) = \left[\frac{\sin\theta\ (\epsilon_{AB}\cos\phi_{AB}+\epsilon_{BA}\cos\phi_{BA})+\cos\theta\ (\epsilon_{AB}\sin\phi_{AB}-\epsilon_{BA}\sin\phi_{BA})}{\cos\theta\ (\epsilon_{AB}\cos\phi_{AB}+\epsilon_{BA}\cos\phi_{BA})+\sin\theta\ (\epsilon_{BA}\cos\phi_{BA}-\epsilon_{AB}\cos\phi_{AB})}\right] \tag{3.65}$$

Like in the case of the correlated cal, measurement of an unpolarized source too, does not allow one to solve for the gain parameters γ & θ independent of the leakages (see also Bhatnagar & Nityananda (2001)). If however, a gain-correction (inversion of the derived gain matrix) is applied to the data using a correlated cal, the residual gain amplitude and phases in the corrected data become functions of only the leakage parameters. Likewise, even in the case of an unpolarized calibrator, the corrected data attains a residual gain-amplitude that is a function of the leakage parameters (although different than the one in the case of the correlated cal). However the residual gain-phase becomes a complicated function of the original gain-phase and the leakage parameters.

In case the leakages follow reciprocity, γ and θ can be derived directly from the measured quantities ($\gamma_{derived}$ and $\tan^{-1}\left(\frac{S4}{S3}\right)$), and the applied correction would make

the residual gain-amplitude unity and the residual gain phase zero.

Furthermore, for an ideal system, (*i.e.* , $\epsilon = 0$) θ cannot be derived using an unpolarized source, since $\frac{S4}{S3} = \frac{0}{0}$.

3.5.1 Properties of unpolarized signals as probes of instrumental fidelity and polarized signals from sky

Unpolarized sources are routinely used for diagnosis of instrumental polarization properties, for example at the GMRT, the VLA, the WSRT, the ATCA *etc* . Here we discuss a few procedures using unpolarized sources that may be useful in diagnosing instrumental polarization characteristics as well as in detection of polarized signatures in the sky. These procedures would be applicable even for single dishes.

1. **Together with the correlated cal:** If a correlated cal is already used for relative gain correction of data on an unpolarized source, the resultant residual γ would actually be the γ' as in equation (3.57), and hence equation 3.64 can be written as:

$$\gamma'^2_{derived} = \left(\frac{1+\epsilon_{BA}^2+2\epsilon_{BA}\cos\phi_{BA}}{1+\epsilon_{AB}^2+2\epsilon_{AB}\cos\phi_{AB}}\right)\left(\frac{1+\epsilon_{AB}^2}{1+\epsilon_{BA}^2}\right)$$

$$= \left[\frac{1+\left(\frac{2\epsilon_{BA}\cos\phi_{BA}}{1+\epsilon_{BA}^2}\right)}{1+\left(\frac{2\epsilon_{AB}\cos\phi_{AB}}{1+\epsilon_{AB}^2}\right)}\right] \tag{3.66}$$

   (a) The quantity $\gamma'_{derived}$ may be used as an indicator of the reciprocity. In case of the leakages following reciprocity, this quantity is expected to be nominally equal to unity. Any significant departure from this expectation would necessarily indicate non-reciprocity in leakages.

   (b) Furthermore, in the general case of non-reciprocal leakages, $\gamma'_{derived}$ derived using measurements on unpolarized sources, is independent of any of the

time-varying gain-parameters g_A, γ & θ. If instrumental leakages could be assumed to vary only slowly with time, significant fluctuations in the quantity $\gamma'_{derived}$ would be indicative of polarized signals from the sky.

2. **Even in the absence of the correlated cal:** For an unpolarized source, the measure of correlation (ρ) between the two nominally orthogonal signals, is independent of the effect of the receiver gains:

$$\begin{aligned}\rho_u &= \left[\frac{(AB^*)(A^*B)}{(AA^*)(BB^*)}\right] \\ &= \left[\frac{S3^2 + S4^2}{S1^2 - S2^2}\right] \\ &= \left[\frac{\epsilon_{AB}^2 + \epsilon_{BA}^2 + 2\epsilon_{AB}\epsilon_{BA}\cos(\phi_{AB} + \phi_{BA})}{(1+\epsilon_{AB}^2)\,(1+\epsilon_{BA}^2)}\right] \end{aligned} \tag{3.67}$$

Any variation in ρ (true for $\gamma'_{derived}$ as well) therefore must be either due to a changing instrument, or due to changing polarization of signal from the sky.

   (a) **Probing instrumental polarization characteristics:** The fidelity of the instrument's polarization response characteristics can be studied using this quantifier ρ. Variation in ρ while tracking an unpolarized source would indicate whether the constancy of instrumental polarization is a valid assumption to make. Of course, several unpolarized sources should be used, so as to avoid interpreting possible transients for example, as instrumental mis-behaviour.

   (b) **Quick survey of all-sky polarization:** If the stability of the instrument's polarization properties could be established, full Stokes data from telescopes operating in drift-scan mode, or transit mode can be used for locating signatures of changing polarization from the sky. For a given set of instrumental leakage parameters, the derived ρ for all unpolarized signals would remain statistically constant, whereas a polarized signal would

cause ρ to vary correspondingly. The detectability of such variations in ρ, besides being dependent on the degree of polarization of the signal, would in general depend on the polarized state as well. And although interpretation of the exact nature of polarization may not be straightforward (but can be explored with relevant analytical formulation as well as simulations), such studies would nevertheless provide a quick means of studying the distribution of polarized radiation across the sky without having to go through the process of instrumental polarization calibration.

This quantifier of polarization ρ could be immensely useful also in transient detections, including any RFI, and provides a powerful way of monitoring changes with immunity to system gain variations. In general, it will be worthwhile therefore, to keep recording data even when the telescopes slew across seemingly un-interesting parts of the sky in between the interesting target sources.

3.6 Exploring new methods for Instrumental calibration

In this section we discuss a few potential techniques for calibrating the instrument. An elegant Fourier-based method applicable for new generation telescopes that are being designed with an additional degree of freedom *viz.* rotation about the dish-axis, is presented. We also discuss usefulness of circularly polarized signals in characterizing certain instrumental parameters. We point out the occurrence of pure circular states in the ultra short-time duration (nano seconds) Crab giant pulses and discuss their usefulness in instrumental calibration, in particular, the band-pass calibration.

3.6.1 Instrumental calibration using rotating feeds: estimating the Mueller matrix parameters through matched-filtering

The apparent polarization position angle of a linear polarized source rotates with parallactic angle, when "tracked" with telescopes having non-equatorial (such as alt-azimuthal) mounts. This rotation of the angle of polarization with parallactic angle, is fruitfully & routinely used in instrumental polarization calibration exercises. (See for example, Sault et al. (1996); Heiles et al. (2001)). Similar apparent change in the polarization angle of a linearly polarized calibrator, relative to that of the feed, can be equivalently, and more importantly much more quickly, achieved if the feeds had an additional degree of freedom *viz.* rotation of its PA in the plane of the sky. New generation radio telescopes, like the ASKAP, are being built with provisions for rotation of the dish about its axis. These situations have not yet been explored in detail, and we formulate below the essential details, taking the ALFA (Arecibo L-band Feed Array)[2] system as an illustrative example. We discuss in particular, a Fourier transform based instrumental calibration method suitable for telescopes having feed/dish rotation facilities, and point out the advantages inherent in such a scheme over the parallactic angle tracking method.

Let us consider the response M of a linear feed, resulting in $(S1, S2, S3, S4) = (I, Q, U, V)$, to an incoming linearly polarized signal $(I_0,\ dp\cos 2\chi,\ dp\sin 2\chi,\ 0)$, where dp & χ are respectively the degree of linear polarization and the polarization

[2]The Arecibo Observatory is operated by SRI International under a cooperative agreement with the National Science Foundation (AST-1100968), and in alliance with Ana G. Mendez-Universidad Metropolitana, and the Universities Space Research Association.

position angle respectively, of the source:

$$\begin{pmatrix} I \\ Q \\ U \\ V \end{pmatrix} = g_A \begin{pmatrix} m_{11} & m_{12} & m_{13} & m_{14} \\ m_{21} & m_{22} & m_{23} & m_{24} \\ m_{31} & m_{32} & m_{33} & m_{34} \\ m_{41} & m_{42} & m_{43} & m_{44} \end{pmatrix} \begin{pmatrix} I_0 \\ dp\ I_0\ \cos 2\chi \\ dp\ I_0\ \sin 2\chi \\ 0 \end{pmatrix}$$

The exact dependences of the Mueller matrix elements m_{ij} on $\gamma,\ \theta,\ \epsilon_{BA},\ \epsilon_{AB},\ \phi_{BA}$ & ϕ_{AB} are provided in equation 3.13. In the units of $g_A I_0 = 1$, we will have:

$$I(\chi) = m_{11} + m_{12}\ dp\ \cos 2\chi + m_{13}\ dp\ \sin 2\chi \tag{3.68}$$

$$Q(\chi) = m_{21} + m_{22}\ dp\ \cos 2\chi + m_{23}\ dp\ \sin 2\chi \tag{3.69}$$

$$U(\chi) = m_{31} + m_{32}\ dp\ \cos 2\chi + m_{33}\ dp\ \sin 2\chi \tag{3.70}$$

$$V(\chi) = m_{41} + m_{42}\ dp\ \cos 2\chi + m_{43}\ dp\ \sin 2\chi \tag{3.71}$$

We note that the surviving terms in the means of the quantities on the LHS of equations (3.68)-(3.71) measured as χ changes from zero to π, are the terms $m_{j1},\ (j = 1, 2, 3, 4)$ of the first column of the Mueller matrix:

$$< I(\chi) > = m_{11}$$
$$< Q(\chi) > = m_{21}$$
$$< U(\chi) > = m_{31}$$
$$< V(\chi) > = m_{41}$$

Hence the measured Stokes parameters, averaged over feed rotation angles in the range zero to π directly provide estimate of elements in the first column of the instrumental Mueller matrix. As discussed below, the 2nd and the 3rd columns of the Mueller matrix are given by the real and the imaginary parts of the Fourier trans-

forms (FT) of the sequences of the measured Stokes parameters as a function of feed rotation angle χ.

It is easy to see that the sine and the cosine terms in equations (3.68)-(3.71) would form exactly ONE cycle for $\chi \in [0,\ \pi]$, with uniform sampling at adequately fine steps in χ. Hence the modulation amplitudes would appear in only the "1st" Fourier components, and the mean values would appear as the "zero-th" components. Furthermore, the coefficients $m_j 2, (j = 1, 2, 3, 4)$ corresponding to the cosine (even) components, would appear in the real parts of the 1st components of the Fourier transforms, while the coefficients $m_j 3, (j = 1, 2, 3, 4)$ of the sine (odd) components would show up in the imaginary parts of the 1st Fourier components. Thus this equivalent matched filtering provides the following estimates.

$$m_{11} = \mathcal{I}(0) \qquad m_{12} = 2/dp\ \Re\ [\mathcal{I}(1)] \qquad m_{13} = 2/dp\ \Im\ [\mathcal{I}(1)] \tag{3.72}$$

$$m_{21} = \mathcal{Q}(0) \qquad m_{22} = 2/dp\ \Re\ [\mathcal{Q}(1)] \qquad m_{23} = 2/dp\ \Im\ [\mathcal{Q}(1)] \tag{3.73}$$

$$m_{31} = \mathcal{U}(0) \qquad m_{32} = 2/dp\ \Re\ [\mathcal{U}(1)] \qquad m_{33} = 2/dp\ \Im\ [\mathcal{U}(1)] \tag{3.74}$$

$$m_{41} = \mathcal{V}(0) \qquad m_{42} = 2/dp\ \Re\ [\mathcal{V}(1)] \qquad m_{43} = 2/dp\ \Im\ [\mathcal{V}(1)] \tag{3.75}$$

$\mathcal{I},\ \mathcal{Q},\ \mathcal{U}\&\ \mathcal{V}$ denotes the Fourier transforms of the Stokes parameters $I(\chi)$, $Q(\chi)$, $U(\chi)$ & $V(\chi)$ respectively. $\Re$ denotes the real part of the Fourier transforms, while $\Im$ denotes the imaginary parts.

The Fourier transform method applied to Stokes data obtained at different feed rotation angles $\chi \in [0, \pi]$, readily provides 12 of the 16 Mueller matrix elements, if the degree of polarization dp, is known (as is the case with several standard calibrators).

We are left with 4 more elements that are not probed when the source's Stokes V = 0 – the elements corresponding to the 4-th column of the Mueller matrix. These, as also the derived 12 elements, are not all mutually independent, but a combination of 6 instrumental parameters, and the degree of polarization of the calibrator used.

As discussed, the degree of polarization *dp* must be known apriori (or estimated from the feed-rotation data on Q and/or U wherever the small leakage approximation is valid). The three amplitudes corresponding to the two leakages and the gain-ratio can be obtained directly using the following measured quantities:

$$\epsilon_{BA}^2 = \left[\frac{(m_{11}+m_{21})-(m_{12}+m_{22})}{(m_{11}+m_{21})+(m_{12}+m_{22})}\right] \tag{3.76}$$

$$\epsilon_{AB}^2 = \left[\frac{(m_{11}-m_{21})+(m_{12}-m_{22})}{(m_{11}-m_{21})-(m_{12}-m_{22})}\right] \tag{3.77}$$

$$\gamma^2\epsilon_{AB}^2 = \left[\frac{(m_{11}+m_{12})-(m_{21}+m_{22})}{(m_{11}+m_{12})+(m_{21}+m_{22})}\right] \tag{3.78}$$

$$\frac{\gamma^2}{\epsilon_{BA}^2} = \left[\frac{(m_{11}-m_{12})-(m_{21}-m_{22})}{(m_{11}-m_{12})+(m_{21}-m_{22})}\right] \tag{3.79}$$

$$\tag{3.80}$$

Finally the three phase terms can be solved for from the three equations below. However, since these are trigonometric equations with possibilities of multiple solutions, one must be cautious in accepting these solutions for the phases. Spectral smoothness of these quantities, which is to be expected in practice, may however be used in constraining the solutions.

$$\theta + \phi_{AB} = \tan^{-1}\left[\frac{m_{41} + m_{42}}{m_{31} + m_{32}}\right] \tag{3.81}$$

$$\theta - \phi_{BA} = \tan^{-1}\left[\frac{m_{41} - m_{42}}{m_{31} - m_{32}}\right] \tag{3.82}$$

$$\frac{\epsilon_{BA}\cos\phi_{BA}}{\epsilon_{AB}\cos\phi_{AB}} = \gamma^2\left[\frac{m_{13} + m_{23}}{m_{13} - m_{23}}\right] \tag{3.83}$$

With the formulation of the estimation path in this section, we proceed to demonstrate below this Fourier based method of instrumental calibration using real data from the central beam of the Arecibo L-band Feed Array (ALFA).

3.6.2 The ALFA system

The Arecibo L-band Feed Array (ALFA) is a focal plane array at the prime focus of the Arecibo single dish, with 7 dual linear feeds forming 7 beams in the sky, with provision to rotate the feeds about the axis of the central beam. A schematic of the ALFA beams is shown in Figure 3-2.

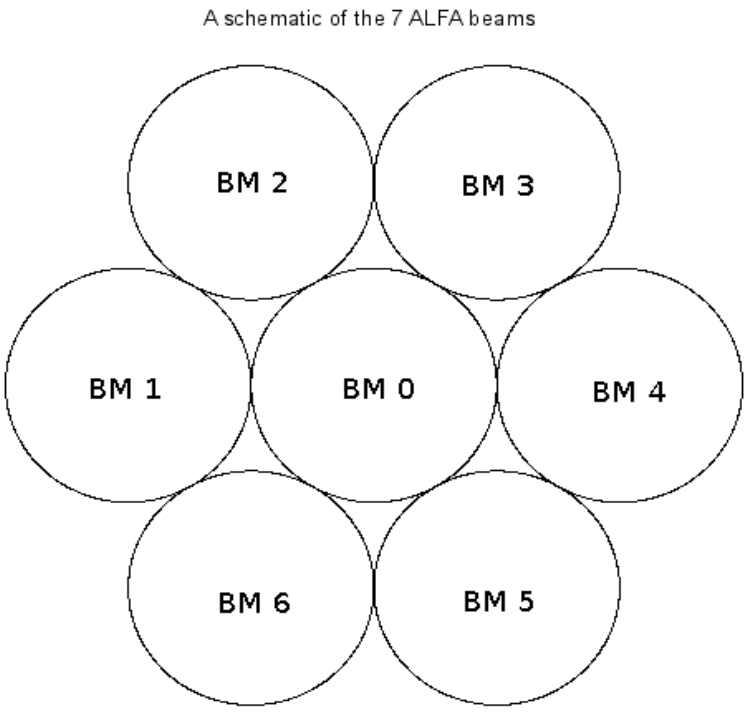

Figure 3-2: *A schematic showing the 7 ALFA beams.*

3.6.3 Observations & data reduction

In July 2005, ALFA was used to observe the linearly polarized calibrator source 3c286 in the tracking mode[3]. For a given feed-rotation angle χ, data was recorded in all four Stokes sampling 100 MHz band-width around the center frequency of 1385 MHz with a spectral resolution of 195.312 kHz (512 number of spectral channels). To calibrate the time-dependent effects, a correlated cal was injected at the rate of 25 Hz. Although the temporal resolution of an output spectra was 1 ms, we have used a pair of average spectra integrated over the entire 20 seconds spent on the source at any given feed-rotation angle, corresponding to CAL-ON and CAL-OFF measurements. The feed was rotated in discrete steps of 2 degrees between $\pm 90^{\circ}$.

For a given spectral channel, the data are first corrected for any relative gain vari-

[3]These data were taken by Deshpande *et al.* during test observations of the ALFA system

ations using the correlated cal. The sequences of the relative-gain corrected Stokes parameters, each as a function of the feed-rotation angle are then Fourier transformed, and the Mueller matrix elements of the ALFA system are computed from the estimated coefficients of the zeroth and the first Fourier components (see equations 3.72-3.75). The final calibrated data are obtained by multiplying the relative gain-calibrated data with the inverse of the derived Mueller matrix.

At this stage, the derived Mueller matrix for any spectral channel would be defined *w.r.t.* a frame for which the feed-rotation angle is zero. Furthermore, it would also include the Faraday rotation effect corresponding to the rotation measure (RM) of the calibrator source. Hence, an additional de-rotation of the linearly polarized axes (as a function of frequency) is thus essential to define the Mueller matrix elements in the frame of the sky, and corresponding to RM = 0. This additional rotation must be derived for each frequency channel from the knowledge of the RM and the intrinsic PA of the calibrator. Since the RM in the direction of 3c286 is very close to zero (*i.e.* small compared to the potential RM resolution offered by the λ^2 coverage), presently the Mueller matrix has not been de-rotated for any RM-dependent rotation across the band. However the ionospheric RM, if significant, will appear as an "excess" RM for a target source corrected using this Mueller matrix, if the ionospheric RM relevant for the target is substantially different from that relevant when the calibrator was observed.

For the purpose of demonstration of the method, we segregated the data on 3c286 into two sets – one set comprising of only *odd* spectral channels, and another comprising of only *even* spectral channels. The *odd* set was used to derive the Mueller matrix parameters as a function of frequency. The *even* set provided independent data for assessing the calibration. Since the mean of the Mueller matrix parameters can be expected to vary smoothly across frequency, the parameters derived for an *odd*-channel data should be a fairly close representation of the corresponding parameters of their neighbouring *even* channel. Hence we have calibrated the *even*-channel

data using solutions obtained from the odd data set. The *odd*-channel data set was self-calibrated (*i.e.* solutions derived for an odd channel were applied to data for that channel itself). The receiver temperature for the ALFA system is about 30 K. In comparison, the brightness temperature of 3c286 is 150 K. In this demonstration exercise, we have not attempted subtraction of the receiver contribution using off-source measurements.

3.6.4 Data: pre- & post calibration

Figure 3-3, 3-4 and 3-5 shows the raw, relative-gain calibrated and the final calibrated I, Q, U & V data for the calibrator source 3c286 as a function of feed-rotation angle as well as frequency. The data had been acquired and calibrated in the manner described in the preceding sub-section.

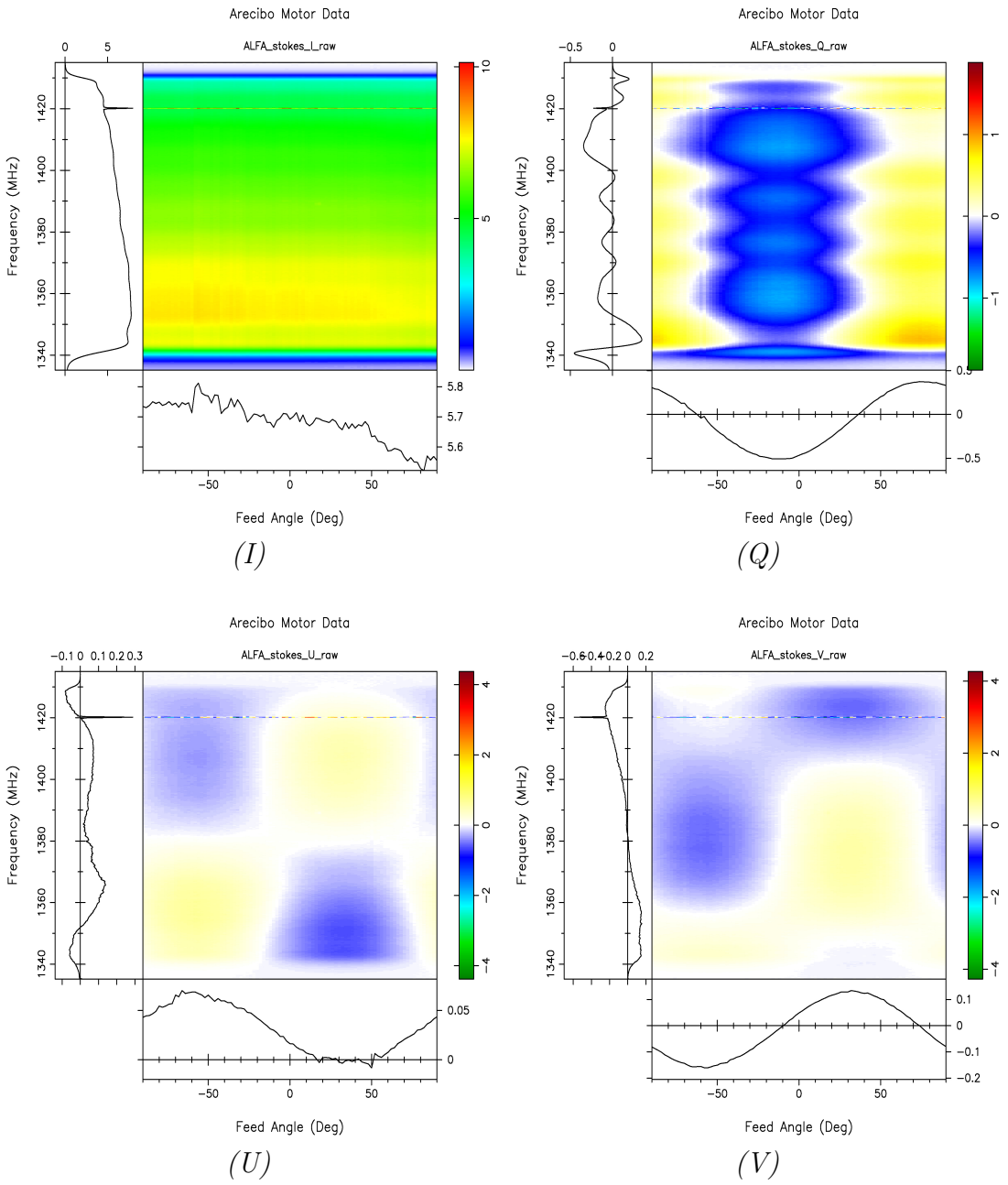

Figure 3-3: *Raw I, Q, U & V spectra of 3c286 at various feed-rotation angles for the ALFA central beam. The panels at the side and at the bottom represent the profile of the mean values along the corresponding axes. The feature close to 1420 MHz is of terrestrial origin (either radio frequency interference, or a possible reference tone, given its apparent degree of polarization as well as spectral width).*

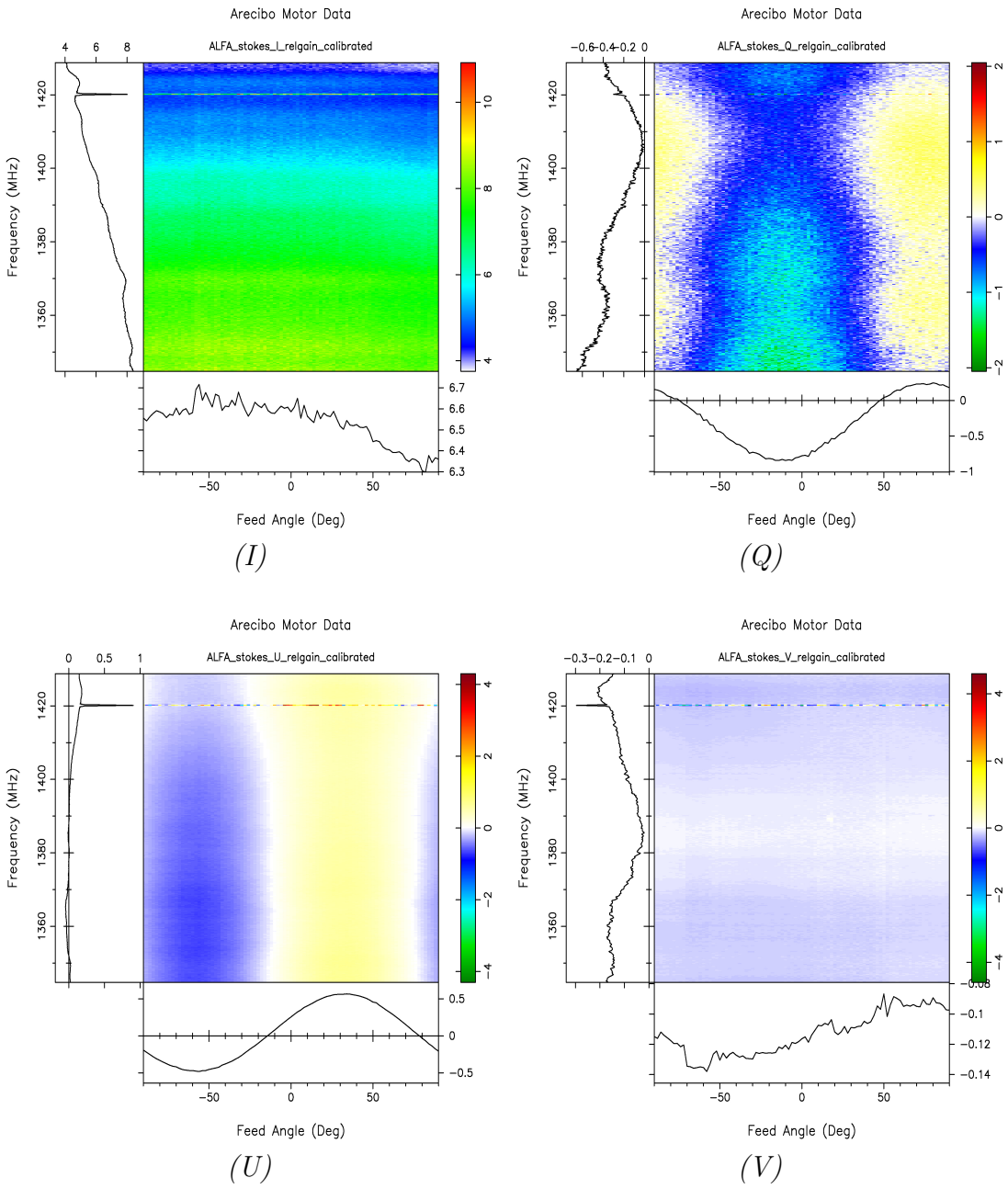

Figure 3-4: *Relative-gain corrected I, Q, U & V spectra of 3c286 at various feed-rotation angles for the ALFA central beam. The panels at the side and at the bottom represent the profile of the mean values along the corresponding axes. The noisy edge channels are not included in these plots.*

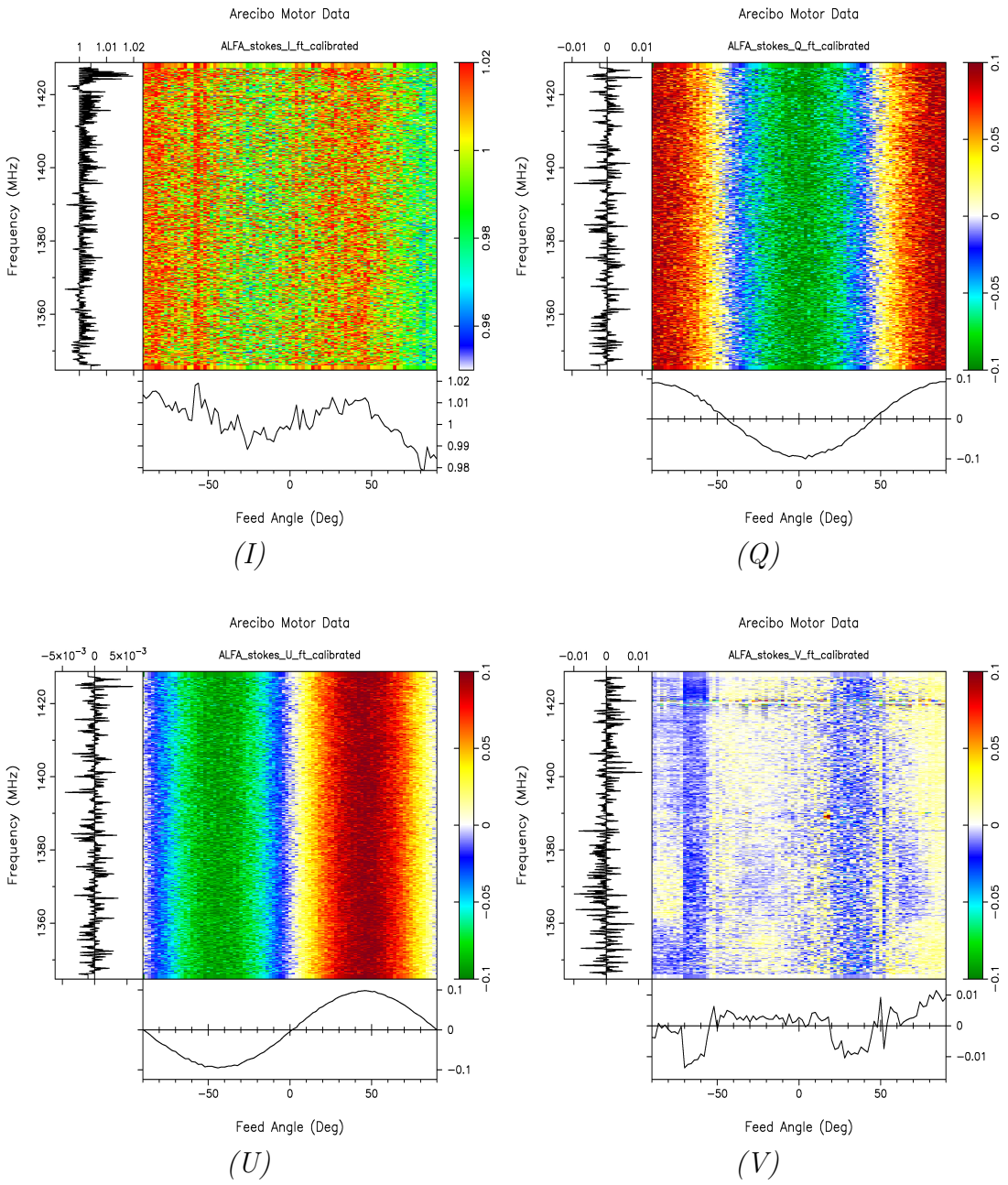

Figure 3-5: *Calibrated I, Q, U & V spectra of 3c286 at various feed-rotation angles for the ALFA central beam. The panels at the side and at the bottom represent the profile of the mean values along the corresponding axes. The noisy edge channels are not included in these plots.*

3.6.5 Results & Discussion

Figure 3-6 shows the spectra corresponding to the first 3 columns of the Mueller matrix derived using the feed-rotation data (see equation 3.72-3.72). The constituent parameters are shown in figure 3-7.

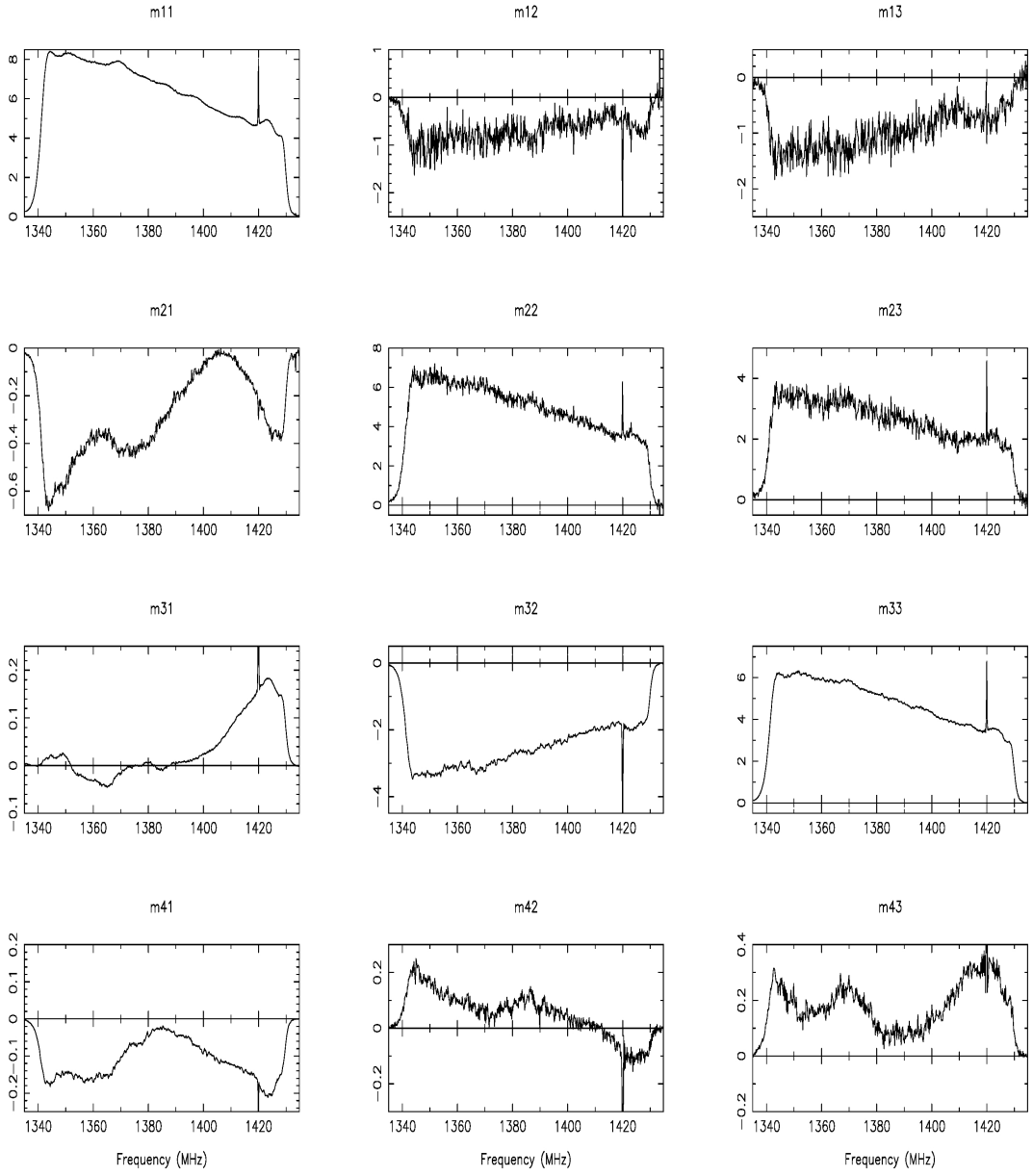

Figure 3-6: *Mueller matrix of ALFA: The three columns correspond to the spectra of the elements of the first three columns of the Mueller matrix derived using the feed-rotation method. The elements are in the units of the system temperature in the direction of the calibrator source 3c286. Hence for absolute calibration, the data corrected using the inverse matrix will have to be further scaled by the flux density of 3c286.*

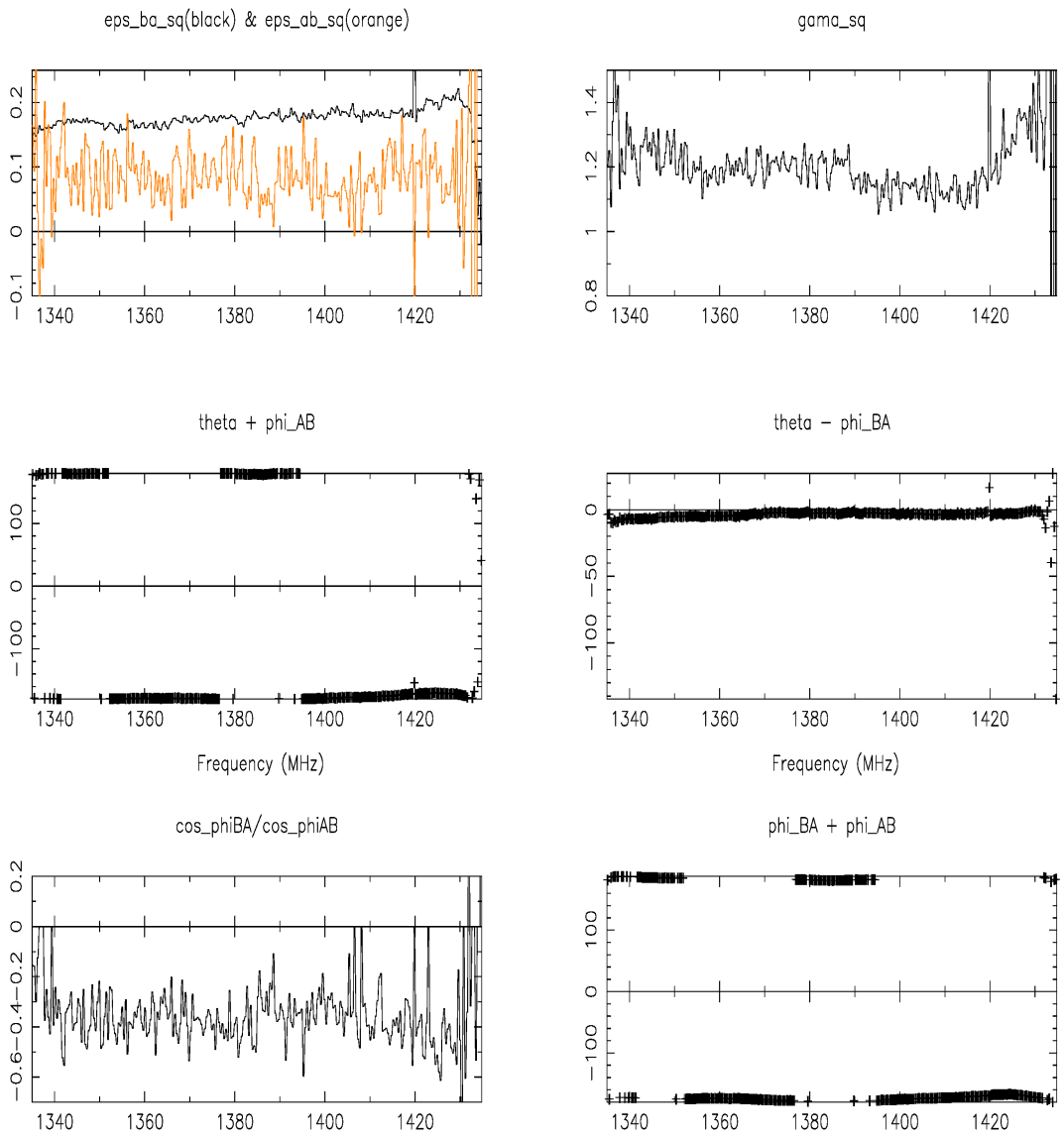

Figure 3-7: *Physical parameters of the Mueller matrix modeled as "effective" leakages and gains after the time-dependent variations have been corrected using a correlated cal. The left panel on the first row shows* ϵ^2_{BA} *(black) and* ϵ^2_{AB} *(orange). The right panel shows the plot of* γ^2*. The two panels on the 2nd row from top shows the* $\theta + \phi_{AB}$ *and* $\theta - \phi_{BA}$*. In the last row, the relation between* ϕ_{AB} *&* ϕ_{BA} *are shown in terms of* $\cos(\phi_{BA})/\cos(\phi_{AB})$ *and* $\phi_{BA} + \phi_{AB}$*.*

The derived leakage amplitudes, ϵs, (see the ϵ^2s shown in the first panel in figure 3-7) are rather high ($\sim 0.3 - 0.4$), and one may tend to expect instrumental polarization to be of the same order. However, from equation 3.63 it can be seen that for

non-reciprocal leakages, even high values of ϵs can lead to lesser apparent polarization leakages depending on the combination of the amplitudes and the phases of the relative gain, and the two leakages. Indeed, the instrumental polarization in the ALFA data before the calibration, is seen to be only about 2-5% (see figure 3-8). Also, non-reciprocity of the leakages will in general lead to different statistical properties of the estimated "effective" leakages. As can be seen in the first panel of Figure 3-7, the noise in the two leakage parameters are different.

The relative gain amplitude is close to unity as would be expected from a near-ideal instrument. It is interesting to note the relationships between the phases of the complex relative gains and the complex leakages. The panels in the 2nd and 3rd rows of figure 3-7 are consistent with all the three phases (*viz.* θ, ϕ_{AB} & ϕ_{BA}) close to 90°. The origin of these relationships between the phases are yet to be understood in terms of the physical parameters of the instrument.

The calibrated Q and U data as a function of feed rotation angle, are sinusoids (see figure 3-5), as would be expected from an ideal system. It is worth noting that averaging the Stokes intensities corresponding to a linearly polarized source across the feed-rotation angles between $-90°$ & $+90°$ synthesizes a perfect unpolarized source for an ideal instrument. We utilize this "synthesized" unpolarized source to assess the results.

The vertical side panels in figures 3-3, 3-4 & 3-5 (see also figure 3-8) shows the response of the instrument to this unpolarized source at the end of various calibration stages. For the raw data, the instrumental leakage is, on the average about 2-5% across the band. The relative gain calibration using the correlated cal changes the spectral profile of the Stokes parameters, but the polarization leakage is on the average, about the same as in the case of the raw data. Furthermore, the relative gain calibration using the correlated cal does not make Stokes-Q (= XX - YY) zero. This suggests that the modeled "effective" leakages for ALFA are not reciprocal (*i.e.*

$\epsilon_{AB} \neq \epsilon_{BA}$).

The final calibration is however able to retrieve the properties expected of an unpolarized source. The residual polarization leakage after the calibration, is less than 0.5%. For the data that was self-calibrated (odd channels), the residuals (deviation of the I, Q, U & V from the expected values) were at the level of machine precision. The residuals for the even channels are therefore not affected by numerical errors, but are manifestations of the noise in the quantities.

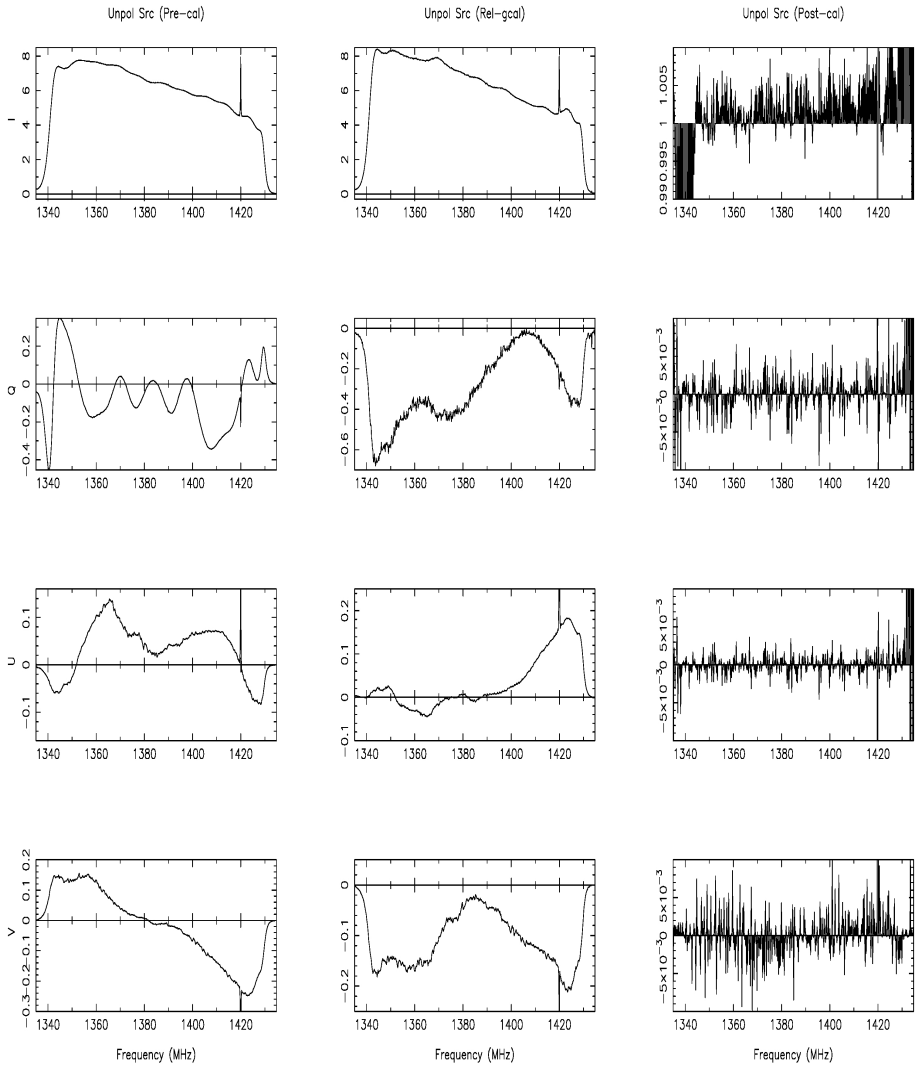

Figure 3-8: *Spectra of the "synthesized" unpolarized source at various stages of calibration. The first column shows the raw spectra corresponding to the synthesized unpolarized source. The middle column corresponds to the data after the relative gains have been corrected for using the correlated cal. The third column shows the data calibrated using the feed-rotation method.*

The Mueller matrix parameters should not however be readily interpreted as the physical parameters of the instrument, for example, as the "gains" or the "leakages", but should be regarded as models for such physical quantities in an "equivalent" sense. As has been discussed earlier (see section 3.4.1), the gain calibration using the correlated cal would correct for any time-dependent effects, but would give rise to a

new Mueller matrix where the "gain" terms are actually a function of the "leakage" terms (see equation 3.57 & 3.58). These leakages could also in principle change with time as discussed below.

3.6.6 Towards a direction-independent Mueller matrix

That the Mueller matrix could in general be direction dependent, can be seen from the results of the calibration exercise on a test region away from the calibrator source 3c286. Indeed for an off-source direction (a direction several degrees away from 3c286), applying the corrections derived using the feed-rotation data on 3c286, leaves a residual Stokes-V at $\sim 2-5\%$ (figure 3-9). Although the linear polarization is also seen at similar levels, it may not be surprising given the high degree of intrinsic polarized emission from the diffused interstellar medium. But the high circular polarization must definitely be spurious. Also the trend of increasing Stokes-I with frequency is opposite of what might be expected from temperature variation across the band as a result of spectral index. All these seem to suggest the direction dependence of the antenna Mueller matrix – the antenna Mueller matrix derived for a given direction is not strictly equal to that for other directions.

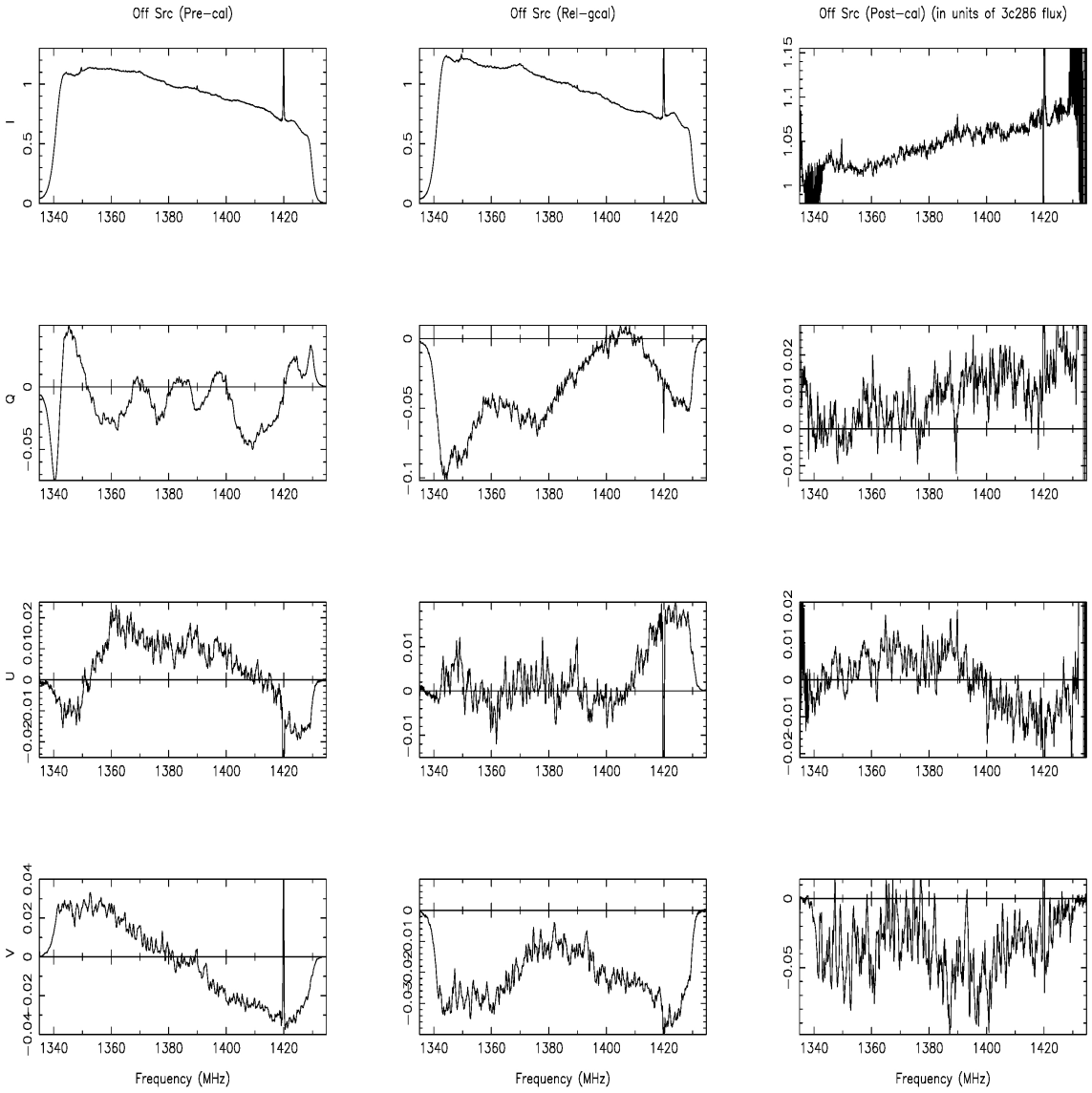

Figure 3-9: *Spectra corresponding to an off-source direction at various stages of calibration. The first column shows the raw spectra corresponding to the off-source direction. The middle column corresponds to the data after the relative gains have been corrected for using the correlated cal. The third column shows the data calibrated using the derived Mueller matrix from the feed-rotation data.*

Since the correlated cal probes only the electronic chain of the receiver system, any time-dependent polarization, exterior to the electronic chain will remain uncorrected. One such source of time-dependent polarization could be the change in the dish's relative orientation (owing to inhomogeneities in the primary reflector surface,

including, wherever relevant, the scattering from various structures other than the main reflector, for example, the support structures like the quadrupods *etc*), *w.r.t.* a source being tracked using an alt-az mount with the 2 conventional rotational degrees of freedom. New telescopes like the ASKAP are being built with dishes having rotation about 3 axes. These telescopes can be used to track any source keeping the relative orientation of the dish *w.r.t.* the sources being observed, fixed throughout the period they are tracked. In other words, these telescopes can be made to point towards any RA & Dec and at any Hour Angle, keeping the PA of any chosen reference orientation in the frame of the dish constant *w.r.t.* the celestial sphere. Thus an additional scheme for a rotating feed, like in the ALFA, will allow determining a single antenna Mueller matrix for calibrating any observation in a *direction-independent* fashion. The related calibration schemes are yet to be explored in detail.

3.6.7 The Fourier-based method *vs.* a few other alternatives

Conventionally, the instrumental polarization parameters are determined by tracking a weakly polarized source over a large range of parallactic angles. Weakly polarized calibrators, together with small-leakage amplitude assumption (wherever applicable), allow algebraic simplicity in the determination of the polarization parameters, which is what most of the existing calibration algorithms make use of. Violation of these assumptions only make the algebra complicated, but does not pose any serious limitation on the calibratibility. Nevertheless, almost all commonly used calibration algorithms solve for the instrumental parameters using non-linear least square methods, that inherently suffer from the potential danger of finding solutions in local minima of the parameter space. Furthermore, tracking a source over a wide range of parallactic angle is essential for reliable determination of the solutions. This would lead to loss of precious telescope time in slewing to the polarization angle calibrators.

The Fourier transform based method is elegant, and can be readily and reliably applied to strongly polarized sources. Even in the case where feed-rotation is not possible, a strongly polarized source might be tracked over a large range of parallactic angles (as in the conventional method), and the Fourier transform could be used to derive the instrumental polarization parameters after appropriate interpolation of the data in the $\pm 90^\circ$ PA range.

It is clear from equations 3.68, 3.69, 3.70 & 3.71 that the matrix elements can in principle be solved by observing a polarized source at only "three" feed orientations, say, χ_0, $(\chi_0 + 45^\circ)$ & $(\chi_0 + 90^\circ)$. However the signal to noise ratio must be high in order to reliably determine the solutions using these minimal number of observations. The redundancy, brought about by observations at more number of feed-orientations, in the case of the Fourier-based method expectedly helps reduce the errors on the estimated quantities. Besides, the Fourier transform method is elegant, and wherever the luxury of having a 3rd degree of rotational freedom exists, one may as well make use of it.

Many pulsars are known to have high degree of linear polarization. Their polarization PA are also known to show systematic variations within their pulsed emission. For such strong calibrators, it might in principle be possible to extract data from sets of 3 longitude bins with successive PAs separated by 45° in each set, and determine the Mueller matrix elements in a straightforward manner. The practical difficulty however lies in both the exact knowledge as well as the non-constancy of the degree of polarization as a function of the pulse longitude.

3.6.8 Circularly polarized sources as potential calibrators

Rarity of circularly polarized sources in the sky has led to a general negligence towards the few potential ones that could be used for instrumental calibration. Often, these giant pulses (flux density typically exceeding 1000 Jy, *e.g.* in Crab pulsar) are found to be in 100% "pure" circularly polarized state. The circular state "flips" between the

two hands (R and L). Additionally, coherent de-dispersion reveals that the intrinsic duration of these giant pulses are extremely short (sub μs to as narrow as few ns at radio frequencies > 5 GHz) (Hankins et al., 2003). We discuss in this section, the potential of emissions from Crab giant pulses (applicable to a few other milli-second pulsars as well) in calibrating some of the instrumental parameters. We also point out that the impulse-like emission from these giant pulses could be used in band-pass calibration.

3.6.8.1 Determining Mueller matrix elements

In sub-section 3.6.1, we demonstrated how a linearly polarized source observed at appropriate, apparent feed angles can be used in match-filtering out 3 of the 4 columns of the antenna Mueller matrix. For a linear feed, the elements of the 4-th column of the Mueller matrix operate only on Stokes-V of the source. The measured (I, Q, U, V) for an input 100% pure circular polarized signal $(I_c, 0, 0, \pm I_c)$ can be written as:

$$I^{\pm} = g_c^2 I_c \left(m_{11} \pm m_{14}\right) \tag{3.84}$$

$$Q^{\pm} = g_c^2 I_c \left(m_{21} \pm m_{24}\right) \tag{3.85}$$

$$U^{\pm} = g_c^2 I_c \left(m_{31} \pm m_{34}\right) \tag{3.86}$$

$$V^{\pm} = g_c^2 I_c \left(m_{41} \pm m_{44}\right) \tag{3.87}$$

Thus measurements on a 100% circularly polarized source, provide a means to filter out the elements of the 4-th column of the Mueller matrix, provided the elements of the first column are determined using for example, an unpolarized source (see sub-section 3.6.1).

Alternatively, if calibrator signals with both kinds of pure circular states ($V^{\pm}$) are available, elements of both the 1st and the 4-th columns of the Mueller matrix can be determined. The sums of respective Stokes parameters corresponding to the two

flipped circular states would give us the Mueller matrix parameters corresponding to the first column.

$$
\begin{aligned}
m^c_{11} &= \frac{1}{2}\left(I^+ + I^-\right) \\
m^c_{21} &= \frac{1}{2}\left(Q^+ + Q^-\right) \\
m^c_{31} &= \frac{1}{2}\left(U^+ + U^-\right) \\
m^c_{41} &= \frac{1}{2}\left(V^+ + V^-\right)
\end{aligned}
$$

Likewise, the differences would give us the Mueller matrix parameters corresponding to the 4-th column.

As mentioned earlier, the giant pulses from the Crab pulsar are not only 100% circularly polarized, but also flip from one kind to the other (*viz.* $\pm V$) thus providing a unique opportunity of using circularly polarized signal from an astronomical source for instrumental calibration. Together with a correlated cal, these giant pulses could be used to determine the Antenna Mueller Matrix.

It may be mentioned here that correlated noise cals with a relative phase offset of $\pm 90^\circ$ between them, would mimic pure circularly polarized signals, and when injected into the two orthogonal receiver chains at adequately frequent intervals (switching between V^+ & V^-), may be used to determine the instrumental parameters as discussed above. However, the purity of the polarization state they generate, may require additional characterization for them to be useful as calibrators. The usefulness of astronomical calibrators in this regard, cannot be overstated.

3.6.8.2 Band-pass calibration using Crab giant pulses

The spectral features intrinsic to a system is usually characterized by studying the response of the system to an impulse (a signal that is short-lived in time, ideally a Dirac delta in case of a continuous time process, or a Kronecker delta in case of a

discrete time process). In general, the spectral response of a system to an impulse occurring within a time interval t & $t + \Delta t$ may be expected to remain "coherent" over a range of frequencies governed by the inverse of the time-interval over which the impulse occurs, *i.e.* $1/\Delta t$. Thus, shorter the duration of the impulse, wider would be the spectral span over which the signal may be expected to be coherent. Deviation from this expected coherence (for example, departure from "flatness" of the amplitude spectra, and any non-linear trend in the spectra of the phase) can be attributed to the inherent spectral content of the system being probed.

The giant pulses from the Crab pulsar (some of them possibly even shorter than 2 ns) would thus provide a potential means of calibrating the instrumental band-pass for correspondingly wide-band systems. In contrast, characterizing continuum calibrators in terms of their spectral indices, before they can be employed for band-pass calibration of very wide-band systems of most current and upcoming instruments, may not be straightforward. Furthermore, the emission from the giant pulses that is expected to remain coherent across a correspondingly wide band (dictated by the inverse of the pulse-width), will provide a means of deriving the phase-relationship between absolute gains of the instrument as a function of frequency. Although such phase relationships may not be crucial for measurements involving the Stokes parameters, knowing these instrumental spectral phase relationships would be useful in various spectro-polarimetric studies involving raw voltages, for example, in coherent de-dispersion of transients like pulsars.

3.6.8.3 Circular polarization and a circular feed:

We would like to briefly note here that a pure circular polarized signal observed using a circular feed would provide direct measurement of the element j_{21} of the antenna

Jones matrix. The relations are shown below:

$$\gamma^2\epsilon_{AB}^2 = \left(\frac{S1 - S2}{S1 + S2}\right) \tag{3.88}$$

$$\theta + \phi_{AB} = \tan^{-1}\left(\frac{S4}{S3}\right) \tag{3.89}$$

3.7 Complications arising from mutually coupled gain-differences and leakages

We mentioned in sub-section 3.4.3 how the time-dependent gains of the amplifiers can get coupled to all the terms of the antenna Jones matrix. As long as the gains and leakages do not vary with time, it does not matter what share of the matrix terms are due to leakage and what are due to gain mis-matches. More specifically, as long as the term $\tilde{j}_{12}$, does not vary with time, the elements can be represented as *effective* gains and leakages through mutual re-distribution of the Jones matrix elements such that the structure of the Jones matrix described in equation (3.62) (for sake of convenience we re-write the equation below) is maintained.

$$[J_{lg}] = \tilde{g}_A \begin{bmatrix} 1 & \epsilon_{BA}\ e^{i\phi_{BA}} \\ \epsilon_{AB}\ e^{i\phi_{AB}}\gamma\ e^{i\theta} & \gamma\ e^{i\theta} \end{bmatrix}$$

This would make the leakages (as we call them, based on the fact that their location in the Jones matrix replicates the effect of cross-coupling) non-reciprocal. Much of the simplicity in the algebra associated with reciprocal leakages is lost. However, this general model of non-reciprocal leakages takes into account certain modifications that cannot be modeled using reciprocal leakages (as discussed in section 3.4.3). Furthermore, certain symmetries provided by a correlated cal, and the Jones matrix above, allow a reasonable framework for instrumental calibration, albeit with a slightly more complex algebra as compared to that in the reciprocal leakage case. If however, the term $\tilde{j}_{12}$ of the antenna Jones matrix includes a time-dependent param-

eter of the instrument (due to the hybrid placed after the pre-amplifiers, or the cables to the two channels before the pre-amplifiers, and changing electrical lengths due to their exposure to a changing temperature *etc*), the only way for calibrating such a system would be to use a winking cal that could adequately frequently inject, in addition to the polarization state that the correlated cal provides (Stokes-U in case of linear feeds), other suitable 100% polarized states as well.

We would like to emphasize that antenna-based polarization calibration should be preferred over baseline-based methods, since the measured visibilities would not be independent of the baseline lengths as expected from a point source calibrator, but would vary for different baselines owing to the strong Galactic polarized emission that is known (but far from being well-characterized) to have rich structure. Furthermore, coupling need not necessarily occur between nearby antennas only. Common structures associated with the elements (for example reflections from the dishes/quadrupod-structures *etc*) can in principle lead to coupling.

3.8 Conclusions

Modification caused due to an incoming pair of signals by various components of the instrument is discussed. Properties of various calibration sources are described and their respective roles in determining the instrumental parameters are presented. Certain conserved quantities have been identified that may be useful in probing instrumental polarization fidelity as well as in identifying signatures of changing polarization across the sky.

The need for invoking non-reciprocity of leakages, and the caveats encountered if simplified assumptions are made about them, is emphasized. In all our derivation we have assumed the leakages to be non-reciprocal.

The role of the winking cal in calibrating instrumental effects that vary with time,

is elaborately discussed. Limitation of such a calibrator in cases where the time-varying effects are coupled to all elements of the antenna Jones matrix is pointed. Caution to be exercised in designing receiver systems so as to avoid such coupling is mentioned briefly.

A few new polarization calibration opportunities are explored, one using *feed rotation*, and others using *circular polarization signals* and *pulsed emission*. The feasibility of the Fourier transform based feed rotation method that requires observing a linearly polarized calibrator, is demonstrated using data from the ALFA receiver system of the Arecibo telescope. We note that, although in principle, measurements at 3 orientations ($\chi,\ \chi + 45^\circ$ & $\chi + 90^\circ$) for the feed suffice in solving the Mueller matrix parameters, the high signal-to-noise ratio that can be achieved through redundant measurements at more number of orientations would reduce uncertainties in the estimated parameters.

We argue that a rotating feed in the focal plane of dishes that have the additional degree of rotational freedom about the pointing direction, would be useful in deriving antenna Mueller matrix that is independent of pointing direction.

We also discuss the possibility of using the short duration Crab giant pulses for instrumental band-pass calibration. The potential of using pure circularly polarized signals for determining certain instrumental parameters is briefly touched upon.

At low radio frequencies, where continuum polarized calibrators are rather rare, pulsars may be the only reliable astronomical sources that could be used for instrumental polarization calibration. Pulsars are known to have high linearly polarized flux densities as well as systematic variations of PA across their pulse longitudes may be used for calibrating the instrumental polarization. However the degree of polarization as well as PA variation as a function of pulse longitude that would be required, may not always be precisely known.

Lastly we emphasize that dish-based calibration methods should be preferred over baseline-based methods since measurement of a calibrator source using the latter will be affected by structures in the Galactic polarized emission. Single dish measurements are less likely to be affected by these small angular-scale structures.

Chapter 4

GMRT Polarimetry: practical considerations

4.1 The GMRT system capabilities relevant to spectro-polarimetric imaging

The GMRT[1] is a low frequency interferometric array with moderate bandwidths and high spectral resolutions that provide high Rotation Measure (RM) resolution and minimal bandwidth-depolarization respectively. Its baselines extending to 27 km provide high angular resolution that minimizes beam-depolarization. At the same time, it also offers high sensitivity for large scale angular structure (owing to the compact configuration of its 12 central-square antennas).

Although we had proposed for observations in three GMRT bands with the aim

[1]We express our gratitude to the staff of the GMRT for their help and support in conducting these observations as well as the many tests prior to it. GMRT is run by the National Centre for Radio Astrophysics of the Tata Institute of Fundamental Research.

Table 4.1: GMRT specification for full polar observations

Band	Band Width	n_chan	δRM	ΔRM	Angular resolution
MHz	MHz		rad/m^2	rad/m^2	$arcsec$
327	16	256	~ 40	$\sim \pm 4500$	~ 10

of enhancing the RM-resolution through appropriate combination of the multi-band data, allocated time was adequate for a full-synthesis observation only at one band. We chose to observe at 327 MHz (P-band), given the high RM-resolution that this frequency provides amongst the clean bands available at the GMRT, and the good angular resolution that we hoped would result in tolerably small amounts of beam depolarization. Table 4.1 shows some of the GMRT parameters relevant for our spectro-polarimetric imaging data. δRM refers to the resolution in RM, while ΔRM indicates the maximum range of RMs that can be probed without aliasing. In this chapter, we discuss the practical considerations in the observations and analysis of the 327 MHz GMRT spectro-polarimetric data, and demonstrate the feasibility of spectro-polarimetric measurements at the low frequencies of the GMRT. The feasibility of polarimetric studies at the 610 MHz band with the GMRT has been very recently demonstrated by Farnes et al. (2013).

4.1.1 Large data sets

The data from the ~ 9 hour synthesis observation in dual circular polarization channels (R & L available through a hybrid) were processed through the GMRT software correlator Roy et al. (2010), recording the complex visibilities in all four Stokes parameters (I, Q, U, V), with 256 spectral channels spanning the 16 MHz bandwidth. The integration time was kept short, 2 seconds, so as to minimize possible corruption of the data due to shorter time-scale RFIs. The resultant "uv-data", corresponding to the full synthesis of Cas A, was a few tens of GBs in size.

Parallel processing of such large data sets should be an obvious methodology to adopt for speedy reduction. However, AIPS and MIRIAD (the only commonly used software packages for radio astronomical data processing available at the time) are inherently built on serial structures, and we had to devise ways to minimize the processing time, for example by splitting the data as a function of frequency channels and processing these in multiple work-stations.

4.1.2 Complex RFI structures

Baseline-based, strong RFIs in data output from the GMRT software correlator have substantially reduced compared to their occurrences in data from the hardware correlator. Nevertheless, the structure of these RFIs, as a function of time, frequency, baseline, antennas and polarization continues to be complex. Careful flagging becomes crucial, particularly for polarimetric imaging, since the intrinsic polarized intensities are generally weak, and even relatively weak RFIs, that do not seem to severely affect Stokes-I images, introduce spurious structures in the polarized images. Given data sets with $\sim$18000 visibility points per Stokes parameter, per baseline, and per spectral channel, even using the tasks that AIPS provides for data/RFI visualization, identification of RFI as a function of time, frequency, baseline and antenna, is a huge task, if attempted manually.

4.1.3 Need for automation

Keeping in mind the need for possible iterations through the data in reduction of our large database, we automated our data reduction pipeline, including the operation of flagging bad data. In addition to minimizing possibility of errors occurring during human intervention, this enabled us to simultaneously process independent chunks of the data, (for example, individual spectral channels), on multiple workstations, speeding up the data processing.

4.2 Observing Strategies

4.2.1 Choice of time of the day for observing

Solar activity affects the RM introduced by the ionosphere (Figure 4-14). Hence to keep our data as free as possible from the RM-fluctuations coming from the ionosphere, we conducted our observations mostly during night-time.

4.2.2 The observational strategy for the various calibrators

For flux-density and bandpass calibration, it usually suffices to observe a strong point-source calibrator just once during a given session. Phase calibration may be done either by *self calibration* on the target source itself, or by visiting a calibrator source frequently enough to sample and correct possible variations in the refractive index of the ionosphere. For instrumental polarization calibration, an unpolarized, or a weakly polarized source is tracked over a wide range of parallactic angle. The absolute polarization position angle (PA) calibration may be obtained from a single observation of a polarized calibrator with known position angle.

Choosing an unpolarized point source close to the target direction enabled us to visit it frequently (at one hour intervals) without much loss of precious observing time on the target due to slewing between the sources. We used these frequent measurements on the unpolarized source for preliminary phase calibration. At the same time, the wide parallactic angle range over which this source was tracked, was used to provide the instrumental leakage calibration.

A few notes on the calibration are:

1. Although the RR and LL band-shapes are expected to be fairly stable over long duration, their relative levels or overall gains may have faster variations with time. Hence, a single observation of the bandpass calibrator will not be sufficient to correct for the relative gain differences between the RR and the LL spectra. Thus, even though the average band "shapes" can be derived, the time-dependent variations in their relative strengths would lead to spurious polarized intensities. For single dishes, correlated noise injected into both the orthogonal channels at appropriate rates can be used to calibrate these gain differences (Chapter 3). However, for an interferometer with 30 dishes, adopting similar schemes for each of the dishes has practical difficulties. Using the target

source itself for bandpass calibration may be possible in certain cases. However the feasibility of this needs to be carefully assessed.

2. Once the instrumental polarization leakage is calibrated, one will have to additionally observe a polarized source with known position angle to get the absolute PAs. In the absence of such calibration, the continuum PA maps will be uncertain by only a single value of rotation across the entire map, much as in the absence of an absolute flux density calibrator, flux density values will be uncertain by only a single scaling factor. In both cases, internal consistency would exist across the maps.

4.2.3 Linearly polarized sources with known RMs for calibrating RL-phase

The phase responses of both hands of polarization channels of each antenna are referenced to the corresponding polarization channels of a chosen reference antenna throughout the gain calibration exercise. For polarization calibration, the relative phase between the orthogonal hands of polarization for the reference antenna must also be determined. For the circular feeds of the GMRT, these additional *frequency-dependent* relative phases between the R- and the L-hands of the reference antenna, if not corrected for, would result in a different $PA\ vs.\lambda^2$ trend than that due to the Faraday Rotation Measure(s) of the propagating medium along the line of sight. Any constant uncorrected phase shift will result in error in PA, while uncorrected linear gradients in phase will cause an undesired offset in the associated RMs. Any higher order terms in the uncorrected RL phase across the spectrum will manifest as corresponding depolarization of the features in the tomograph, as well as distortion of the response function in RM domain. This situation described here is largely analogous to an imperfectly phased array. The need to make this correction for each spectral channel thus necessitates the observation of a polarized calibrator with known RM. We observed two such calibrators (3C345 and 3C303) listed as WSRT polarized

calibrators at the 327 MHz band, to provide internal consistency checks.

4.3 Data reduction & data quality assessment

The data reduction was done using configurable scripts and procedures that perform the various stages in an automated way. Most of the image-processing was done primarily in the AIPS and MIRIAD packages. The RM-synthesis as well as various analysis of the images used softwares that were locally developed.

4.3.1 Flagging and primary calibration

RFI detection and mitigation was performed using the short integration time (2 seconds) data. AIPS-readable flag files were generated using programs that were locally developed to efficiently detect RFI in the data. These codes were designed to recognize common patterns in the data associated with "bad" visibility points (RFI) that are very complicated functions of TIME, ANTENNA, BASELINE, FREQUENCY-CHANNEL as well as POLARIZATION. A visibility point is identified as "bad" if its Stokes-I and/or Stokes-V values exceeds the corresponding range (indicated by their expected noise) about the respective mean values. The code identifies the "causes" of bad visibilities (much like a human would using the various TV-tools in AIPS) from a list extracted using AIPS task UVFND with OPCODE=VCLP, if Stokes V is used, or OPCODE = CLIP, if Stokes-I is used for bad-data detection criteria (we use both iteratively) together with appropriate APARM parameters to specify the thresholds. We do not use the linear Stokes visibilities for identifying bad data since high Q and U visibilities could result from structures in the linearly polarized emission from the Galaxy itself (Wieringa et al., 1993).

The code does not merely do CLIPPING (*i.e.* does not exclude **only** the outliers, but flags even the "apparently good" visibilities resulting from the same "causes" corresponding to the identified bad visibilities). Clipping although might work well

for studies depending only on Stokes-I, for polarization imaging, it is a bad idea to clip on the basis of the visibility amplitudes. Since the polarized intensity from the sky is generally low, the phases of even low level baseline-based RFIs could corrupt the polarization image. Furthermore, the flagging has to be done separately for each spectral channel. Frequency-dependent RFIs will otherwise give rise to spurious features in the Rotation Measure domain.

Typically 7000 bad visibilities for a given frequency channel could be described by only 250 lines of flag commands that were then used as inputs to AIPS task UVFLG for applying the flags to the data. Once flagging and initial calibration had been performed, we reduced the data to a more manageable size by integrating the 2-second uv-data to 16 seconds, taking care to copy the flag and calibration tables for the new averaged data set. AIPS task UVAVG was used for this purpose.

Figure 4-1 shows both the raw and edited visibilities for spectral channel 82, as an example.

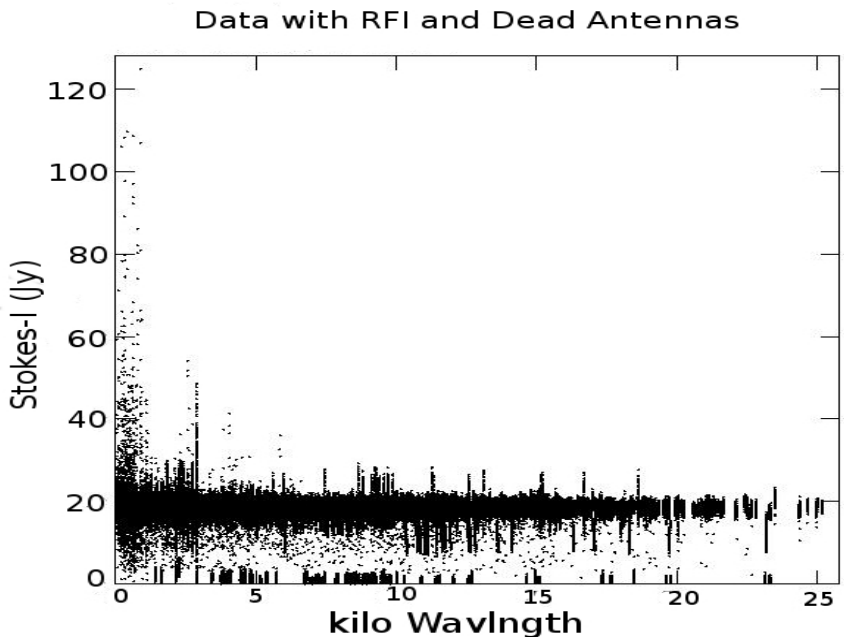

(a) Raw UV-data

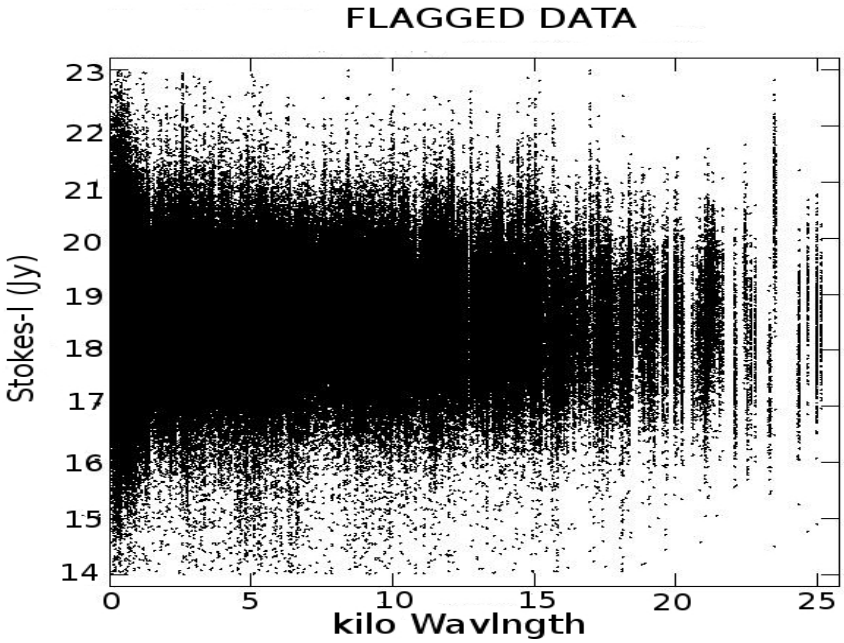

(b) UV-data post flagging

Figure 4-1: *An illustration of application of Automated Flagging: (a) Raw visibilities for a representative spectral channel infested with RFI. (b) The visibilities after bad data have been detected and rejected using our flagging routines. The plots are for the calibrator source 3C468.1.*

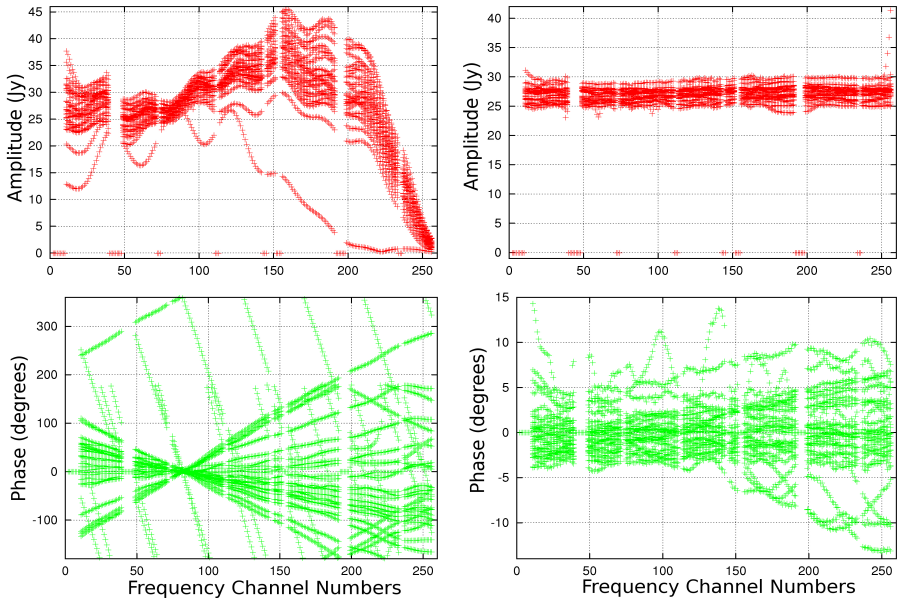

(a) Stokes LL

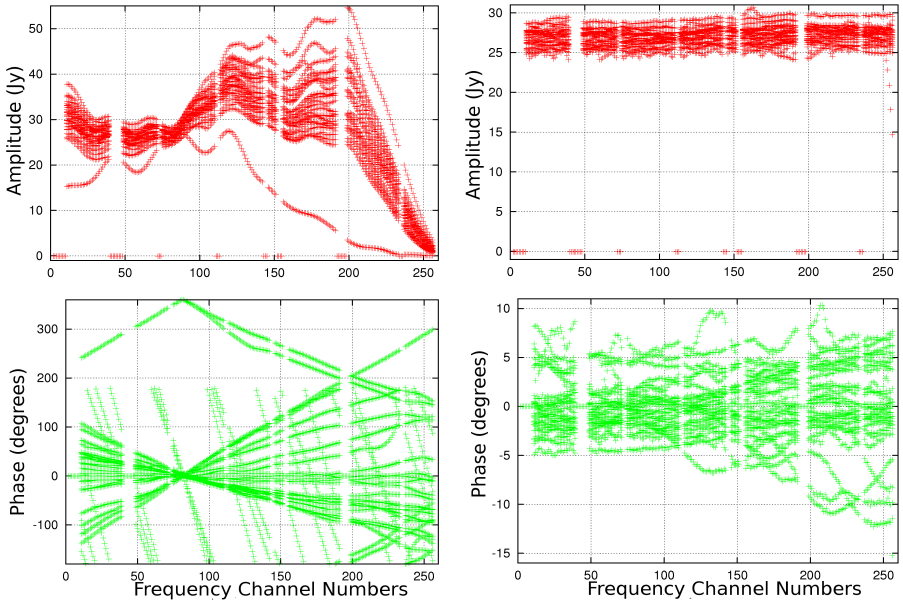

(b) Stokes RR

Figure 4-2: *Bandpass calibration on 3C286: (a) LL & (b) RR; The upper panels in both (a) and (b) are the amplitudes of the cross-spectra on point source 3C286 for all baselines formed with the reference antenna; the bottom panels are the corresponding spectra for the relative phases. The panels on the left are band shapes before bandpass calibration is applied. Those on the right are the calibrated band-shapes. Note the changed scales for particularly the phase plots in the right panels.*

Primary gain and bandpass calibrations were performed on these flagged data in AIPS using calibration sources, 3C286 and 3C468.1. The flag & calibration tables were preserved. Figure 4-2 shows the amplitude and phase of the cross-spectra on 3C286 for all baselines formed with the reference antenna before and after the calibration. The variation in the relative phase as a function of frequency for a given antenna is less than a degree in most cases. A few bad spectral channels are visible in these plots, and these were further flagged before subsequent stages.

Although the calibrated band shapes look desirably flat, we should mention here that we did not have a correlated calibration signal for calibrating variations of RR and LL with time. Hence, solutions obtained from 3C286 and the regularly observed calibrator 3C468.1 (observed once every one hour during the full synthesis) were interpolated and applied for the times during which the target was observed. This might pose limitations in attaining the theoretical *rms* in the final images, should the relative gain ratio of the RR and LL channels vary at a faster rate compared to the calibration rate.

4.3.2 Splitting the data into single source files

For ease of processing, the single multi-source, multi-channel file obtained above, was split into many single-source, single-channel files. The calibration and flagging information obtained in the previous step were applied to these single-source data sets. Splitting into single source files considerably speeds up AIPS, while splitting into individual frequency channels allows parallel processing using several identical work-stations, thereby reducing the processing time by a considerable factor.

4.3.3 Clean & Self-cal cycles

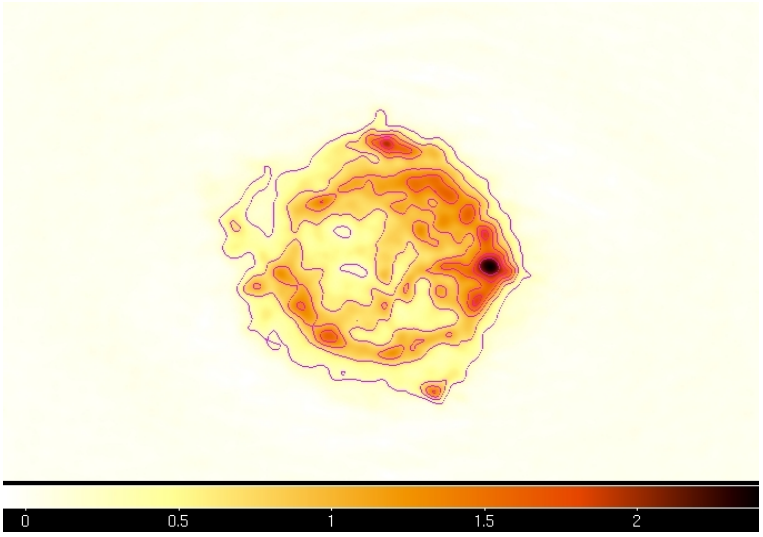

(a)

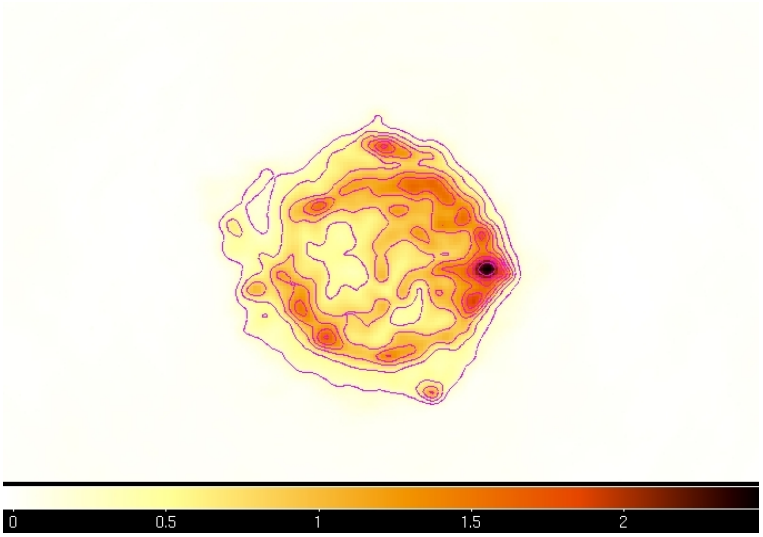

(b)

Figure 4-3: *(a) A single-channel self-calibrated Stokes-I image of Cas A using our P-band data. (b) a VLA L-band image of Cas A*[3] *for comparison. The flux-density scales are arbitrary. Both these images have been convolved to* $(15'' \times 15'')$.

The gain solutions for each single-channel, 4-Stokes parameter uv-dataset for a given source were refined by imaging the Stokes-I data in a series of *Clean* and *Self-Calibration* cycles. AIPS tasks IMAGR and CALIB were used for this step. The

data were scaled assuming an integrated flux density for Cas A of $\sim$ 7000 Jy at 327 MHz, consistent with a flux density of 2720 Jy at 30 cm, and a spectral index α of 0.77 (Green, 2009), where $S_\nu = \nu^{-\alpha}$. An accurate calibration would require details of the secular intensity variability of Cas A (O'Sullivan & Green, 1999; Reichart & Stephens, 2000; Helmboldt & Kassim, 2009) in our band.

Figure 4-3 shows a single spectral channel map of Cas A obtained from our P-band data alongside a VLA L-band image for comparison. The two images are remarkably similar. All the primary features of the L-band image are also clearly seen in our image – the bright radio ring and the western hotspot, as well as the knots and the filaments. This gives reassurance concerning the reliability of our gain calibration.

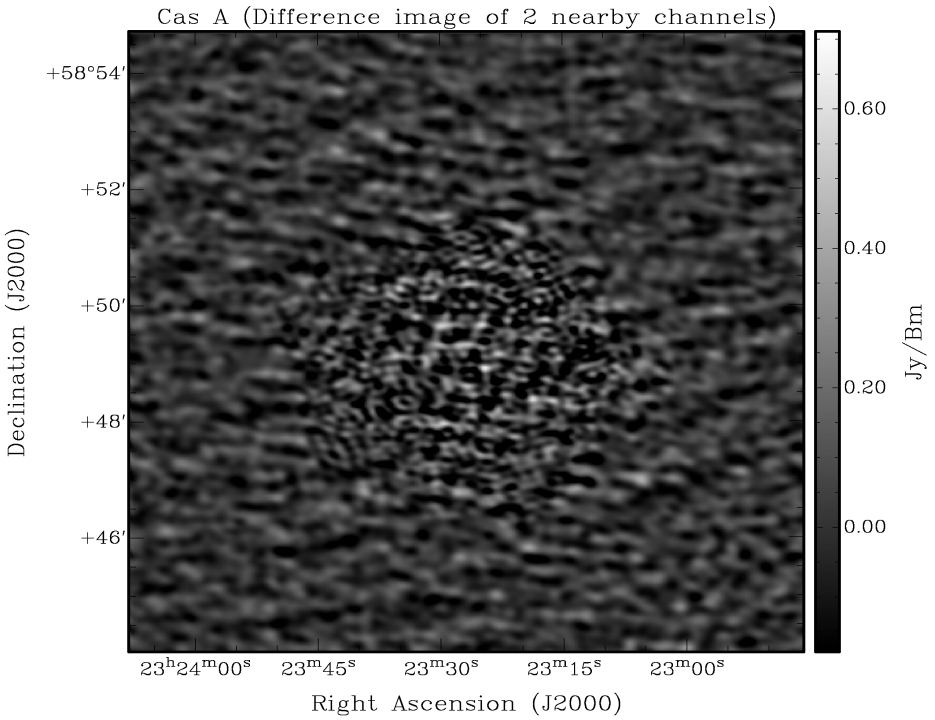

Figure 4-4: *The difference of two close-by single-channel (channels 80 and 84) self-calibrated Stokes-I images of Cas A.*

The *rms* noise in the difference maps obtained by subtracting the gain-calibrated Stokes-I maps of two nearby channels (*e.g.* the difference of channels 80 and 84

is shown in Figure 4-4) is $\sim$ 170 mJy Beam^{-1}. Taking into account the self noise McCullough (1993); Vivekanand & Kulkarni (1991); Anantharamaiah et al. (1991) of Cas A, the brightest radio source, the theoretically expected *rms* is $\sim$ 7 mJy Beam^{-1}. The *rms* estimated from the difference map is thus much larger than that expected ($\sim 7\sqrt{2}$mJy Beam^{-1} in the difference map). We therefore further assess the system noise at a given image pixel, making use of the independent measurements we have across multiple spectral channels. The theoretically expected *rms* σ at any location in an aperture-synthesis image is given in McCullough (1993) to be:

$$\sigma \simeq \frac{1}{\sqrt{B\tau n_p n_b \eta_q f_{eff}}}(S+N) + \frac{n-2}{\sqrt{B\tau n_p n_b \eta_q f_{eff}}}(S^*) \tag{4.1}$$

where, S is the single-dish flux density of the source, N is the equivalent flux density corresponding to the receiver noise, S^* is the observed flux density within a synthesized beam at which the *rms* is being computed and n is the number of antennas used. Both S and N add a term of constant intensity offset to all the pixels in the image. Following McCullough (equation 4.1) we plot the *rms* flux densities across channels of the on-source pixels of Cas A as a function of the observed mean flux densities at the corresponding image pixels (Figure 4-5). The *rms* noise estimated across the 167 "good" spectral channels is $\sim$ 175 mJy Beam^{-1} as against 7 mJy Beam^{-1} expected theoretically. This discrepancy is due to spectral index variation across the source, as well as residual modulation in the band (after bandpass calibration). However, the *rms* noise corresponding to the random fluctuations across the band is on the average $\sim$ 20 mJy Beam^{-1}. This is still higher than the theoretically expected value of $\sim$ 7 mJy Beam^{-1}, but may not be unexpected for dynamic-range limited systems such as the GMRT. Figure 4-6 shows the Stokes-I spectra of two typical on-source regions of Cas A. The relevant parameters used for the estimation, *viz.* single channel bandwidth, total observation time (t_{obs}), number of antennas used (n_{ante}), the effective fraction of on-source time (f_{eff}, taking into account the data loss due to flagging), the quantization efficiency (η_q), the number of orthogonal polarizations used for the I-image (n_p) and the number of baselines (n_b), are shown in Table 4.2.

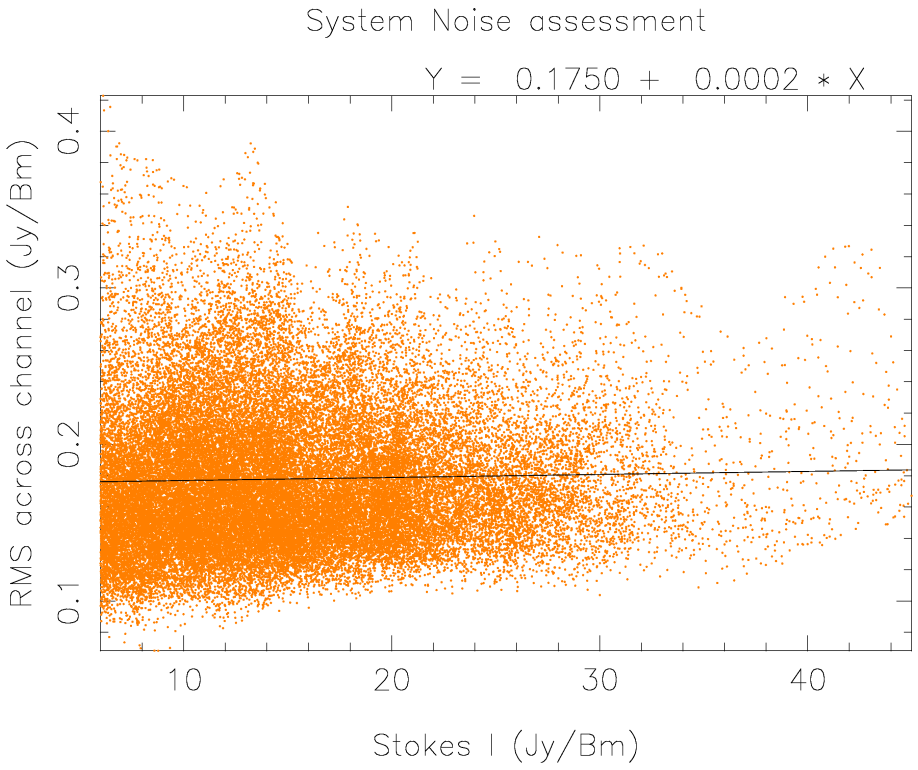

Figure 4-5: *The rms across the 167 "good" frequency channels is plotted against the mean Stokes-I for on-source pixels only. The straight line is a fit to the data and not the theoretical relation.*

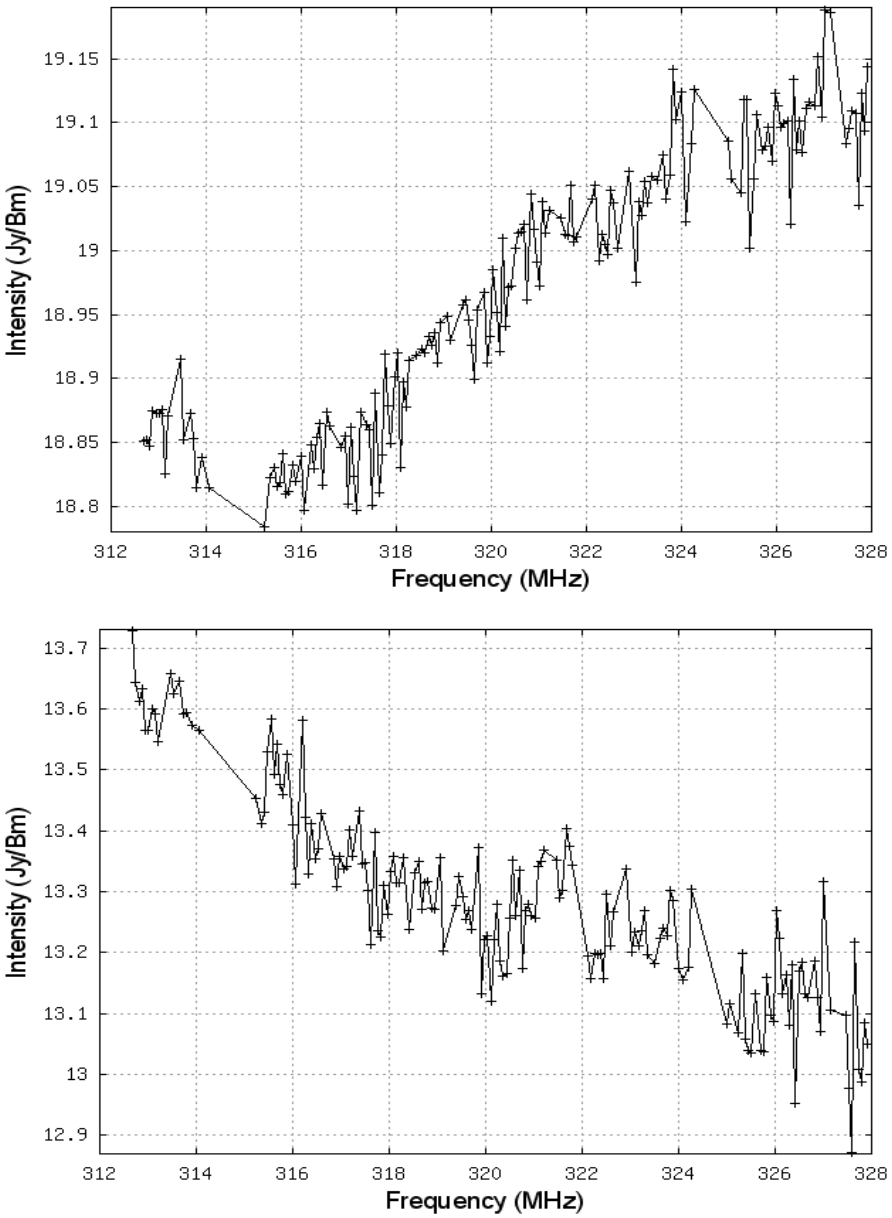

Figure 4-6: *Typical gain-corrected Stokes-I spectra of Cas A. The rms of the random residual fluctuations is* $\sim 15 - 30$ mJy Beam^{-1}. *The top and bottom panels correspond to two lines-of-sight towards outer and inner regions of Cas A respectively.*

Table 4.2: *Parameters relevant to the estimation of source noise in the 327 MHz Cas A image (Stokes-I).*

channel BW(Hz)	$t_{obs}(secs)$	n_{ante}	f_{eff}	η_q	n_p	n_b
6.4×10^4	3.2×10^4	28	0.8	1	2	378

4.3.4 Instrumental polarization calibration

1. **Leakage calibration:** The instrumental polarization (leakage terms) for telescope systems with alt-azimuthal mounts can be solved for by observing even an unpolarized point source tracked over a large range of parallactic angle (Sault et al., 1996). While the projection of the feed on the celestial sphere (feed parallactic angle) has a distinct dependence on hour angle, feed-elevation and declination of the source being tracked, any instrumental polarization may be expected to remain constant with time. Thus by observing a source over a wide range of parallactic angle, one is able to solve for both the source and the instrumental polarization. The only assumption in deriving this solution is that the calibrator used must be either unpolarized or only weakly polarized. This assumption is because of the approximate modeling of the leakage terms, retaining only first order terms, in the calibration tasks in routinely used packages. The MIRIAD task "GPCAL" was used for the instrumental polarization leakage calibration. 3C468.1 was adopted as the parallactic angle calibrator. The parallactic angle coverage for this source is shown in Figure 4-7. To get the absolute polarization position angle, one will have to additionally observe a polarized source of known PA (the unpolarized source 3C468.1 does not provide this information).

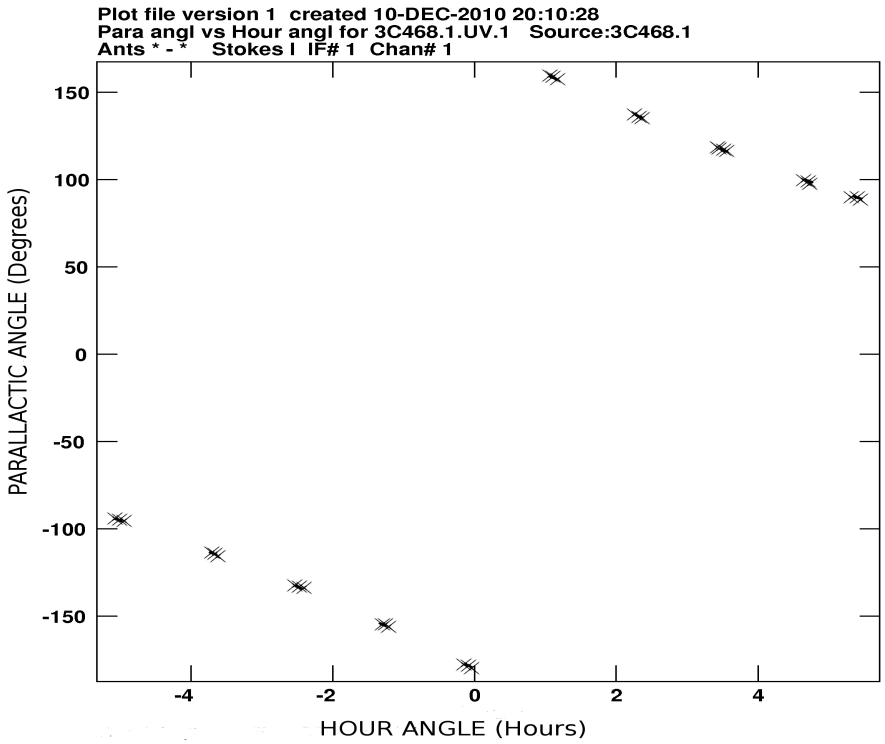

Figure 4-7: *Parallactic Angle coverage for the instrumental leakage calibrator – 3C468.1*

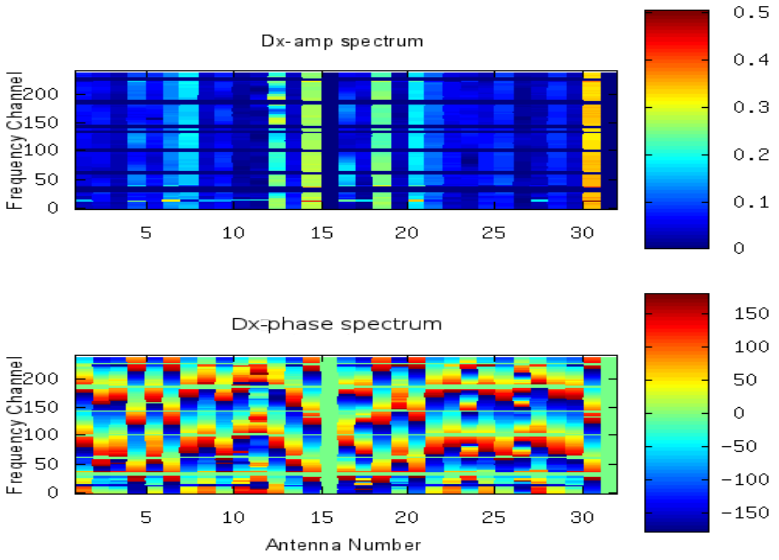

(a) Dx

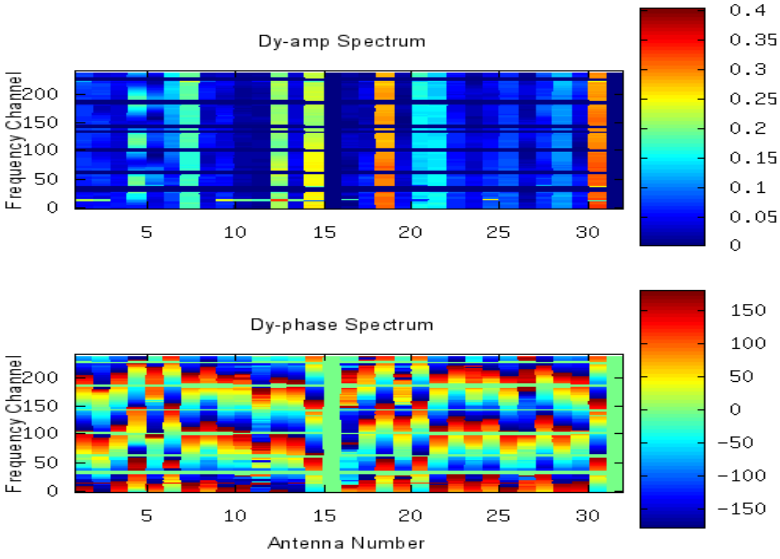

(b) Dy

Figure 4-8: *Plot showing the leakage amplitudes and phases derived using the calibrator 3C468.1. Although the feeds used were circularly polarized, we use the conventionally used leakage terms – Dx and Dy – to describe leakages corresponding to the two orthogonally polarized feed elements. Dx and Dy are in general complex. Antenna number 31 refers to a dummy antenna and should be ignored.*

Figure 4-8 shows the derived instrumental leakage parameters. Except for a

small number of antennas, the leakage amplitudes ($|Dx|$ & $|Dy|$) were found to be less than 10% for all frequency channels. The systematic variation of the leakage phases as a function of frequency for all the antennas is indeed encouraging. Antennas with leakage amplitude exceeding 20% were flagged during the polarization imaging, although the number of antennas involved at a given time never exceeded two.

2. **RL-phase calibration:** The co-polar visibilities of each antenna are referenced *w.r.t.* the corresponding polarization channel of the reference antenna used. The phase relation between the orthogonal hands of the reference antenna is generally unknown, and must be determined particularly for polarimetric studies. The effect of this phase difference depends on the nature of the feed systems involved. For linear feeds, the XY-phase difference would lead to leakage of Stokes U into Stokes V and vice versa. For circular feeds, the RL-phases will introduce leakage between Stokes Q and Stokes U. Additionally, the RL-phases are frequency-dependent, and if left uncorrected would lead to a different PA *vs.* λ^2 trend than that expected from the Faraday Rotation Measure(s) of the propagating medium along the line of sight. The various manifestations of the RL-phases, if left uncorrected for have been discussed in section 4.2.3. The need to make this correction for each spectral channel thus necessitates the observation of a polarized calibrator with known RM and intrinsic PA. We observed the sources 3C345 and 3C303 that are both polarized at these frequencies, and their catalogued RMs are listed in Table 4.3.

   Figure 4-9 shows the PA vs λ^2 curves in the presence of the instrumental RL-phases. Whereas both the sources are expected to show phase ramps with positive slopes (their RMs are positive), the instrumental RL-phases make the apparent slopes negative in both these cases. We would like to mention here that **the RL-phase manifests as an additive effect on the phase-angle**

corresponding to the linearly polarized Stokes *viz.* $\tan^{-1}(U/Q)$**, and not on the polarization position angle (PA) which is** $\frac{1}{2}\tan^{-1}(U/Q)$**. Although in the texts below, we mention the RL-phases in the same breath as the polarization angle, the factor of 2 between the PA and the phase-angle of (Q,U) is implicitly assumed, and has been taken into account in all the corrections applied to the data.**

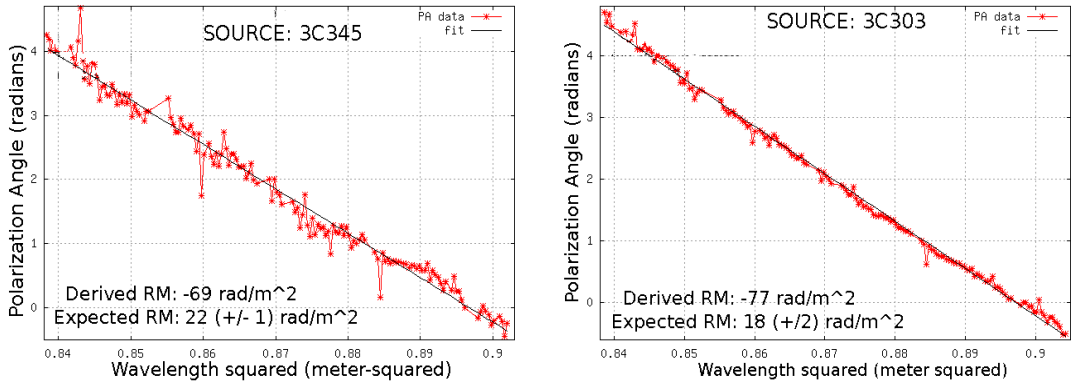

(a) *(b)*

Figure 4-9: *Apparent Rotation Measures for (a) 3C345 & (b) 3C303, derived using the PA-λ^2 relationship, before applying RL-phase corrections. [M:]*

In principle, the instrumental RL-phases need not have a linear relationship with λ^2. However, from Figure 4-9 the combined effect of the RL-phases and the source PAs within the observed λ^2-range at 327 MHz appear to follow a nearly linear relationship with λ^2. While we designate the excess slope to be the "instrumental RM" or "spurious RM", we emphasize that this spurious component need not necessarily be describable in terms of a linear relation between the instrumental RL-phases and λ^2.

The excess RL-phase at any given λ^2 is derived by subtracting from the corresponding PA-value of the measured PA-λ^2 curve, an amount equal to "$RM \times \lambda^2$", where RM is the rotation measure of the relevant polarized calibrator (using

its catalog value Simard-Normandin et al. (1997)). The residual would thus be the RL-phase of the instrument plus the contribution from the RM of the ionosphere in the direction of the calibrator. Note that in deriving their values using the polarized calibrator, we did not assume any model whatsoever for the instrumental RL-phase's dependence on λ^2 Applying this RL-phase correction to target sources would over-correct the instrumental RL-phases by an amount corresponding to the difference in the ionospheric RM towards the target and the calibrator. Furthermore, we assume the intrinsic PA of the calibrator to be zero, since we could not obtain reliable estimates from literature. Hence the derived polarization position angles would be referenced *w.r.t.* the intrinsic PA of the polarized calibrator. The GMRT data presented in the thesis have been calibrated using 3C345 as the primary polarized calibrator.

To assess the reliability of the derived RL-phases, we subtracted these from the data on the second polarized calibrator, and computed the slope of the PA-λ^2 curve. The derived RM for this second source exceeded the catalogued value by $+2$ rad/m^2, which is within the error quoted for the source in the catalog. The difference in RMs of the two sources in our data is ~ 6 rad/m^2, consistent with the maximum difference of 7 rad/m^2 quoted in Simard-Normandin et al. (1997). However, since the ionospheric RMs in the directions of the two calibrators during the time of our observations, could not be precisely known, the actual RMs of the sources would be in error by this uncertain difference in the ionospheric RMs. We chose to use RM values for both of the sources such that, keeping the measured RM-difference the same, the absolute deviations of each RM from their catalog values are equal. Any error in the RL-phase calibrator would only result in a constant excess (or deficit) in the RMs of targets when corrections are made using the calibrator. However, this would be much smaller than the width of an RM-resolution bin (~ 40 rad/m^2) in our data.

Table 4.3: Table comparing the RM values of the two calibrators derived from our data with catalog values. IPA is the intrinsic position angle[5].

	RM (rad/m^2)	[IPA] (°)	Reference
3C303	+18(+/- 2)	+36(+/- 5)	*Simard-Normandin et al (1981)*
3C303	+17	–	*Our data*
3C345	+22(+/- 1)	+33(+/- 1)	*Simard-Normandin et al (1981)*
3C345	+19.5	–	*de Bruyn (private communication)*
3C345	+23	–	*Our data*

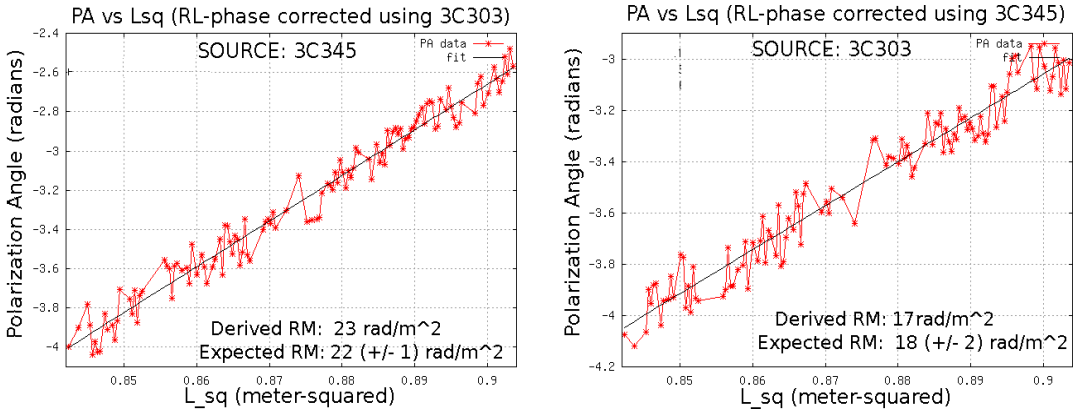

(a) *(b)*

Figure 4-10: *Rotation measures of (a) 3C345 & (b) 3C303, derived after applying RL-phase corrections. The corrections for 3C345 were obtained using data on 3C303, while those for 3C303 were obtained from data on 3C345. In the absence of recent measurements on these calibrators, we used RM values for both that minimized each of their absolute deviations from their catalogued RMs.*

3. **Unpolarized sources and RL phases:** We found that the RL-phases also affected the unpolarized sources in our data. Both 3C468.1 and 3C286 are unpolarized at 327 MHz. The PA-λ^2 curve for these sources prior to RL-phase corrections are shown in Figure 4-11. The spurious apparent RM offset like phase trend introduced by the instrumental RL-phases in the case of the unpolarized sources is same as the apparent "excess" RM for the polarized sources.

The 3C286 data are noisier than the data on 3C468.1 since the effective observation time on 3C286 was shorter ($\sim$ 10 minutes), compared to that on 3C468.1 ($\sim$ 50 minutes). The deviation from a linear trend for the instrumental RL-phase is also clearly visible in the 3C468.1 data corrected for the phase wraps.

The constancy of the RL-phases of the reference antenna is apparent from the PA-λ^2 trends for both classes of calibrators (i.e. both polarized and unpolarized sources) that were observed at different times and in different directions. In general, RL-phases derived using unpolarized sources would be noisier, and hence only polarized calibrators should be used for their determination. However, if there is significant instrumental leakage, and provided this leakage between the orthogonal hands of the reference antenna follows reciprocity, unpolarized sources may in principle be used to determine the RL-phases reliably (see discussion in Chapter 3).

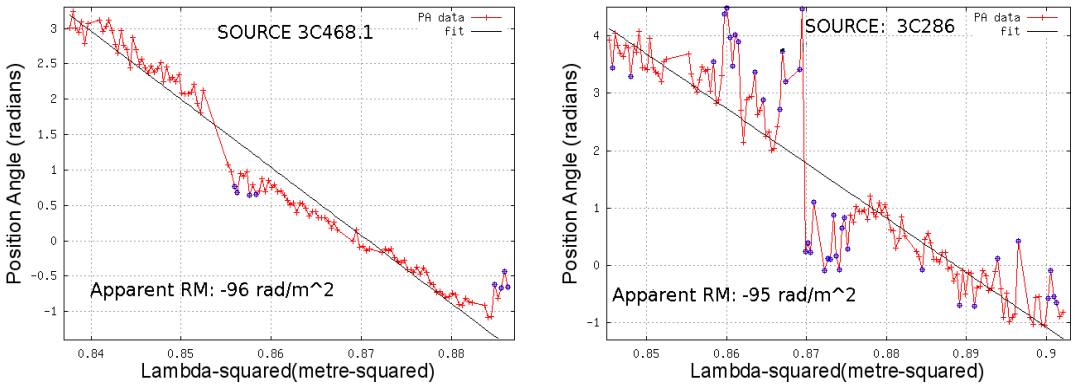

(a) *(b)*

Figure 4-11: *Apparent PA-λ^2 profile of the unpolarized sources (a) 3C468.1 & (b) 3C286 due to instrumental RL-phases. Phases were un-wrapped before the fitting. The blue points were discarded as outliers during the fitting.*

The RL-phases are indeed the gain-phase θ, in the case of circular feeds discussed in Chapter 3. Even when polarization studies may not be the goal, the RR and the

LL data should be first calibrated separately, and then added to get Stokes-I.

Note: We would like to mention here that prior to its 31st December 2010 version, AIPS tasks to deal with spectral data cubes, did not have a provision to de-rotate the RM-induced RL-phases of the calibrator before correcting for this instrumental RL-phase on a spectral channel-by-channel basis. Hence users of these AIPS versions **had to rely on** polarized calibrators lying along lines-of-sights whose RMs are close to zero when dealing with synthesis telescopes having *circular hybrids*. At higher frequencies, one uses the polarized calibrator 3C286 which has an RM very close to zero ($+33\ rad/m^2$). However, at low radio frequencies the problem is two-fold – firstly, polarized calibrators at low radio frequencies are rather rare, and secondly, those that are polarized have polarized diffuse foregrounds with significant RMs. Splitting the uv-data into single-channel files and adherence to automation enabled us to solve for the instrumental RL-phase on a channel-by-channel basis. The AIPS task RLDIF was used to solve for the instrumental RL-phase by providing the frequency-dependent RM-induced RL-phases corresponding to our polarized calibrator, to the parameter POLANGLE (intrinsic PA of the calibrator) which RLDIF needs to first subtract from the observed RL-phases. The PA reference is set to the intrinsic (but unknown) PA of the polarized calibrator, as of now, but this has no bearing on the outcome of the calibration exercise.

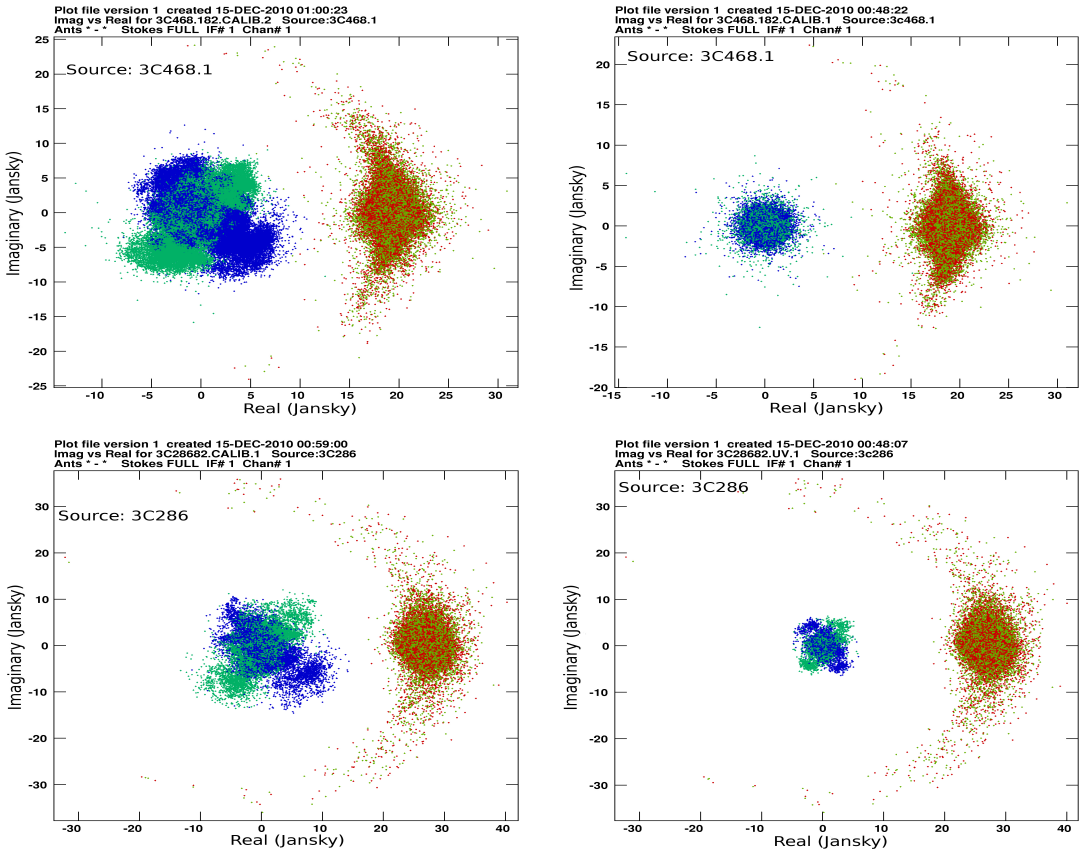

(a) Self calibrated data *(b) Self calibrated + Leakage Calibrated*

Figure 4-12: *Real vs. Imag part of RR (red), LL(light-green), RL(blue) and LR(dark-green) visibilities pre and post calibration (left and right panels respectively) for sources 3C468.1 (top panels) and 3C286 (bottom panels). The scatter plots shown here as an illustration, are for a single representative spectral channel.*

4.3.5 Assessing leakage calibration using unpolarized calibrators

We used the unpolarized point source calibrators for assessing the success of our procedure for estimation and correction of leakage using 3C468.1. The panels in Figure 4-12 are scatter plots of the real and imaginary parts of the RR (red scatter plot), LL (light-green), LR (blue) and RL (dark-green) visibilities pre- and post-leakage calibration for these sources. Since both the sources, 3C468.1 & 3C286 are "de-polarized" at

327 MHz, we should expect the centroid of the distribution in the real *vs.* imaginary parts of the visibilities of both RL and LR to lie at (0,0).

Although the leakage-calibrated scatter plots for 3C468.1 seem consistent with the above expectation, both in terms of its flux density and polarization state (*viz.* unpolarized), the LR & the RL scatter plots for 3C286 data for a small number of baselines show polarization that is inconsistent with the rest. This problem was traced to antenna no. 17 during the time 3C286 was observed. This is an example of the complexities involved in the flagging exercise. We also like to point here that this antenna is not apparent as "bad" in the Stokes-I data.

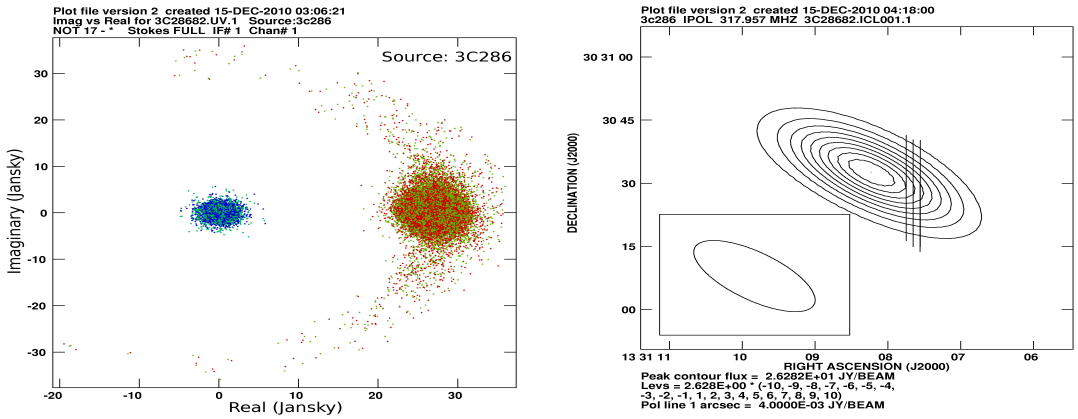

(a) *(b)*

Figure 4-13: *(a) Scatter diagram of the real and imaginary parts of RR, LL, LR and RL for 3C286 after antenna no. 17 had been flagged. The colour code is the same as that adopted in Figure 4-12. (b) The Stokes-I image of 3C286 derived from this data. Polarization vectors (fractional polarization* $\sim$ *0.4%) are overlayed on the Stokes-I contours. The synthesized beam is shown in the lower left corner*

Figure 4-13 (a) shows the scatter plots of the real *vs.* imaginary parts of the various Stokes terms for 3C286 after the bad antenna (#17) had been removed. Figure 4-13 (b) shows a single-channel leakage-calibrated image of 3C286 with polarization vectors overlayed on the Stokes-I contours. The degree of linear polarization in the above leakage calibrated, single-channel image of 3C286 is found to be 0.4%. This is the residual instrumental polarization leakage remaining after the leakage calibration

exercise.

The arc-like features in the plots of real *vs.* imaginary parts of the RR and LL visibilities for a few baselines, show a relative phase difference of $\sim 90^{\circ}$ between their respective real and imaginary parts. This is also seen in similar plots for 3C468.1. The origin of this relative phase ($\sim 90^{\circ}$) between the real and the imaginary parts of both the RR and the LL visibilities, is not fully understood.

4.4 Assessment of ionospheric behavior

For Faraday tomography, it is important that the ionospheric RM remains unchanged throughout the duration of the observation. A time-varying ionosphere may lead to severe depolarization depending on the degree of fluctuations in its rotation measure, unless the variations can be known and corrected. We therefore characterized the ionospheric contribution to RM using Electron Density and Geo magnetic Field Models provided by NASA for the day these observations were carried out. For the earth's magnetic field, we used the IGRF model (Finlay et al., 2010), while the IRI model (based on real data)[6] was used for n_e estimates. On the average, the RM contributed by the ionosphere relevant for the observing period for which our target field was observed is estimated to be $\sim 1\ rad/m^2$ with a variation in RM of confined to only a fraction of this mean value. The variation is well below the size of our RM resolution bin ($\sim 40\ rad/m^2$). The maximum RM for the day in other directions, however, was slightly higher: $\sim 4\ rad/m^2$. This value corresponds to the ionospheric contribution when the polarized calibrators (3C303 and 3C345) were being observed (close to sunset). Since B_{tot} was used (rather than $B_{||}$) for the field values, the estimated RM contribution of the Ionosphere is in fact over-estimated, and hence can be regarded as an upper limit for the Ionosphere's contribution to RM during our observation.

[6]http://omniweb.gsfc.nasa.gov/vitmo/iri2012_vitmo.html

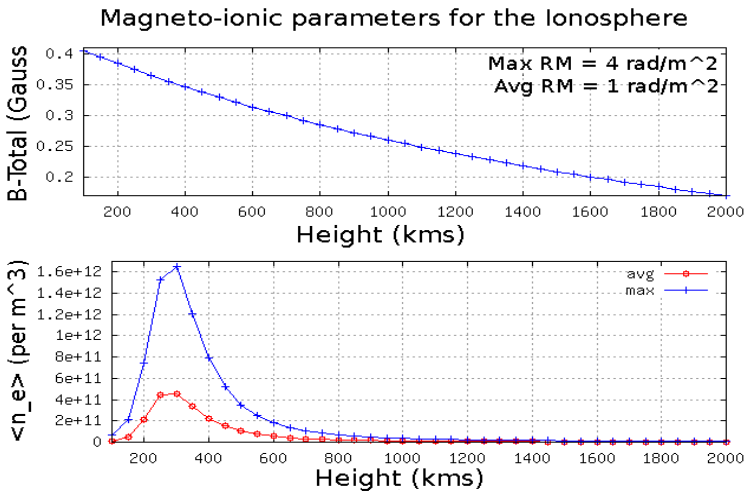

(a)

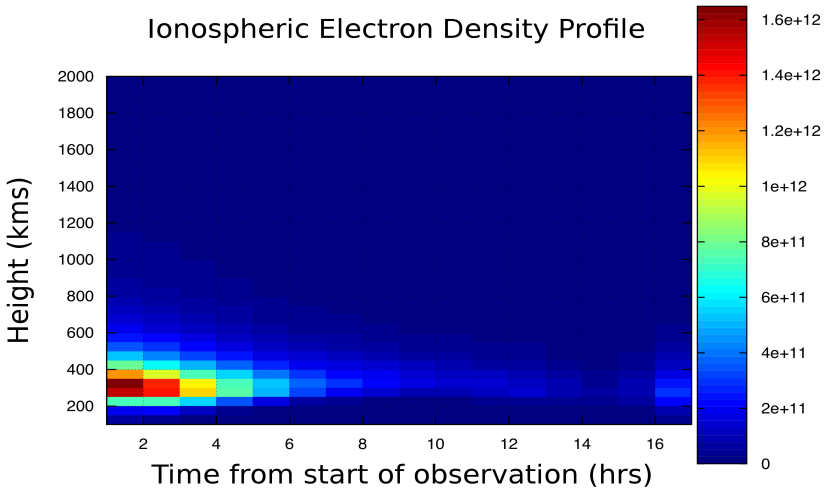

(b)

Figure 4-14: *Ionospheric RM: (a) The top panel shows the total Geo magnetic field as a function of altitude at GMRT. The bottom panel shows the maximum as well as the time-averaged electron density profile for the day of the observations. The RM values quoted in the top panel correspond to the integral contribution estimated using the magnetic field profile in the top panel and the electron density profiles in the bottom panel. (b) The electron density as a function of altitude and time. The sporadic variation in electron density is seen at an altitude of about 300 km and lies very close to sunset. The electron density profiles were obtained using the IRI model, while the Geo magnetic field was estimated using the IGRF model.*

The start time of our observations referred to in Figure 4-14 *(b)* is about 1500 hours IST. The sporadic variation in electron density is seen at an altitude of about 300 kms and only very close to sunset, after which the ionosphere remained roughly unchanged throughout the night. This re-emphasizes the importance of night-time observations for sensitive spectro-polarimetric studies.

4.5 Proof of concept: Tomography on several calibrators

Once all the calibrations had been applied on the data, we processed the uv-data to produce the spectral image cubes in all four Stokes parameters. The (Q + iU) image cube was then discrete Fourier transformed (DFT) along the spectral axis to produce the complex "dirty" RM cube, *i.e.* an image cube with the two usual image axes (RA and Dec) and a third corresponding to the RM. Each pixel value in this cube is a complex number representing a measure of the components of the complex linearly polarized intensity as a function of RA, Dec and RM. We take the cases of a few simple sources here, and present their RM spectra as preliminary illustrations of the feasibility of spectro-polarimetric studies at the 327 MHz band with the GMRT. Polarization studies of a more complex source (Cas A) is discussed in Chapter 5.

1. Un-polarized Calibrators:

   The tomographs of calibrated unpolarized sources are expected to contain mere random fluctuation reflecting the measurement noise, without any significant feature. However there could always be a small residual instrumental polarization contribution corresponding to remnant leakage from Stokes-I that could not be completely corrected during calibration. RL-phase calibration, using polarized calibrators having high S/N in Q and U Stokes parameters, is expected to have removed any frequency-dependence of this residual leakage. Any constant I-dependent leakage, if significant compared to the fluctuations due to noise in the Q and U-spectra, would then show up at RM ~ 0. We investigate these

issues using data on the unpolarized calibrators.

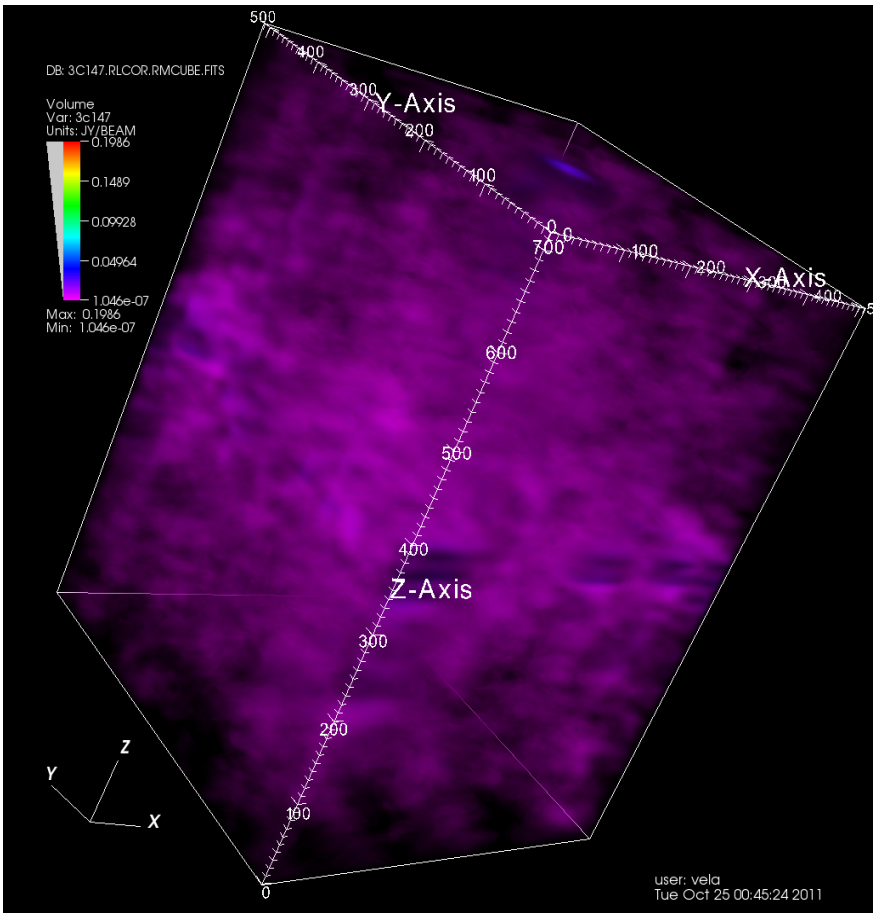

(a)

Figure 4-15: *RM cube for 3C147: Linearly polarized intensity (Jy/beam) as a function of RA (x-axis), Dec (y-axis) and RM (z-axis) for unpolarized calibrator, 3C147. The axes are in units of pixel numbers of the image cube used.*

Figure 4-15 shows the 3-D tomograph for a region centered at the unpolarized source, 3C147. Most of the volume is filled with noise fluctuations as would be expected from lines of sight having no significant linearly polarized emission components. The *rms* noise along the RM-axis passing through the source (Figure 4-16) is higher compared to other lines of sight. This is expected since the unpolarized flux density of a strong source would dominate the system

temperature and also the fluctuations in its spectra (self noise), including the polarization spectra. The relative contribution of a point (or point-like) source to the off-source regions is expected to be small. The system noise in the off-source regions are dominated by the receiver noise and the total flux density within the beam, compared to the flux density in the given off-source direction. The noise in the spectra in any off-source direction would therefore be significantly lower (a calibrator, by virtue of its being a "calibrator", is expected to have significant contrast of on-source flux density *w.r.t.* the background flux densities). Hence, most of the volume within the RM-cube of 3C147 is expected to contain contribution from mainly the receiver noise & total flux density in the beam.

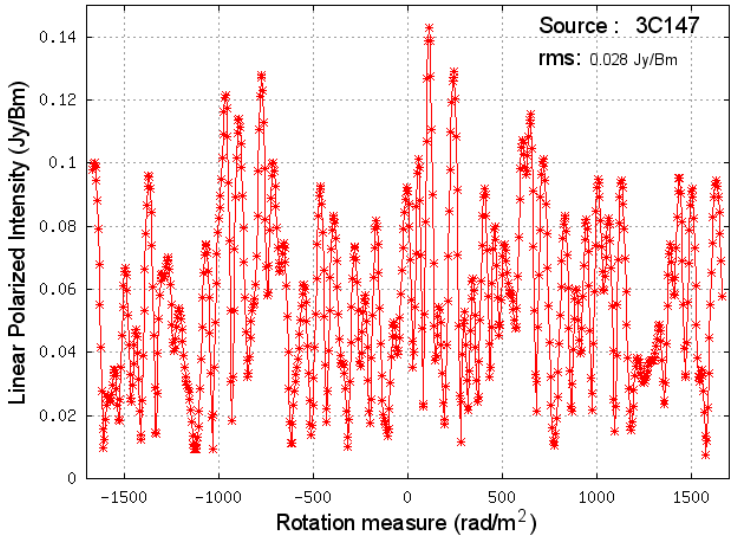

Figure 4-16: *The RM profile for the line-of-sight towards the unpolarized source, 3C147.*

If the Q and U spectral data along a sight-line are Gaussian white noise, each with standard deviation σ, the noise in the amplitude of the Fourier transform of $Q + iU$ (which is the RM profile), is expected to be $\sqrt{2} \times \frac{\sigma}{\sqrt{n}}$, where n is the number of spectral channels; (n = 167 in our case, after rejecting the bad channels). Figures 4-16, 4-17 and 4-18 are the RM profiles in the direction of unpolarized sources 3C147, 3C286 and 3C468.1 respectively. The *rms* de-

viations across their RM profiles are consistent with Q and U (in the spectral domain) being Gaussian white noise. Table 4.4 lists the flux densities of the unpolarized sources and the *rms* derived from their spectra. In Table 4.5, a comparison between the *rms* in the RM-profiles of the unpolarized sources and the expected values from their spectra is shown.

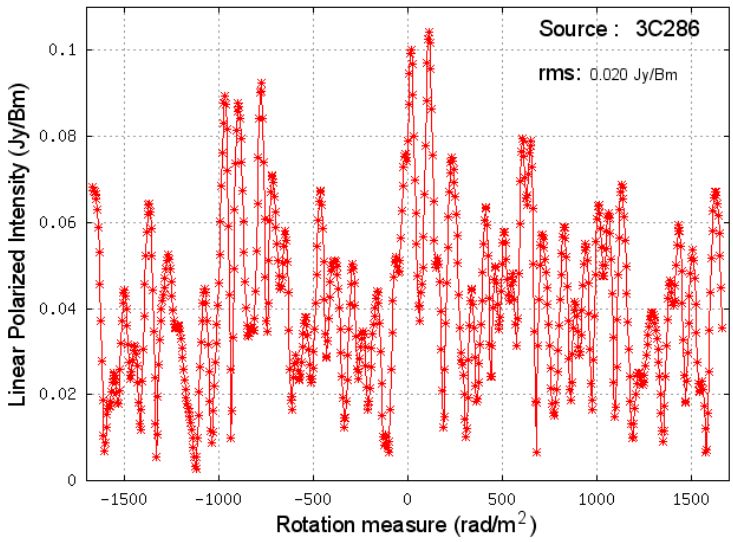

Figure 4-17: *RM profile for the line-of-sight towards the unpolarized source 3C286.*

Table 4.4: On-source noise of unpolarized calibrator sources estimated from their spectra

Source	Flux density (Jy)	σ_I (Jy/Beam)	σ_Q (Jy/Beam)	σ_U (Jy/Beam)
3C147	48	0.2	0.25	0.3
3C468.1	19.5	0.12	0.10	0.12
3C286	26	0.25	0.17	0.19

Table 4.5: Comparison of noise in RM profiles of unpolarized sources with those in their Q & U-spectra. $\sigma_{\rm P,RM}$ is the robust *rms* computed from the polarized intensity profile as a function of RM.

Source	σ_Q (Jy/Beam)	σ_U (Jy/Beam)	$\sigma_{P,RM}$ (Jy/Beam)	$< \sigma_{P,RM} >$ (Jy/Beam)
3C147	0.25	0.3	0.028	0.04
3C468.1	0.10	0.12	0.01	0.01
3C286	0.17	0.19	0.02	0.02

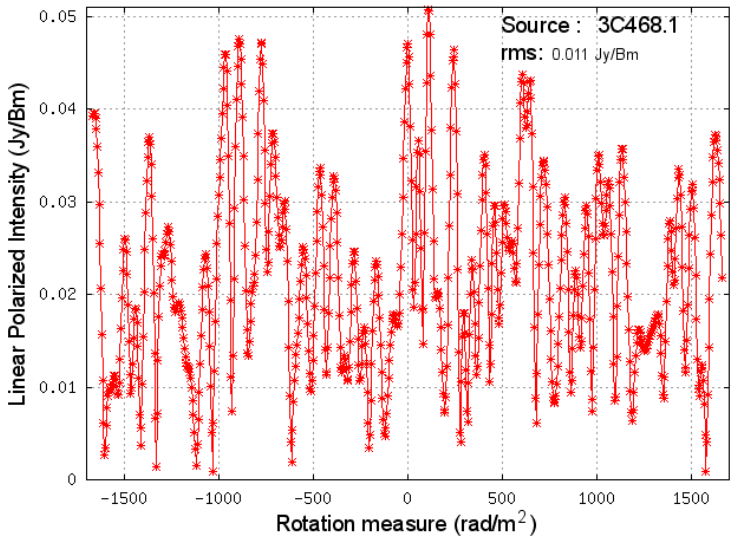

Figure 4-18: *RM profile for the line-of-sight towards the unpolarized source 3C468.1.*

Table 4.6: Typical OFF-source noise in the fields of unpolarized calibrator sources estimated from their spectra, and the expected *rms* in their RM profiles

Source	Flux density (Jy)	$\sigma_{I,off}$ (Jy/Beam)	$\sigma_{Q,off}$ (Jy/Beam)	$\sigma_{U,off}$ (Jy/Beam)	$< \sigma_{P,RM} >$ (Jy/Beam)
3C147	48	0.03	0.005	0.005	0.0005
3C468.1	19.5	0.002	0.002	0.002	0.0002
3C286	26	0.03	0.005	0.004	0.0005

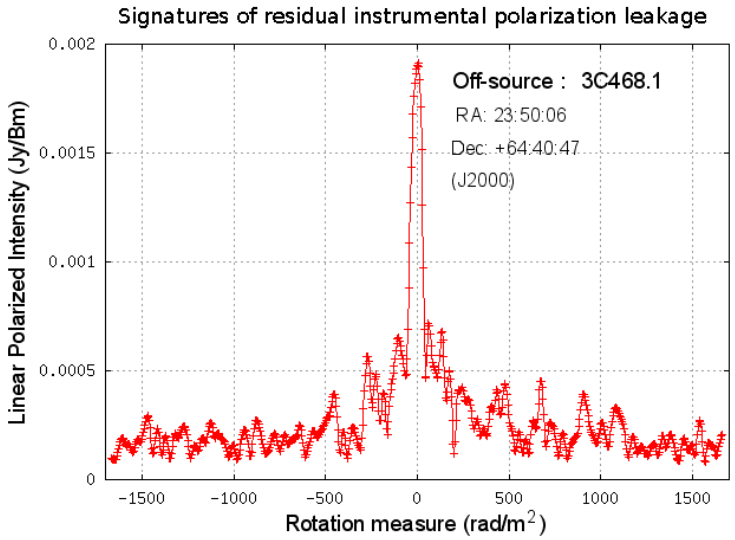

Figure 4-19: *A typical tomograph of an off-source region around 3C468.1. The significant component at RM = 0 rad/m^2 has contributions partly from the leakage of Stokes-I, corresponding to the diffuse Galactic emission, into the polarized Stokes parameters.*

The RM profiles of the unpolarized sources do not reveal any "significant" linearly polarized flux density. However, the lack of a significant polarized component in the RM-profiles of the unpolarized calibrator sources does not rule out the possibility of small polarization contribution corresponding to any residual instrumental polarization leakage. Indeed the "band-averaged" polarized flux densities of the unpolarized sources are $\sim$ 0.5% of their respective Stokes-I. This indicates the level to which the residual instrumental polarization is reduced. The direction towards 3C468.1 has significant diffuse Galactic emission

compared to those towards the other calibrators. A significant component at $RM = 0$ appears in the RM profiles of most sight-lines around this source. This could partly be due to the instrumental leakage of Stokes-I from the diffuse background into the polarized Stokes parameters (Figure 4-19). It is non-trivial to "extract" the linear dependence of the residual instrumental polarization using its corresponding Stokes-I. Pixels with faint Stokes-I emission will also have a contribution from the true sky polarization, whose relationship with Stokes-I is expected to be far more complicated in general. Wherever the I-dependent leakage dominates over the polarized emission from the sky, we indeed see a correlation between the polarized intensity (at RM = 0) and the Stokes-I intensity. In Chapter 5 we discuss in detail the problem of the I-dependent leakages obscuring signatures of the faint polarization from the supernova remnant Cas A.

2. Linearly Polarized Calibrators:

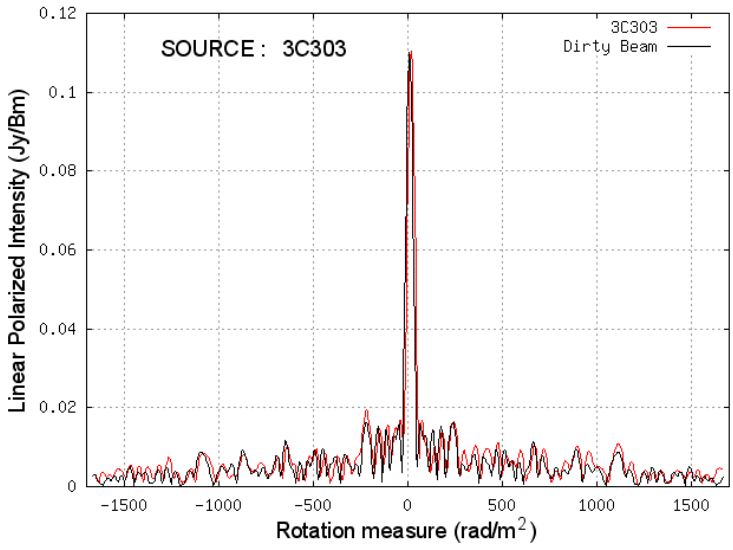

Figure 4-20: *The red curve is the tomograph for polarized source 3C303. The black curve is the simulated dirty RM-beam for the source's RM of +17 rad/m^2 with its peak scaled to the peak flux density in the tomograph derived for the source.*

Figure 4-20 shows the tomograph (red curve) of the polarized calibrator 3C303 derived using the calibrated data. The RM of the source is found to lie at $+ \sim 17\ rad/m^2$ as discussed earlier (Table 4.3). The black curve is the simulated dirty RM-beam for $+17\ rad/m^2$ scaled to the peak height of the tomograph. No significant peak, other than the primary one is evident. The minor deviations are a result of the noise in the 3C303 RM-profile. The degree of polarization for 3C303 is found to be $\sim 4\%$, while that for 3C345 is found to be $\sim 3\%$. Compared with the instrumental leakage of $\sim 0.5\%$ derived using the unpolarized sources, the polarized fractions for both these linearly polarized sources is significantly higher. These parameters for the polarized calibrators, close to the time of our observations, could not be compared with corresponding parameters from data taken with systems routinely used for polarization studies, such as the WSRT. We could only get the RM values for these calibrators established with data from observations made many years ago with the WSRT (A. G. de Bruyn, private communication). Nevertheless, the internal consistency in the derived RM values for both of the polarized sources, as well as the consistency in the data on the unpolarized sources discussed, are indicative of the quality of the overall polarization calibration (leakage, as well as RL-phase calibration).

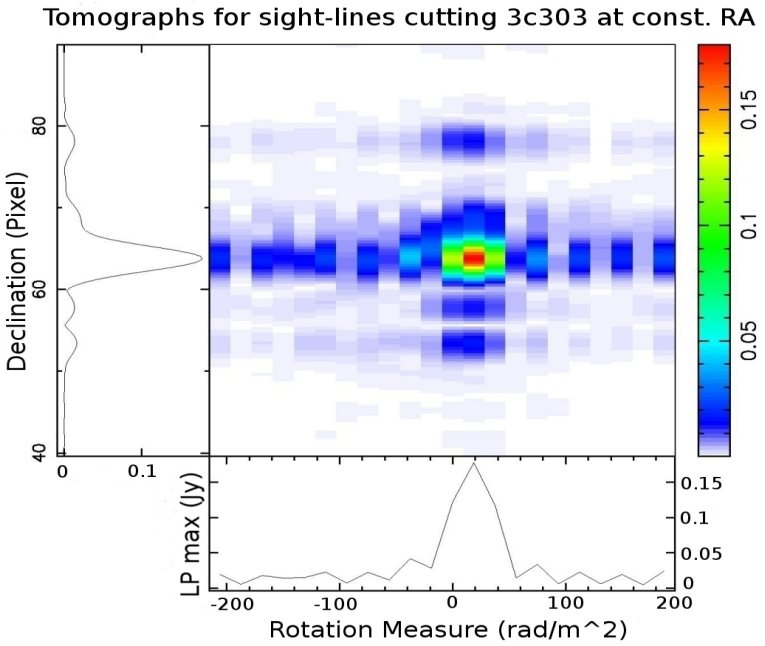

Figure 4-21: *Tomographs along sight-lines of constant RA ($RA = RA_{3C303}$).*

Figure 4-21 shows a plane of constant RA ($RA = RA_{3C303}$) extracted from the 3-D tomograph corresponding to a $\sim 10'$ region around 3C303. These plots are richer in information content than plots along a single sight-line. Further, while 3-D plots such as Figure 4-15 may be useful, they fail to convey the details that lie within their volumes.

4.6 Polarization from the diffuse Galactic background

In certain directions, additional features are seen at RMs around -80 rad/m^2 (Figure 4-22). This value is consistent with the RMs in these directions derived using pulsars[7]. Estimates of typical off-source noise around these source directions, along with the expected *rms* in their RM profiles, are presented in Table 4.6 to emphasize the significance of these features in the tomographs. The expected dirty RM response function

[7]see for example, the ATNF pulsar catalog at http://www.atnf.csiro.au/people/pulsar/psrcat/

(or the dirty RM-beam) at $RM = 0\ rad/m^2$, corresponding to our λ^2-sampling, is shown in Figure 4-23. The expected side-lobe levels are much lower than the height of the component at $RM \simeq -80\ rad/m^2$ relative to the feature at $RM = 0\ rad/m^2$. For a few lines-of-sight, the $RM \simeq -80\ rad/m^2$ component is even stronger than the $0\ rad/m^2$ RM feature.

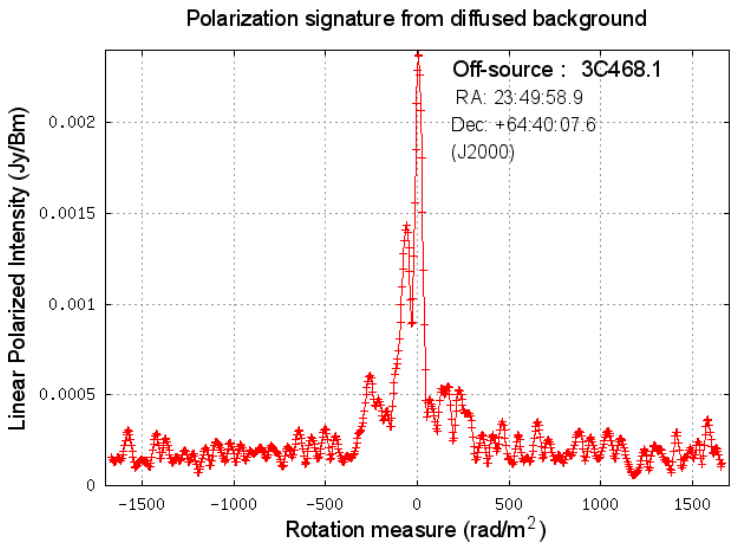

Figure 4-22: *Tomograph of an off-source region around 3C468.1. The component at* $RM \sim -80\ rad/m^2$ *is significantly higher than the expected side-lobe levels from our dirty RM-beam (Figure 4-23).*

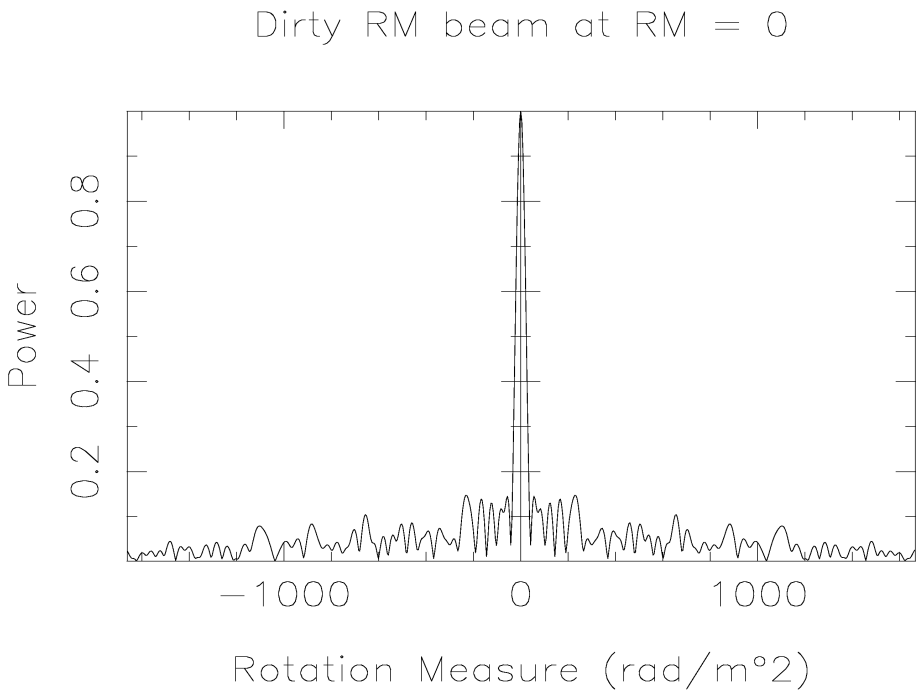

Figure 4-23: *Dirty RM response function at* $RM = 0\ rad/m^2$.

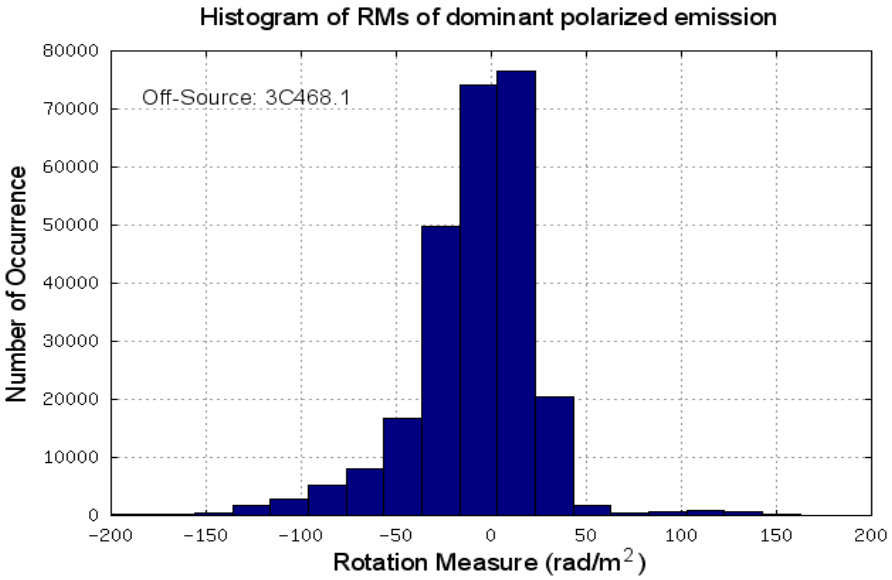

Figure 4-24: *Histogram of RMs of the dominant polarized emission components along sight lines around 3C468.1. The distribution is skewed towards negative RMs.*

Figure 4-24 shows the histogram of the RMs corresponding to the most dominant

polarized component along sight-lines towards the $\sim 10'$ region around the source 3C468.1. The distribution is skewed, and indicates the presence of a significant number of components with negative RMs. In figure 4-25 we plot the RMs corresponding to the dominant polarized flux densities for any given image pixel, against the signal-to-noise ratio of their corresponding components; the noise is estimated from the *rms* of the polarized flux densities along the RM axis at their respective image pixel. All pixels within the $10'$ region around 3C468.1 are used in the plot. Not only is the number of negative RM components more, a significant fraction of these also have higher S/N than their positive RM counterparts. The skew in the RM-distribution, together with the associated S/N of the RM components leading to the skewness, is a likely signature of these being contributions from the diffuse Galactic emission, that is expected to be intrinsically highly polarized. The negative RM components have a significant scatter across this celestial region, and are not concentrated close to the strong calibrator, noise in which could also have led to such features.

The distribution of the RMs of these dominant polarized components in the sky-plane, are shown in the Figure 4-26. The colour range is adjusted to crudely match the RM-resolution ($\sim 40\ rad/m^2$) in our data. Blue traces the zero RM components. Magenta traces the polarized emission that must have survived beam depolarization, as well as internal (front-to-back) depolarization within the Galaxy. This must have either originated from relatively strong, diffuse Galactic synchrotron emission and/or propagated through relatively "thin" Faraday foregrounds.

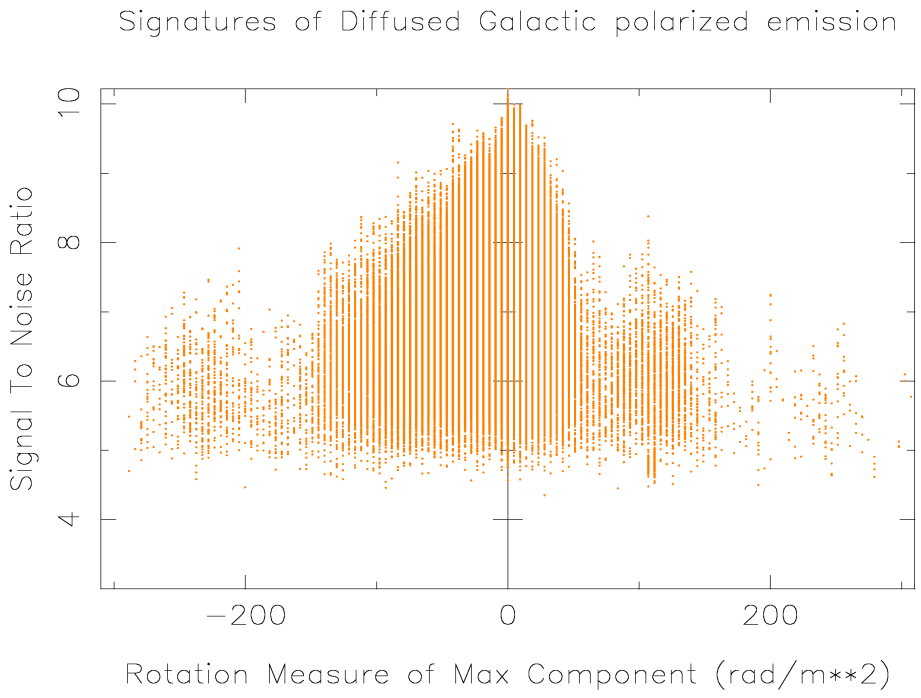

Figure 4-25: *The RMs corresponding to the brightest polarized component,found along each of the sight-lines, are plotted against their respective signal-to-noise ratios. All pixels around the direction of 3C468.1 are shown in the scatter plot.*

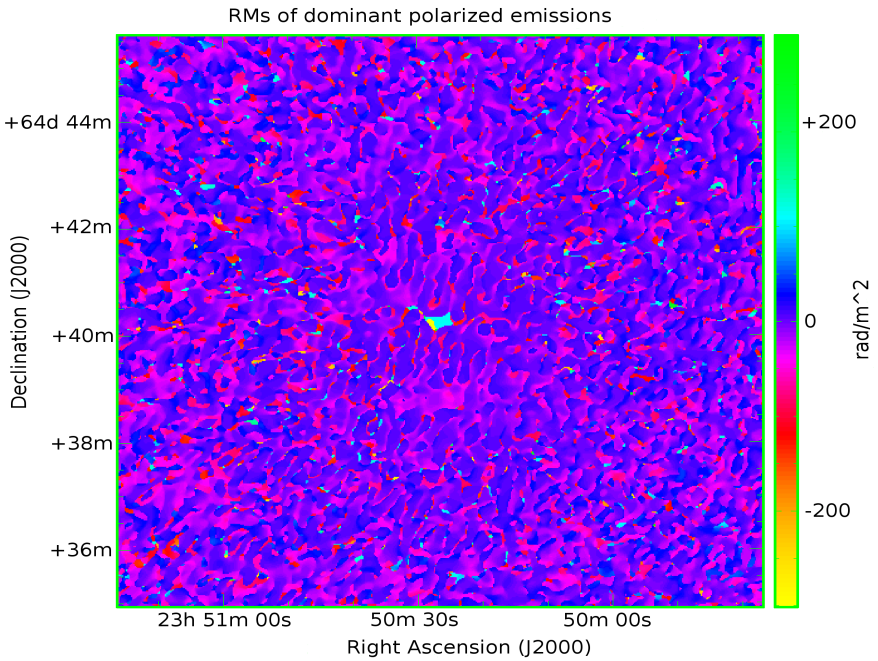

Figure 4-26: *Map of RMs corresponding to the dominant polarized component along sight-lines around 3C468.1. The RM at the center is dominated by the self noise of the point source, and hence not to be taken seriously.*

We note that the RMs in Figure 4-24, 4-25 & 4-26 are just those of the most dominant component along corresponding sight-lines. Hence, not applying RM-clean to the data at this stage should not alter the argument about this part of the Galaxy having stronger polarized emission components with negative RMs.

The component at RM = 0 rad/m^2 need not necessarily be from the instrument alone (as we had assumed). It is possible that polarized emission from the Galaxy, surviving the bandwidth depolarization across the observing band, also contributes to this component. A plot of the fractional polarization *vs.* the RM of the dominant components are shown in Figure 4-27. Only pixels with Stokes-I flux density [$> 6\ mJy/Bm$] (which is 3σ in the Stokes-I map of 3C468.1) are used for deriving the fractional polarization. The fractional polarization of the dominant polarized components in the RM domain are high, some even exceeding unity. The higher than 100% polarization are not artifacts of noise, but a manifestation of the fact that the structure in linearly polarized intensity has higher amplitude than the structure on similar

scales in Stokes-I, and is a result of not including the zero spatial-frequency components in the maps. However, the degree of polarization of the Stokes-I dependent instrumental polarization leakage should not be affected by the non-inclusion of the zero spatial frequency measurement. It is therefore likely that the higher than 100% polarization appearing as significant components in the RM domain are indeed from the celestial diffuse emission, and not merely the result of instrumental polarization leakage. These also include components at RM = 0 $rad\ /m^2$. Such high polarization has been seen in small scale polarized emission features in the diffuse Galactic emission (Wieringa et al., 1993).

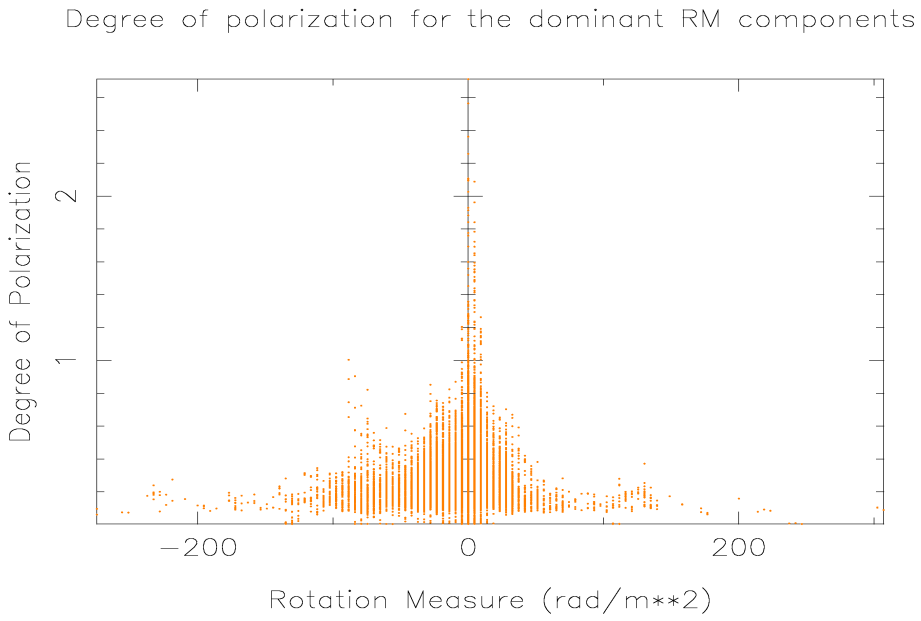

Figure 4-27: *Fractional polarization of the dominant polarized components are plotted as a function of their RMs. Only pixels with Stokes-I intensity greater than 6 mJy/Bm (3σ in the I-map of 3C468.1) are used. The higher than 100% polarization are seen as a result of not including the zero-spatial frequency component of Stokes-I in the map, due to which the smoothly varying fraction of Stokes-I is missed, resulting in systematic underestimation of Stokes-I.*

Disentangling the instrumental polarization from the sky polarization would require independent measurements. A potential method to disentangle these two com-

ponents has been demonstrated in Chapter 5.

4.7 Conclusions

The 327 MHz polarimetric calibration exercise for the GMRT has been discussed, and the feasibility of Faraday tomography demonstrated using several compact radio sources. The instrumental polarization leakage could be calibrated to less than 0.5%, which is comparable to the levels of residual polarization achieved for VLA data. This residual instrumental polarization ascertained using strong unpolarized sources, appear as features near zero-RM in directions with significant background emission. However, a straightforward association of the flux densities at zero RM with the corresponding Stokes-I cannot be established. This is as the measured polarization, in addition to being a result of the spurious polarization through leakage of Stokes-I into the other Stokes parameters, also have contributions from the Galactic synchrotron emission that is expected to be intrinsically highly polarized. The apparent higher than 100% polarization of these components in fact indicate the presence of significant sky polarization. The non-inclusion of the zero-spatial frequency measurements in the maps of Stokes-I underestimates the total intensity at a given image pixel that may have significant Fourier components in the polarized emission. Polarization leakage, being Stokes-I dependent, could not possibly have structures in angular and RM domains that are different from and stronger than those seen in Stokes-I. Hence polarization leakage cannot result in the apparent degrees of polarization exceeding unity. In the next chapter, we discuss in detail the problems of ascertaining the true polarization from the sky in the presence of weak instrumental polarization, and present a potential method to detect true polarization even in the presence of leakage.

In achieving good calibration, and to ensure high fidelity in the polarization images, detection and mitigation of the rather complex RFIs is crucial. These RFIs vary as a function of all the parameters – *viz.* time, frequency, baseline and antenna, as well as polarization. While looking at the data using only representative sub-sets

of these parameters would allow quick identification of RFIs, this would not present the complete picture of the contamination. For instance, baseline B, when probed using calibrator C, may appear interference-free at time T in the frequency channel N. However, the same baseline B could show anomalies for various combinations of the other parameters. Threshold-based clippings do not necessarily eliminate the weaker RFIs, and although these may be ignored as "weak" for the purposes of Stokes-I imaging, they may be significant for polarimetry. Whereas the baseline-based RFIs would introduce features in the sky maps, the spectral contamination by RFIs would affect the RM-data. Even if only a tiny fraction of spectral channels are affected by RFIs that may not appreciably corrupt the band-averaged total-intensity images, features in the band due to such RFIs will corrupt the RM-data. Automation is the only way to detect and mitigate RFIs, particularly for large data sets such as those we encountered during our full-synthesis observation.

Additionally, a well-behaved ionosphere is important for Faraday rotation measure-related studies, and hence night times are ideal for these observations. In the next chapter, we demonstrate the feasibility of spectro-polarimetric studies of extended sources using the GMRT.

Chapter 5

GMRT Spectro-polarimetric studies of the supernova remnant Cassiopeia A

Cassiopeia A (Cas A) is a young supernova remnant (SNR) in our Galaxy, believed to have resulted from the explosion of a massive star some 300 years ago. Ever since its detection, it has been widely studied at all wave bands. It is the brightest extra-solar radio source in the sky, and has been studied both in total intensity, and polarization. The non-thermal emission from Cas A is significantly polarized around the near-circular morphology of its shell. However, the degree of polarization along the ring reduces from about 5% at 6-cm wavelength to as small as $\sim$0.3% at 20-cm (Downs & Thompson, 1972). The heavy depolarization is seen to have a tight correlation with soft X-ray counts (Anderson et al., 1995). This correlation suggests the presence of both thermal and non-thermal plasma within Cas A, with the non-thermal polarized emission suffering depolarization due to Faraday rotation in the thermal plasma within the remnant itself. This opens up the possibility as well as emphasizes the necessity of determining the distribution of non-thermal emission along the sight-line as a function of the internal Faraday rotation measure (or Faraday depth), i.e. performing Faraday tomography.

In GMRT Proposal Cycle 17, we proposed spectro-polarimetric observations of SNR Cassiopeia A at 3 GMRT bands – 1280, 610 and 327 MHz – with the aim of performing multi-band Faraday Rotation Measure (RM) Synthesis. However, noting that instrumental polarization calibration strategies for the GMRT were not readily available, the time allocated (in Nov. 2009) was only sufficient for a full-synthesis at a single band. Potential depolarization depends on the product of the angular and RM resolutions (see Chapter 6). For arrays with fixed configuration and usable bandwidth, as at GMRT, this depolarization would decrease with decreasing observing frequency (see equation 6.3). With this view, we chose to observe at 327 MHz, which provides high RM resolution as well as a fairly good angular resolution amongst the available bands that are not severely affected by radio frequency interference (RFI). However, given that Cas A is substantially depolarized at these low radio frequencies, very careful instrumental polarization calibration is required to obtain reliable estimates of intrinsic polarization. Meeting this requirement is challenging, in polarization studies with a synthesis imaging instrument in general and particularly so when such measurements are being attempted for the first time at this low frequency with the GMRT.

The instrumental calibration as well as data reduction has been discussed in detail in Chapter 4. Even though absolute flux density is not important for the presented work, we have scaled the data assuming the integrated flux density of Cas A to be $\sim$ 7000 Jy at 327 MHz, consistent with a flux density of 2720 Jy at 1 GHz, and a spectral index of $\alpha = 0.77$ (Green, 2009), where $S_\nu \propto \nu^{-\alpha}$. An accurate calibration would require details of the secular changes in the flux density of Cas A in our band.

In section 5.1 below, we present GMRT total intensity map of Cas A at 327 MHz and compare this with existing radio maps of comparable resolution from the VLA for consistency checks and data-quality assessment. The calibrated linear polarization maps are presented in section 5.2. The problems of detecting weak polarization in the presence of the inevitable residual instrumental leakage are discussed in section 5.2.1.

We also demonstrate a potential technique for detecting weak sky polarization even in the presence of contamination due to residual instrumental polarization leakage. Key results from Faraday tomography are discussed in section 5.3. Construction of simple 3-D models of the thermal and the non-thermal emissivities from Cas A is discussed in section 5.4. Though very simple, these models can qualitatively explain some of the observed features in the polarimetric data. Discussion of the results and conclusions are presented in section 5.5

5.1 GMRT 327-MHz Continuum imaging of Cas A in Stokes-I

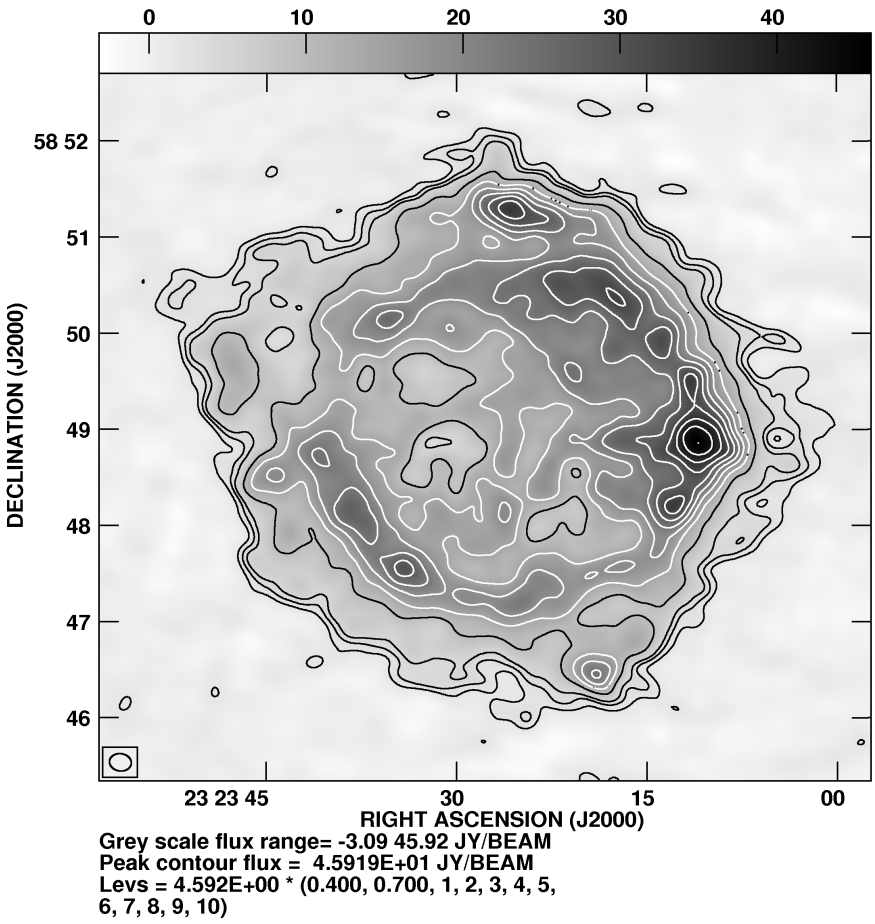

Figure 5-1: *GMRT 327-MHz continuum Stokes-I image of Cas A. The flux density is scaled such that the integrated flux density for the source is 7000 Jy. The synthesized beam ($14'' \times 11''$) is shown in the bottom left corner of the image.*

Cas A is a complex source having rich structure distributed over a range of spatial scales. Its prominent features include a bright shell, compact knots and an extended plateau of emission. The radio shell is generally associated with a region of high magnetic field, amplified by Raleigh-Taylor instabilities arising in the contact surface between the relatively dense supernova ejecta and the shock-heated ISM as the rem-

nant begins to decelerate.

In its overall morphology, the 327-MHz Stokes-I image appears strikingly similar to the VLA image of identical angular resolution (Figure 5-2). The image on the left is our GMRT image. The radio-bright ring is prominent as are the knots and filaments. As expected, the ring is situated $\sim 100''$ from the remnant center (Figure 5-3).

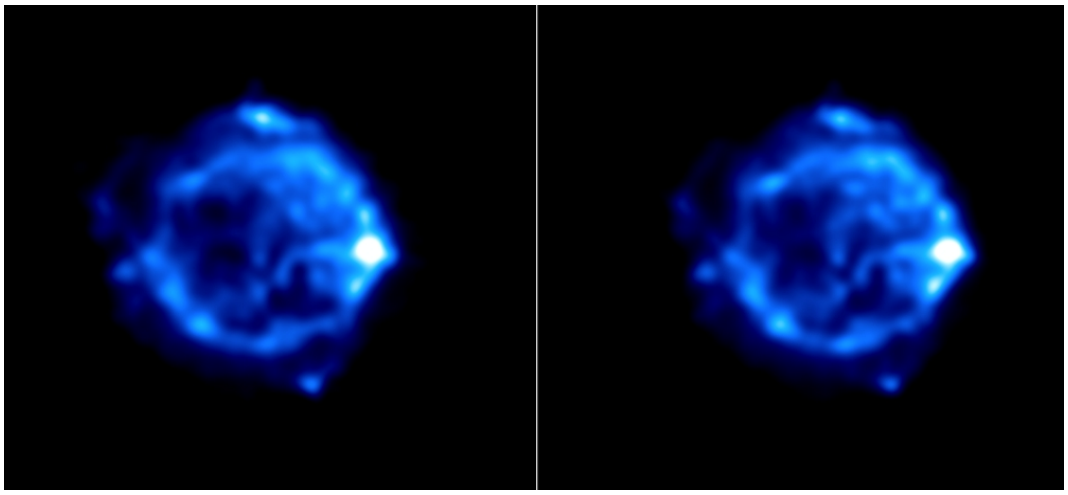

Figure 5-2: *The GMRT 327-MHz Stokes-I image of Cas A (left) alongside a 1420-MHz image of the remnant from the VLA. The striking morphological similarity of the two images demonstrates the very good data quality within the the GMRT 327-MHz band. The angular resolution in both these images is* $15'' \times 15''$.

The visible appearance of the 327-MHz image itself is indicative of the high quality of date from our GMRT observations. Given that the RFI level at the GMRT at night-time is generally lower than during the day-time, we specifically requested scheduling of the telescope so as to observe Cas A mostly during the night. Additionally, we conducted extensive test observations over the few days prior to the scheduled observations. This allowed us to choose an appropriate center frequency that consistently gave less RFI in the 16-MHz band around it. Furthermore, the exhaustive and automated flagging of residual bad data contributed to the high quality of our GMRT images. The similarity of our P-band image to the VLA image indicates

reliable complex gain calibration.

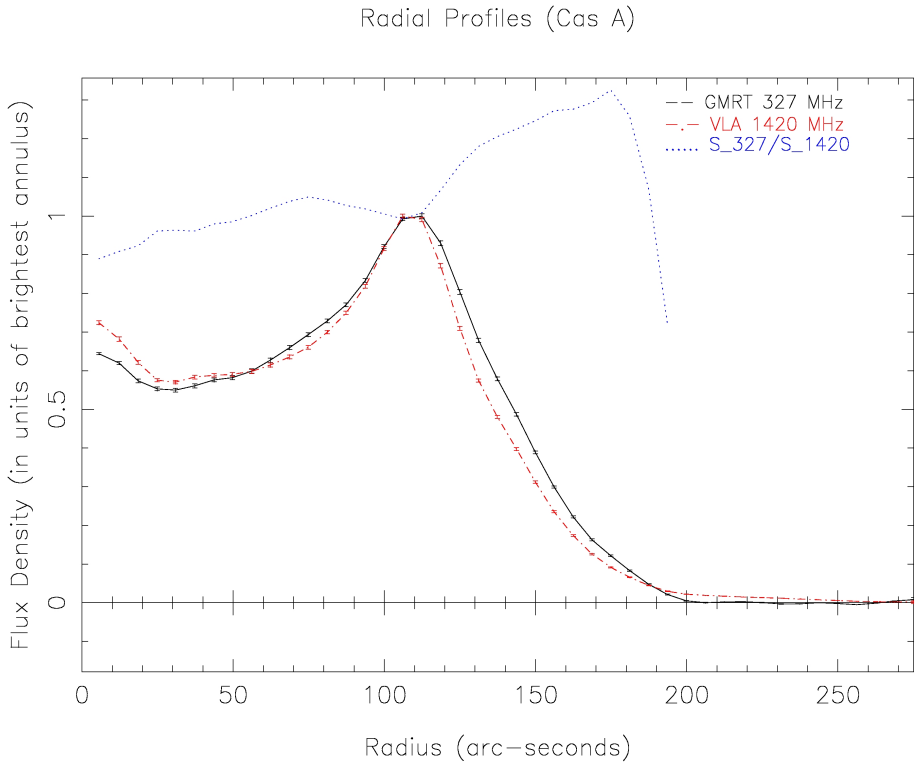

Figure 5-3: *Azimuthally averaged radial profiles of Stokes-I intensity across SNR Cassiopeia A at 327 MHz (black continuous curve), and 1420 MHz (red dashed curve). Both profiles are normalized by the mean flux density within the corresponding brightest annuli of the two images. The blue dotted line is the ratio of the normalized radial profiles obtained at the two frequencies. In computing the azimuthal averages, the thickness of the annuli was taken to be equal to the HWHM of our synthesized beam, i.e. close to* $7''$.

The radial profiles of Stokes-I at 327 and 1420 MHz are presented in Figure 5-3. Although the radial profiles are qualitatively similar in the two images, the intensity at the remnant's edges (relative to the brightest annulus) in the P-band image is somewhat higher than the corresponding L-band intensity at the same radius. Spectral steepening towards the edges has been reported in earlier works (Kassim et al., 1995). The apparent increase in the remnant's radius at 327 MHz relative to the 1420-MHz image, towards the outer edges ($120 - 160''$) is about $7''$ (Figure 5-3). However the epochs of the images used at the two frequencies are separated by 7

years. The 327-MHz image corresponds to observation epoch 2009, while the L-band image was observed at epoch 2002. If the expansion rates are independent of frequency, then the analysis of Agüeros & Green (1999) would imply that the remnant would have expanded by $\sim 4.2''$ in the 7 year span between the VLA L-band and our 327-MHz observations. Hence the relative brightening at the edges of the 327-MHz image when compared to the L-band image could at least partly be due to expansion of the remnant into the ISM. To disentangle these two effects (bulk expansion & spectral steepening), one would require comparison of the remnant at the same frequency observed at different times, as well as at different frequencies observed at similar times.

We note that in producing a radial profile, the fiducial center of the SNR was taken to be the pixel for which the radial profile of the variances encloses minimum area.

In Figure 5-4 we show the distribution of Stokes-I in Cas A at 327 MHz as a function of radial distance and azimuth angle for the best center derived. Although the information content is the same as in the images in Figure 5-2, such an image brings out very clearly the conical features (Raleigh Taylor fingers) expected in the turbulent regions where the remnant interacts with the ISM, their filling fraction, as well as the radial extent of the emission.

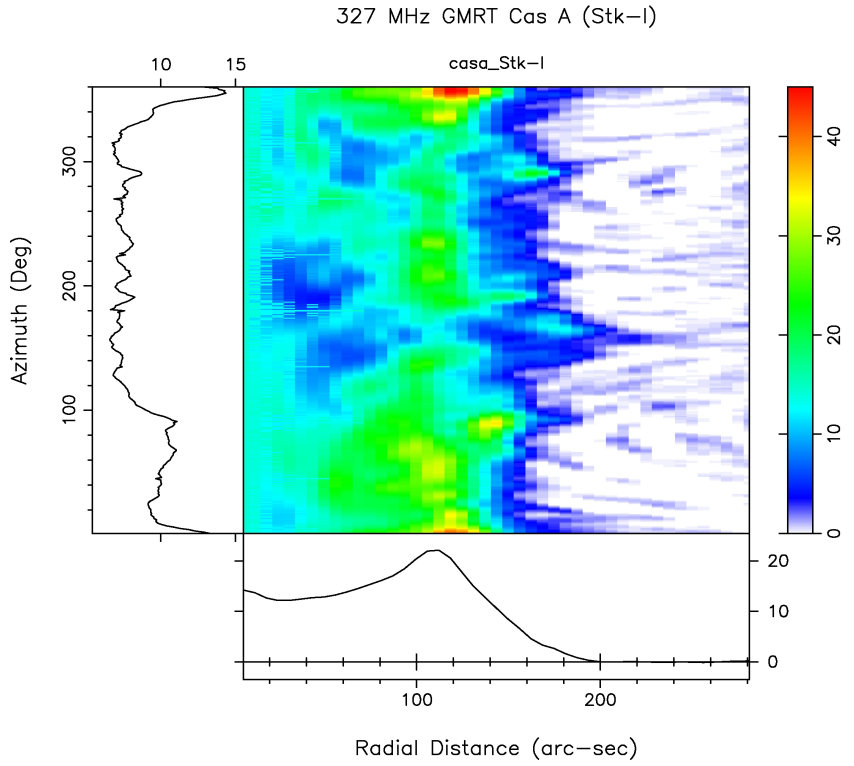

Figure 5-4: *Stokes-I intensity for Cassiopeia A as a function of radial distance and azimuth at 327 MHz. The zero of the azimuth angle is defined as the direction pointing West from the remnant center, North is* 90°*, East* 180° *and South* 270°*. The subplots show the averages along the corresponding collapsed axes.*

5.2 Continuum polarimetric imaging of Cassiopeia A at 327 MHz

The additional steps crucial to polarimetric imaging of the data include instrumental leakage calibration using the parallactic angle tracking method (3C468.1 was used as the calibrator), and calibration of the frequency dependent RL-phases of the reference antenna (we used polarized calibrators 3C303 and 3C345 (Chapter 4). The band-averaged linearly polarized intensity maps as well as the polarization angle maps pre- and post-leakage calibration are shown in Figures 5-5 and 5-6.

The distributions of both the polarized intensity and the polarization position angle (shown in insets of respective images) become narrower, attaining significant mean-values after the polarization calibration. The average degree of polarization across the source is about $\sim 1.5\%$, of which the residual leakage is estimated to be $< 0.5\%$ from the pixels with the highest Stokes-I flux densities, where it is expected that the Stokes-I dependent leakage would dominate the polarized fraction (as illustrated in Figure 5-7). This is in agreement with the residual leakage estimated using the unpolarized point sources.

We have corrected our polarization images for any I-dependent leakage, which would remove any contribution in (Q,U) that would be correlated with Stokes-I. For a nearly unpolarized source like Cas A at 327 MHz, the noise fluctuations in Q and U will be mutually independent, as well as uncorrelated with those in Stokes-I, although all of them will have similar rms value, say σ. In computing the polarized intensity as $\sqrt{(Q^2 + U^2)}$ there will be a statistical bias resulting from the mentioned noise fluctuations. This bias will exist even if the mean values of both Q & U were to be zero, but then the bias will be minimum ($\sqrt{2}\sigma$), and in our case it is estimated to be 20 mJy, which for most parts of Cas A will imply a bias of 0.15% in the degree of polarization. Noting the smallness of this bias compared to the minimum believable polarization fraction (0.5%), we have not explicitly corrected for this statistical bias in estimates of the polarized intensity. For a bright source like Cas A, the system temperature is dominated by 'source noise', and hence the above mentioned bias, if left uncorrected, will mimic Stokes-I dependent polarization leakage. Our correlation analysis (with Stokes-I binning) is immune to Stokes-I dependent contributions, including polarization leakage and similar contributions, and hence the already small uncorrected bias is unlikely to affect our results.

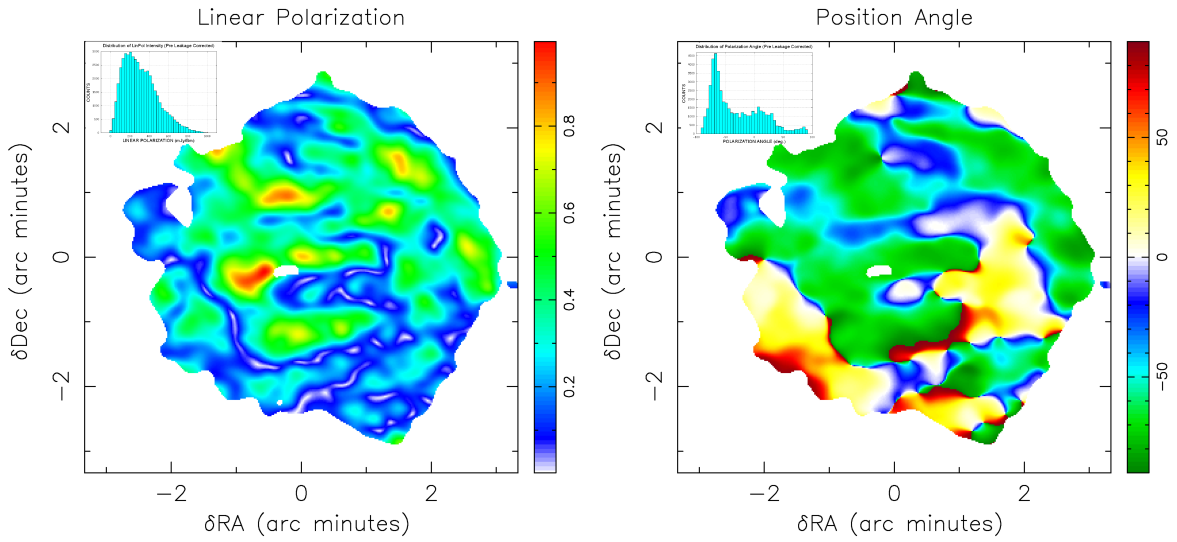

(a) *(b)*

Figure 5-5: *Pre-leakage calibration maps: (a) Linear polarized intensity. (b) Polarization position angle in degrees. The flux density scale used is same as that used in Figure 5-1. The insets show the distribution of the respective quantities. In subsequent plots, the same flux density scale will be used unless otherwise mentioned.*

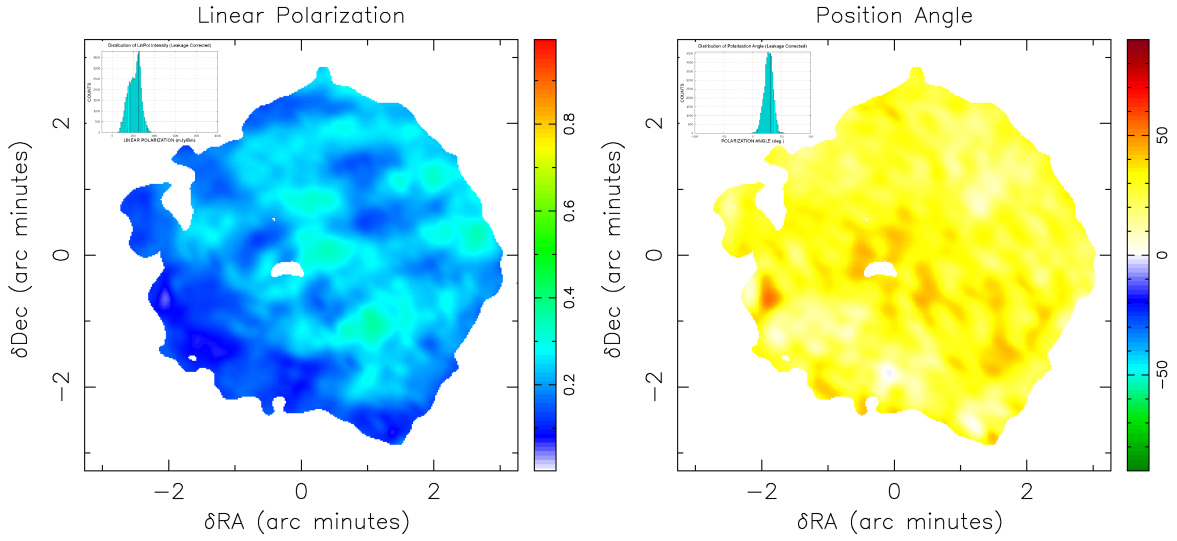

(a) *(b)*

Figure 5-6: *Leakage calibrated maps: (a) Linear polarized intensity. (b) Polarization position angle. The insets show the distribution of the respective quantities.*

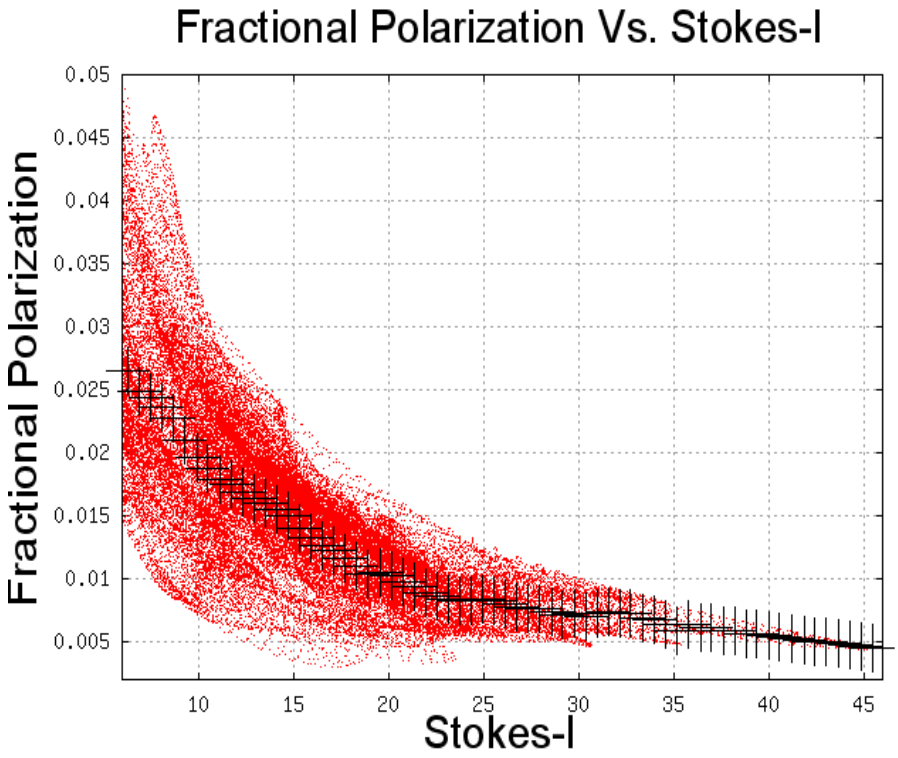

Figure 5-7: *Degree of linear polarization as a function of leakage-calibrated Stokes-I. Only pixels lying within Cas A are plotted. The black crosses show the average degree of polarization within each of the I-bins. A lower flux density cut-off was used to exclude pixels with low S/N, as well as regions outside the extent of Cas A.*

The polarization position angle distribution across Cas A appears uniform from the PA map ($\sigma_{\rm PA} \sim 5^\circ$; see Figures 5-6(b) & 5-12). Whether this is a manifestation of a coherent magnetic field across Cas A, and/or the result of a dominating instrumental polarization leakage (that is expected to remain constant across such small areas in the sky), cannot be ascertained trivially. The problems associated with this issue, plus a possible way out, are discussed in the following sections.

5.2.1 The Origin of the Observed 327-MHz Polarized Intensity: Intrinsic or Instrumental?

The apparent 327-MHz polarization of Cas A is found to be very weak (Figure 5-13), as would be expected from the severe internal depolarization (Downs & Thompson, 1972). The mean degree of polarization is only about 1.5%. In the presence of noticeable residual instrumental polarization ($< 0.5\%$ in our case, as ascertained from several unpolarized calibrators), it is rather challenging to prove the intrinsic nature of the observed polarization. Although a lack of correspondence between the maps of polarized intensity and Stokes-I (Figure 5-12), also verified through formal cross-correlation analysis (see the scatter plot in Figure 5-9), provides strong evidence against the polarization being instrumental in origin, the uniform orientation of the observed linear polarization across the remnant (Figures 5-6 & 5-12) calls for additional independent scrutiny.

Fortunately, the degree of depolarization is known to correlate well with soft X-ray intensity (Anderson et al., 1995), and we use such a correlation as a critical additional test in assessing the intrinsic nature of the observed polarization. Although the correlation was established by comparing data at two radio frequencies (Anderson et al., 1995), even at a given frequency the spatial distribution of the "degree" of linear polarization, if intrinsic, should in principle show an anti-correlation with that of the soft X-radiation. If observed, such an anti-correlation can ideally be taken as strong evidence for the intrinsic nature of the observed polarization, provided that possible contamination of the correlation from any Stokes-I dependent effects can be arrested.

For example, if Stokes-I (used for computing the degree of polarization) and the X-ray intensities are spatially correlated, the apparent *degree* of polarization would still show such anti-correlation, even if the polarized intensity were to be random. Unfortunately, the radio and X-ray intensities are, on the average, indeed spatially correlated in the present case. Hence an unconventional approach is invoked to probe

the correlation.

Figure 5-8 shows a soft X-ray Chandra image of Cas A (right) alongside the 327-MHz Stokes-I (left) image of the remnant. The morphologies in the two images indicate a spatial correspondence between the two intensities. Such correspondence have also been independently verified through formal cross-correlation of the two images.

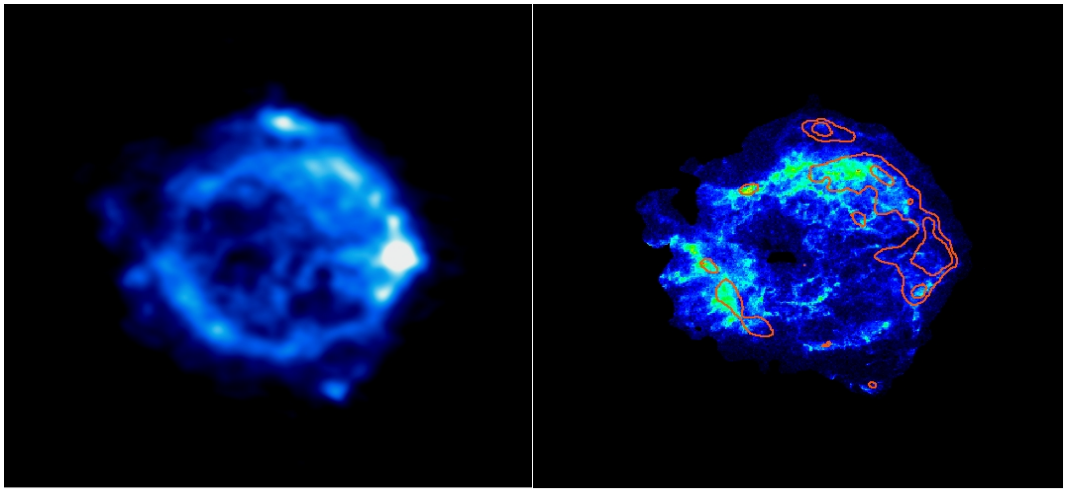

Figure 5-8: *The 327-MHz GMRT Stokes-I image of Cas A (left) alongside a soft X-ray image of the remnant from the 0.5-1.5 keV band of Chandra. (See the text towards the end of this section for description of the red contours in the right panel.)*

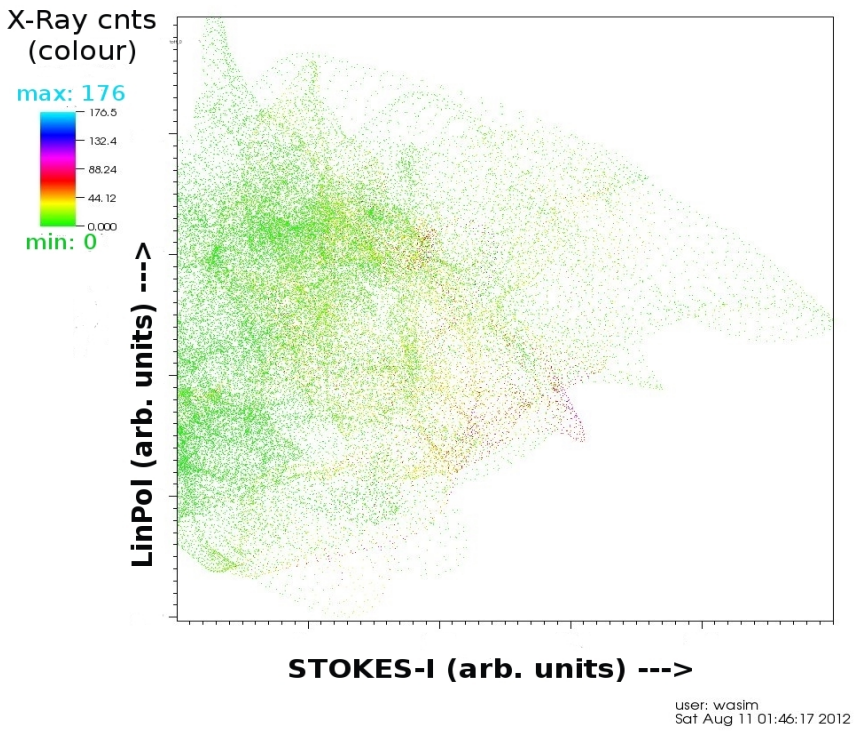

Figure 5-9: *Scatter plot of Linearly Polarized Intensity against Stokes-I. Soft X-ray counts are in colour. The contents of this plot are used to extract underlying correlations between Linear Polarization and X-ray emission at any given Stokes-I, as discussed in this section.*

Recognizing the explicit dependence of the potentially contributing contamination from Stokes-I, we consider narrow ranges (or bins) of Stokes-I separately, and for data within each such bin, compute the cross-correlation between the X-ray counts[1] and the corresponding linearly polarized intensities, which for any given I-bin is directly proportional to the degree of polarization. Even in this case, an underlying

[1]The soft X-ray (0.5-1.5 keV) image (X-ray image credit: NASA/CXC/SAO/D.Patnaude et al.) used for the correlation analysis was available in the public domain, and was made from Chandra X-ray observations of 2007. Unable to re-locate the image in more recent times in the Chandra repositories, we verified our correlation results by repeating the analysis with soft X-ray images processed and kindly provided by Dr. Harsha Raichur using 2009 ACIS data from Chandra. The X-ray images were made compatible with our radio images by first transforming the former using AIPS task HGEOM, and then convolving to the resolution in our radio images using AIPS task CONVL. The X-ray counts have not been corrected for the high absorption in the foreground column (Keohane et al., 1996). However, this would have little effect on the correlation between X-radiation and the linearly polarized intensities, since the dispersion of X-ray optical depth (τ) about the mean value of ~ 1 is small enough (Keohane et al., 1996) not to introduce any significant differential structure in the X-ray emission across the remnant.

anti-correlation of the X-radiation with linearly polarized intensity is likely to be contaminated if polarized intensity were to follow Stokes-I tightly and certainly from any residual instrumental polarization which is invariably I-dependent. However such contamination would introduce a positive bias to the correlation we wish to examine. Any significant anti-correlation, if seen despite this bias, will provide strong evidence for at least a part of the observed polarization being intrinsic.

Ideally the bin-width in Stokes-I should be as small as possible, so that there is little variation in I-dependent contaminants. Constant offsets could still be present, but they will not affect the correlation that depends on the relative variations of the relevant quantities. However, to ensure reasonable statistics in each bin, we used a bin size of 0.5 Jy beam^{-1}, within which the Stokes-I dependent contaminations would continue to contribute corresponding amount of (positive) bias to the sought correlation. The presence of such a bias is clearly visible in the correlation profile obtained using data prior to our primary polarization calibration. The correlation profiles for the data before and after the polarization calibration are shown in the top two panels of Figure 5-10, along with the corresponding profiles of mean and rms of X-ray counts (central panel). The clear difference between the two correlation profiles is a direct manifestation of the I-dependent bias, which is effectively removed by the polarization calibration exercise. Even in the profile (top-most panel) for the un-calibrated data dominated by the positive bias, the contribution of the underlying anti-correlation is apparent. This underlying signature (expected for intrinsic polarization) stands out distinctly in the correlation profile for the polarization calibrated data (panel 2), emphasizing both the need for, and the reliability of, the calibration exercise.

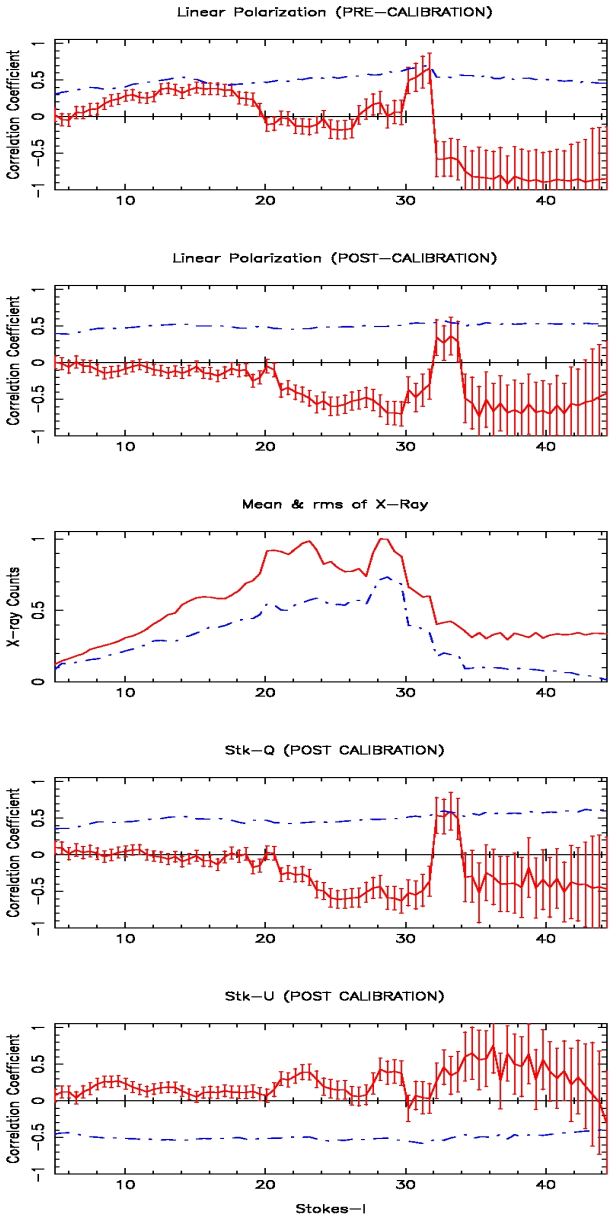

Figure 5-10: *The top two panels show the profiles of the correlation between soft X-radiation and the linearly polarized intensity as a function of Stokes-I before and after primary polarization calibration respectively. The* $\pm 1\sigma$ *error bars on the correlation-coefficients are also shown. The central panel shows the profile of the mean (solid line) and the rms (dash-dot line) of X-ray counts (both the profiles have been normalized by the maxima of the profile corresponding to the mean X-ray count). Correlation profiles of calibrated Stokes-Q and Stokes-U with X-ray emission are shown in the 4th and the 5th panels respectively. The mean of the polarized intensities within the I-bins (dash-dot lines) are plotted in the respective panels. For ease of display, the magnitudes of the means within the I-bins are normalized by twice their global means (*$\sim$ *360, 217, 168 & -130 mJy) for quantities in panels 1, 2, 4 & 5 respectively.*

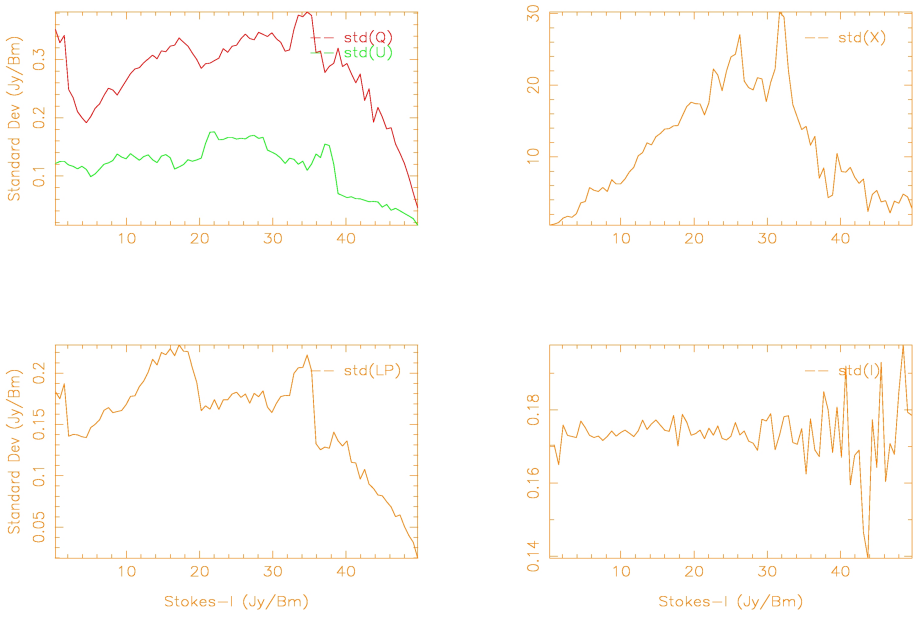

(a)

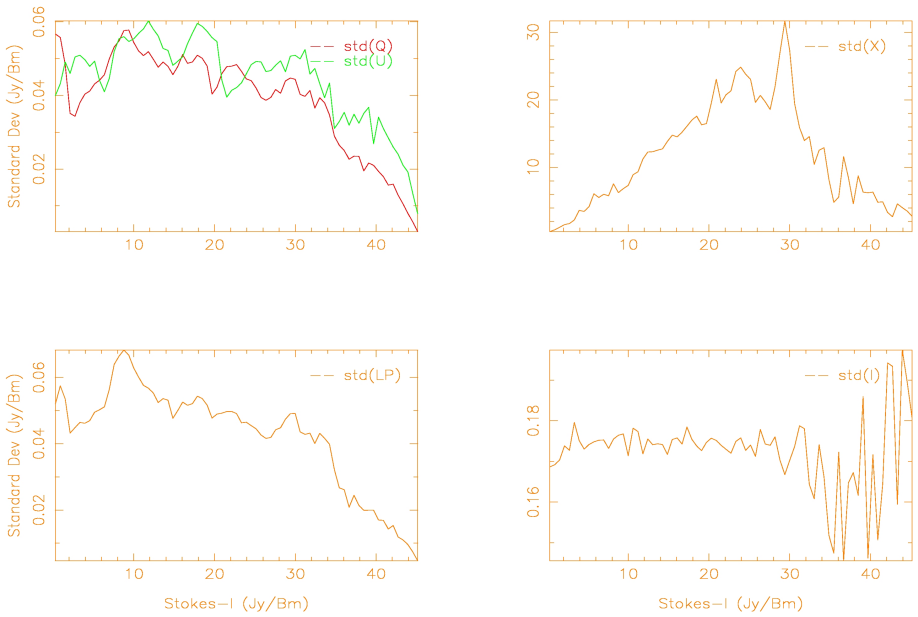

(b)

Figure 5-11: *Standard deviation of various quantities as a function of Stokes-I bins (clockwise from top left panel: Q & U, X-ray, Stokes-I and Linear polarization) (a) pre leakage calibration and (b) post leakage calibration.*

As can be seen from Figure 5-11, primary instrumental polarization calibration

has dramatically reduced the *variance* in the observed Q & U (by almost an order of magnitude[2]). Nonetheless the presence of residual Stokes-I dependent polarization leakage might continue to bias the correlation. Hence, even for the calibrated data, performing the correlation analysis within separate Stokes-I bins, ensures improved immunity to any remaining bias. We have further assessed such residual linear dependence of Stokes-Q and -U on Stokes-I in the band-averaged maps, and corrected the respective data cubes by removing the Stokes-I dependent components of Q & U (~ 0.2 & 0.1% of Stokes-I). In the process we may have, in principle, subtracted part of the intrinsic polarization. The remaining polarization therefore represents a lower limit to the intrinsic polarization. For the present data, the correlations discussed above are not sensitive to the bin-size used.

The pixels associated with any I-bin are in general, scattered over the image. Therefore the correlations would be corrupted by any trend in off-axis instrumental polarization. However the $(5' \times 5')$ extent of Cas A is only a tiny fraction of the $\sim 1.5^\circ$ primary beam, and significant differential off-axis polarization is not expected. Even otherwise, it is unlikely to have any spatial correspondence with the X-radiation over the source, let alone be anti-correlated.

We argue that the significant anti-correlation[3] evident between the X-radiation and the degree of linear polarization, together with its excellent correspondence with the profiles of both the mean and the spread in X-ray counts (central panel of Figure 5-10, which is very similar to the profile for the spread in X-ray counts), underlines the intrinsic nature of the derived 327-MHz polarization. The pixels showing the highest anti-correlation lie mostly within the bright radio ring (see the single-value contours in red tracing these pixels in the right panel of Figure 5-8).

[2]Note that Figure 5-11 shows the standard-deviations, and not the variances.

[3]Although the correlations are estimated using highly over-sampled (but matched in angular-resolutions) images, the $\pm 1\sigma$ error bars on the correlation coefficients are estimated noting the effective number of independent image-pixels only. The large error bars for the bins at the brightest Stokes-I (> 32 Jy/Bm) reflect the poor statistics corresponding to an area largely confined to the brightest spot at the Western edge of Cas A.

Similar correlation profiles for the components of calibrated polarization vector (Q, U) are shown in the bottom two panels of Figure 5-10. Note that the spatial correlation of X-rays with the polarization vectors (as opposed to its magnitude) across the source survives at the level of the correlation with its magnitude, implying a nearly uniform orientation of the polarization vectors across Cas A. If there were a significant spread in PA across the source, it would have led to a correspondingly significant reduction in the magnitudes of the correlation with the vector components. Although the formal sign of the correlation with U is positive, it is still consistent with anti-correlation, considering that here the sign of U itself happens to be negative.

5.3 Faraday tomography of Cas A

Having established that the observed polarization is indeed intrinsic to Cas A, and not an artifact of the instrument or analysis, we processed the calibrated Stokes-Q and U- spectral data cubes to produce the dirty RM cube. The Faraday tomography revealed the brightest components of polarized emission along all Cas A lines-of-sight to be situated at an RM of $\sim +5 \pm 3$rad m^{-2}. The subsequent discussion would be based on the polarization emission components situated at this RM, unless otherwise mentioned.

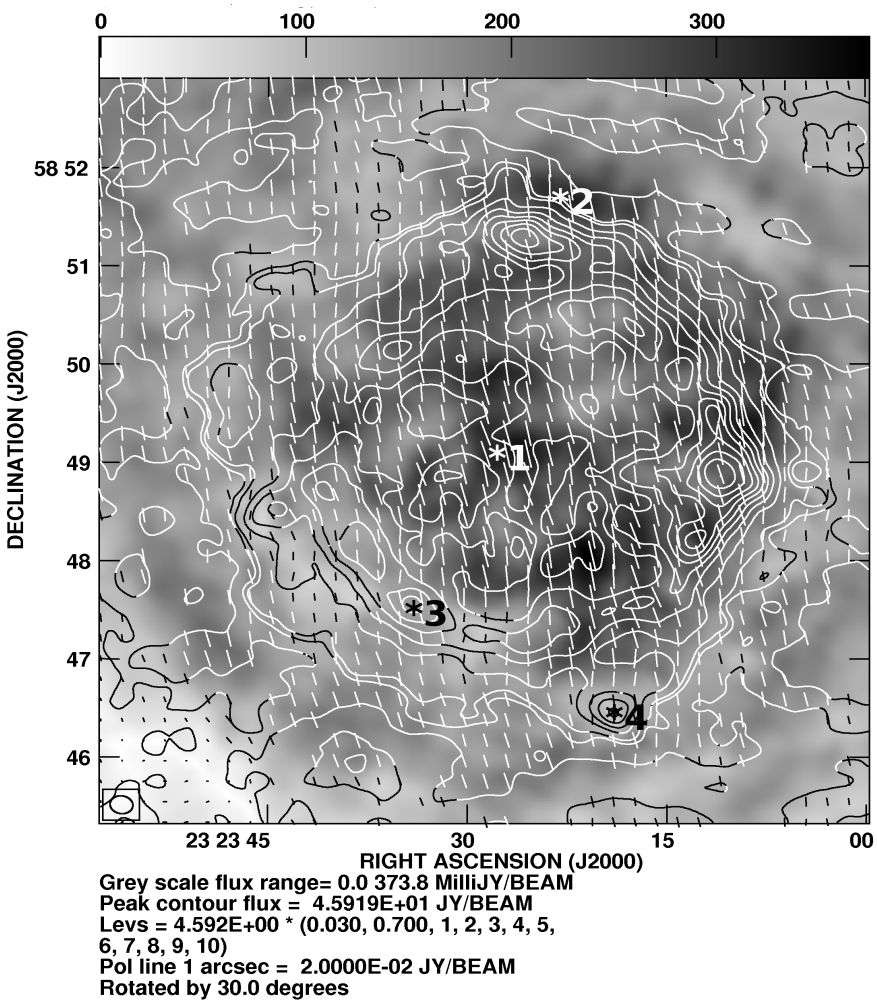

Figure 5-12: *Cas A linear polarization at 327 MHz. The grey scale represents the linearly polarized intensity, with overlaid polarization vectors. (The polarization angle reference is arbitrary.) The contours represent the Stokes-I intensity over the field. The asterisks marked in this figure are to show lines-of-sight along which a few representative tomographs have been presented later (Figure 5-14).*

Figure 5-12 shows the linearly polarized intensity (in grey scale) along with the polarization vectors for the image plane at RM = $\sim$ +5rad m^{-2}. As noted earlier, the polarized emission does not follow the intensity pattern in Stokes-I (shown as contours), and is mostly prominent in the central parts of the image, and the north-west. The spatial distribution is significantly different from that at 6 cm, where the

polarized intensity is distributed largely along the bright shell (Rosenberg, 1970).

One of the most surprising findings from our maps of polarized emission at 327 MHz is the near-constant orientation (rms spread $\sim 5^{\circ}$) of the polarization vectors across the source. This surprising feature is in marked contrast with the systematic PA variation seen at higher frequencies (Mayer & Hollinger, 1968; Rosenberg, 1970; Downs & Thompson, 1972; Gull, 1973; Braun et al., 1987; Jun & Norman, 1996).

The high degree of correlation seen between X-ray emission and the Stokes components, Q and U separately, also independently imply nearly uniform PAs across the source, and that possible polarized emission with significant variation in PA across the source, if any, is relatively small. Although their contributions cannot be separated readily, in regions where the relative PA differs significantly, their superposition would contribute to additional depolarization. Thus, if the emission associated with the radial field in Cas A (Mayer & Hollinger, 1968; Rosenberg, 1970; Downs & Thompson, 1972; Gull, 1973; Braun et al., 1987; Jun & Norman, 1996) were to be sufficiently strong even at the low frequencies of our observation, one would expect enhancement (or reduction) in the fractional polarization in regions where the radial vector is aligned in (or orthogonal to) the direction of the uniform orientation component. We looked for such a modulation in the azimuthal profiles of the degree of polarization for several annuli, including the ring, but found no obvious imprint of any superposed emission associated with a radial field.

The uniform orientation component, dominating the polarized emission across the remnant, implies an internal RM of $\sim +40$rad m^{-2} considering the RMs for the ISM in the foreground of Cas A, as estimated by Downs & Thompson (1972), is ~ -35 rad m^{-2}.

The radial profile of the fractional polarization (ratio of linearly polarized intensity to that of Stokes-I) corresponding to the dominant component at RM $= +5\ rad\ m^{-2}$ is shown in Figure 5-13. Close to the center of the remnant, the polarized fraction is about 2%. As would be expected, the polarization fraction is the least ($\sim 1\%$) within

the Faraday thick ring, while close to the edges of the remnant where the medium is Faraday thin, the polarized fraction increases, again as expected, reaching upto 5%.

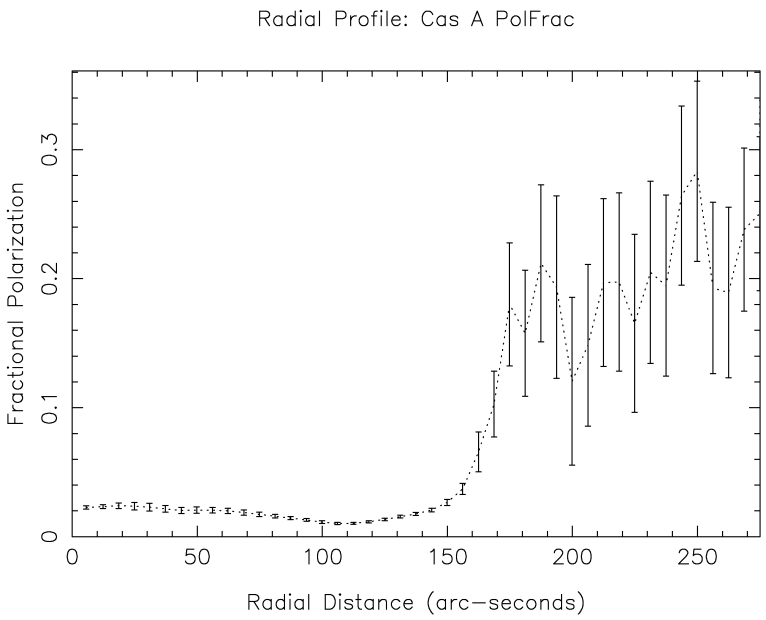

Figure 5-13: *Radial profile of the degree of linear polarization for the polarized component in Cas A at RM* $= +5$ rad m^{-2}.

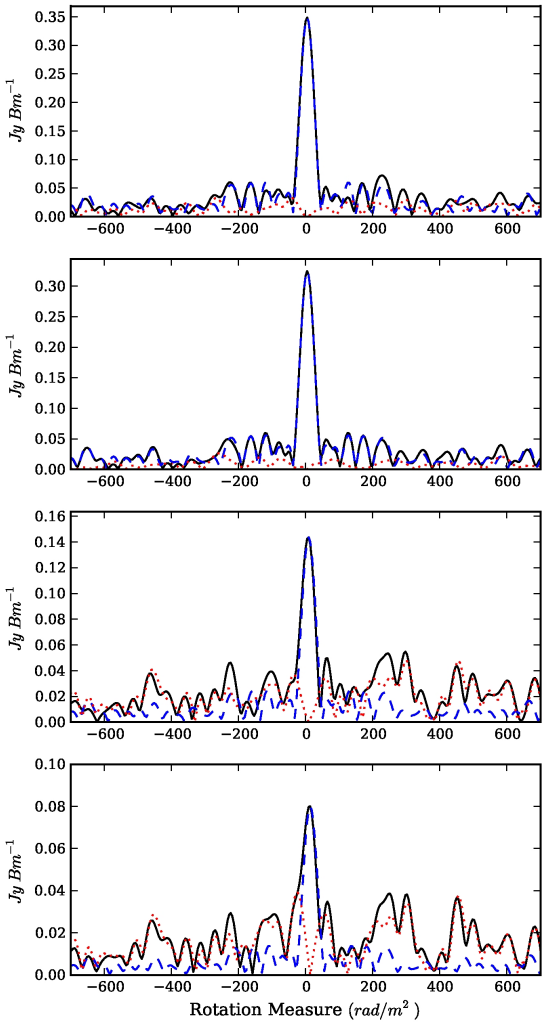

Figure 5-14: Faraday tomographs (solid lines) of Cas A along four different lines-of-sight. The corresponding locations on Cas A are marked in Figure 5-12, with the numbers corresponding to the panel-numbers here from the top. The feature at RM $\sim +5$ $rad\ m^{-2}$ is prominent in all tomographs, including those shown here. The "dirty" response corresponding to the brightest component in a given panel is shown by dashed lines. The residuals obtained after peeling off the strongest component are plotted as red dotted lines (see main text for details).

In Figure 5-14 we present the tomographs for four representative sight-lines marked in Figure 5-12. The residuals obtained by *"peeling"* off the strongest component at +5 rad m^{-2} using a complex version of Clean (following Högbom (1974), and suitably modified for cleaning 1-D tomographs, also accounting for gaps in λ^2 span due to RFIs), reveal significant polarized emission components even at higher Faraday depths. We show these tomographs to illustrate the potential for detailed probe of the distribution of the polarized emission. A detailed discussion of the individual features is beyond the scope of the current work. Some of the tomographs (*e.g.* the bottom two) reveal significant polarized emission from surviving components even at higher RMs with signal strengths $> 20\sigma_{expected}$ (*e.g.* at $\sim -25,\ +55,\ +300,\ +455$ rad m^{-2}).

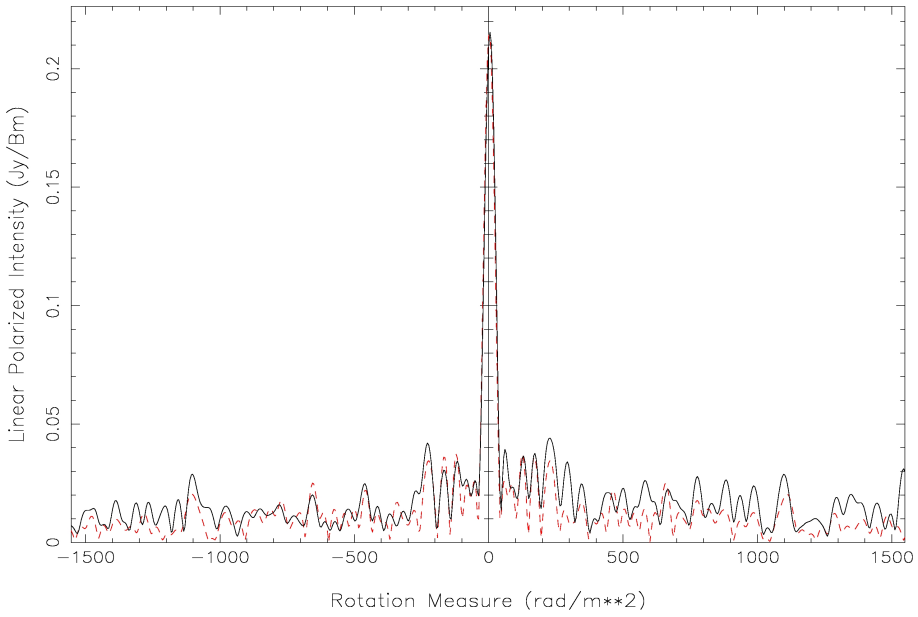

Figure 5-15: Distribution of average polarized emission of Cas A along RM. The dashed red line is the response of the brightest component at RM = +5 *rad* m^{-2}.

Even at Faraday depths where confusion from the brightest component at +5rad m^{-2} is negligible (*e.g.* at ~ -100 & $+298$ rad m^{-2} in the tomograph averaged over the face of Cas A; see Figure 5-15), the associated intrinsic PA is surprisingly largely uniform across the image. And although the polarized intensities at these RMs are found to be spatially correlated with Stokes-I, the degree of polarization however,

still shows significant anti-correlation with X-ray within the I-bins suggesting that at least part of the polarization is intrinsic.

The polarization maps at these two RMs are shown in Figures 5-16 and 5-18 respectively. Although the polarized intensities at these RMs are found to be spatially correlated with Stokes-I image, we do see significant anti-correlation between X-ray and linearly polarized intensity within the I-bins (Figures 5-17 & 5-19), suggesting that even at these Faraday depths part of the polarized emission is intrinsic to the source. Analysis of these maps at higher RMs are beyond the scope of this thesis.

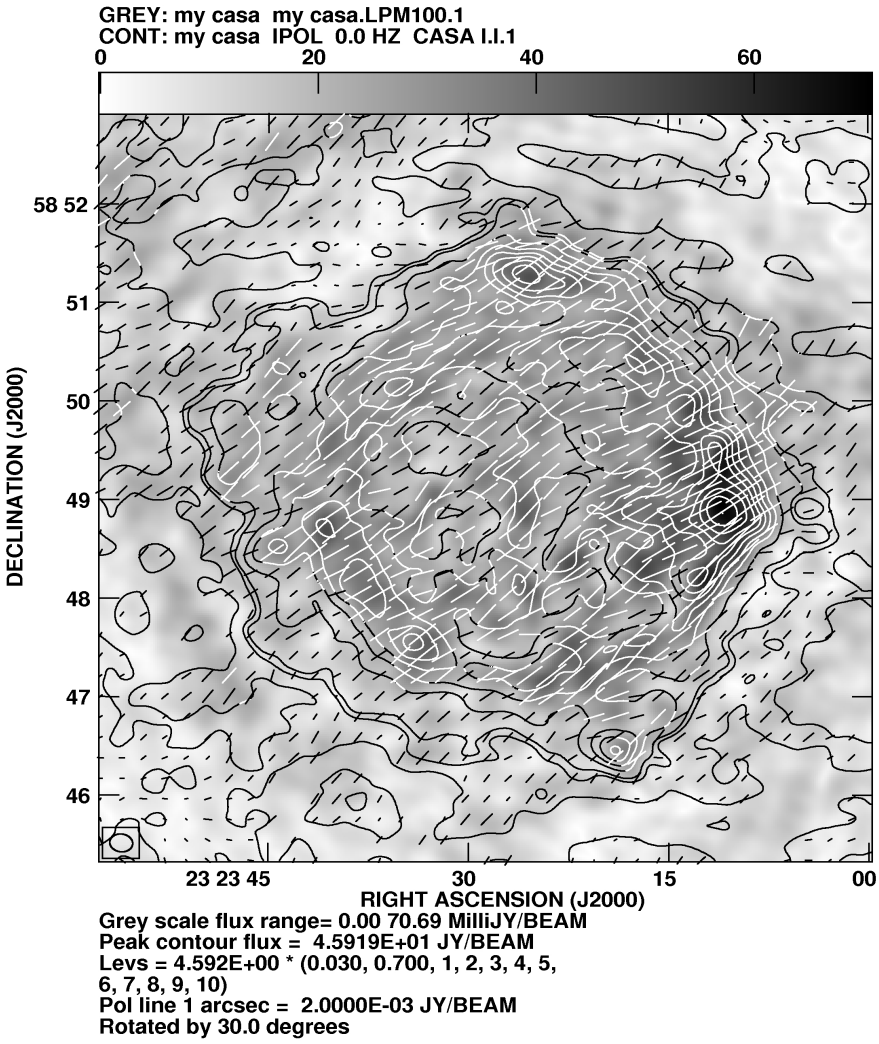

Figure 5-16: Image of Cas A at RM = –100 $rad\ m^{-2}$. The grey-scale represents linearly polarized intensity. The Stokes-I contours are overlaid for reference. Polarization vectors, whose lengths are proportional to the polarized intensity, and with orientations representing the polarization position angle, are also shown. The polarization angle reference is arbitrary.

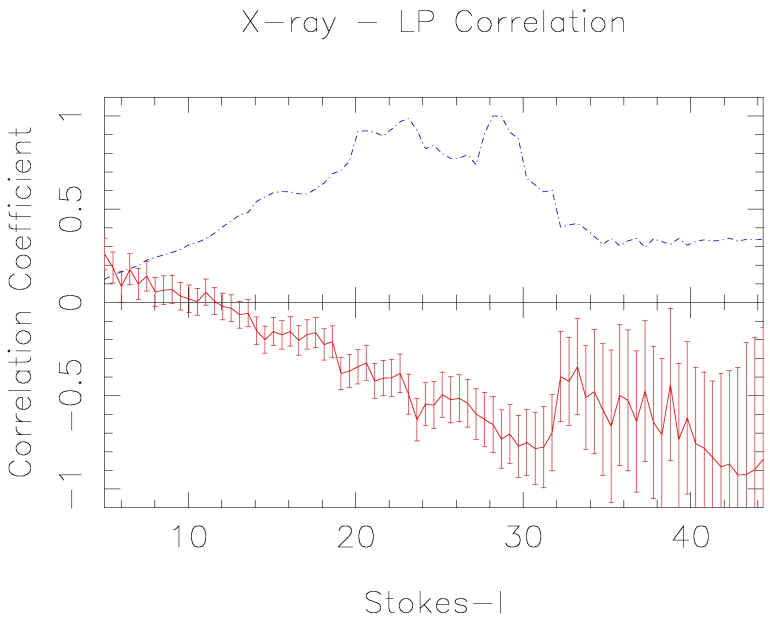

Figure 5-17: Correlation of linearly polarized intensity (at RM = -100 $rad\ m^{-2}$) with soft X-ray counts. For ready reference, the top profile shows relative variation in the average X-ray counts (normalised *w.r.t.* its peak).

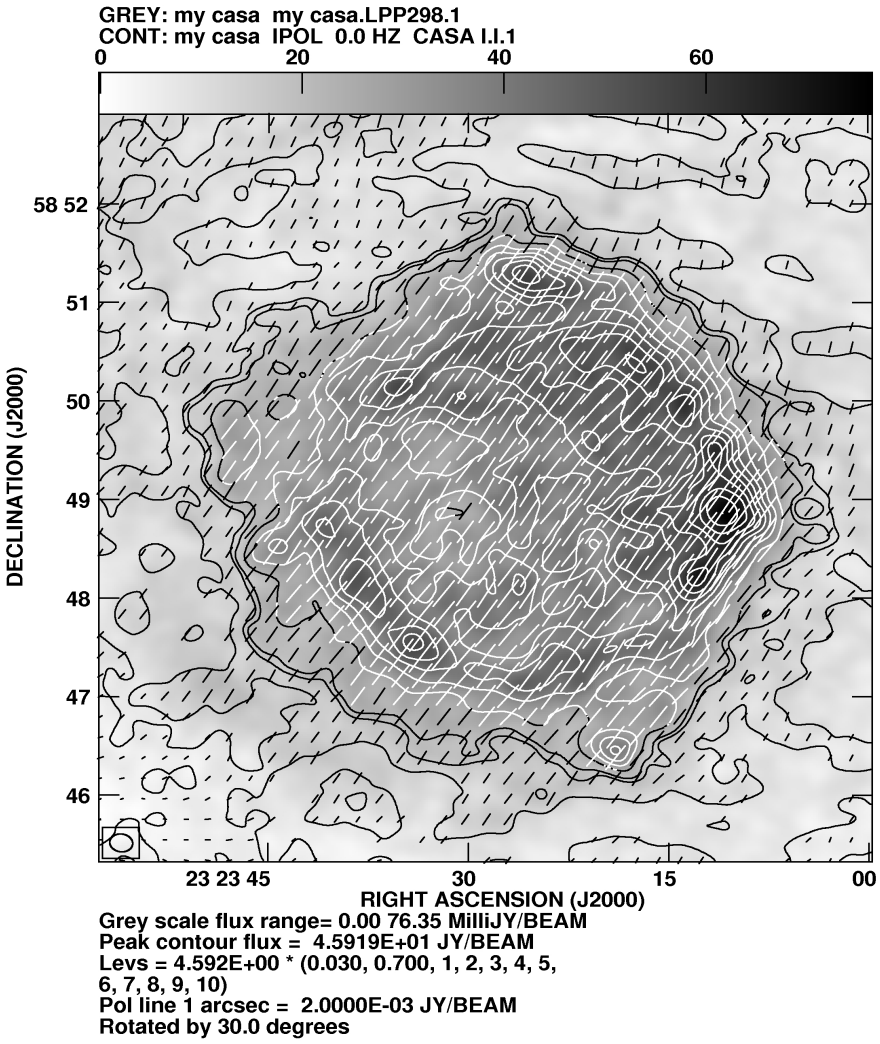

Figure 5-18: Image of Cas A at RM = +298 $rad\ m^{-2}$. The total intensity and polarization are represented as in Figure 5-16.

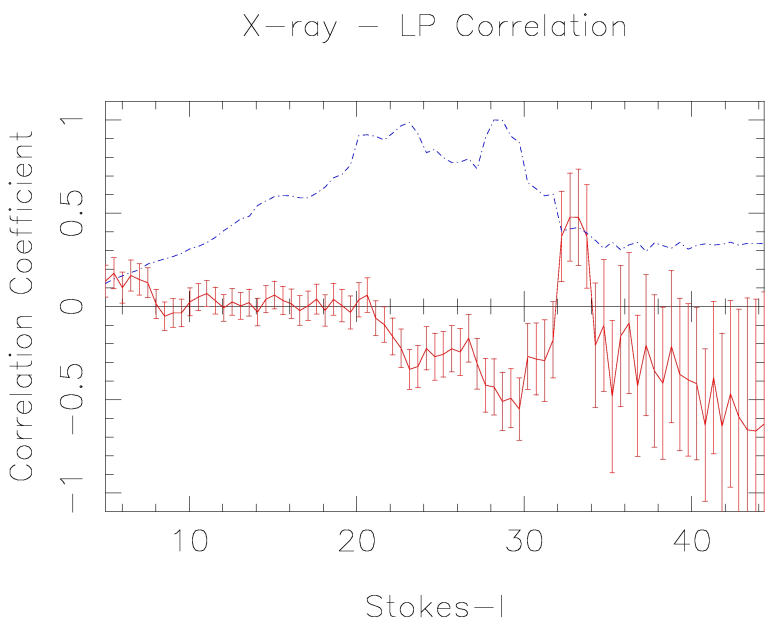

Figure 5-19: Correlation of linearly polarized intensity (at RM = +298 $rad\ m^{-2}$) with soft X-ray counts. The top profile is same as in Figure 5-17.

5.4 Modeling the 3-D thermal and non-thermal emissivities from Cassiopeia A

With the aim of understanding several of the intriguing revelations from the 327 MHz polarization study of cas A, we construct models of the 3-D distribution of thermal and non-thermal emissivities within the remnant. In constructing these models for the emission components, we impose the condition that their integrals along the lines-of-sight match the corresponding radial profiles in the "observed" images. Both the thermal and the non-thermal emissivities are modeled as spherically symmetric concentric Gaussian shells. The magnetic field is taken to be radial, as expected for young supernova remnants (Mayer & Hollinger, 1968; Rosenberg, 1970; Downs & Thompson, 1972; Gull, 1973; Braun et al., 1987; Jun & Norman, 1996), with the amplitude independent of the radial distance. Tangled or random component of magnetic field is not considered in our present model. The best-fit parameters of the model, viz., the number of shells, their radii (r, in units of R_{casa}), widths (w, in units of R_{casa})

and the emissivity (A, in the same units of intensity as that of the respective thermal and non-thermal maps), are obtained by minimizing the deviation between the radial profile obtained by integrating the modeled emission from each location along the line of sight, and the observed radial profile.

The observed non-thermal radial profile could be accurately reproduced using 4 shells with parameters (r, w, A) = (0.14,0.24,14.4), (0.21,0.13,703), (0.78,0.06,7.4) & (0.85,0.19,12.7) respectively The nominal Cas A radius is $R_{casa} = 150''$. Very high non-thermal emission in an inner shell located at 21% of R_{casa} away from the center of the remnant, is required to accurately reproduce the observed emission profile at smaller radii.

The 3-D distribution of thermal emission (soft X-ray) could be modeled using three shells with (r, w, A) parameters as (0.72,0.03,24), (0.80,0.05,20) & (0.98,0.12,4.8) respectively. There is little thermal emission from the inner parts of the remnant.

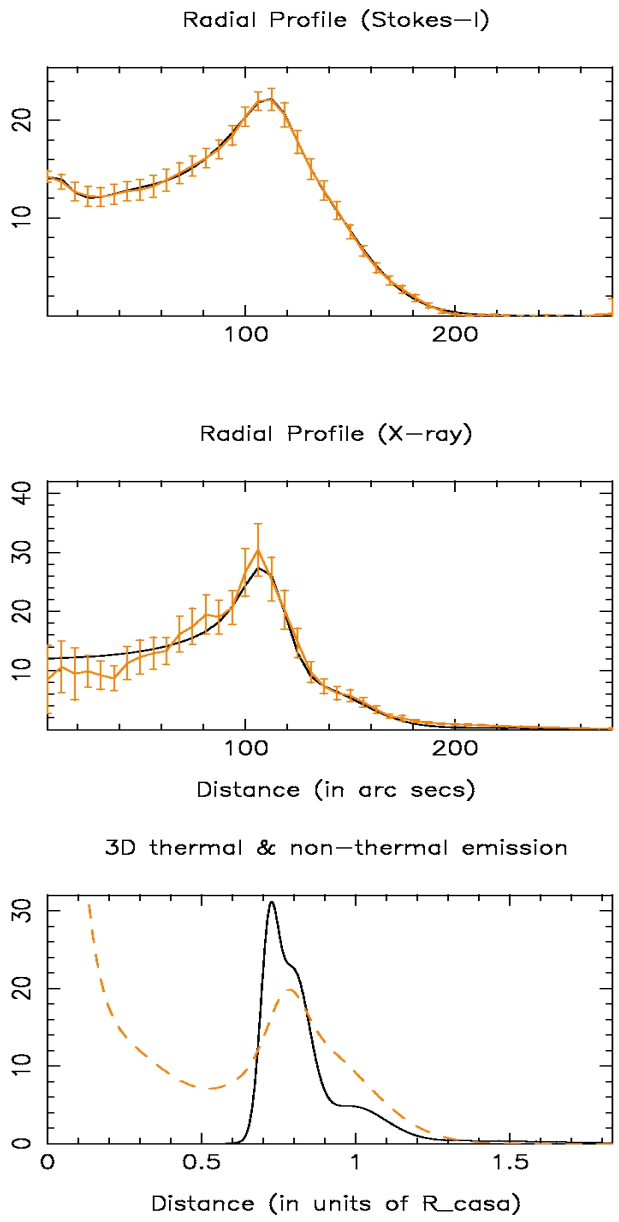

Figure 5-20: The top two panels show the observed (red solid lines) radial profiles for the observed emission as projected on the sky plane for the 327-MHz and the soft X-ray Chandra image respectively, with $\pm 1\sigma$ standard errors on the derived flux densities at any given radius. Similar radial profiles derived from the modeled emissivities are shown as black lines. The bottom panel shows the 3-D emissivities as a function of distance from the center of the remnant for the 327 MHz (dashed red line) and the soft X-ray data (solid black line). For ready comparison between the sky-coordinates in arc-seconds, and the physical dimension of the remnant, we have deliberately labeled the x-axis in the last panel in units of Cas A radius instead of arc-seconds (as in the first two panels). The radius of Cas A is taken to be $150''$.

The bottom panel of Figure 5-20 shows the 3-D distribution of thermal (solid line) and the synchrotron emission (dashed line) as a function of distance from the remnant's center. The resulting radial profiles of the projected emission on the sky-plane are overlaid on top of the corresponding observed profiles of radio (top panel) and the soft X-ray (middle panel). In modeling the synchrotron emissivity, the transverse component of the radial magnetic field is considered.

Figure 5-21 shows for a given radius, the cumulative emission from regions outside that radius, as a fraction of the total emission from the remnant. It can be seen that a considerable fraction ($\sim 25\%$) of both the thermal and the non-thermal emission comes from shells of radius greater than $150''$, which is also the nominal radius of Cas A. The implications of these are discussed in Section 5.5.

Detailed 3-dimensional modeling of Cas A using infrared and Chandra X-ray Doppler velocity measurements, can be found in DeLaney et al. (2010); Isensee et al. (2010). Since our aim here is to assess the magneto-ionic medium in Cas A only qualitatively, our simple models suffice for demonstrating the salient features of the remnant's 3-D magneto-ionic morphology.

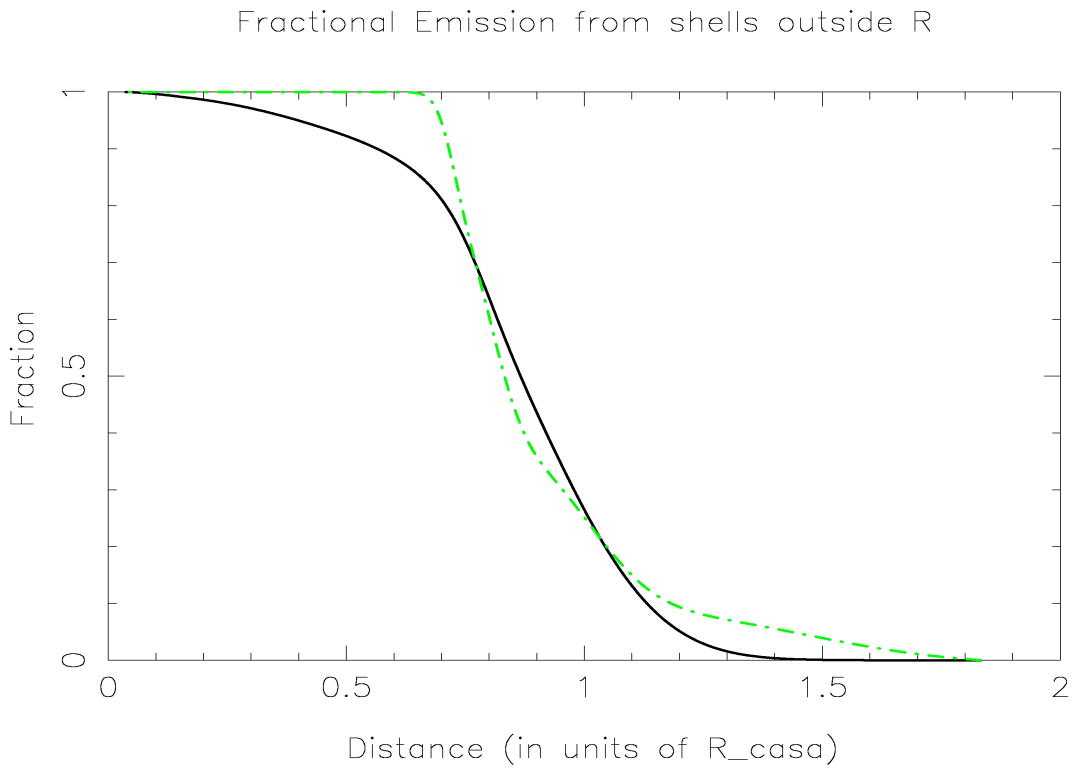

Figure 5-21: For a given radius, the solid line shows the cumulative emission from regions outside that radius as a fraction of the total non-thermal emission from the remnant. The dashed line shows the similar profile for the thermal emission.

5.5 Discussion & Conclusions

In its overall morphology, the 327-MHz Stokes-I image of Cas A appears similar to images at higher radio frequencies. The bright ring is prominent at a radius of $\sim 100''$ as would be expected, as also are the knots and the filaments. Comparison with the L-band image suggests regions of steeper spectral index along the outer edge of the remnant, as has also been reported in earlier studies.

The correlation of depolarization with soft X-radiation suggests that the non-thermal emission components responsible for the polarized intensity at 327 MHz must co-exist with the Faraday rotating thermal plasma within the source, consistent with the conclusions drawn from higher frequency data (Anderson et al., 1995). At higher

frequencies, where Faraday rotation and the associated depolarization in such mixed plasma are negligible, the PA corresponding to the magnetic vector is found to be oriented radially. This would be expected if the magnetic fields within the young remnant are also directed radially, as is believed to be the case in Cas A (Mayer & Hollinger, 1968; Rosenberg, 1970; Downs & Thompson, 1972; Gull, 1973; Braun et al., 1987; Jun & Norman, 1996). In general, for any spherically symmetric distribution of magneto-ionic material, the observed polarized emission can be shown to be dominated by a region closer to and symmetric about the mid-plane (*i.e.* the plane through the SNR center, orthogonal to the line of sight). Hence the observed orientation would reflect the field distribution close to the mid-plane, as well as the Faraday rotation both within and outside of the source. The near constancy of the PA observed across our 327-MHz image is therefore intriguing, and cannot be explained by a radial magnetic field distribution alone, unless Faraday rotation were to have a very special azimuthal dependence. This appears highly unlikely. Thus the constancy of the PA necessarily implies constant orientation of magnetic field in the region responsible for the polarized emission at 327 MHz. However, the region must lie within the "shell" of the remnant where the soft X-ray emission exists (Fabian et al., 1980). Such a field has not been reported in earlier studies of this young remnant.

The surviving polarization at high frequencies, resulting from frequency-independent depolarization due to irregular magnetic fields in Cas A, is about 7% (Downs & Thompson, 1972; Anderson et al., 1995), *i.e.* 10% of the maximum intrinsic value ($\sim$ 70%) expected for synchrotron emission. The average fractional polarization in our 327-MHz Cas A data is about 1.5%. The additional depolarization at these low radio frequencies would be expected from Faraday depolarization internal to the source (Downs & Thompson, 1972; Anderson et al., 1995). If the magneto-ionic medium in Cas A is considered to be distributed in a "uniform slab" (Burn, 1966; Sokoloff et al., 1998) an RM of $\sim +3\ rad/m^2$ would be required to produce the depolarization apparent at our observing band. Adopting values of magnetic field ($\sim 200\ \mu G$) and free electron-densities ($\sim 2\ cm^{-3}$) in Cas A from Downs & Thompson (1972), the physical length corresponding to an RM of $\sim +3\ rad\ m^{-2}$ is only about 0.01 pc,

which is about 0.25% of the Cas A diameter. Given that the polarization position angle is constant across the entire image, it is unlikely that the polarized emission surviving at the low radio frequencies of our observations would have a distribution along the remnant's depth, and it must have its origin within a thin shell at the outer surface of the SNR.

To check whether the polarized emission at 327 MHz can originate from the outermost regions of the remnant, and as described in the earlier section, we constructed spherically symmetric 3-D models for, a) the synchrotron non-thermal emissivity so as to match the observed radial profile of Stokes-I intensity, and b) the X-ray emitting thermal plasma, consistent with the radial profile derived from the Chandra soft X-ray map. The flux density contributed from the outermost layers of Cas A ($radius > 150''$), the emission from which is expected to suffer minimum depolarization, is sufficiently high ($\sim 25\%$ of the total) to account for the polarized component seen in our 327-MHz image, even if the depolarization factor locally is ~ 10. Furthermore, there is also significant X-ray emission ($\sim 25\%$), even beyond the nominal Cas A radius of $150''$, implying a possible depolarization imprint on the radio emission from these outer regions. This is consistent with the anti-correlation seen between soft X-ray and the 327-MHz polarized intensity. The cumulative emission profile (Figure 5-21) for the soft X-ray extends beyond that for Stokes-I, and these outermost regions could account for an apparent "internal" RM ($\sim +40$ rad m^{-2}) without further depolarization.

Another puzzling aspect is that the fractional polarization ($\sim 0.3\%$) reported at L-band (Anderson et al., 1995) is less than that seen in our 327-MHz data. The polarized intensity at 327 MHz is seen to have little structure within the $5'$ extent of the source. Hence, inadequate sampling of the short uv-spacings could, in principle, render the data less sensitive to such uniform polarized emission. Although the polarization imaging of the remnant at L-band by Anderson et al. (1995)[4] is expected to have the necessary short spacings, it is not clear if the short spacing data were "flagged" out for reasons pertaining to poor data quality (for example, corruption due to van

[4]using VLA data including in the D-configuration (Braun et al., 1987)

Vleck bias that affected the short spacings in a similar data set Anderson & Rudnick (1995)).

The fact that even the earlier single-dish observations (Mayer & Hollinger, 1968) do not show any hint of the polarized component with uniform orientation might appear consistent with the above mentioned interferometric observations. In contrast to this, however, a recent survey of the Galactic plane by Sun et al. (2011) at 6 cm indeed reveals a uniform magnetic field across Cas A, as well as across several other SNRs in the survey sample. It is not surprising that the polarization orientation that Sun et al. (2011) see is uniform, given their angular resolution to be $9.5'$ at which Cas A remains unresolved. What is really surprising to us is that, even after possible depolarization due to vector averaging of polarized emission within their wide beam, Sun et al. (2011) see a surviving polarized component of about 36 Jy at 6 cm, which intriguingly matches the integrated polarized flux density reported at the same wavelength from observations (Rosenberg, 1970; Downs & Thompson, 1972) with significantly higher angular resolution (and hence correspondingly much less beam depolarization). Given that in the latter case the association of the polarized emission is with a radial morphology of the magnetic field, a significant mismatch should have been seen in the mentioned flux densities. These apparent discrepancies remain to be resolved, but if we were to compare our observation with that by Sun et al. (2011), the implied spectral index for the polarized flux density appears to be much flatter than that for the Stokes-I intensities.

To summarize,

1. Despite the expected severe depolarization, our GMRT observations reveal detectable polarized emission from Cas A at 327 MHz.

2. The RM of the dominant component in the Faraday tomographs is found to be $\sim +5 \pm 3$ rad m^{-2}, along with weaker components at higher RMs.

3. The lack of correlation between the polarized intensity and Stokes-I rules out any instrumental origin of the observed polarized component. A clear anti-correlation of the degree of polarization with soft X-ray emission, assessed

through a novel binning method, provides additional support for the polarization being intrinsic to the source.

4. The dominant polarized emission component shows a nearly constant PA[5] across the remnant, with only a small dispersion ($\sim 5^\circ$) in the PA. This constancy of the PA is intriguing and is in direct contrast with the PA distribution apparent in earlier studies of the remnant at higher frequencies.

It is clear that the depolarization at the lower frequencies is due to wavelength-dependent Faraday rotation within the source, and the suggested field strength & free electron densities (Downs & Thompson, 1972) imply that the non-thermal emission from inner radii is likely to be almost completely depolarized, possibly erasing any memory of the internal field structure. But for the possibility that the observed polarized emission originates from the outer regions of the source, where the magnetic field orientation is uniform, it is difficult to explain together, the PA constancy and the polarized fraction apparent in the 327 MHz observation.

The near constancy of the PA associated with the polarized emission could in principle be a manifestation of compressed ambient uniform magnetic field as a result of an expanding spherical shell (van der Laan, 1962). As the remnant continues to expand, the shell could be disrupted by possible density inhomogeneities encountered within the volume swept by the ejecta. Nonetheless, the orientation of the field apparent to us in projection would continue to be more or less uniform. For the apparent PA to remain constant across the face of the source, the Faraday screen in front of the regions of polarized emission however needs to be uniform. Finer structures resulting from the Rayleigh-Taylor (RT) instabilities in the outer regions of the remnant, unresolved at our angular resolution, are unlikely to cause any significant non-uniformity in the local Faraday screen, given the narrow sizes of the RT *fingers* combined with their small occupancy fraction. In this more likely picture, our observed polarized emission originates from outer layers of the shell, wherein the PA

[5]While the relative orientations or PAs are reliable, the absolute reference PA has not been calibrated.

uniformity is dictated by that in the compressed ambient magnetic field. If indeed this is the case, then we expect the orientation of the magnetic field suggested by our polarized component to match that of the galactic plane (assuming of course that the ambient field to be parallel to the galactic plane).

There is one intriguing aspect we wish to note below, particularly since it might be suggesting a different, and rather interesting, origin for the observed polarized emission and its PA uniformity. The distribution of polarized intensity, relative to that of Stokes-I, in our 327 MHz maps (Figure 5-12) shows a significant spatial offset in approximately North-West direction, about which the somewhat patchy spatial distribution of polarized intensity is also roughly symmetric. Although the x-ray intensity in some parts of the South-East sector, devoid of polarized emission, is high, lack of a strict correspondence within this sector itself (and also across the source) makes it unlikely for any selective depolarization in this wide region to be the explanation for the truncated morphology apparent in our polarized intensity image. Such a morphology is strikingly reminiscent of shapes and structures associated with pulsar wind nebulae (PWN) (Rees & Gunn, 1974; Radhakrishnan & Deshpande, 2001; Dodson et al., 2003). Indeed, there have been reports relating to the possible existence of a compact remnant in Cas A (*e.g.* Hwang et al. (2004)). As discussed by Rees & Gunn (1974), owing to the rotation of the compact star, the resultant configuration of the magnetic field (carried along with the particle flow) well outside the so-called light-cylinder would essentially be toroidal. This would naturally imply significant uniformity in PA associated with the polarized emission expected from such a nebula driven by the wind from the compact object. The level of PA uniformity however depends on our viewing geometry (*e.g.* Rees & Gunn (1974); Dodson et al. (2003)).

The proper motion of the compact object (indicated by the red arrow in Figure 5-22) as estimated by Pavlov et al. (2000) & Thorstensen et al. (2001), and shown by the red arrow in Figure 5-22, is also interestingly roughly aligned along this implied rotation axis as would be expected for young pulsars (Harrison & Tademaru, 1975;

Johnston et al., 2005; Lai et al., 2001). This provides additional support for the exciting prospect of a pulsar wind nebula in the young remnant Cassiopeia A.

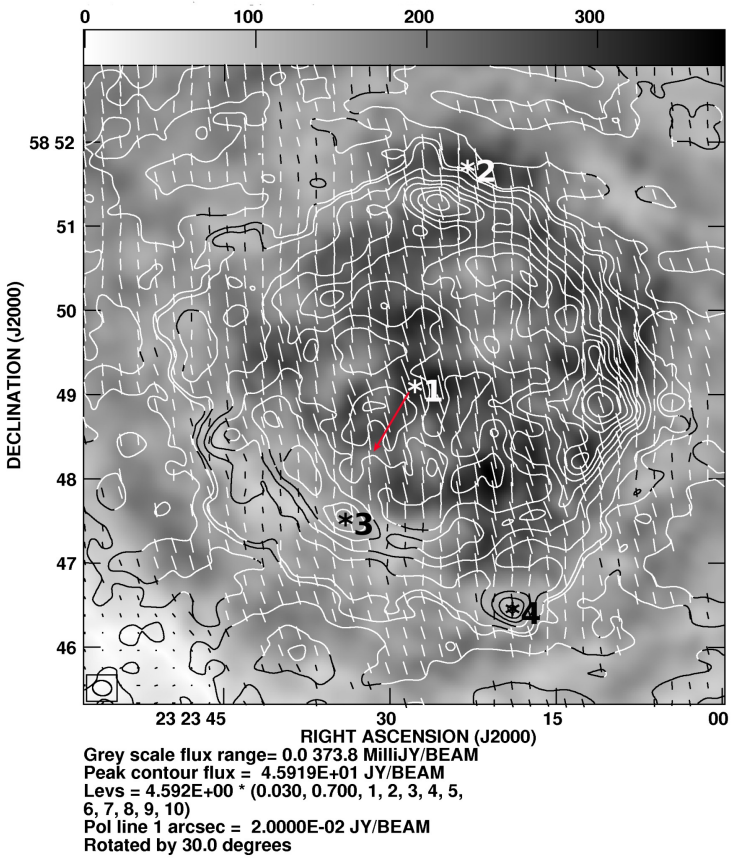

Figure 5-22: The 327 MHz GMRT Stokes-I image of Cas A: contours are for Stokes-I, while grey scale depicts the linearly polarized intensity. The polarization vectors are also overlaid. The proper motion of the central compact object is shown by the red arrow.

While these expectations could in principle offer an attractive and consistent model for the observed polarized emission, we have no indication yet for the possible existence of such a PWN in Cas A, and neither of a pulsar. In the standard picture of a fully developed PWN (Rees & Gunn, 1974), the compact object is surrounded by a compact cavity. The sustained energy input includes both, the magnetic dipole radiation and the collimated relativistic particle flow from the central object (Rees & Gunn, 1974; Radhakrishnan & Deshpande, 2001). This and the characteristics of the surrounding together dictate the size and the shape of the cavity. For a very young

object such as Cas A, the centrally located pulsar-like object is unlikely to be surrounded yet by a compact cavity, and hence a compact nebula is yet to be born. If a highly magnetized and fast rotating neutron star does indeed exist in this SNR, then the energy input in the forms mentioned must be operative, regardless of whether or not the compact object reveals itself as a pulsar (including the considerations of viewing geometry required for it to be *visible*). Thus, we might be witnessing a rare phase of *a young nebula in making*!

In our understanding, the compact cavity is not created by any explicit clearing of immediately surrounding matter, but rather by filling the extended SNR cavity inwards to the extent determined by the pressure balance as detailed in Rees & Gunn (1974). At the present epoch, the SNR cavity may be just beginning to be filled, as the relativistic particles streaming out from the pulsar's magnetic poles (Radhakrishnan & Deshpande, 2001) would travel largely unhindered till they encounter the dense shell at the inner boundary of the SNR, and thus the nebular emission may be yet confined to inner layers close to the SNR shell. The magnetic field accompanying the particle flux is deposited and thus enhanced at these inner boundaries that are expected to progressively shrink. The toroidal morphology of this field when viewed by us in projection would appear to have largely uniform orientation, as long as the angle between the rotation axis and our sight-line is large (as in the cases of the Vela and the Crab PWNe, see for example, Dodson et al. (2003); Deshpande & Radhakrishnan (2007)).

If the polarized emission we observe in Cas A is indeed from a yet forming PWN associated with a central compact object, the projection of its rotation axis on the sky plane must align with the axis of symmetry in the spatial distribution of the polarized emission, *i.e.* along NW-SE direction. The observed uniformity in PA (see Figure 5-22)[6] implies suitably large inclination of the rotation axis with our sight-line,

[6]We wish to recall again, that the relative orientations are reliable, but the absolute value is not calibrated as mentioned earlier.

and also that relevant foreground Faraday rotation variation across the source size is small. Although further investigation would be necessary before attributing origin of the observed morphology of the polarized emission in Cas A at 327 MHz to a possible PWN in making, formation of a wind nebula in Cas A (and its emission contribution) seems unavoidable if the central compact remnant happens to be a pulsar.

In any case it would be of importance to know whether the necessary field with uniform orientation corresponds to the compressed version of the ambient field (van der Laan, 1962) or to any coherent component of the field internal to the source, including that associated with a radio wind nebula powered by a compact remnant (Dodson et al., 2003). Follow-up observations at intermediate radio frequencies (particularly at 610 MHz) with the GMRT would help clarify several of these intriguing features seen at 327 MHz, and might also pave way for useful quantitative inferences.

Chapter 6

Slicing Faraday-thick components: tomography using multi-band data

In Chapter 2 we have discussed the considerations in spectral sampling for Faraday tomography experiments. In designing the observations, one must also consider inherent depolarization within the relevant *resolution elements*. The resolution elements in the RM and the two angular coordinates are given by:

$$\delta RM \propto \frac{1}{\lambda^2(\frac{d\nu}{\nu})} \tag{6.1}$$

$$\delta^2\theta_{sky} \propto \lambda^2 \tag{6.2}$$

The *volume resolution element* would therefore be:

$$\begin{aligned} \delta V &\propto \delta RM \times \delta^2\theta_{sky} \\ &\propto \frac{1}{\left(\frac{d\nu}{\nu}\right)} \\ &\propto \frac{1}{\lambda d\nu} \end{aligned} \tag{6.3}$$

which is inverse of the fractional bandwidth. Thus, depolarization within the element volume can be expected to decrease with increasing fractional bandwidths.

For a fixed band-width and a fixed telescope aperture, the depolarization would be lesser at longer λs. Thus, observations at longer wavelengths appear favourable both in terms of enhanced resolution along RM as well as minimal overall depolarization. However, resolving Faraday-thick features (*i.e.* large scale feature in RM domain) along the line-of-sight is facilitated by measurements at shorter wavelengths (Brentjens & de Bruyn, 2005; Brentjens, 2007). In Faraday tomography, the shortest wavelength dictates the sensitivity to the largest RM-scale over which the polarized emission is distributed along a sight-line:

$$\text{max RM scale} \sim \frac{1}{\lambda^2_{min}} \tag{6.4}$$

In order to be able to detect extended emission along RM, observations must include adequately short wavelengths.

Ideally therefore, an observation should include the shortest wavelengths covering as wide a spectral span, with as fine a sampling in λ^2, as possible. However there are practical limitations in realizing such wide-band systems. Moreover, storage and analysis of the huge data volume resulting from such wide-band systems would be non-trivial. The presence of strong RFIs in certain bands makes it difficult for one to utilize the entire wide band in any case. An optimal alternative therefore, would be to sample a wide spectral region in a non-contiguous manner, selecting portions of the spectra that are minimally contaminated by RFIs. The many advantages of such a multi-band system has been discussed and demonstrated by Maan et al. (2013). Although the system described by Maan et al. (2013) allows simultaneous observation at the different bands, Faraday tomographic studies of the Galactic continuum emission does not crucially depend on this "simultaneity" feature.

The difficulty however lies in the ability to interpret the *dirty tomograph* obtained

through Fourier inversion of such linearly polarized spectra that has been sparsely sampled in λ^2. This is because, sparse sampling with large gaps in λ^2 would lead to higher side-lobe levels for the point-spread function or the convolving response function (*dirty RM-beam*) in the RM-domain, and hence would result in confusion in finding the true distribution of the polarized components across RM. These artifacts are similar to the features encountered in *dirty images* of interferometric data having incomplete/sparse *uv-coverage*. The effect of such artifacts in a dirty image are cured using deconvolution techniques, one of the most widely used being the *Hogbom Clean*. For Faraday tomography, we have developed a one-dimensional complex version of Hogbom clean that takes into account the uneven sampling[1] in λ^2. This chapter demonstrates the feasibility of these new tools for Faraday slicing polarized radio sources with enhanced sensitivity towards large-scale structure in RM, as well as with enhanced RM-resolution.

We would like to note here an important issue when the analogy of Faraday tomography with interferometry may be extended a little further – measurement at $\lambda^2 \rightarrow 0$ is very similar to measurement of the zero spatial frequency in interferometry. Much like the zero spatial frequency measured by a single dish provides information about the total power received, measurement at $\lambda^2 \rightarrow 0$ would provide the "net" polarized flux (vector) along a line of sight, *i.e.* at all RMs, but without any modification due to Faraday rotation. We would like to point out however that unlike in the case of the total power, which is a scalar quantity, the linearly polarized intensity $(\mathrm{Q} + \mathrm{iU})$ is a vector. Hence the net polarized flux for a given sight-line, obtained using measurement at $\lambda^2 \rightarrow 0$ does not guarantee measurement of the "total" polarized flux along the line-of-sight. Depending on the spread in the orientations (*i.e.* PAs) of the linearly polarized emission components and their intensities within a given synthesized beam, the observed polarized flux at $\lambda^2 \rightarrow 0$ could be anything between 0 & $\mathrm{P_{max}}$, where $\mathrm{P_{max}}$ is the sum of the amplitudes of polarized intensity vectors of

[1]Such a clean was already developed and successfully used for unevenly sampled pulsar timing data by Deshpande et al. (1996) in their study of pulsar timing noise, requiring very high dynamic range reconstruction.

the individual components within the beam. This depolarization along the line-of-sight is unavoidable even at $\lambda^2 \rightarrow 0$. Similarly the "net" polarized intensity vector even at $\lambda^2 \rightarrow 0$ can, in principle, have any orientation. Therefore absence of the sample at $\lambda^2 = 0$ is not a handicap in the present context.

6.1 Fourier inversion of the polarized spectra & deconvolution of the dirty tomograph: Demonstration using simulations

With the aim of performing Faraday tomography (RM synthesis) using data sparsely sampled in λ^2, we used DFT for the Fourier inversion of the polarized spectra as against FFT that inherently requires uniform sampling of the λ^2 space. In principle, one could re-grid the data into uniformly spaced λ^2s (Heald et al., 2009). However, the strategy of using traditional DFT for inverting unevenly spaced λ^2s allows us to readily combine data observed at widely separated frequencies and with different channel widths. Such a scheme would be useful even for single band data. In general in the cases of large gaps between bands or when contamination of significantly large contiguous parts of a given occurs due to RFIs, it is advantageous to treat those spectral regions as unmeasured, rather than interpolate, since such interpolation could be very un-reliable.

We have also discussed in Chapter 2, as also in the previous section, a deconvolution scheme (RM-clean) appropriate for data unevenly sampled in λ^2. In the following sub-sections we demonstrate the feasibility of our RM-clean algorithm using simulated data, and also present preliminary results of the tomography performed by combining L- and P-band data from the GALFACTS pilot region observed with the Arecibo Telescope.

6.1.1 Description of the simulations

For the purpose of demonstrating the potential of Faraday tomography using multi-band data, we show here simulated polarized spectra for a line-of-sight having an unresolved component along RM-axis, as well as a Faraday-thick component of emission extended in RM. The extended feature is modeled as a top-hat function along RM. For simplicity, we assume both the sources to be point-like in the angular domain. The parameters of observations are listed in Table 6.1, while the input parameters for the simulated sources are shown in Table 6.2.

Table 6.1: Assumed observation parameters for multi-band tomography simulation

Band	ν_c (MHz)	$\Delta\nu$ (MHz)	$\Delta\lambda^2$ (m^2)	λ^2_{min} (m^2)	δRM ($rad\ m^{-2}$)	$max\ RM\ scale$ ($rad\ m^{-2}$)
P	300	30	0.201	0.907	15.6	3.6
L	1200	120	0.013	0.057	250.1	55.4
P+L	-	-	0.214	0.057	14.7	55.4

Table 6.2: Assumed source parameters for multi-band tomography simulation

Source type (at P band)	Source type (at L band)	RM ($rad\ m^{-2}$)	Amplitude ($\frac{Jy}{rad\ m^{-2}}$)	$PA_{intrinsic}$ (Deg)
Un-resolved	Un-resolved	-100	15	0
Resolved	Un-resolved	100-130	5	0

6.1.2 Faraday tomography simulation at a single high frequency band: poor RM resolution

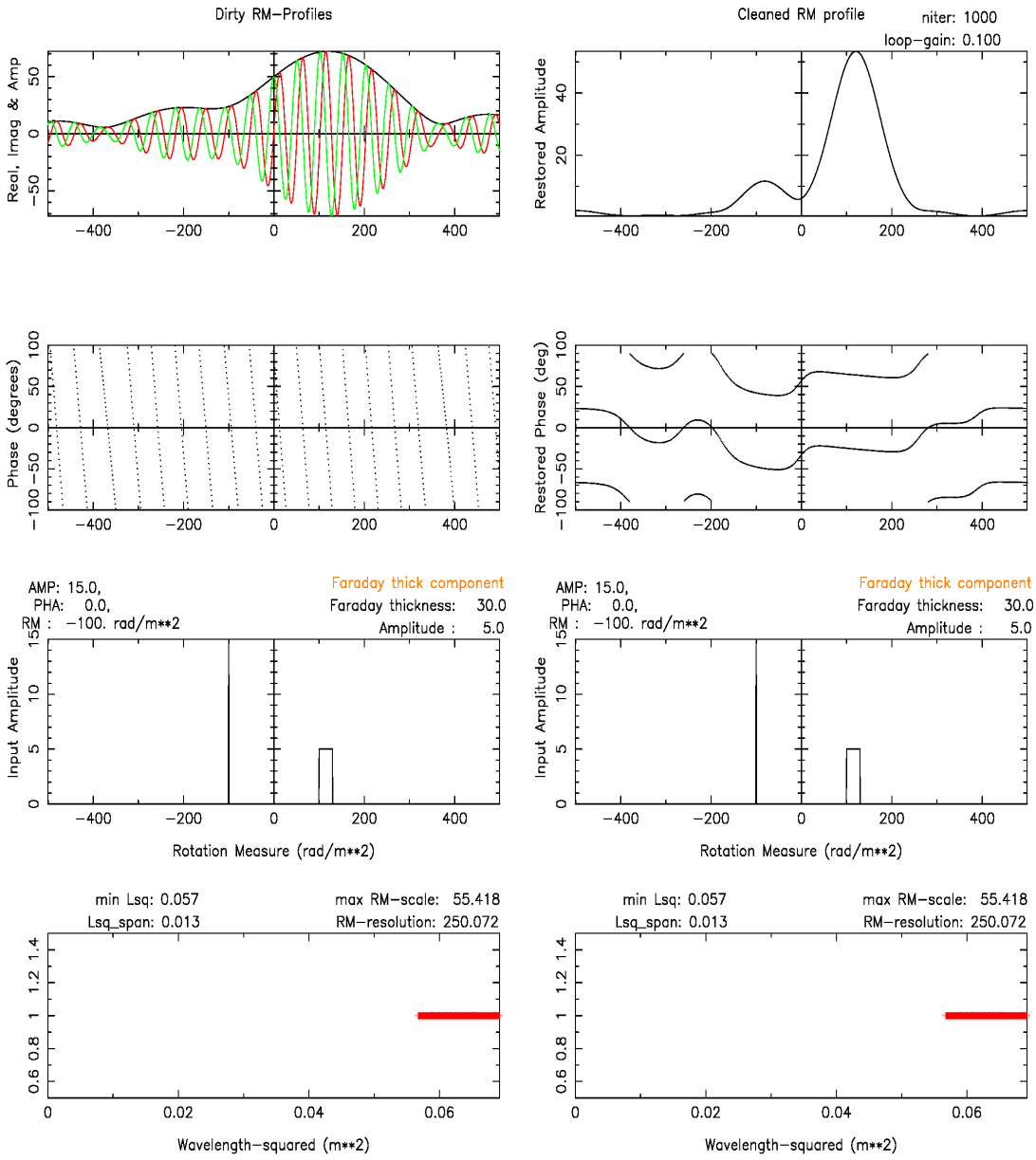

Figure 6-1: *Faraday tomography simulation at the high frequency L-band: The top two panels on the left column show the amplitude and phase of the dirty tomograph. The 3rd panel from top shows the input polarized emission structure along RM used in the simulation. The bottom panel shows the λ^2 coverage for the observations. The right column shows the same quantities but corresponding to "clean"-ed and restored profile. The bottom two rows have redundancy in the plots shown.*

Figure 6-1 shows the result of Faraday tomography performed at the L-band, with simulated data. The top two panels in the left column shows the dirty tomographs while the top two panels of the right column shows the tomographs after "RM-clean"-ing and "restoration" using a Gaussian of FWHM equal to the RM-resolution at the L-band (see Table 6.1). The true components along RM are shown in the 3rd panels from top. The bottom panels show the λ^2 coverage.

The amplitude for the true input components (3rd panels from top) are expressed in units of *Jy per unit RM* while the amplitudes for the dirty and the clean-ed components are expressed in units of *Jy per unit RM-beam*.

For these simulations, the RM-resolution (δRM) at the L-band is about 250 rad m^{-2}, which is larger than the maximum RM scale of 55 rad m^{-2} allowed by the minimum λ^2 within this band. The extended source remains un-resolved as would be expected.

6.1.3 Faraday tomography simulation at a single low frequency band: Poor sensitivity to extended structure

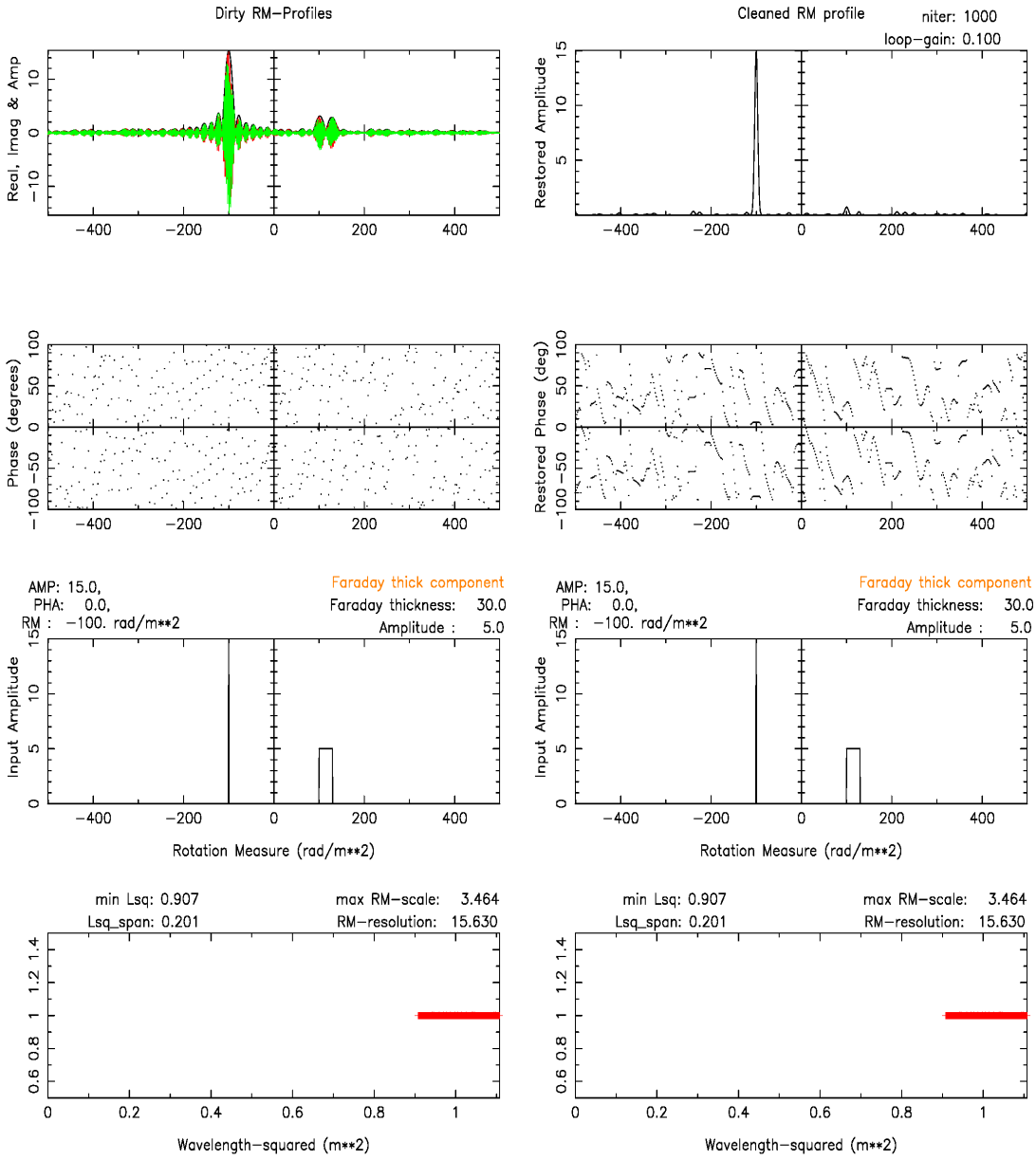

Figure 6-2: *Faraday tomography simulation at the low frequency P-band. The panel description is same as in Figure 6-1.*

Figure 6-2 shows the result of Faraday tomography performed at the P-band using simulated data. The RM-resolution at this low frequency is high enough for resolving

the extended emission component. However, lack of data at sufficiently short λ^2 values makes these observation insensitive to the extended emission along RM. The cleaned tomograph shows no significant trace of the extended feature. The amplitude as well as the RM corresponding to the point-like source however is retrieved reliably.

6.1.4 Faraday tomography using multi-band data: L- and P-band data combined

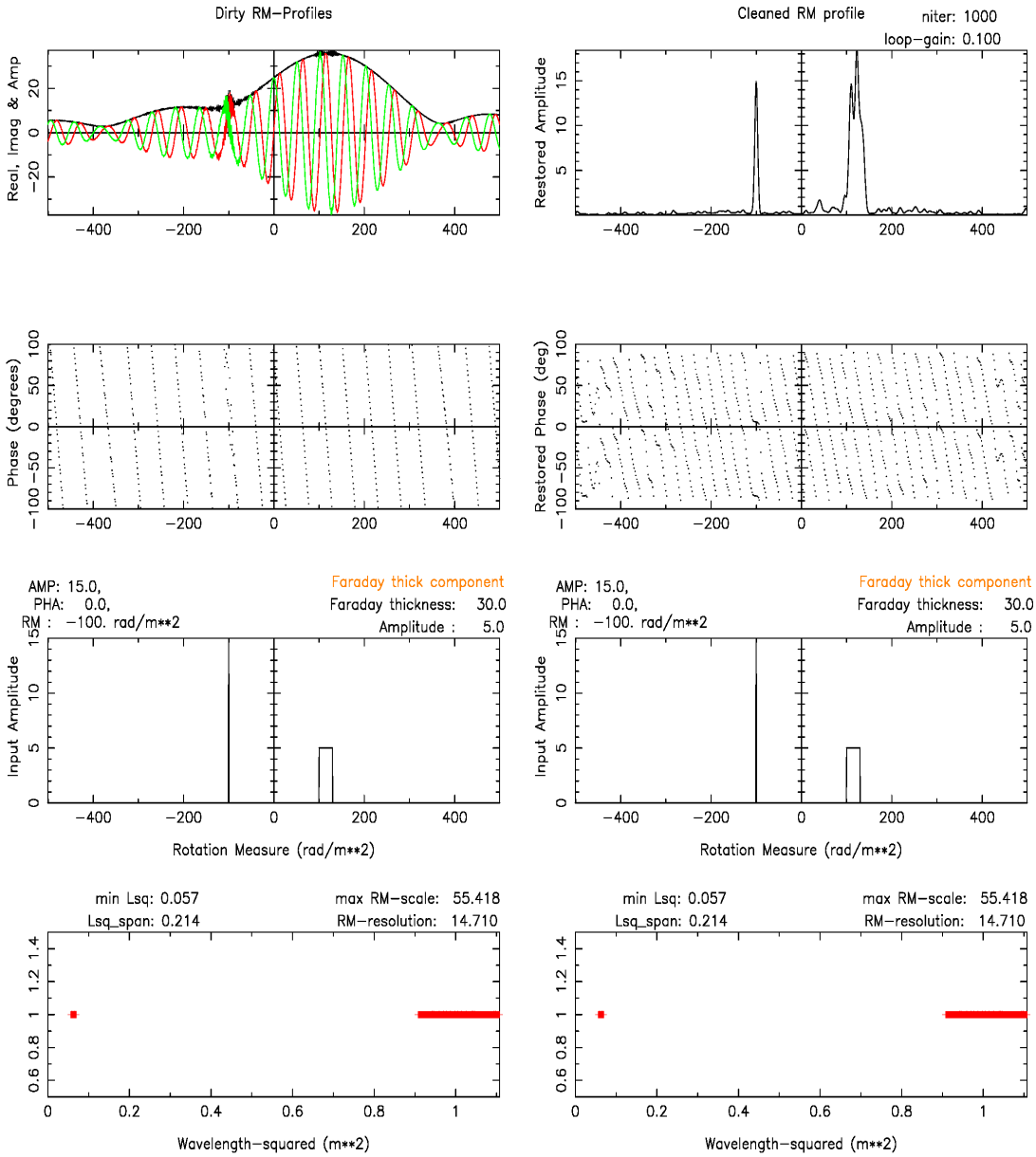

Figure 6-3: *Faraday tomography simulation of multi-band data. The panel description is same as in Figure 6-1.*

Figure 6-3 shows the result of Faraday tomography performed by combining the L-band and the P-band data. The spectra have been assumed to be flat in these sim-

ulations. We would like to point here that the RM-resolution is not governed merely by the separation between the minimum and the maximum λ^2 sampled. The effective RM-resolution is provided by the sum of the λ^2-spans at the two individual bands. Since in these simulations we have kept the ratio of the band-width to the center frequency of observation **constant** ($\sim 1:10$, which is what is the typically achievable value for most telescope systems in operation), the λ^2-span at the higher frequency L-band would be much smaller than that at the low frequency P-band. Hence the effective resolution would be provided largely by the λ^2-span at the P-band.

On the other hand, the minimum λ^2, and hence the sensitivity to large scales in RM, is provided by the L-band observation.

The cleaned tomograph now retrieves a significant fraction of the flux density for the extended feature. The amplitude as well as the RM corresponding to the point-like source is also reliably retrieved.

6.1.5 Message from the multi-band simulation

The simulations above demonstrate qualitatively the potential of combining multi-band data for Faraday tomography for enhanced sensitivity towards extended structures in RM. Combining multi-band data also enhances the RM-resolution. Although the *dirty RM-beam* has finiteness on the scales of inverse of the "total λ^2 range" of measurements, the "effective" RM-resolution is provided by the sum of the λ^2-spans of the individual bands. Hence sampling more number of intermediate bands would correspondingly enhance the effective RM-resolution.

The key to making use of multi-band data for the tomography lies in the ability to deconvolve the artifacts of highly sparse sampling of the λ^2. Generally, for a contiguous band, FFT is used for RM-synthesis after having re-gridded the data into uniformly sampled λ^2. For such uniformly sampled data, the RM-beam (RM response function) is independent of RM if the differential depolarization effects within the

"fixed" channel bandwidths (and hence "different" λ^2 widths) discussed in Chapter 2 were to be ignored. The Fourier inversion as well as the RM-clean stage would then become computationally faster. However, for highly sparse sampling, re-gridding the data into uniformly sampled λ^2 consistently within the different bands would not be straightforward. Hence we used traditional DFT for the Fourier inversion which does not rely on uniform sampling of the abscissa coordinates, and developed an RM-clean algorithm that takes into account the RM-dependence of the RM-beam, which in any case is ideally required, considering the additional spectral modulation resulting from intra-channel depolarization that is RM-dependent. A more detailed assessment of the performance of these algorithms needs to be done and is beyond the scope of the thesis.

6.2 Faraday tomography of diffuse polarized emission from the Galaxy: combining Arecibo data at P- and L-band

In this section, we present preliminary results of Faraday tomography performed performed on astronomical data. Here, we combine Arecibo data at the L- and the P-band. The test region of GALFACTS observation at L-band is used for this purpose, and P-band observations of the region were made as a part of this thesis work. These are the first results of tomography performed by combining real data at two widely separated frequency bands, and are presented here primarily for completeness and as a demonstration of the technique. In the presence of possible residual instrumental effects further analysis and interpretation of the tomographs are not attempted in this thesis.

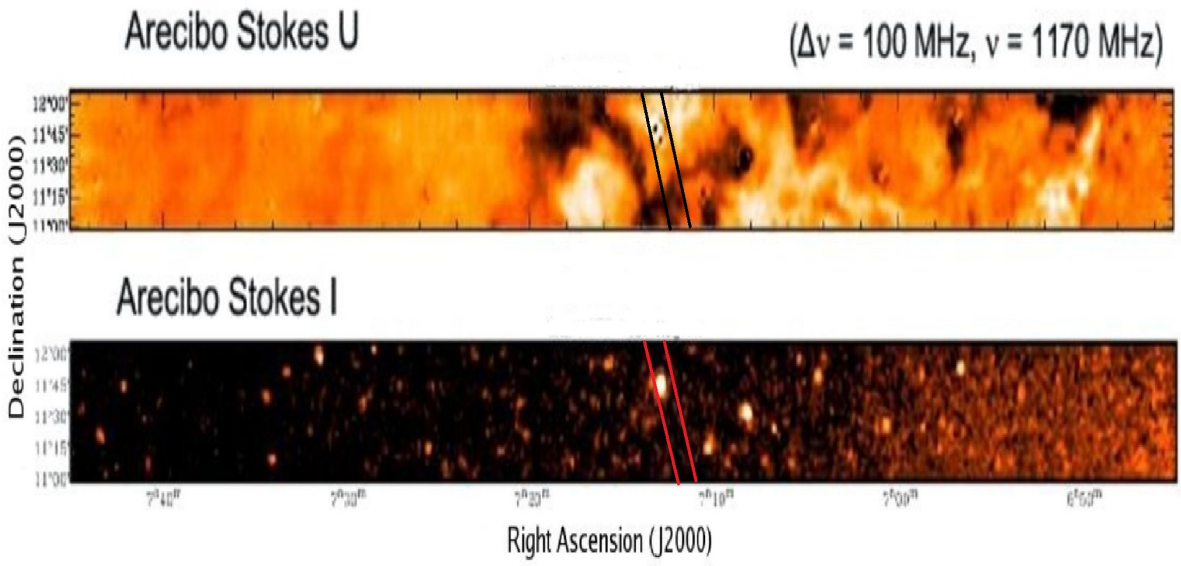

Figure 6-4: *The GALFACTS pilot region: The top panel shows the band-averaged Stokes-U intensity. The bottom panel shows band-averaged Stokes-I intensity. These observations were conducted at the L-band. The two parallel lines in both the images indicate the region for which the tomography presented in this thesis was performed.*

6.2.1 The GALFACTS pilot region

A $15^\circ \times 1^\circ$ patch of the Galaxy (Haslam et al., 1970) centered at $RA = 07h\ 15m$ and $Dec = 11^\circ\ 30'$ had been imaged via the GALFACTS (Galactic Arecibo L-band Feed Array Continuum Transit Survey) precursor proposal using both the L-band Wide (Project Id: A1863) and the ALFA (Project Id: A1947) receivers of the Arecibo telescope. The resultant band-averaged images (Figure 6-4) already revealed rich structure in linearly polarized intensity with no counterpart in Stokes-I.

We proposed and obtained time for full Stokes observation at 327 MHz of the same patch of the sky using the Arecibo telescope (Project Id: A2303) with the aim of studying in details the structure in the polarized emission along Faraday depth by combining the 327 MHz data with the data at L-band.

6.2.2 The observations and Data reduction

Both the L-band and the P-band observations were conducted in the *meridian nodding* mode – the telescope keeps scanning the declination range (1° in our case) about the zenith, as the sky drifts past. Figure 6-5 shows the sampling of the RA-Dec grid as the telescope "nods" in declination while the sky drifts. The sequence of triangular cuts across RA-Dec plane corresponding to the sampled points is called a "track".

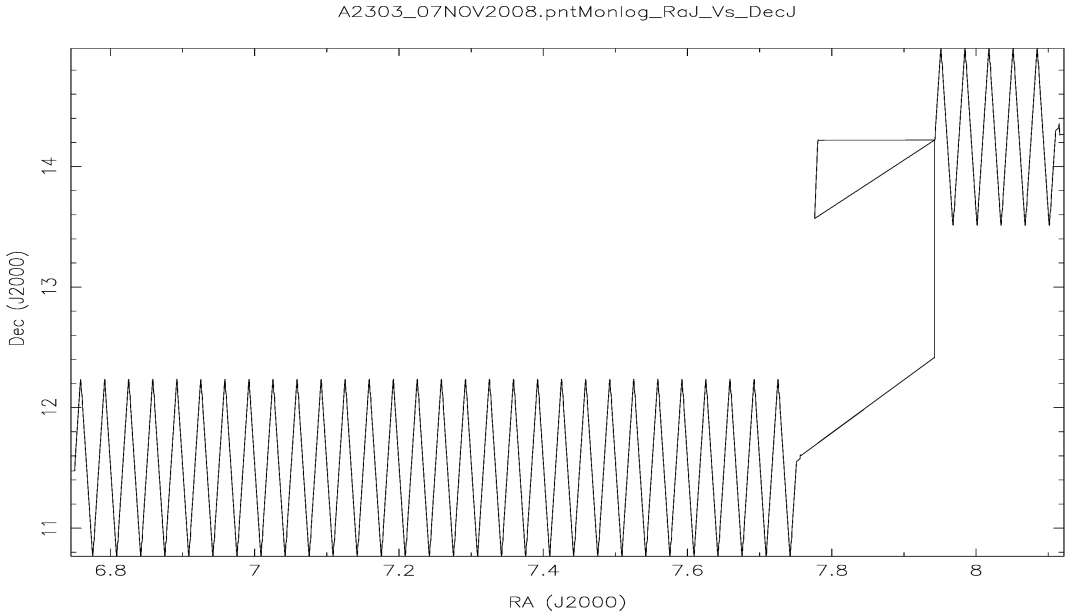

Figure 6-5: *A "track" showing the (RA,Dec) points that were sampled during a meridian nod observation. The additional track centered at Dec* $\simeq 14^\circ$ *is to sample a calibrator source.*

Observations repeated on different days, by beginning the meridian nodding at a staggered RA, will sample new tracks on the RA-Dec plane. The entire $15^\circ \times 1^\circ$ region was sampled by appropriately staggering the RA at the start of the observations each day. We refer to one full cycle of nodding (comprising of 1-up & 1-down scan) as one Λ.

The image-cubes used for the L-band data are from the preliminary observations for the GALFACTS project (Arecibo proposal Id: A1863) that used the L-wide band receiver of the Arecibo telescope. For the L-band data used here, the band-width is 100 MHz, centered around 1170 MHz. The spectral resolution is 390.625 kHz

(corresponding to the 256 spectral channels). These data had been calibrated for instrumental gains, making use of a *correlated cal* (noise diode) winking at 25 Hz. For each frequency channel, the calibrated data were mapped to the RA-Dec grid by refining the calibration further, using the technique of "basket-weaving" (Haslam et al., 1981). Polarization leakage calibration had not been attempted in these preliminary images at L-band.

The raw P-band (327 MHz) data from our observation were reduced using standard software available at the Arecibo observatory, and the dynamic spectra were obtained for all four Stokes. For the data presented here, the band-width at the P-band is 25 MHz, centered around 319.5 MHz. 2048 spectral channels were initially used for detecting and rejecting channels corrupted by RFIs. After RFI excision, the fine channels were suitably averaged to obtain spectra with coarse resolution, but retaining the original spectral sampling. The effective number of independent channels used thus is 200 with a channel resolution of $\sim 120kHz$.

The gain calibration was done using a correlated cal winking at 25 Hz. The instrumental polarization leakage calibration has been attempted for each given spectral channel, wherein the possible Stokes-I dependent contribution to the Q and the U data is estimated via correlation, and then removed. We also removed from the Q and U data, their respective channel-wise global means computed using the data within one-half of a Λ. We have not yet mapped the P-band data into the RA-Dec plane using basket-weaving. The tomography presented here correspond to a 1-D cut encompassing one half-Λ (marked in Figure 6-4).

Since the spectra are not flat across the P and the L-band, the data must be relatively scaled. In order to make the Stokes-I spectral energy densities at the two bands equal, we scale the spectra of all 4 Stokes at the L-band appropriately. Also the L-band data are convolved to match the angular resolution of the P-band data. About 6 non-overlapping beams (of $\sim 15'$) cover the 1-D half-Λ cut that has been used for the present demonstration of the tomography with the Arecibo data.

Although preliminary, the results of combining data from disparate frequency bands seem encouraging.

6.2.3 Faraday tomography using the L-band data

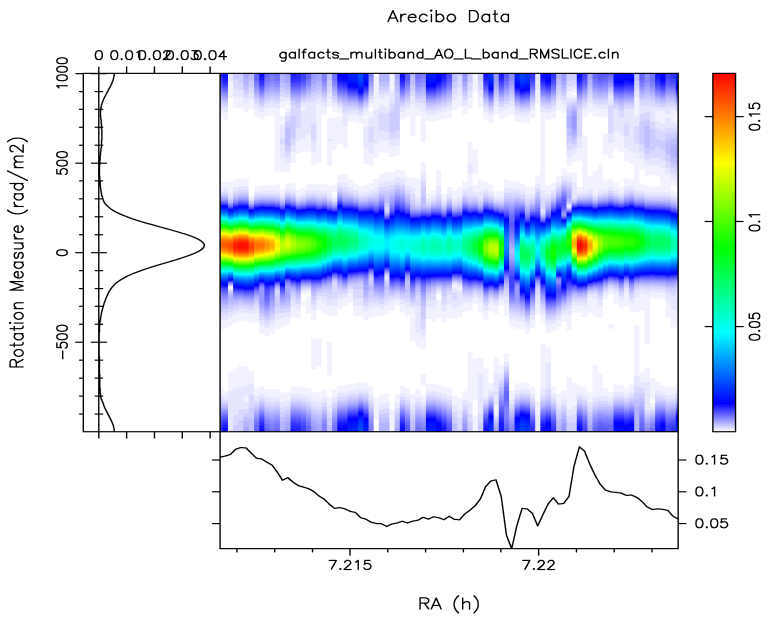

Figure 6-6: *Faraday tomograph of data from a test GALFACTS region at L-band: The colour plot shows the linearly polarized intensity as a function of sky-position (depicted by only the RA) and RM. The side panel on the left shows, for a given RM, the rms across the sky-position. The bottom panel shows, for each RA, the maxima of the polarized intensity across RM profiles at the respective directions. The quantities in the side panels are for diagnosis and assessment of the data quality, and are not of relevance in further discussion.*

Figure 6-6 shows the RM-cleaned polarized intensity as a function of sky position and RM. Although the x-axis shows only the RA, in reality, it is related to both RA & Dec corresponding to the 1-D cut as outlined in Figure 6-4. The RM is shown as the y-axis. As expected, the resolution along RM is poor at the L-band. No significant structure is apparent along RM. Any significant polarized emission is confined to the RM-resolution bin close to RM = 0.

6.2.4 Faraday tomography using P-band data

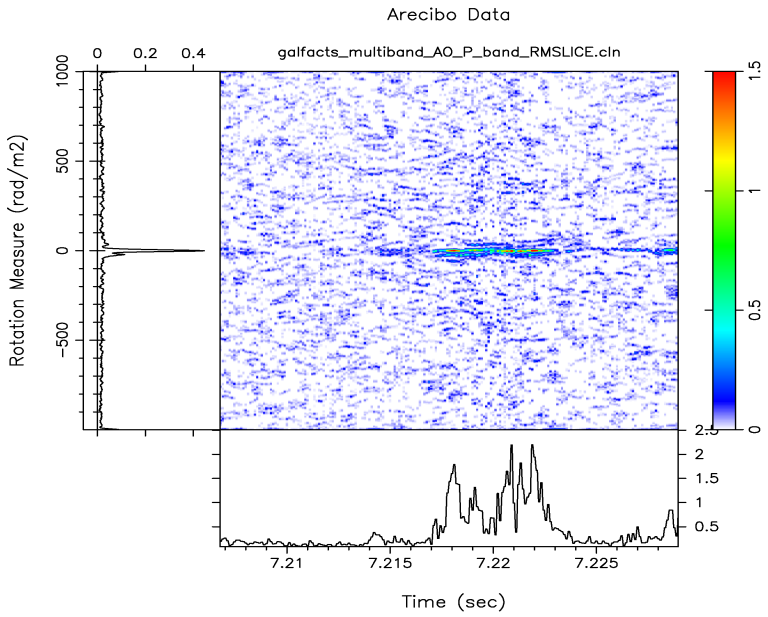

Figure 6-7: *Similar to Figure 6-6, but now showing result of Faraday tomography of the test region using our data at P-band.*

Figure 6-7 shows the RM-cleaned polarized intensity at P-band as a function of sky position and RM. The enhanced resolution in RM seem to reveal resolved polarized emission components very close to RM = 0 along certain sight-lines. However the polarized component appearing at RA = 7.212h in the tomograph obtained from the L-band data (Figure 6-6) is absent from the P-band tomograph. This could possibly be due to a Faraday thick structure which the P-band observations are not sensitive to, owing to lack of adequately short λ^2s.

6.2.5 Faraday tomography after combining data at L- and P-bands

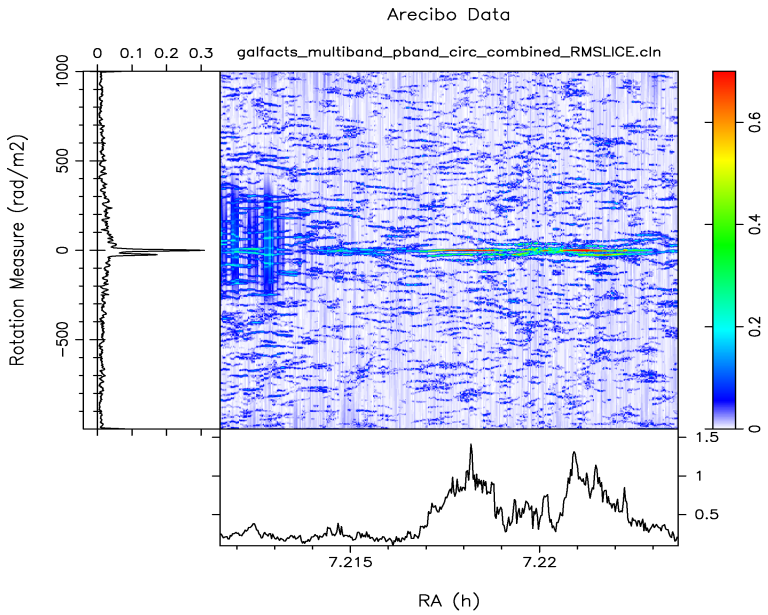

Figure 6-8: *Faraday tomograph of the GALFACTS test region data, after combining L- & P-band. The panel description are same as in in Figure 6-6.*

The high RM-resolution provided by the lower frequency P-band data together with the enhanced sensitivity to large scale RM-structure provided by the high frequency L-band data is expected to reveal details of the underlying polarized structures across RM. Indeed, the potential Faraday thick component at RA = 7.212h that was unresolved at the L-band (Figure 6-6), and to which the P-band data (Figure 6-7) was insensitive to, appears and is now resolved in the tomographs obtained from the combined data, and also shows significant polarized flux. These features in Figure 6-8 are unlikely to be of instrumental origin, since the apparent polarization encouragingly shows significantly different distribution in RM across the 6 independent lines of sight for which the tomographs have been presented, and for which the contribution of the instrumental polarization may be expected to have a similar distribution along RM.

These preliminary, nevertheless interesting results are being analyzed. We are

probing existence of possible structures in the polarized emission along both the RM and the angular dimensions. A pipeline is being developed to combine and analyze the P-band data with more recent GALFACTS data. We would like to note here that the number and choice of frequency bands required for multi-band Faraday tomography would depend on the wavelength-dependent depolarization effects in operation along a line-of-sight. The same signal, can have different signal-to-noise ratios in different wave-bands due to wavelength-dependent depolarization. As mentioned earlier, one would ideally require as wide a frequency coverage (with adequately high and low frequencies sampled), as permissible. In cases where wide-band contiguous spectral coverage is not feasible, measurement at more number of discrete bands would help enhance the signal-to-noise ratio. New telescopes that are being designed with wide-band systems would probe the polarization structures along Faraday depth, in details.

6.3 Conclusions

For a Faraday tomographic study to be sensitive towards both fine and large scale polarization structures, one would ideally require observation at adequately short wavelengths, and cover as wide a spectral span, with as fine a spectral resolution as possible. The practical difficulties in designing such an experiment have been pointed out. In this chapter, we have presented an optimal solution *viz.* performing Faraday tomography by combining multi-band data. A deconvolution algorithm (RM-clean) suitable for data unevenly sampled in λ^2 has also been demonstrated. The ability of combining multi-band data for Faraday tomography opens up an exciting prospect of studying the rich structure in the diffuse polarized emission from the Galaxy as a function of Faraday depth.

Chapter 7

Summary

The thesis explores the potential of the relatively new spectro-polarimetric tools and techniques in studying magneto-ionic media of astrophysical systems, and addresses general issues one would encounter in such studies. Following sections summarize briefly the key aspects explored in the thesis.

7.1 Faraday Tomography: multi-band approach

In Chapter 2 we briefly discuss the recently developed technique of Faraday tomography or RM synthesis. A modified version of the technique capable of handling data that are unevenly sampled in λ^2 space is presented along with a relevant deconvolution (RM-clean) scheme that does not require re-gridding of the data into uniformly spaced λ^2 domain. The relevance of our choice of uneven sampling in λ^2 for data infested with radio frequency interference (RFI) that corrupts wide chunk of the observation band-width, and for multi-band data in general, is discussed. More importantly, attention is drawn to the complex depolarization occurring within even the finite spectral channel-widths. We derive analytical expressions for estimating this effect, which should be included as an additional RM-dependent spectral modulation while computing dirty response in the RM domain, for use in RM-clean. This is particularly important for high dynamic range tomography.

Chapter 6 demonstrates the feasibility of enhancing the RM-resolution by com-

bining data from widely separated frequency bands. A study using simulations as well as real data is presented. Combining multi-band data for Faraday tomography improves both, the RM resolution and the sensitivity to Faraday-thick features. It is expected to open up an exciting prospect of studying a rich variety of structure in the diffuse polarized emission from the Galaxy as a function of Faraday depth.

7.2 Instrumental calibration issues

We have revisited instrumental calibration issues in detail. Modification to an incoming pair of signals by various components of the instrument is discussed. Properties of various calibrator sources are described and their respective roles in determining the instrumental parameters presented. Certain statistical identities have been identified that may be useful in probing instrumental polarization fidelity as well as in identifying signatures of changing polarization across the sky.

The need for invoking non-reciprocity of polarization leakages is discussed, along with the caveats encountered if certain simplified assumptions are made about the nature of leakage. In all our derivation we have assumed the leakages to be non-reciprocal, which corresponds to a most general situation.

The role of the "winking cal" in calibrating instrumental effects that vary with time, is elaborately discussed. Limitation of such a calibrator in cases where the time-varying effects are coupled to all elements of the antenna Jones matrix is pointed. The caution to be adopted in designing receiver systems, so as to avoid such coupling, is mentioned briefly.

A new method for instrumental calibration, that can make use of feed and/or dish rotation capabilities of new upcoming telescopes (*e.g.* ASKAP), is proposed, formulated and also demonstrated using data from Arecibo telescope obtained on a calibrator using rotating feeds.

The potential of circularly polarized signals for instrumental calibration is discussed. We point out a unique opportunity of using circularly polarized "astronomical" signals – the Crab giant pulses, for instrumental calibration. We also emphasize

the potential of these impulse-like giant pulses (some of which could possibly be even shorter than 2 ns) in calibrating the instrumental band-pass for even wide-band systems.

7.3 GMRT polarimetry

Chapter 4 discusses the practical considerations relevant for GMRT polarimetry. Using several calibrator sources, we demonstrate feasibility of spectro-polametric studies (Faraday tomography) at the low frequencies of the GMRT. Signatures of polarized emission from the diffuse component of the ISM in certain directions, are presented.

We would like to emphasize here that for polarimetric studies, it is of utmost importance that the complex structure of the RFIs across time, baseline, frequency and polarization be carefully assessed, and "flagged". Automation of data reduction procedures helps.

7.4 Faraday tomographic studies of Cassiopeia A

Chapter 5 discusses results from our spectro-polarimetric imaging of the young supernova remnant Cassiopeia A at 327 MHz using the GMRT. We have presented the highest resolution maps of the remnant so far at meter wavelengths. Our data in full Stokes parameters, benefiting from both high angular resolution and wide spectral span, reveal significant (although weak) polarized emission from the remnant even at these low radio frequencies where earlier studies had indicated the remnant to be completely depolarized. That the observed polarization is intrinsic to the source, and not a mere artifact of the instrument, is established rigorously using two independent methods: (a) by establishing the lack of any correlation between the linearly polarized intensity and Stokes-I intensity, and (b) revealing the expected anti-correlation between the degree of linear polarization and soft X-radiation, using a novel method of binning the data in Stokes-I. The calibrated images at 327 MHz show the polarization position angles (PA) to be nearly constant across the entire face of the remnant. This

is intriguing given that observations at higher frequencies indicate the polarization PAs corresponding to the electric field to be tangential. Furthermore, the RMs of the brightest components along all sight-lines passing through the remnant is found to be constant at 327 MHz. This too contradicts observations at high frequencies where considerable spread in the apparent RMs had been observed. The implication of these observations on the magneto-ionic morphology of the supernova remnant has been discussed. 3-D toy models of the thermal and non-thermal emissivities derived using the observed soft X-ray and radio Stokes-I images respectively, as observational constraints, provide support for the emission region corresponding to the observed polarization at 327 MHz to be towards the outer surfaces of the remnant.

Two plausible physical scenarios that can consistently explain the observed polarization morphology have also been presented. One of these conjectures the interesting possibility of the observed polarization at 327 MHz to be the result of a pulsar driven wind nebula (PWN) in its formation stage. Compression of an ambient uniform magnetic field as a result of an expanding spherical shell (van der Laan, 1962) could be another possibility.

7.5 Future work

In the thesis, we have tried to address some of the general issues related to spectro-polarimetric studies including instrumental calibration as well as development of new/refined tools and techniques for performing Faraday tomography. Simulations as well as application to astronomical data (Cassiopeia A and the GALFACTS pilot region) already emphasizes the potential of these tools for studying the magneto-ionic medium of these sources in much finer details.

Follow-up observations of the supernova remnant Cassiopeia A at higher frequencies will help resolve several intriguing properties of the remnant revealed through our 327-MHz GMRT study. We plan to propose new spectro-polarimetric observation of this young remnant, at suitably higher frequencies, and perform multi-band tomography by combining the data with the existing 327-MHz data. As discussed

in Chapter 6, multi-band tomography would provide an optimal way of studying the 3-D magneto-ionic morphology of a complex source like Cassiopeia A.

The high sensitivities towards both small and large-scale structures in RM, provided by multi-band tomography, are expected to reveal rich structure in the diffuse Galactic polarized emission along the Faraday depth. Such data obtained using single dish measurements would however, have poor angular resolution. Nevertheless, multi-band data from single dishes would be ideal for studying the large angular-scale magnetic fields in the Galaxy (Tucci et al., 2002). We plan to follow up our preliminary demonstration of the technique of performing tomography using multi-band data, by producing the RM data cube for the entire $15^\circ \times 1^\circ$ test patch to probe large angular-scale structures in the Galactic magnetic fields.

It will be exciting to assess practical applicability of the new methods of instrumental calibration discussed in the thesis. Some of these experiments, using correlated noise sources are being conducted at the DSP lab of the institute.

Appendix A

Polarization ellipse, Stokes parameters and the Poincare sphere representation of polarization states

Any instantaneous electric field can be represented as linear combination of two orthogonal basis vectors. In the linear basis, the two orthogonal components can be written as:

$$\begin{aligned} \tilde{E}_x &= E_1 \ \sin(\omega t) \ \hat{\mathbf{e}}_x \\ &= E_0 \cos(\theta) \ \sin(\omega t) \ \hat{\mathbf{e}}_x \qquad \text{(A.1)} \\ \tilde{E}_y &= E_2 \ \sin(\omega t + \phi) \ \hat{\mathbf{e}}_y \\ &= E_0 \sin(\theta) \ \sin(\omega t + \phi) \ \hat{\mathbf{e}}_y \qquad \text{(A.2)} \end{aligned}$$

where $\mathrm{E}_1 = \mathrm{E}_0 \cos(\theta)$ & $\mathrm{E}_2 = \mathrm{E}_0 \sin(\theta)$ are the amplitudes of the two orthogonal components and ϕ is the relative phase between them. The state of polarization, which is a time-averaged entity can be obtained by eliminating the parameter time from the

above equations:

$$\frac{E_x^2}{E_1^2 \sin^2(\phi)} - \frac{2\cos(\phi)}{E_1 E_2 \sin^2(\phi)} E_x E_y + \frac{E_y^2}{E_2^2 \sin^2(\phi)} = 1 \tag{A.3}$$

Equation (A.3) represents a general ellipse in the Ex-Ey plane, and is referred to as the polarization ellipse. The two parameters of this ellipse (*viz.* tilt-angle and axis-ratio) can completely describe any 100% polarized state. The tilt-angle is defined as the angle that the major axis of the ellipse makes with the x-axis of the reference frame, and the axis ratio is the ratio of the two axes of the ellipse. The parameters of the ellipse are easier to obtain in a frame of reference with the x-axis aligned with the ellipse's major axis. Let $\tau^\dagger$ be the angle of rotation (tilt-angle) required to align the x-axis of the new rotated frame (denoted by $'$) with the major axis of the ellipse (we use $\tau^\dagger$ tentatively since the algebra used to determine the required rotation does not distinguish between the major and the minor axes of the ellipse):

$$\begin{bmatrix} \mathbf{E}'_x \\ \mathbf{E}'_y \end{bmatrix} = \begin{bmatrix} \cos(\tau^\dagger) & \sin(\tau^\dagger) \\ -\sin(\tau^\dagger) & \cos(\tau^\dagger) \end{bmatrix} \begin{bmatrix} \mathbf{E}_x \\ \mathbf{E}_y \end{bmatrix} \tag{A.4}$$

In this new frame, the cross terms would vanish, and the ellipse would assume the simple form:

$$\frac{E_x'^2}{a^2} + \frac{E_y'^2}{b^2} = 1 \tag{A.5}$$

where "a" and "b" are the semi-major and semi-minor axes of the ellipse. The tilt angle $\tau^\dagger$, in terms of the polarization parameters is given by:

$$\tau^\dagger = \frac{1}{2} \tan^{-1}[\tan(2\theta)\cos(\phi)] \tag{A.6}$$

However $\tau^\dagger$ given by Equation (A.6) ensures merely that any of the major or the minor axis is aligned with the x-axis of the new rotated frame. A further rotation (depending on ϕ & θ) is required for ensuring the alignment of the x-axis with the

ellipse's major-axis:

$$\begin{aligned}
\tau &= \tau^{\dagger} && ;\ if\ (\phi = 0)\ or\ (\cos(\phi) \geq 0\ \&\ \theta \leq \frac{\pi}{4}) \\
&= \frac{\pi}{2} + \tau^{\dagger} && ;\ if\ (\cos(\phi) \geq 0\ \&\ \theta > \frac{\pi}{4})\ or\ (\cos(\phi) < 0\ \&\ \theta > \frac{\pi}{4}) \\
&= \pi + \tau^{\dagger} && ;\ if\ (\cos(\phi) < 0\ \&\ \theta \leq \frac{\pi}{4})
\end{aligned}$$

Once the tilt-angle is derived, the semi-major and the semi-minor axes of the polarization ellipse is given by:

$$a^2 = \frac{\sin^2(\theta)\cos^2(\theta)\sin^2(\phi)}{\sin^2(\tau)\cos^2(\theta) + \cos^2(\tau)\sin^2(\theta) - 2\sin(\tau)\cos(\tau)\sin(\theta)\cos(\theta)\cos(\phi)} \tag{A.7}$$

$$b^2 = \frac{\sin^2(\theta)\cos^2(\theta)\sin^2(\phi)}{\cos^2(\tau)\cos^2(\theta) + \sin^2(\tau)\cos^2(\theta) + 2\sin(\tau)\cos(\tau)\sin(\theta)\cos(\theta)\cos(\phi)} \tag{A.8}$$

An equivalent representation of polarization states can be made in terms of the Stokes parameters (I, Q, U & V) defined as a linear combination of time-averaged self- and cross-correlations of the components of the electric field. When the electric field is represented in a linear basis, the Stokes parameters are defined as:

$$\begin{bmatrix} I \\ Q \\ U \\ V \end{bmatrix} = \begin{bmatrix} < E_x E_x^* > + < E_y E_y^* > \\ < E_x E_x^* > - < E_y E_y^* > \\ < E_x E_y^* > + < E_x^* E_y > \\ i\ (< E_x^* E_y > - < E_x E_y^* >) \end{bmatrix} \tag{A.9}$$

The first term I, is the total intensity, Q & U are components of linear polarized intensity, and V represents the circularly polarized component.

Each polarization ellipse in the $E_x - E_y$ plane can be uniquely mapped to the

surface of a sphere through the following transformations:

$$\tau = \theta \tag{A.10}$$

$$\begin{aligned} \epsilon &= \cot^{-1}(\frac{a}{b}) \ ; \ if \ \phi \geq 0 \\ &= \cot^{-1}(-\frac{a}{b}) \ ; \ if \ \phi < 0 \end{aligned} \tag{A.11}$$

where 2ϵ & 2τ are the spherical coordinates corresponding to the latitude and the longitude respectively of the sphere. The radius of the sphere signifies the net polarized intensity. This sphere is called the Poincare sphere. The Stokes parameters can be represented on the Poincare sphere as:

$$Q = I_p \cos(2\epsilon)\cos(2\tau) \tag{A.12}$$

$$U = I_p \cos(2\epsilon)\sin(2\tau) \tag{A.13}$$

$$V = I_p \sin(2\epsilon) \tag{A.14}$$

where I_p denotes the polarized intensity.

Appendix B

Modeling propagation and instrumental effects using Jones matrices

Any modification to a vector in 2d can be described without loss of generality, using a 2×2 Jones matrix. If the two components of the input vector are complex, the elements of the Jones matrix would also have to be complex in general.

$$\begin{bmatrix} \tilde{X}^m \\ \tilde{Y}^m \end{bmatrix} = \begin{bmatrix} \tilde{J}_{11} & \tilde{J}_{12} \\ \tilde{J}_{21} & \tilde{J}_{22} \end{bmatrix} \begin{bmatrix} \tilde{X}^0 \\ \tilde{Y}^0 \end{bmatrix}$$

This is the most general transformation that an input signal would undergo during its propagation. The transformation matrix **J** is the resultant of various transformations corresponding to different regions in the signal path, each of which assumes specific forms depending on the physical processes responsible for transforming the incoming signal in the respective regions. We write down here several transformation Jones matrices relevant in our study of polarized emission and propagation effects, including those relevant for the paths through the instrument. We shall, use $\hat{\mathbf{e}}_x$ *and* $\hat{\mathbf{e}}_y$ to describe unit vectors in the linear basis, while $\hat{\mathbf{e}}_R$ *and* $\hat{\mathbf{e}}_L$ for describing unit vectors in the circular basis.

1. **Transformations between Linear and Circular Basis**

$$\begin{bmatrix} \hat{\mathbf{e}}_R \\ \hat{\mathbf{e}}_L \end{bmatrix} = \begin{bmatrix} 1 & i \\ i & 1 \end{bmatrix} \begin{bmatrix} \hat{\mathbf{e}}_x \\ \hat{\mathbf{e}}_y \end{bmatrix} \tag{B.1}$$

$$\begin{bmatrix} \hat{\mathbf{e}}_x \\ \hat{\mathbf{e}}_y \end{bmatrix} = \frac{1}{2} \begin{bmatrix} 1 & -i \\ -i & 1 \end{bmatrix} \begin{bmatrix} \hat{\mathbf{e}}_R \\ \hat{\mathbf{e}}_L \end{bmatrix} \tag{B.2}$$

2. **Faraday Rotation (Circular birefringence):** The Faraday effect results in a relative phase between the two orthogonal circular hands of polarization ($\hat{\mathbf{e}}_R,\ \hat{\mathbf{e}}_L$). If ϕ_{RM} is the phase difference between $\tilde{\mathbf{E}}_R$ and $\tilde{\mathbf{E}}_L$, then

$$\begin{bmatrix} \tilde{E}_{R,RM}\ \hat{\mathbf{e}}_{R,RM} \\ \tilde{E}_{L,RM}\ \hat{\mathbf{e}}_{L,RM} \end{bmatrix} = \begin{bmatrix} e^{-i\ \frac{\phi_{RM}}{2}} & 0 \\ 0 & e^{i\ \frac{\phi_{RM}}{2}} \end{bmatrix} \begin{bmatrix} \tilde{E}_R\ \hat{\mathbf{e}}_R \\ \tilde{E}_L\ \hat{\mathbf{e}}_L \end{bmatrix}$$

From equation (B.2):

$$\begin{bmatrix} \tilde{E}_{x,RM}\ \hat{\mathbf{e}}_{x,RM} \\ \tilde{E}_{y,RM}\ \hat{\mathbf{e}}_{y,RM} \end{bmatrix} = \frac{1}{2}\begin{bmatrix} 1 & -i \\ -i & 1 \end{bmatrix}\begin{bmatrix} \tilde{E}_{R,RM}\ \hat{\mathbf{e}}_{R,RM} \\ \tilde{E}_{L,RM}\ \hat{\mathbf{e}}_{L,RM} \end{bmatrix}$$

$$\begin{bmatrix} \tilde{\mathbf{E}}_{x,RM} \\ \tilde{\mathbf{E}}_{y,RM} \end{bmatrix} = \frac{1}{2}\begin{bmatrix} 1 & -i \\ -i & 1 \end{bmatrix}\begin{bmatrix} e^{-i\frac{\phi_{RM}}{2}} & 0 \\ 0 & e^{i\frac{\phi_{RM}}{2}} \end{bmatrix}\begin{bmatrix} \tilde{\mathbf{E}}_R \\ \tilde{\mathbf{E}}_L \end{bmatrix}$$

$$\begin{bmatrix} \tilde{\mathbf{E}}_{x,RM} \\ \tilde{\mathbf{E}}_{y,RM} \end{bmatrix} = \frac{1}{2}\begin{bmatrix} 1 & -i \\ -i & 1 \end{bmatrix}\begin{bmatrix} e^{-i\frac{\phi_{RM}}{2}} & 0 \\ 0 & e^{i\frac{\phi_{RM}}{2}} \end{bmatrix}\begin{bmatrix} 1 & i \\ i & 1 \end{bmatrix}\begin{bmatrix} \tilde{\mathbf{E}}_x \\ \tilde{\mathbf{E}}_y \end{bmatrix}$$

$$\begin{bmatrix} \tilde{\mathbf{E}}_{x,RM} \\ \tilde{\mathbf{E}}_{y,RM} \end{bmatrix} = \begin{bmatrix} \cos(\frac{\phi_{RM}}{2}) & \sin(\frac{\phi_{RM}}{2}) \\ -\sin(\frac{\phi_{RM}}{2}) & \cos(\frac{\phi_{RM}}{2}) \end{bmatrix}\begin{bmatrix} \tilde{\mathbf{E}}_x \\ \tilde{\mathbf{E}}_y \end{bmatrix} \tag{B.3}$$

$$\begin{bmatrix} \tilde{\mathbf{E}}_{x,RM} \\ \tilde{\mathbf{E}}_{y,RM} \end{bmatrix} = \begin{bmatrix} \cos(\chi_{RM}) & \sin(\chi_{RM}) \\ -\sin(\chi_{RM}) & \cos(\chi_{RM}) \end{bmatrix}\begin{bmatrix} \tilde{\mathbf{E}}_x \\ \tilde{\mathbf{E}}_y \end{bmatrix} \tag{B.4}$$

Where χ_{RM} is the rotation of the plane of polarization due to Faraday Rotation. We note here the relation between χ_{RM} and the phase difference ϕ_{RM} between $\tilde{\mathbf{E}}_R$ and $\tilde{\mathbf{E}}_L$:

$$\chi_{RM} = \frac{\phi_{RM}}{2} \tag{B.5}$$

3. **Cotton Mouton Effect (Linear birefringence):** Whereas the Faraday effect results in a relative phase difference between the two circular polarized components of radiation, the Cotton Mouton effect results in a phase difference between the two linear components of radiation, leading to mixing of linear and circular polarization. And although most astronomical sources are found to have negligible intrinsic circular polarization, the λ^3-dependent Cotton Mouton (CM) effect would lead to observation of apparent circular polarization, particularly at very low radio frequencies. We therefore, present here a means of probing

this effect wherever it may be significant.

Let ϕ_{CM} be the phase difference between $\tilde{\mathbf{E}}_x$ and $\tilde{\mathbf{E}}_y$.

$$\begin{bmatrix} \tilde{E}_{x,CM}\ \hat{\mathbf{e}}_{x,CM} \\ \tilde{E}_{y,CM}\ \hat{\mathbf{e}}_{y,CM} \end{bmatrix} = \begin{bmatrix} e^{-i\ \frac{\phi_{CM}}{2}} & 0 \\ 0 & e^{i\ \frac{\phi_{CM}}{2}} \end{bmatrix} \begin{bmatrix} \tilde{E}_x\ \hat{\mathbf{e}}_x \\ \tilde{E}_y\ \hat{\mathbf{e}}_y \end{bmatrix} \tag{B.6}$$

The equivalent transformation undergone by the Stokes parameters is given by:

$$\begin{bmatrix} I_{CM} \\ Q_{CM} \\ U_{CM} \\ V_{CM} \end{bmatrix} = \begin{bmatrix} 1 & 0 & 0 & 0 \\ 0 & 1 & 0 & 0 \\ 0 & 0 & \cos(\phi_{CM}) & -\sin(\phi_{CM}) \\ 0 & 0 & \sin(\phi_{CM}) & \cos(\phi_{CM}) \end{bmatrix} \begin{bmatrix} I \\ Q \\ U \\ V \end{bmatrix} \tag{B.7}$$

Thus the Cotton Mouton effect rotates the UV-plane. I and Q remains unchanged.

4. **Feed Rotation:** Let χ_{feed} be the angle by which the feed system rotates about the pointing direction *w.r.t.* the coordinates in the celestial sphere. The effect of such a rotation is different for different feed types. For a linear feed system, the effect is a rotation of the xy-plane:

$$\begin{bmatrix} \hat{\mathbf{e}}_{x,feed} \\ \hat{\mathbf{e}}_{y,feed} \end{bmatrix} = \begin{bmatrix} \cos(\chi_{feed}) & -\sin(\chi_{feed}) \\ \sin(\chi_{feed}) & \cos(\chi_{feed}) \end{bmatrix} \begin{bmatrix} \hat{\mathbf{e}}_x \\ \hat{\mathbf{e}}_y \end{bmatrix} \tag{B.8}$$

The corresponding transformation for a circular feed system can be derived

using equation (B.1):

$$\begin{bmatrix} \hat{\mathbf{e}}_{R,feed} \\ \hat{\mathbf{e}}_{L,feed} \end{bmatrix} = \begin{bmatrix} 1 & i \\ i & 1 \end{bmatrix} \begin{bmatrix} \hat{\mathbf{e}}_{x,feed} \\ \hat{\mathbf{e}}_{y,feed} \end{bmatrix}$$

$$\begin{bmatrix} \hat{\mathbf{e}}_{R,feed} \\ \hat{\mathbf{e}}_{L,feed} \end{bmatrix} = \begin{bmatrix} 1 & i \\ i & 1 \end{bmatrix} \begin{bmatrix} \cos(\chi_{feed}) & -\sin(\chi_{feed}) \\ \sin(\chi_{feed}) & \cos(\chi_{feed}) \end{bmatrix} \begin{bmatrix} \hat{\mathbf{e}}_x \\ \hat{\mathbf{e}}_y \end{bmatrix}$$

$$\begin{bmatrix} \hat{\mathbf{e}}_{R,feed} \\ \hat{\mathbf{e}}_{L,feed} \end{bmatrix} = \frac{1}{2} \begin{bmatrix} 1 & i \\ i & 1 \end{bmatrix} \begin{bmatrix} \cos(\chi_{feed}) & -\sin(\chi_{feed}) \\ \sin(\chi_{feed}) & \cos(\chi_{feed}) \end{bmatrix} \begin{bmatrix} 1 & -i \\ -i & 1 \end{bmatrix} \begin{bmatrix} \hat{\mathbf{e}}_R \\ \hat{\mathbf{e}}_L \end{bmatrix}$$

$$\begin{bmatrix} \hat{\mathbf{e}}_{R,feed} \\ \hat{\mathbf{e}}_{L,feed} \end{bmatrix} = \begin{bmatrix} e^{i\ \chi_{feed}} & 0 \\ 0 & e^{-i\ \chi_{feed}} \end{bmatrix} \begin{bmatrix} \hat{\mathbf{e}}_R \\ \hat{\mathbf{e}}_L \end{bmatrix} \tag{B.9}$$

Thus if the feed is rotated by an angle χ_{feed} about the pointing direction, $\hat{\mathbf{e}}_R$ and $\hat{\mathbf{e}}_L$ acquires a phase difference of 2 χ_{feed} as a result.

5. **A Note on the quadrature Hybrid:** A hybrid is a feed-system that can electronically convert native linear feeds, into effective circulars (or vice versa). We have already defined in equation (B.1) the transformation matrix for conversion of the linear basis to circular. However another transformation (B.10) can achieve the same, albeit with the introduction of a relative phase of $\frac{\pi}{2}$ between $\hat{\mathbf{e}}_R$ and $\hat{\mathbf{e}}_L$ of equation (B.1).

$$\begin{bmatrix} \hat{\mathbf{e}}_{R,CHII} \\ \hat{\mathbf{e}}_{L,CHII} \end{bmatrix} = \begin{bmatrix} 1 & i \\ 1 & -i \end{bmatrix} \begin{bmatrix} \hat{\mathbf{e}}_x \\ \hat{\mathbf{e}}_y \end{bmatrix} \tag{B.10}$$

The transformation matrix in equation (B.1) and that in equation (B.10) are related as:

$$\begin{bmatrix} \hat{\mathbf{e}}_{R,CHII} \\ \hat{\mathbf{e}}_{L,CHII} \end{bmatrix} = \begin{bmatrix} 1 & 0 \\ 0 & e^{-i\ \frac{\pi}{2}} \end{bmatrix} \begin{bmatrix} \hat{\mathbf{e}}_{R,CH} \\ \hat{\mathbf{e}}_{L,CH} \end{bmatrix} \tag{B.11}$$

Depending on whether one uses the transformation in equation (B.1) or the one in equation (B.10), the Poincare Sphere would rotate by an angle $\frac{\pi}{2}$ about the $V-axis$. In other words, the QU-plane in one description would be rotated by 90° relative to the other.

Thus one should be cautious to keep this in mind, and observatories should explicitly mention which of the transformation is actually used in their hybrids.

From equation (B.1) & (B.10) we have

$$\begin{pmatrix} \hat{\mathbf{e}}_{R,CH} \\ \hat{\mathbf{e}}_{L,CH} \end{pmatrix} = \begin{pmatrix} \hat{\mathbf{e}}_x + \hat{\mathbf{e}}_{y,90^\circ} \\ \hat{\mathbf{e}}_{x,90^\circ} + \hat{\mathbf{e}}_y \end{pmatrix} \tag{B.12}$$

$$\begin{pmatrix} \hat{\mathbf{e}}_{R,CHII} \\ \hat{\mathbf{e}}_{L,CHII} \end{pmatrix} = \begin{pmatrix} \hat{\mathbf{e}}_x + \hat{\mathbf{e}}_{y,90^\circ} \\ \hat{\mathbf{e}}_x + \hat{\mathbf{e}}_{y,-90^\circ} \end{pmatrix} = \begin{pmatrix} \hat{\mathbf{e}}_x + \hat{\mathbf{e}}_{y,90^\circ} \\ \hat{\mathbf{e}}_x + \hat{\mathbf{e}}_{y,270^\circ} \end{pmatrix} \tag{B.13}$$

Given the symmetry (in the treatment of both $\hat{\mathbf{e}}_x$ and $\hat{\mathbf{e}}_y$) in the transformation described by equation (B.1) & (B.12), most observatories would find it practical to adopt this transformation. Moreover, the second transformation given by (B.10) & (B.13), in addition to acting upon only one of $\hat{\mathbf{e}}_x$ or $\hat{\mathbf{e}}_y$ (potentially making their measurements statistically different), requires two "different" kinds of phase shifters, non-idealities in which would in general, be different, leading possibly to non-reciprocal leakages between the orthogonal polarization channels, which is un-desirable from the point of view of "simplicity" in calibration, as will be seen in chapter 3. In all our discussion here onwards, we shall always be using equation (B.1) for linear to circular conversion. *i.e.*

$$\begin{bmatrix} \hat{\mathbf{e}}_{R,CH} \\ \hat{\mathbf{e}}_{L,CH} \end{bmatrix} = \begin{bmatrix} 1 & i \\ i & 1 \end{bmatrix} \begin{bmatrix} \hat{\mathbf{e}}_x \\ \hat{\mathbf{e}}_y \end{bmatrix} \tag{B.14}$$

6. **Gain Medium:** Differential gains/absorption between the two orthogonal

polarized components leads to change in the polarization state of the incoming signal. The transformation corresponding to a complex gain medium can be written as:

$$\begin{bmatrix} \tilde{A}_g \\ \tilde{B}_g \end{bmatrix} = \begin{bmatrix} \tilde{g}_A & 0 \\ 0 & \tilde{g}_B \end{bmatrix} \begin{bmatrix} \tilde{A}_0 \\ \tilde{B}_0 \end{bmatrix} \tag{B.15}$$

The complex elements of the Jones matrix takes into account any additional phase difference introduced between the two orthogonal polarized states, in addition to the differential gain/absorption. The amplifiers in a receiver system are classic examples of such complex gain media. Since the Poincare sphere description of the resultant of such a transformation would depend on the basis used for representation of the polarization vectors, we use the symbols $\tilde{A}$ *and* $\tilde{B}$ to keep the description abstract.

7. **Leakage Medium:** As the name suggests, propagation in such a medium leads to *mixing* of or *leakage* between one orthogonal polarization with the other. It is also referred to as *coupling* between the two polarizations. This may arise due to misalignment of the feed dipoles (*i.e.* if the dipoles are not orthogonal), or due to *mutual induction* between the signal carrying cables not properly shielded.

$$\begin{bmatrix} \tilde{A}_l \\ \tilde{B}_l \end{bmatrix} = \begin{bmatrix} 1 & \tilde{\epsilon}_{BA} \\ \tilde{\epsilon}_{AB} & 1 \end{bmatrix} \begin{bmatrix} \tilde{A}_0 \\ \tilde{B}_0 \end{bmatrix} \tag{B.16}$$

Some Points to Note:

1. In general, the elements of the Jones matrices are complex.
2. The instrumental gain phases mimic birefringence in their effect.
3. In general the Jones matrices are non-commutative under the operation of product.

Appendix C

The Antenna Mueller Matrix

In the presence of leakage and gain-differences between the two orthogonal channels (say, A and B) of a telescope system, the measured voltages are affected in the following way:

$$\tilde{A}^m = \tilde{g}_A[\tilde{A}^0 + \tilde{\epsilon}_{BA}\tilde{B}_0] \tag{C.1}$$

$$\tilde{B}^m = \tilde{g}_B[\tilde{B}^0 + \tilde{\epsilon}_{AB}\tilde{A}_0] \tag{C.2}$$

where the "$\sim$" is to emphasize the complex nature of the quantities involved. The model assumes that leakage happens before the signal gets pre-amplified through the two nominally orthogonal receiver chains. This is intuitive since achieving electromagnetic shielding close to the feed itself although practically difficult, the same becomes easier once the signal is transmitted further down the chain (co-ax cables, shielded metal chambers etc.)

The *Antenna Mueller Matrix* connects the measured and the true Stokes:

$$\begin{pmatrix} S_1^m \\ S_2^m \\ S_3^m \\ S_4^m \end{pmatrix} = \begin{pmatrix} m_{11} & m_{12} & m_{13} & m_{14} \\ m_{21} & m_{22} & m_{23} & m_{24} \\ m_{31} & m_{32} & m_{33} & m_{34} \\ m_{41} & m_{42} & m_{43} & m_{44} \end{pmatrix} \begin{pmatrix} S_1^0 \\ S_2^0 \\ S_3^0 \\ S_4^0 \end{pmatrix} \tag{C.3}$$

Defining the four Stokes Parameters as:

$$\begin{pmatrix} S_1 \\ S_2 \\ S_3 \\ S_4 \end{pmatrix} = \begin{pmatrix} \tilde{A}\tilde{A}^* + \tilde{B}\tilde{B}^* \\ \tilde{A}\tilde{A}^* - \tilde{B}\tilde{B}^* \\ \tilde{A}\tilde{B}^* + \tilde{A}^*\tilde{B} \\ i[\tilde{A}\tilde{B}^* - \tilde{A}^*\tilde{B}] \end{pmatrix} \tag{C.4}$$

Let us define the complex relative gain ratio $\tilde{\gamma} = \gamma\ e^{i\theta}$ where

$$\frac{\tilde{g}_B}{\tilde{g}_A} = \gamma\ e^{i\theta} \tag{C.5}$$

We derive the *Mueller Matrix* elements for the most general case, *i.e.* when the leakages $\tilde{\epsilon}_{AB}$ & $\tilde{\epsilon}_{BA}$ are regarded independent of each other.

$$\begin{pmatrix} m_{11} \\ m_{12} \\ m_{13} \\ m_{14} \end{pmatrix} = \begin{pmatrix} \frac{1}{2}g_A^2[(1+\epsilon_{BA}^2) + \gamma^2(1+\epsilon_{AB}^2)] \\ \frac{1}{2}g_A^2[(1-\epsilon_{BA}^2) - \gamma^2(1-\epsilon_{AB}^2)] \\ g_A^2[\epsilon_{BA}\cos(\phi_{BA}) + \gamma^2\epsilon_{AB}\cos(\phi_{AB})] \\ g_A^2[-\epsilon_{BA}\sin(\phi_{BA}) + \gamma^2\epsilon_{AB}\sin(\phi_{AB})] \end{pmatrix} \tag{C.6}$$

$$\begin{pmatrix} m_{21} \\ m_{22} \\ m_{23} \\ m_{24} \end{pmatrix} = \begin{pmatrix} \frac{1}{2}g_A^2[(1+\epsilon_{BA}^2) - \gamma^2(1+\epsilon_{AB}^2)] \\ \frac{1}{2}g_A^2[(1-\epsilon_{BA}^2) + \gamma^2(1-\epsilon_{AB}^2)] \\ g_A^2[\epsilon_{BA}\cos(\phi_{BA}) - \gamma^2\epsilon_{AB}\cos(\phi_{AB})] \\ -g_A^2[\epsilon_{BA}\sin(\phi_{BA}) + \gamma^2\epsilon_{AB}\sin(\phi_{AB})] \end{pmatrix} \tag{C.7}$$

$$\begin{pmatrix} m_{31} \\ m_{32} \\ m_{33} \\ m_{34} \end{pmatrix} = \begin{pmatrix} g_A^2\gamma[\epsilon_{AB}\cos(\theta+\phi_{AB}) + \epsilon_{BA}\cos(\theta-\phi_{BA})] \\ g_A^2\gamma[\epsilon_{AB}\cos(\theta+\phi_{AB}) - \epsilon_{BA}\cos(\theta-\phi_{BA})] \\ g_A^2\gamma[\cos(\theta) + \epsilon_{AB}\epsilon_{BA}\cos(\theta+\phi_{AB}-\phi_{BA}) \\ g_A^2\gamma[-\sin(\theta) + \epsilon_{AB}\epsilon_{BA}\sin(\theta+\phi_{AB}-\phi_{BA}) \end{pmatrix} \tag{C.8}$$

$$\begin{pmatrix} m_{41} \\ m_{42} \\ m_{43} \\ m_{44} \end{pmatrix} = \begin{pmatrix} g_A^2\gamma[\epsilon_{AB}\sin(\theta+\phi_{AB}) + \epsilon_{BA}\sin(\theta-\phi_{BA})] \\ g_A^2\gamma[\epsilon_{AB}\sin(\theta+\phi_{AB}) - \epsilon_{BA}\sin(\theta-\phi_{BA})] \\ g_A^2\gamma[\sin(\theta) + \epsilon_{AB}\epsilon_{BA}\sin(\theta+\phi_{AB}-\phi_{BA}) \\ g_A^2\gamma[\cos(\theta) - \epsilon_{AB}\epsilon_{BA}\cos(\theta+\phi_{AB}-\phi_{BA}) \end{pmatrix} \tag{C.9}$$

Bibliography

Agüeros, M. A., & Green, D. A. 1999, MNRAS, 305, 957

Alfvén, H., & Herlofson, N. 1950, Physical Review, 78, 616

Anantharamaiah, K. R., Deshpande, A. A., Radhakrishnan, V., et al. 1991, in Astronomical Society of the Pacific Conference Series, Vol. 19, IAU Colloq. 131: Radio Interferometry. Theory, Techniques, and Applications, ed. T. J. Cornwell & R. A. Perley, 6–9

Anderson, M. C., Keohane, J. W., & Rudnick, L. 1995, ApJ, 441, 300

Anderson, M. C., & Rudnick, L. 1995, ApJ, 441, 307

Bhatnagar, S., & Nityananda, R. 2001, A&A, 375, 344

Bracewell, R. N., Cooper, B. F. C., & Cousins, T. E. 1962, Nature, 195, 1289

Braun, R., Gull, S. F., & Perley, R. A. 1987, Nature, 327, 395

Brentjens, M. A. 2007, PhD thesis, University of Groningen

Brentjens, M. A., & de Bruyn, A. G. 2005, A&A, 441, 1217

Burn, B. J. 1966, MNRAS, 133, 67

Clark, B. G. 1980, A&A, 89, 377

Conway, R. G., & Kronberg, P. P. 1969, MNRAS, 142, 11

Cornwell, T. J. 1983, A&A, 121, 281

DeLaney, T., Rudnick, L., Stage, M. D., et al. 2010, ApJ, 725, 2038

Deshpande, A. A., Alessandro, F. D., & McCulloch, P. M. 1996, Journal of Astrophysics and Astronomy, 17, 7

Deshpande, A. A., & Radhakrishnan, V. 2007, ApJ, 656, 1038

Dodson, R., Lewis, D., McConnell, D., & Deshpande, A. A. 2003, MNRAS, 343, 116

Downs, G. S., & Thompson, A. R. 1972, AJ, 77, 120

Duncan, A. R., Reich, P., Reich, W., & Fürst, E. 1999, A&A, 350, 447

Fabian, A. C., Willingale, R., Pye, J. P., Murray, S. S., & Fabbiano, G. 1980, MNRAS, 193, 175

Farnes, J. S., Green, D. A., & Kantharia, N. G. 2013, ArXiv e-prints, arXiv:1310.7589

Finlay, C. C., Maus, S., Beggan, C. D., et al. 2010, Geophysical Journal International, 183, 1216

Gaensler, B. M., Dickey, J. M., McClure-Griffiths, N. M., et al. 2001, ApJ, 549, 959

Ginzburg, V. L., & Syrovatskii, S. I. 1969, ARA&A, 7, 375

Green, D. A. 2009, Bulletin of the Astronomical Society of India, 37, 45

Gull, S. F. 1973, MNRAS, 161, 47

Hankins, T. H., Kern, J. S., Weatherall, J. C., & Eilek, J. A. 2003, Nature, 422, 141

Harrison, E. R., & Tademaru, E. 1975, ApJ, 201, 447

Haslam, C. G. T., Klein, U., Salter, C. J., et al. 1981, A&A, 100, 209

Haslam, C. G. T., Quigley, M. J. S., & Salter, C. J. 1970, MNRAS, 147, 405

Heald, G., Braun, R., & Edmonds, R. 2009, A&A, 503, 409

Heiles, C., Perillat, P., Nolan, M., et al. 2001, Publications of the Astronomical Society of the Pacific, 113, 1274

Helmboldt, J. F., & Kassim, N. E. 2009, AJ, 138, 838

Högbom, J. A. 1974, A&AS, 15, 417

Hwang, U., Laming, J. M., Badenes, C., et al. 2004, ApJ, 615, L117

Isensee, K., Rudnick, L., DeLaney, T., et al. 2010, ApJ, 725, 2059

Johnston, S., Hobbs, G., Vigeland, S., et al. 2005, MNRAS, 364, 1397

Jun, B.-I., & Norman, M. L. 1996, ApJ, 472, 245

Kassim, N. E., Perley, R. A., Dwarakanath, K. S., & Erickson, W. C. 1995, ApJ, 455, L59

Keohane, J. W., Rudnick, L., & Anderson, M. C. 1996, ApJ, 466, 309

Kiepenheuer, K. O. 1950, Physical Review, 79, 738

Lai, D., Chernoff, D. F., & Cordes, J. M. 2001, ApJ, 549, 1111

Maan, Y., Deshpande, A. A., Chandrashekar, V., et al. 2013, ApJS, 204, 12

Mayer, C. H., & Hollinger, J. P. 1968, ApJ, 151, 53

Mayer, C. H., McCullough, T. P., & Sloanaker, R. M. 1962a, ApJ, 135, 656

—. 1962b, AJ, 67, 581

McCullough, P. R. 1993, AJ, 106, 797

O'Sullivan, C., & Green, D. A. 1999, MNRAS, 303, 575

Pavlov, G. G., Zavlin, V. E., Aschenbach, B., Trümper, J., & Sanwal, D. 2000, ApJ, 531, L53

Radhakrishnan, V. 1989, Royal Astronomical Society, Quarterly Journal, 30, 181

Radhakrishnan, V., & Deshpande, A. A. 2001, A&A, 379, 551

Radhakrishnan, V., & Roberts, J. A. 1960, Physical Review Letters, 4, 493

Ramkumar, P. S., & Deshpande, A. A. 1999, Journal of Astrophysics and Astronomy, 20, 37

Rees, M. J., & Gunn, J. E. 1974, MNRAS, 167, 1

Reichart, D. E., & Stephens, A. W. 2000, ApJ, 537, 904

Rosenberg, I. 1970, MNRAS, 151, 109

Roy, J., Gupta, Y., Pen, U.-L., et al. 2010, Experimental Astronomy, 28, 25

Saikia, D. J., & Salter, C. J. 1988, ARA&A, 26, 93

Sault, R. J., Hamaker, J. P., & Bregman, J. D. 1996, A&AS, 117, 149

Simard-Normandin, M., Kronberg, P. P., & Button, S. 1997, VizieR Online Data Catalog, 204, 50097

Sokoloff, D. D., Bykov, A. A., Shukurov, A., et al. 1998, MNRAS, 299, 189

Spoelstra, T. A. T. 1984, A&A, 135, 238

Sun, X. H., Reich, P., Reich, W., et al. 2011, A&A, 536, A83

Thorstensen, J. R., Fesen, R. A., & van den Bergh, S. 2001, AJ, 122, 297

Tucci, M., Carretti, E., Cecchini, S., et al. 2002, ApJ, 579, 607

van der Laan, H. 1962, MNRAS, 124, 125

Vivekanand, M., & Kulkarni, S. R. 1991, in Astronomical Society of the Pacific Conference Series, Vol. 19, IAU Colloq. 131: Radio Interferometry. Theory, Techniques, and Applications, ed. T. J. Cornwell & R. A. Perley, 1–5

Westerhout, G., Seeger, C. L., Brouw, W. N., & Tinbergen, J. 1962, Bulletin of the Astronomical Institutes of the Netherlands, 16, 187

Westfold, K. C. 1959, ApJ, 130, 241

Wielebinski, R. 2012, Journal of Astronomical History and Heritage, 15, 76

Wielebinski, R., & Shakeshaft, J. R. 1962, Nature, 195, 982

Wieringa, M. H., de Bruyn, A. G., Jansen, D., Brouw, W. N., & Katgert, P. 1993, A&A, 268, 215